Fabrication and Research of 3D Complex Scaffolds for Bone Tissue Engineering Based on Extrusion Deposition Technique

By

Zhichao Chen

A Doctoral Thesis

Submitted in partial fulfilment of the requirements

for the award of

Doctor of Philosophy of Loughborough University

June 2017

Abstract

Fabrication of scaffold is the key for bone tissue engineering, which is commonly regarded as the most potential route for repairing bone defects. Previously, porous ceramic scaffolds were fabricated through a variety of traditional methods, like moulding and casting, but most of them cannot produce customised tissue-engineered scaffolds. Therefore, 3D printing methods are gaining more attention and are currently being explored and developed to make scaffolds with acceptable biocompatibility.

With the considerable development of bone tissue engineering, the bio-imitability of scaffolds is becoming increasingly demanded, which leads to new methods and techniques to produce highly biomimetic bone scaffolds. In this study, a new fabrication process to optimise the structures of scaffolds was developed, and intensive researches were performed on the porous scaffolds to confirm their advantages in biological performance. Specifically, by combination of motor assisted extrusion deposition and gas-foaming (graphite as the porogen) technique, hierarchically porous scaffolds with improved microstructures, *i.e.* multi-scaled pores from nanometre to millimetre (nm-μm-mm), can be successfully fabricated.

In this thesis, the optimal content of porogen for scaffolds was studied in terms of compressive strength and in-rod porosities. The most concerned physicochemical properties of scaffolds were carefully examined, and the results revealed that such scaffolds exhibit excellent physicochemical properties owing to hierarchically porous structures. Due to additional in-rod micropores and increased specific surface area, along with better hydrophilicity, hierarchically porous scaffolds exerted complete superiority in biological activity, including promoting cellular proliferation of osteoblasts, adhesion and spreading status, as well as the ability to induce cellular differentiation.

Keywords*: Bone tissue engineering, 3D bio-printing, Hydroxyapatite, Graphite porogen, Hierarchical porosity, Biomimetic scaffold.*

Acknowledgements

I am grateful to my supervisor, Prof. Changqing Liu, for his kind guidance and constant support throughout the course of my Ph.D., particularly his incomparable contribution to this thesis and journal papers. I would also like to thank Prof. Xianglin Zhang (HUST) for giving me the opportunity to be seconded to China for part of my Ph.D. work. In addition, my appreciation goes to Dr. Yang Liu (co-supervisor) and Prof. Yufeng Zhang (WU) for the many helpful discussions along the course.

This doctoral thesis would not have been possible without the support of my warm-hearted colleagues. Firstly, I would like to thank Dr. Kui Zhou, Dr. Lei Shi and Dr. Wenchao Li (all from HUST) for their valuable advice throughout the project. In particular, my deep gratitude is given to Dr. Kui Zhou for his continuous help in most experiments. Besides, special acknowledgement would be given to Dr. Quan Wu and Mr. Wei Huang for their initial systematic characterisation of the extrusion machine. In HUST, I am grateful to Mr. Penghua Chen, Mr. Kang Liu, Mr. Kefeng Zhi and Dr. Chuanliang Cao for their wonderful collaborations in developing 3D bio-printer and other important equipment. While in LU, I am indebted to Dr. Ana Rodrigues-Rebelo, Dr. Nicholas Wragg and Prof. Mark Lewis for their technical consultation and practical implementation of biological evaluation. My appreciation also goes to Mr. Yang Yang in WU for his knowledge and assistance in cell culture.

Finally, I would like to express my heartfelt thanks to my family for their enthusiastic love, great understanding, endless patience and rich encouragement during all the years of this education. Furthermore, I want to specially appreciate my wife, Mrs. Meili Han, for her kind and unceasing support in my pursuit of a doctoral degree.

All in all, I am sincerely thankful for all of them.

Note: HUST -- Huazhong University of Science and Technology, LU -- Loughborough University, WU -- Wuhan University.

List of Publications

Journal Articles

1. **Zhichao Chen**, Xianglin Zhang, Yang Yang, Kui Zhou, Nicholas Wragg, Yang Liu, Mark Lewis, Changqing Liu. “Fabrication and characterisation of 3D complex hydroxyapatite scaffolds with hierarchical porosity of different features for optimal bioactive performance”. *Ceramics International, 2017, vol. 43, no. 1, pp. 336-344.*

2. **Zhichao Chen**, Xianglin Zhang, Kui Zhou, Hao Cai, Changqing Liu. “Novel fabrication of hierarchically porous hydroxyapatite scaffolds with refined porosity and suitable strength”. *Advances in Applied Ceramics*, 2015, vol. 114, no. 3, pp. 183-187.

3. **Zhichao Chen**, Xianglin Zhang, Penghua Chen, Wenchao Li, Kui Zhou, Lei Shi, Kang Liu, Changqing Liu. “3D multi-nozzle system with dual drives highly potential for 3D complex scaffolds with multi-biomaterials”. *International Journal of Precision Engineering and Manufacturing, 2017, vol. 18, no. 5, pp. 755-761.*

4. Kui Zhou, Xianglin Zhang, **Zhichao Chen**, Lei Shi, Wenchao Li. “Preparation and characterization of hydroxyapatite - sodium alginate scaffolds by extrusion freeforming”. *Ceramics International, 2014, vol. 41, no. 10, pp. 14029-14034.*

5. Kui Zhou, Chunfa Dong, Xianglin Zhang, Lei Shi, **Zhichao Chen**, Yanlin Xu, Hao Cai. “Preparation and characterization of nanosilver-doped porous hydroxyapatite scaffolds”. *Ceramics International, 2014, vol. 41, no. 1, pp. 1671-1676.*

6. Chunfa Dong, Kui Zhou, Xianglin Zhang, Hao Cai, Guangrong Xiong, Chuanliang Cao, **Zhichao Chen**. “Semen cassiae extract mediated novel route for the preparation of silver nanoparticles”. *Materials Letters, 2014, vol. 120, pp. 118-121.*

7. Kang Liu, Xianglin Zhang, Kui Zhou, Lei Shi, **Zhichao Chen**, Penghua Chen. “Preparation and evaluation of scaffolds prepared with bovine hydroxyapatite composites by 3D printing”. *Journal of Wuhan University of Technology*, 2017,

publication in press.

8. Cheng Luo, **Zhichao Chen**, Kui Zhou, Xinran Yang, Xianglin Zhang. “A novel method to significantly decrease the die roll during fine-blanking process with verification by simulation and experiments”. *Journal of Materials Processing Technology*, 2017, DOI: 10.1016/j.jmatprotec.2017.07.024.

9. Wei Wu, Hongzhi Cao, Hao Ou, **Zhichao Chen**, Xianglin Zhang, Zhonghan Luo, Shenlin Chen, Rongfeng Li. “Effects of punching process on crystal orientations, magnetic and mechanical properties in non-oriented silicon steel”. *Journal of Magnetism and Magnetic Materials*, 2017, DOI: 10.1016/j.jmmm.2017.07.003.

Authorised Patents

1. Penghua Chen, Xianglin Zhang, Yungan Wang, **Zhichao Chen**, Kui Zhou, Lei Shi, Wenchao Li, Xuan Wang. “A new bio-printer with multi-nozzles”. *C.N. Patent, Issued no. 201620155933.2, 2016.*

Conference Papers

1. **Zhichao Chen**, Kui Zhou, Lei Shi, Xianglin Zhang, Changqing Liu. “Novel fabrication of hierarchically porous hydroxyapatite scaffolds”. *International Conference in Advanced Manufacturing for Multifunctional Miniaturised Devices (ICAM3D), 2014, pp. 179-180.*

2. **Zhichao Chen**, Kui Zhou, Lei Shi, Penghua Chen, Xianglin Zhang, Changqing Liu. “Fabrication of highly biomimetic bone precursor by 3D bio-printing”. *International Conference in Advanced Manufacturing for Multifunctional Miniaturised Devices (ICAM3D), 2015, pp. 233-234.*

Table of Contents

Appendix. Development of 3D Multi-nozzle System Highly Potential

List of Figures

List of Tables

List of Abbreviations

3D	three-dimensional
3DP	three-dimensional printing
AC-SBF	acidic-corrected simulated body fluid
AM	additive manufacturing
AP	analytically pure
BET	Brunauer-Emmett-Teller
BMP	bone morphogenetic protein
BTE	bone tissue engineering
calcein-AM	acetoxymethyl calcein
C-SBF	corrected simulated body fluid
CAD	computer-aided design
CAM	computer-aided manufacturing
CATIA	computer-aided three-dimensional interactive application
CCK	cell counting kit
CPCG	cell-populated collagen gel
CPD	critical-point drying
CT	computed tomography
D	diameter
DAPI	4’,6-diamidino-2-phenylindole
DMEM	Dulbecco’s modified eagle medium
DNA	deoxyribonucleic acid
DOD	drop on demand
DSC	differential scanning calorimetry
Dv	discrete value
EDM	extrusion deposition moulding
EDX	energy dispersive X-ray analysis

ESP	electrospinning
F	force
F-actin	fibrous actin
FBS	foetal bovine serum
FDM	fused deposition modelling
FITC	fluorescein isothiocyanate labelled
FT	firing temperature
G	graphite/gravity
H	height
HA	hydroxyapatite
HA-G(-X)	hydroxyapatite and graphite (X vol.%) composite scaffold
HA-nG(-X)	hydroxyapatite and nano-graphite (X vol.%) composite scaffold
HA-μG(-X)	hydroxyapatite and micron-graphite (X vol.%) composite scaffold
HA-P	normal hydroxyapatite scaffold for control
HG-DMEM	high-glucose Dulbecco's modified eagle medium
HPMC	hydroxypropyl methylcellulose
HT	holding time
IGF	insulin-like growth factor
JCPDS	Joint Committee on Powder Diffraction Standards
L	length
LDPSA	laser diffraction particle size analyser
LDW	laser direct writing
MAM	motor assisted micro-syringe system
MRI	magnetic resonance imaging
MSC	mesenchymal stem cell
MTT	3-(4,5-dimethylthiazol-2-yl)-2,5-diphenyltetrazolium bromide
MW	molecular weight
NAP	negative air pressure

nG	nano graphite
NH_4-PAA	ammonium polyacrylate
OD	optical density
OpenGL	open graphics library
P	pressure
P/S	penicillin/streptomycin
PAM	pneumatics assisted micro-syringe system
PAP	positive air pressure
PCL	polycaprolactone
PDF-#	phase diffraction filter number
PDLLA	poly-(D, L-lactic) acid
PEG	polyethylene glycol
PGA	poly glycolic acid
PI	propidium iodide
PLA	poly lactic acid
PLGA	poly lactic-co-glycolic acid
PLLA	poly L-lactic acid
PMMA	polymethyl methacrylate
PS	polystyrene
PVL	polyvinyl alcohol
Q	quantity of flow
R	radius
RE	reverse engineering
RP	rapid prototyping
SA	sodium alginate
SBF	simulated body fluid
SEM	scanning electron microscope(y)
SFF	solid freeform fabrication

SLA	stereo lithography apparatus
SLS	selective laser sintering
SSA	specific surface area
STA	synchronous thermal analysis
STL	stereo-lithography
TCP	tri-calcium phosphate
TE	tissue engineering
TEM	transmission electron microscope(y)
TGA	thermal gravimetric analysis
TGF	transforming growth factor
TIPS	thermally induced phase separation
TRITC	tetramethylrhodamine B isothiocyanate labelled
TTCP	tetracalcium phosphate
UG	Unigraphics
UV	ultraviolet
V	velocity
W	weight
WST	water-soluble tetrazolium
XRD	X-ray diffraction
YAG	yttrium aluminium garnet
α-MEM	alpha modified eagle medium
μG	micron graphite
ρ	density
θ	contact angle
γ	surface tension
μ	viscosity

Chapter 1. Introduction

1.1 Research background

1.1.1 Repair of Bone Defect

In addition to serving as support of the human body, such as load bearing and conduction, human bone tissues can also protect internal organs, and participate in physiological processes including haematopoiesis and metabolism [1]. However, because of serious trauma, tumour resection, congenital malformation or infection of bone, large area of bone defects or relevant diseases may occur in human bone tissues [2]. For healthy adults, the average growth rate of bone tissues is quite slow, only about 1 μm per day, making it almost impossible to recover such large defects by self-repair [3]. According to statistics, more than 3.5 million Chinese people are suffering from different degrees of bone defects due to various reasons, for instance, traffic accidents, unintentional injuries, aging, bone diseases *etc.* [2]. There are more than 0.5 million clinical cases related to bone transplantation in U.S. every year, and the annual cost in orthopaedics, neurosurgery and dental defects is as much as 2.2 billion dollars [4]. Globally, the number of fracture cases can reach up to 15 million, and about 10% of these patients have to receive further surgery to get recover [5].

Currently, the most popular treatment for large bone defects is based on bone graft substitute. Besides, transplantation or implantation of bone graft is also an effective surgical procedures for the repair of bone tissues [6]. Generally, autografts, allografts, xenografts and synthetic materials are the most potential substitutes in terms of bone graft for clinical applications [7, 8]. Specifically, autograft refers to the harvest of tissues from the patient’s own donor site [9]. Because of no immune rejection after transplantation surgery, it is almost an ideal substitute for bone regeneration, which greatly improves the success rate of surgery and the process of postoperative recovery. Nevertheless, due to low availability and possible morbidity after transplantation, the clinical application of autograft is rather limited. Available alternatives are allografts (harvest of bone tissues from other patients) and xenografts (obtained from other species, *e.g.* bovine bone) [10], which are also very effective in terms of bone regeneration. But in allograft, there is high risk of disease infection from donors and immunologic rejection which requires additional immunosuppressant during recovery [11]. In spite of sufficient supply, such risk is even higher in xenograft due to different species. The best advantage of synthetics [12] is the adequate supply for patients, and they can just satisfy the demand of regeneration without obvious rejection from immune system. As synthetics are usually biologically inert and lack of bioactivity after implantation, the practical repair effect is merely acceptable. Even worse, they may induce foreign-body reaction in severe cases. In other words, constant technological innovation in synthetic materials is still necessary to expand the scope of clinical applications.

In view of graft substitutes from all resources, although the ratio of successful bone grafting can be 66% - 94%, only 20% of these cases could achieve desired treatment and recovery [12], mainly the result of insufficient biological properties, like self-repair ability, blood supply, and the adaptability to mechanical loading [13], which are fundamental for survival. All in all, the repair of bone defects by graft substitutes mentioned above is not as satisfactory as expected. As a result, development of bone graft substitutes through other techniques has already become one of current research hotspots, due to the limitations described above of autograft, allograft, xenograft and synthetic materials when applied in surgery.

1.1.2 Bone Structure and Regeneration

The regeneration process is closely related to the structure of bone tissues, as shown in Figure 1.1 and Figure 1.2 (anatomy). The periosteum is mainly composed of fibrous connective tissues, which is complex network of blood vessels rich in nerves and usually stimulates the process of bone growth and regeneration [14]. The periosteum is generally made of two layers. The outer layer is dense and contains numerous collagen fibres with high tensile and flexural strength, which serve as the framework for bone [13]. The collagen fibres (about 500 nm in length) are made of orderly arranged protein chains, usually of nanometre size (~ 10 nm) with a triple helix structure [15]. The inner layer is much loose, containing osteoblasts and osteoclasts, which play main role in generating new bones and absorbing the non-required bones respectively [16].

$$\textit{Bone tissue}\begin{cases}\textit{Periosteum}\text{: }\textit{fibrous connective tissue (vessel, nerve, osteoblast)}\\ \textit{Bone matrix}\left.\begin{cases}\textit{Compact bone}\text{: }\textit{white, dense and compact}\\ \textit{Spongy bone}\text{: }\textit{red, porous and honeycomb}\end{cases}\right\}\textit{main component}\\ \textit{Marrow}\begin{cases}\textit{Yellow marrow}\text{: }\textit{in marrow cavity}\\ \textit{Red marrow}\text{: }\textit{responsible for haematopoiesis}\end{cases}\end{cases}$$

Figure 1.1 Structure of bone tissues

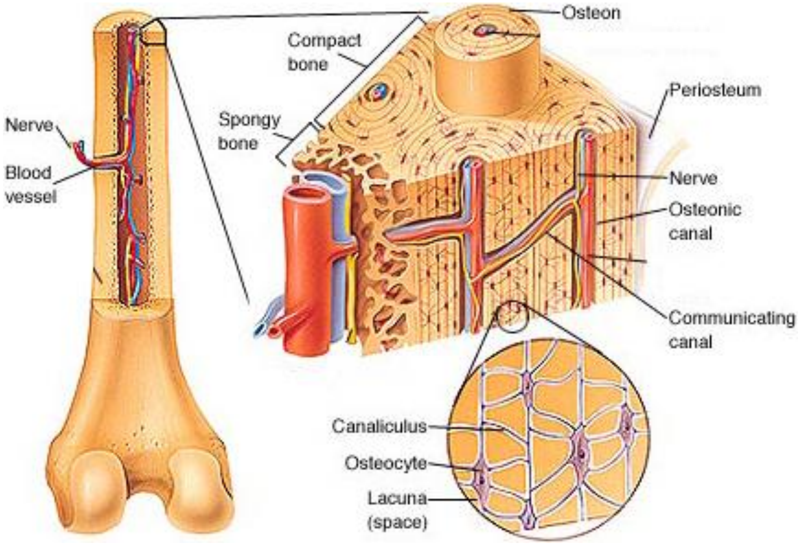

Figure 1.2 Anatomical diagram of bone tissue (from mhhe.com)

Compact bone and spongy bone are the two types of bone [17]. Usually distributed on the surface, compact bone is known for high mechanical strength owing to dense structure, which bears load with large capacity of compression. As its name implies, spongy bone is internally porous with a network of trabeculae with massive macropores, much similar to a sponge [18]. The two kinds grow proportionally together to form a bone. Bone marrow (within the gap of spongy bone and marrow cavity) also has two main types, *i.e.* red marrow and yellow marrow [17]. Red bone marrow is responsible for haematopoiesis, thus there is only red marrow in children. In adult life, part of red marrow will be replaced by adipose tissues, which will later develop into yellow bone marrow (without the ability of haematopoiesis). Interestingly, yellow marrow can reverse to red marrow to recover haematopoiesis in case of bleeding.

If a mature bone is slightly damaged, the biochemical activity of osteoblasts would become more active to repair the defect, which is called osteogenesis (bone formation). In general, the mechanism of osteogenesis is rather complicated [19-21], but it can be easily understood from the angle of the interaction of bone formation (osteoblasts) and absorption (osteoclasts), as illustrated in Figure 1.3. To be more specific, in junior age, the formation of bone is much more active than bone absorption (osteoblast > osteoclast), resulting in bone growth. For an adult, the activity of osteoblasts and osteoclasts are in dynamic balance (osteoblast ≈ osteoclast) [20]. In addition, once damage or defect of bone occurs, more osteoblasts would be activated to promote osteogenesis (*i.e.* osteoblast > osteoclast) [22]. However, if the damage or defect exceeds a threshold, it cannot be repaired by self-remodelling [23]. When it comes to senior age, osteoblasts become less active than osteoclasts (osteoblast < osteoclast), and osteoporosis occurs due to higher resorbing rate, so it is more difficult for the old to achieve self-repair once there is bone defect. As we can see, the key in terms of bone formation is the activity of osteoblasts, which must be higher than osteoclasts. For example, Calvi *et al.* found that regenerative medicine could be used to stimulate the body to activate more osteoblasts in order to re-build the natural three-dimensional and hierarchical architecture of bone [24].

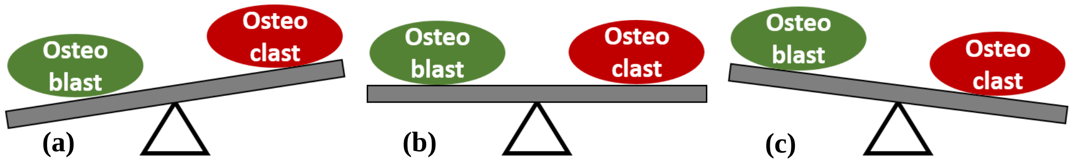

Figure 1.3 Interaction of osteoblasts and osteoclasts at different ages: (a) junior, (b) adult, (c) senior

In the process of osteogenesis, osteoblasts, which differentiates from stem cells, firstly generate collagen fibres and osteoid through the secretion of saliva protein, chondroitin sulphate, lipid, *etc*. [25]. Embedded by osteoid, some osteoblasts will then gradually differentiate into osteocytes with the deposit of calcium, also known as calcification of osteoid, which forms new bone tissue. The main calcium component of bone is hydroxyapatite (HA, needle-shaped crystal) in parallel arrangement along collagen fibres [3, 7]. The process will continue to carry on until the bone has been completely formed. In summary, the formation and calcium deposition of osteoid is the necessary prerequisite to osteogenesis.

1.1.3 Bone Tissue Engineering

The increase of life expectancy determines a rising demand for biological alternatives other than autograft, allograft or xenograft. Fortunately, a paradigm shift from tissue replacement to regeneration through tissue engineering (TE) could provide a solution for such difficulties [26]. A commonly applied definition of TE, as stated by Langer and Vacanti, is “an interdisciplinary field that applies the principles of engineering and life sciences toward the development of biological substitutes that restore, maintain, or improve the function of biological tissue or a whole organ” [27]. Specifically, TE that applied to bone regeneration by developing a tissue-engineered implant is called bone tissue engineering (BTE) [28-32] (Figure 1.4), which have captured significant public attention and scientific imagination to its potential application in bone regeneration. It has been reported that tissue engineering approaches with various combinations of bioactive materials, for instance, proteins, cells and genes, are very promising in terms of as alternatives to bone grafts to restore the function of damaged or degenerated bone [30]. Bone tissue engineering, usually based on biomaterial scaffold, aims to either induce generation of bone from surrounding tissue or provide a template for implanted cells to form bone [29]. In other words, it requires a scaffold beneficial to the adhesion of cells and maintenance of function, as well as a rich source of osteoprogenitors and selected osteoinductive growth factors in BTE [31]. Several critical components are essential for bone regeneration in BTE: bone morphogenetic protein (BMP), osteoblasts in response to bone formation, suitable carrier of biological signals (*i.e.* scaffold, delivering signals to specific sites, and later serving as template for ingrowth of bone cells), and a viable and systematically vascularised environment [30].

The intensive research on BTE could **a)** supervise bone regeneration after transplantation or implantation; **b)** help understand the physiochemical influence factors of cellular responses to scaffolds, and design biomaterial interfaces that could direct cellular proliferation and differentiation; and **c)** enable researchers to attempt different approaches to form new bones.

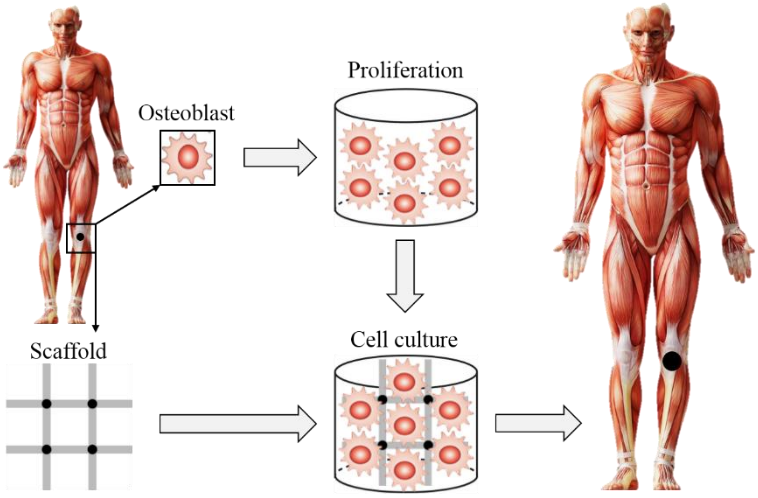

Figure 1.4 Schematic of bone tissue engineering

1.2 Problem Statement and Research Motivation

BTE has been widely accepted as a potential approach to repair bone defects, where the key is the fabrication of biocompatible scaffold. No wonder more researchers are exploring various methods to fabricate scaffolds with satisfactory performance in TE. Most of these works are often through 3D bio-printing or combining rapid prototyping (RP) with other technologies. However, with the development of BTE, the requirement of bio-imitability is becoming increasingly demanded, which is difficult for traditional methods and even additive manufacturing (AM) technology to satisfy. In order to fabricate highly biomimetic bone scaffolds, the following challenges related to preparation and characterisation need to be overcome.

(1) Optimising currently available fabrication methods. Although commercial solid freeform fabrication (SFF) system can be used, it can only achieve simple models, such as cuboid and cylinder, which is obviously unable to satisfy the basic requirement of individualisation and customisation for bone scaffolds. This requires considerable knowledge in mechanical design, programming and algorithm, making this study of interdisciplinary nature.

(2) Achieving a balance between mechanical and biological properties. The mechanical strength and biological performance of HA scaffolds strongly rely on microstructures mainly determined by manufacturing and sintering process. For instance, high temperature normally results in improved mechanical strength; while recent research suggests that highly densified scaffolds tend to exhibit poor performance in BTE. However, high porosity and large pores (beneficial to bioactivity) often lead to low mechanical strength. Therefore, it is of great necessity yet with significant challenge to achieve a balance between mechanical and biological properties.

(3) Developing a new method to fabricate highly biomimetic bone scaffolds. Due to the widely known limitations of traditional preparation techniques, it is almost impossible to produce scaffolds with full consideration of porosity, pore size and mechanical strength. Taking moulding or casting as a typical example, it is difficult to ensure the interconnectivity of macropores as required on the basis of clinical applications. And even recently developed 3D printing techniques are not able to produce porosity in nano-scale, limiting their practical uses in medical science. Hence, new methods to prepare biomimetic bone scaffolds are highly demanded.

(4) Obtaining fine control of porosity and pore structures. Generally, it is quite easy and simple for most 3D bio-printing techniques to gain fine control of macro porosity and pore structures. Nevertheless, most of them become difficult to form pores at micron and nano scale, beyond their capable precision. Despite that some phase separation methods can produce microporosity on scaffolds, the distribution of micro- and nano-pores is hardly controllable. Consequently, further research and development are necessary to enable the creation of biomimetic pore structures.

(5) Determining the advantages of improved scaffolds. Given that the pore structures of improved scaffolds were closer to natural bones, it is hard to conclude that such scaffolds were surely advantageous over the real scaffolds in terms of physicochemical and biological properties, such as biodegradability, hydrophilicity, osteoinduction *etc*. Thus another research motivation is to characterise the actual performance of improved scaffolds to verify the superiority of biomimetic pore structures with reliable and repeatable results.

1.3 Research Aims and Objectives

This thesis mainly aims to address the knowledge gaps with respect to preparation of highly biomimetic bone scaffolds to enhance the repair effect of bone defects. Prior to the fabrication of scaffolds, the SFF system and sintering process must be intensively investigated to ensure the eligibility and validity of scaffolds. The objectives against the aims are therefore stated below:

(1) To upgrade current fabrication system with auto pre-treatment of complicated 3D models, such as 3D transformation, slicing, path planning *etc*.

(2) To determine the most proper holding temperature for the sintering process of HA scaffolds with full consideration of mechanical and biological properties.

(3) To develop a new method to make highly biomimetic bone scaffolds with complex 3D structures that mimic natural bone tissues.

(4) To characterise the physicochemical and biological properties of improved scaffolds in comparison with normal scaffolds, so as to verify their advantages and potentials in BTE.

(5) To study the influence of porosity with different features of microporosity on bioactivity for further optimisation of the fabrication process.

1.4 Contributions to the Body of Knowledge

The main contributions of this study to the body of knowledge are shown as below:

(1) The influence of sintering temperature on the microstructures, physical / chemical / biological properties of scaffolds for BTE were systematically investigated for the first time. This study suggests that high mechanical strength should not be the main criterion for sintering process, since the scaffolds sintered at high temperature may inhibit the deposition of bone-like apatite and adsorption of proteins, and eventually the process of osteogenesis. In this case, the sintering temperature of HA scaffolds should take full account of mechanical properties and bioactivity.

(2) A novel method to fabricate 3D complex scaffolds with hierarchically porous structures by combination of extrusion deposition and gas forming technique was developed. For BTE, this method shows great potential to produce highly biomimetic scaffolds without further sophisticated treatments, which are characterised by hierarchical pore structures (nm-μm-mm) and considerable bulk porosity. In addition, the amount of additional in-rod porosity is able to be finely controlled by adjusting the content of porogen as well.

(3) The influence of shrinkage caused by drying and sintering process on overall / pore size and porosity was analysed in separation for the first time. Generally, only the total shrinkage (caused by drying and sintering process) was concerned. However, we found the separate analysis of drying and sintering shrinkage are also useful. To be more specific, the additional in-rod and bulk porosity of scaffolds were mainly influenced by sintering, while little difference was observed in drying process. Therefore, this study directs a new way to finely control the overall/pore size and porosity of scaffolds.

(4) Scaffolds of significant difference in features and characteristics of hierarchical porosity, *e.g.* the ratios between microporosity and nanoporosity, were researched respectively for the purpose of optimal pore structures. The difference in the ratios of microporosity and nanoporosity would significantly influence the biological performance of scaffolds, especially in biodegradation, cellular interactions and differentiation, regardless of slight impact on adhesion and proliferation. In view of the influence of microporosity and nanoporosity, this work can pave the way for further optimisation of bone scaffolds.

1.5 Thesis Structure

The overall thesis structure is summarised in Figure 1.5. Chapter 1 briefly introduces the research background of this study. Chapter 2 mainly reviews the current research focus in terms of scaffolds for BTE, such as materials, properties, fabrication and improvements. Based on an intensive literature search, scaffolds with hierarchically porous structures were proposed for the purpose of promoting bio-imitability. In Chapter 3, it gives the details of a newly developed fabrication system for bone scaffolds made of bioceramics. And the influence of sintering temperature on the physicochemical and biological performance was studied in Chapter 4. Chapter 3 and Chapter 4 can be regarded as the preparatory work of the subsequent 3 chapters. Chapter 5 presents the detailed preparation process of hierarchically porous scaffolds by combining SFF technique and gas-foaming,

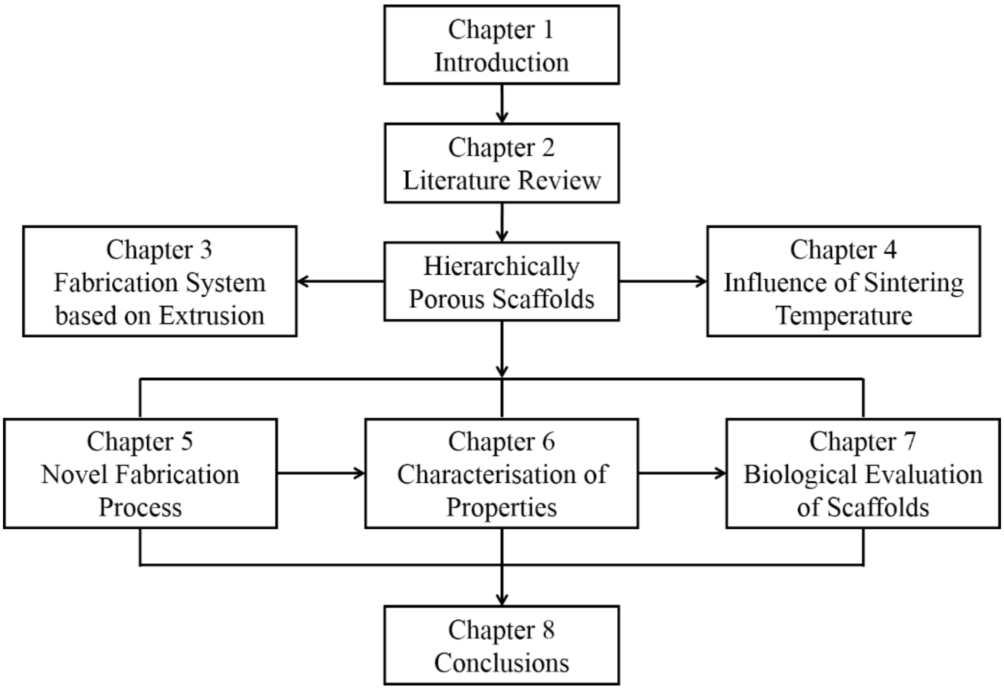

Figure 1.5 Thesis structure

followed by Chapter 6 and Chapter 7, which characterise, evaluate and verify the advantages of hierarchical porosity from the aspect of physicochemical and biological properties respectively. Finally, this thesis ends with conclusions in Chapter 8, where in particular, the specific work for future research can be found.

Chapter 2. Literature Review of Bone Scaffolds

This chapter mainly reviews the research focused on scaffolds for BTE and identifies the challenges towards fabrication of highly biomimetic scaffolds using current techniques.

2.1 Introduction

Scaffold, which provides a template and space for cellular interactions and the formation of extracellular matrix to support newly formed tissues, is a key component in BTE [33]. Actually, scaffolds mainly serve as osteoconductive moieties for bone, since newly formed bone would be deposited through creeping substitution of bone living nearby [34]. It was reported that tissue-engineered constructs generated *ex vivo* by combination of scaffolds, cytokines and cells could provide more effective osteogenesis *in vivo*, compared to that by matrix biomaterials alone [33]. The past 30 years has witnessed a faltering array of biomaterials proposed as "ideal" scaffolds for enhancing cell growth, yet only few have reached the expected clinical efficacy [31].

The general criteria that an ideal scaffold for BTE should meet are listed as following. 1) ***Porosity***: scaffolds should provide template with 2D or 3D supports (porous structure) for bone ingrowth and delivery channel of nutrients [35]. 2) ***Biodegradability***: scaffolds can be absorbed at a reasonable rate coordinative to the process of bone regeneration, and the decomposers should be non-toxic and easily excreted [36]. 3) ***Biocompatibility***: scaffolds should promote the adhesion and interactions of bone cells without cytotoxicity during cell culture [37]. 4) ***Osteoinductivity***: scaffolds should induce and stimulate osteogenesis at the genetic level [38]. 5) ***Stability***: scaffolds should form a stable interface by bonding to the host bone without scar tissues [39]. 6) ***Strength***: newly formed bones exhibits similar mechanical properties (*e.g.* compressive strength, elasticity modulus, stiffness *etc.*) to the host bone after cell culture or TE *in vitro* [40]. 7) ***Customisation***: the scaffolds should better be produced by a RP technique (like SFF), which allows customised design to match bone defects [41]. 8) ***Repeatability***: the production of scaffolds should have the potential to be commercially producible and sterilisable on the condition of satisfying the international standards of clinical use [42]. 9) ***Bioactivity***: scaffolds should supply the essential biological factors, such as insulin-like growth factor (IGF), BMP, transforming growth factor (TGF) *etc*., to promote the proliferation and differentiation of osteoblasts during generating bone matrix from bone precursors [34].

In addition, as a substitute for implantation, scaffolds for BTE must exert certain biological activities, mainly in terms of promoting adhesion, proliferation and differentiation of osteoblasts, so as to achieve the purpose of bone regeneration or repair [3]. Generally, **cellular adhesion** refers to the process that cells interact and attach to a surface, substrate or another cells, which is mediated by interactions between molecules of cell surface. It usually occurs from the action of transmembrane glycoproteins, such as selectin, integrin, syndecan, cadherin and so on [43]. Cellular adhesion is important to preserve multicellular structure, as it can link cells in different ways and play vital role in signal transduction [43]. **Cell proliferation**, or growth of cell populations, often happens along with cell division, which goes through a particular type of exponential growth called doubling [44]. Theoretically, the cellular number of every generation should be twice of the previous, although actually it only gives a maximum figure because not all cells could survive in each generation. Proliferation is one of the most important characteristics in living creatures, which contributes to maintaining the numerical balance of individual cells, as well as normal function. Moreover, the recovery of wound or damage, tissue regeneration and pathological repair has to rely on proliferation [45]. During **cellular differentiation**, a cell usually changes from a type to another more specialised one [46]. Therefore, differentiation would dramatically change the size, shape, membrane potential, metabolic activity, and responsiveness to signals of cells, which are highly controlled by the selective expression at genetic level in time and space [46]. Basically, cellular differentiation is embodied in the production of functional proteins. For example, the differentiation process of MSCs into osteoblasts, also known as osteoinduction, is regulated by osteoinductive proteins such as BMP [47].

It is commonly accepted that the scaffolds for BTE should have at least one of the following biological characteristics: 1) **osteoconduction** [48], providing an interface for bone regeneration and vascularisation, and for the conjunctions of newly formed and host bone tissues; 2) **osteoinduction** [47], which means the scaffolds can induce the differentiation of MSCs into osteoblasts under the stimulation of osteoinductive proteins (like BMP-2), thus making it the key indicator for evaluation of biological activity in BTE; and 3) **osteogenesis** [49], being able to promote the formation of bone tissues on the condition of sufficient in-growth of bone cells (osteoblasts or osteoprogenitors) and appropriate extracellular environment for osteogenesis.

2.2 Available Bio-materials for Scaffold

Recently, significant advancements have been made in material science and technology. According to the studies of Hench [26] and Rose [31] *et al.*, bioceramics and a large number of biomaterials (*e.g.* polymers, metals) have been accepted as candidate materials for scaffolds, which can effectively stimulate the differentiation and conduction of bone tissues as well.

2.2.1 HA and Tri-calcium Phosphate

Due to excellent biocompatibility (especially osteoinductivity) and performance as substitutes in BTE [50, 51], calcium phosphate, such as HA ($Ca_{10}[PO_4]_6[OH]_2$) and tri-calcium phosphate (TCP, $Ca_3[PO_4]_2$), has been widely researched [7, 48, 52-54]. In addition, a wide variety of calcium phosphate ceramics besides HA and TCP are available, owing to the fast development of biocompatible and biodegradable synthetics [55].

As the main mineral component of bones and teeth, HA has the potential to be the most applicable bioceramic material for substitute implants of hard tissues in terms of biocompatibility. In addition, HA also exhibits excellent biocompatibility with skin and muscle tissues without any toxic effects. Moreover, HA can directly integrate with bones [56]. Nonetheless, due to low fatigue resistance, particularly in humid environments, HA is currently not suitable to the application of teeth that requires frequent load-bearing with high humidity [56]. Besides, HA is generally regarded to be non-biodegradable in neutral environment as it cannot be decomposed in short term after implantation during TE [57, 58]. The non-biodegradability of HA is critically disadvantageous to the host tissues surrounding the scaffolds made of HA. Thus β-TCP has been developed for a biodegradable substitute to HA, which can be quickly degraded *in vivo* [54]. On the other hand, many researchers were attempted to properly control the degradation rate by adjusting the mass ratio of HA versus β-TCP [59, 60]. According to Sánchez-Salcedo *et al*. [59], the best mass ratio of in composite materials (HA/β-TCP) is 7 : 3, when it comes to achieving an optimal balance between biodegradability and osteoinduction.

2.2.2 Biodegradable Polymer

Biodegradable polymer is also very popular for bone scaffolds [61]. Generally speaking, there are two types of biodegradable polymers: natural-based materials and bio-fibres. Polysaccharides (such as starch, chitin/chitosan, hyaluronic acid derivatives, alginate *etc*.) or proteins (like soy, fibrin, silk, collagen, gels and so on) are in the first category [62]. More detailed description of bio-fibres can be found in the review report by Mohanty *et al*. [63].

Saturated poly-α-hydroxyl esters, including poly glycolic acid (PGA), poly lactic acid (PLA) and poly lactic-co-glycolic acid (PLGA), are the most commonly utilised biodegradable synthetic polymers for three-dimensional scaffolds at present [62]. The development of biodegradable composite scaffolds based on PLA, PGA and PLGA contributes to overcoming the well-known limitations associated with biodegradability, inflammatory and immunologic reactions when used as carriers for osteoinductive factors [64]. Benefiting from the chemical composition of polymers, they usually degrade through de-esterification *in vivo,* and the monomeric components produced by degradation (*e.g.* lactic and glycolic acids) could be easily cleaned via natural pathways such as metabolism [61]. For instance, PGA will decompose to metabolites, while PLA can also be eliminated through tri-carboxylic acid cycle. As a result, PLA and PGA is absolutely biocompatible. Interestingly, the degradation rates, mechanical and physical properties of PLA/PGA are controllable over a wide range with appropriate addition of other copolymers.

Yet there are also some disadvantages for bone scaffolds: a) because of low mechanical strength and high degradation rate, polymers may fail prematurely during bulk erosion; b) to improve the mechanical properties, polymers are often treated with chemical modification (usually cross-linking), which may result in cytotoxic effects and poor biocompatibility; and c) worse still, abrupt release of acidic degradation products may cause strong inflammatory response after implantation [65].

2.2.3 Bioactive Glass

In 1969, Hench *et al*. [66] found that certain glass compositions also had excellent biocompatibility and osteoconduction. To be more specific, carbonated phosphate layer could be developed on the surface of bioactive glass, through mediated and interfacial reactions with cells, which enables glass composites to be chemically attached on host bones when calcium deficiency happens. Of great significance and influence for TE applications is that bioactive glasses could either support the activity of enzyme [67], induce the process of vascularisation [68], or enhance the adhesion and growth of osteoblasts, as well as promote the differentiation of mesenchyme (mesenchymal stem cells, MSCs) into osteoblasts [69].

Basically, the general components of bioactive glasses are SiO_2, Na_2O, CaO, and P_2O_5. Hench published a detailed overview about different compositions of bioactive glasses and their corresponding bioactivities [70]. Particularly, 45S5-Bioglass® [71] consists of 45 wt.% SiO_2, 24.5 wt.% Na_2O, 24.4 wt.% CaO and 6 wt.% P_2O_5. It was found that the degradation products of bioactive glasses, especially 45S5-Bioglass®, could up-regulate the genetic expression that commands osteogenesis and secretion of growth factors [45, 71], which is a significant finding for BTE. Besides, the structure and chemistry of glasses are possible to be tailored at molecular level by changing chemical composition, or through thermal and environmental processing.

However, the crystallisation of bioactive glasses may decrease the bioactivity and even turn themselves into inert materials, which is a critical disadvantage that restricts the application of bioactive glasses as scaffold materials, since full crystallisation usually occurs prior to densification during sintering process [61].

2.2.4 Metal and Alloy

In recent years, with the development of materials and technology, more and more commercially available and mature metals and alloys are applied to BTE. The representative members of them are titanium (Ti), magnesium (Mg) and tantalum (Ta), along with their alloys. Ti and its alloys have been widely studied and used in the repair of bone fracture, owing to high rigidity and strength, excellent ductility, biocompatibility, and corrosion resistance [72-74]. For instance, Wen *et al*. [74] found that new bone tissues would grow inwardly along the pore structure of 3D porous scaffolds made of titanium, resulting in close connection with host bones. Mg and its alloys are becoming a research hotspot in terms of implantation materials recently, because of favourable formability, biodegradation and bioactivity *in vivo* [75-77]. In addition, magnesium is an essential nutritional element of the human body, and it is almost involved in all of the metabolic activities by activating a variety of enzymes and participating in the generation of polypeptides [78]. Ta is famous for its advantages in hardness, abrasion and corrosion resistance, chemical stability, biocompatibility, and no adverse stimulation to human body [79], thus mainly used in production of cardiac pacemaker, vascular clip femoral prosthesis, and the filling material for bone defect.

But the drawbacks of metals and alloys are obvious. To name just a few, the biological activity is less satisfactory than the other biomaterials, especially in osteogenic ability and the interaction with bone cells [80], which limits the research and application in BTE.

2.3 Important Properties

2.3.1 Porosity

Kuboki *et al*. [35] fully verified the necessity for porosity in osteogenesis through an ectopic model of rat and intensive research of BMP-2 (BMP type-II) delivery by implanting macro HA scaffolds (both solid and porous). It turned out that direct regeneration of bone occurred in the porous group, while no formation of new bone was found on the solid ones. Svehla *et al*. [73] provided further support for this by the studies of comparison with porous-coated metal implants and non-coated ones. They found that a porous coating of sintered titanium beads (Porocoat®) on the surfaces improved the repair effect of cortical implants recovered from sheep tibiae, while solid implants without coating did not have expected enhancement. Not coincidentally, Harvey *et al*. [81] also discovered that Ti-fibre coated porous scaffold with moderate porosity (approximately 45%) and macropores (about 350 μm in average) could maximise the osteogenesis and increase the potential for bone absorption of femoral stems in an arthroplasty model of canine total hip. Besides, Chang *et al*. [72] also got a similar result by plasma spray coating of titanium implants with 56% - 60% porosity. They found that bone ingrowth was maximised if coated with a Ti-fibre mesh (open porosity of 60% and pore size of 170 μm in average) and polyvinyl alcohol (PVA) hydrogel through plasma spray.

Although macroporosity (most pore sizes are larger than 50 μm) exerts a great influence on osteogenic generation, Yuan *et al*. [82] indicated that the importance of microporosity (pore sizes < 10 μm) as well as wall roughness should never be neglected. According to their research, HA scaffolds (~ 200 μm in size) with dense rods and smooth walls failed to induce ectopic bone regeneration in dogs; on the contrary, HA scaffolds with porous structure (about 400 μm) and rough walls succeeded in producing osteogenesis. As they explained, larger surface area resulted from microporosity contributes to higher exchange rate of nutrients, more efficient absorption of BMP, and faster formation of bone-like apatite through degradation and calcification; while wall roughness, on the other hand, could promote the adhesion, proliferation and differentiation of osteoblasts during cell culture [82].

2.3.2 Pore Size

100 µm was initially defined as the minimum pore size of porous scaffold by Hulbert *et al*. [83]. And many researchers also had tried to explore larger range of pore sizes (more or less than 100 µm) so as to find out the influence of pore sizes on BTE [84, 85]. For instance, Tsuruga *et al*. [84] prepared a series of porous HA blocks with different pore sizes (*[106 - 212]*, *[212 - 300]*, *[300 - 400]*, *[400 - 500]*, and *[500 - 600]*; unit: µm) to be implanted subcutaneously in rats. It was found that the range of *[300 - 400]* was the critical size, not only because capillaries were obviously observed, but also the activity of alkaline phosphatase, the content of osteocalcin and the rate of osteogenesis were the highest among the series. In addition, scaffolds with pore sizes lower than the accepted minimum (100 µm) were compared by Liu *et al*. [85], which also resulted in excellent osteogenesis in repairing rat calvarial defects when increasing pore size from 35.4 to 45.7 µm.

Another interesting point of such effect in terms of pore size lies in the progress of bone regeneration [33]. Kuboki *et al*. [86] once designed honeycomb shaped HA scaffolds with small (90 - 120 µm) and large (~ 350 µm) tunnel diameters for BMP-2 delivery and subcutaneous implantation in rats. At last, new bone was formed directly in scaffolds with larger diameter; while only chondrogenesis occurred without osteogenesis in smaller tunnels. According to their analysis, the enhanced vascularisation observed in tunnels of larger diameter contributed to more favourable conditions for direct osteogenesis, such as higher concentration of oxygen and nutrient supply. Moreover, the geometry of pores may also have great impact on direct osteogenesis. As reported by Jin *et al*. [87], bone formation only existed on the outer surface of the HA scaffolds with long and curved pores, which hindered the penetration of mesenchyme and capillaries; while mature generation of new bone was found in the scaffolds with complex and open porosity.

2.3.3 Mechanical Properties

In addition to porosity and pore sizes when developing scaffolds, the role of mechanical properties should also be considered, especially in the realm of applications require load-bearing function. It is commonly known that scaffolds with excellent mechanical properties are favoured in products for hard tissues, such as bone and teeth. Moreover, mechanical loading is also important in cartilage formation, which regulates the metabolic process of chondrocytes *in situ* [88]. In recent years, the role of mechanical stimuli *in vitro* has captured increasing attention in the development of tissue-engineered cartilage [89-91]. For example, Lee *et al*. [89] found that, even isolated from cartilage and cultured in hydrogels, chondrocytes were capable of responding to mechanical loading as well, although Buschmann *et al*. [90] reported that the stimulus of mechanical loading after depositing an extracellular matrix within non-native environment was valid merely on the condition of being given enough time. Besides, mechanical loading of chondrocyte cultures and hydrodynamic shearing of polymer constructs is able to improve the histologic and mechanical properties in long term; yet short-term mechanical loading of chondrocytes seeded into PGA scaffolds also showed an increase in the generation rate of proteoglycans [91]. Furthermore, improved mechanical properties will ultimately promote bone formation by creating a stable interface and connection with host bones [92]; so it is essential to possess similar mechanical properties (*e.g.* compressive strength, elasticity modulus, stiffness *etc*.) to host bones after cultured *in vitro* for BTE [93]. In summary, mechanical strength must be considered in well-designed 3D porous scaffolds to enable load-bearing function in bone tissues.

2.3.4 Other Factors

Another important factor is the interconnectivity of pores. The potential advantages of hierarchical structures with interconnected pores in scaffolds were interpreted in Ref. [13, 77]. However, the complexity of architecture and the variability of properties (*e.g.* mechanical properties, mineralization, gradient feature of cytokines *etc*.) establish the major challenges in fabricating bio-mimetic scaffolds [37]. In addition, much more individual factors, such as age differences, diverse activities, current nutrition status, and personal disease, may also be considered to meet the specific demand of every patient [33].

2.4 Preparation Techniques

On the whole, the widely applied preparation techniques of scaffold can be classified into two types: phase separation and additive manufacturing.

2.4.1 Phase Separation

The basic principle of phase separation technique is to separate the sacrificial phase from scaffold base through physical or chemical routes to form desired (usually porous) structures.

2.4.1.1 Thermally induced phase separation

Thermally induced phase separation (TIPS) is currently the most popular phase separation technique to make porous scaffolds [94]. TIPS generally refers to thermal stratification of a homogeneous solution of polymer solvent into two separated phases, *i.e.* the polymer-rich and polymer-poor phase, either by exposing the solution to another immiscible solvent or by cooling it to the temperatures under the bimodal solubility curve (shown in Figure 2.1(a)) [95].

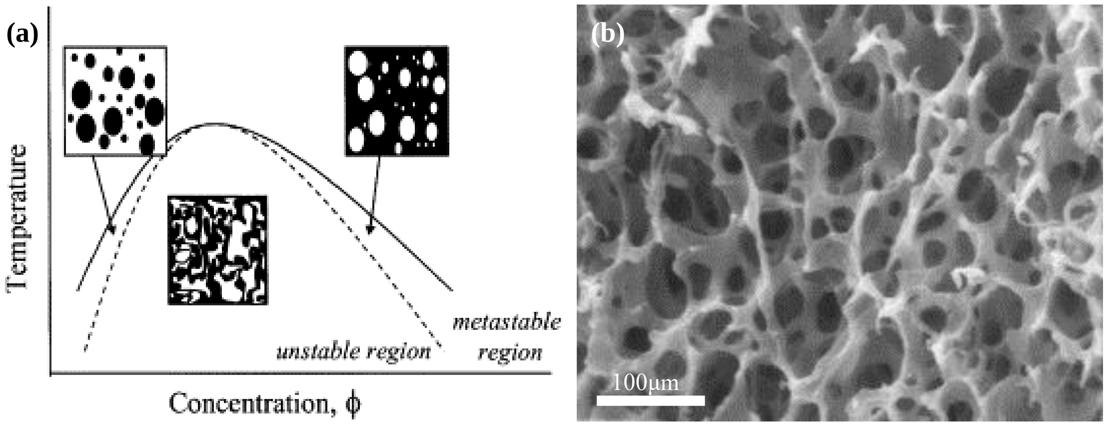

Figure 2.1 TIPS: (a) technical principle, (b) morphologies of a sample

The most attractive advantage of TIPS is that the porous structures could be easily controlled via adjusting different thermodynamic and kinetic parameters [96]. Nam *et* *al*. [95] once applied the TIPS technique to prepare porous scaffolds for bone generation (Figure 2.1(b)). There are also many studies about microporous and isotropic morphologies in response to a minor change of TIPS parameters. However, whether the microporosity and interconnectivity can be available throughout the scaffolds has not been reported yet. As mentioned before, they are essential parameters of scaffolds for osteogenesis and vascularisation in BTE. Therefore, it limits the application of TIPS in preparation of scaffolds a great deal.

2.4.1.2 Freeze drying

Similar to TIPS, the mechanism of freeze drying is based on the phase diagram of water, that is, vapour (gas) - water (liquid) - ice (solid), as shown in Figure 2.2(a) [97]. The solution composed of water and polymer will firstly be exposed to a temperature low enough for freezing; after quick exposure to room temperature, the ice will preferably become vapour instead of liquid water, resulting in porous structures. Obviously, the porous structures obtained in this way have to be carefully maintained. Figure 2.2(b) shows the scaffold prepared by Wu *et al*. [98] with freeze drying method. Unfortunately, the whole fabrication process of scaffolds is too time-consuming and laborious to be efficient and economically competitive. Another common problem is the occurrence of surface skin, restricting the practical application of freeze drying in BTE as well. In addition, the temperature must be controlled low enough so that the polymer could resist

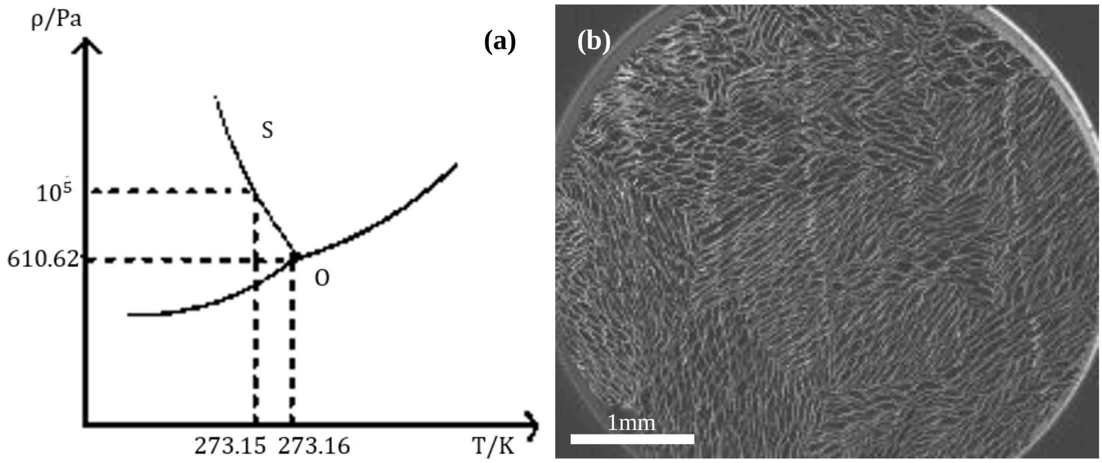

Figure 2.2 Freeze drying: (a) technical principle, (b) morphologies of a sample

the interfacial tension caused by evaporation of solvent. In practice, liquid nitrogen has to be constantly used to prevent the elevation of temperature [99], which increases the cost of freeze drying on the other hand.

2.4.1.3 Salt leaching

Salt leaching has been widely known for easiness and usability [100], because various water-soluble salts (*e.g.* NaCl, Na_2SO_4 *etc.*) can be used as leaching porogen. It is particularly suitable for macroporous structures, as the size of macropores can be easily adjusted in response to the particle size of salts [101]. Generally, salt particulates will be dissolved into polymer solvent at first, and then the sample scaffolds can be obtained by mould casting and vacuum drying thereafter, finally leaching out the salt particles with water to generate porosity (Figure 2.3(a)). So the whole operation and process of salt leaching is very simple. In addition, the bulk porosity can be finely controlled by changing the concentrated amount of salt [102]. The scaffold made by Taboas *et al*. [103] using salt leaching is illustrated in Figure 2.3(b). But this method has its own limitations for application as well, for instance, residual salts in scaffold, irregular shape of pores and so on. Worse still, the dispersity of salt within the polymer solution is heterogeneous, due to the difference of polymer solvent and salt particles in density, making it difficult to prepare complex 3D scaffolds with uniform distribution of pore size. Fortunately, this may be improved by combining other techniques [104].

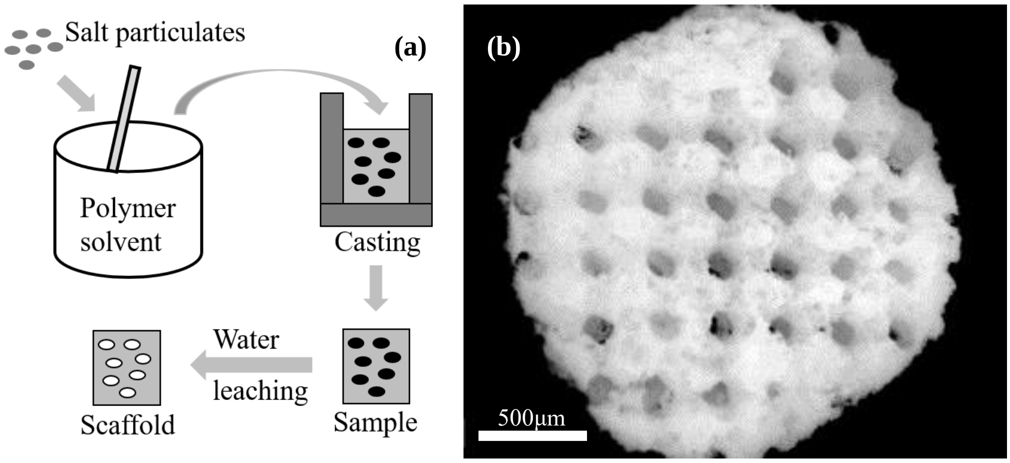

Figure 2.3 Salt leaching: (a) technical principle, (b) morphologies of a sample

2.4.1.4 Gas foaming

Another famous technique for porous scaffold is gas foaming (physically or chemically). In the physical method, the homogeneous mixture of polymer and solvent is usually placed into a chamber with gas (*e.g.* CO_2, N_2) at high pressure, in order to achieve a final pressure of dozens of times of atmospheric pressure. After equilibrated and saturated with gas for few days, the samples will turn into a solution with a single polymer/gas phase. When out of the chamber and kept at room temperature (about 20 - 23 ℃) for some while (15s or so), the samples will become porous due to instant release of gas [105] (Figure 2.4(a)). However, this expansion technique often results in closed porosity, which is unsuitable for TE, but a combination of gas-induced foaming and porogen leaching recently reported could help improve the pore structures [104, 106]. Nam *et al.* [104] succeeded in producing macroporous biodegradable polymer scaffolds (shown in Figure 2.4(b)) by gas foaming and salt leaching.

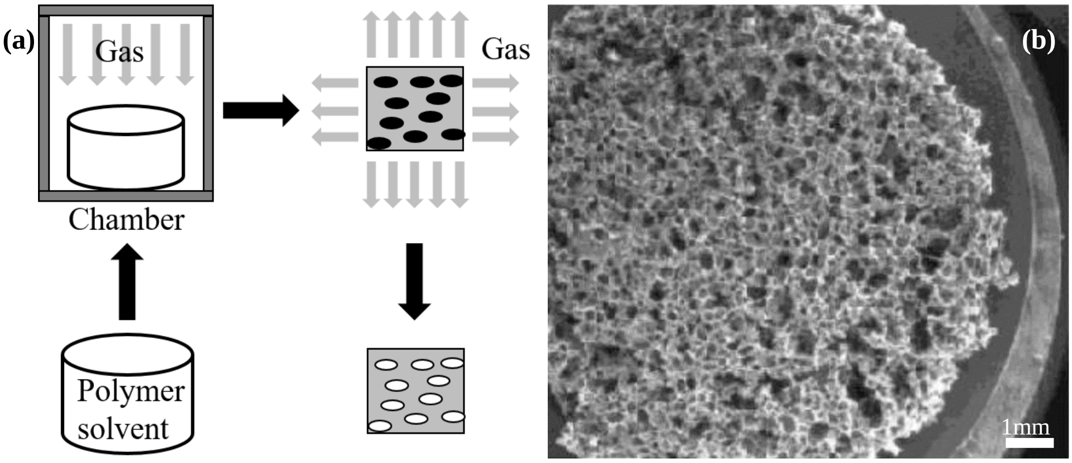

Figure 2.4 Gas foaming: (a) technical principle (physically), (b) morphologies of a sample

Porogen foaming (chemically) is also often used to fabricate scaffolds especially those made of biological ceramics (*e.g.* HA/β-TCP, bio-glasses). Initially in porogen foaming, a mixture of ceramics and porogen in powder, such as sucrose [107], polyvinyl alcohol (PVA) [108], starch [109], polymethyl methacrylate (PMMA) and graphite [110], is prepared before sintering. A 3D structure with interconnected macroporosity will be formed in scaffolds after complete oxidation of pore former during sintering. Owing to the controllability of particle size and content of pore former as well as sintering process, macroporous structures with desirable bulk porosity could be easily obtained, which is favourable for bone scaffolds. Besides, low cost and little workload in gas foaming is attractive to researchers as well.

2.4.2 Additive Manufacturing

Compared to traditional methods, AM or RP is taking a leap in BTE application due to the ability of achieving 3D complex products with customised structures at low cost of raw materials.

2.4.2.1 Electrospinning

Electrospinning (ESP) is gaining more attention as a newly developed process with high efficiency, remarkable rapidity and inexpensive cost. Normally, ESP uses electric field with high voltage to control the deposition of polymers [111] (Figure 2.5(a)). In ESP, under a critical voltage, the charge imbalance between electrical field and grounded target overcomes the surface tension of polymer to carry out deposition, known as Taylor cone. During fabrication, a single continuous filament is produced under the guidance of electric field and gathers on the grounded collector to form a scaffold [112].

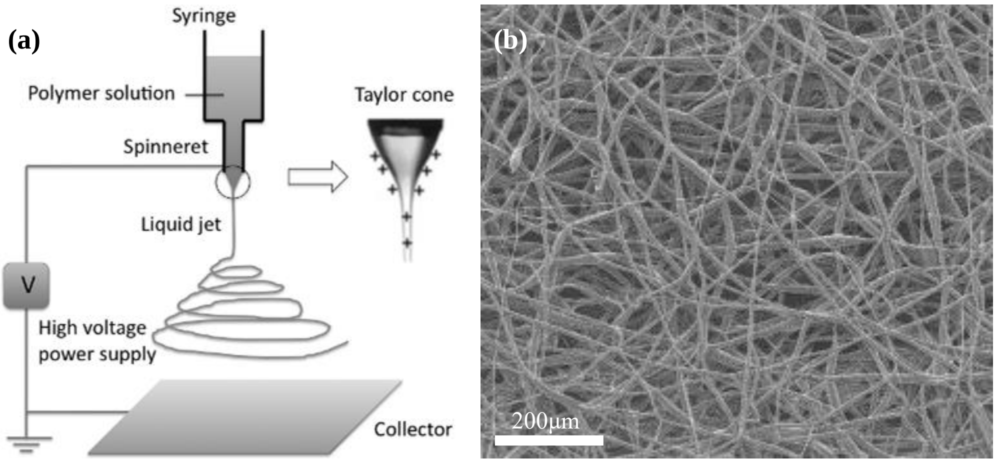

Figure 2.5 ESP: (a) technical principle, (b) morphologies of a sample

Notably, with this technique, it is possible to generate polymer fibres of submicron dimensions, even down to about 0.05 μm, which is particularly attractive to researchers, as heretofore this size range is very difficult to access but of great interest in TE [113]. Figure 2.5(b) shows the morphologies of a scaffold sample made by Yoshimoto *et al.*

[114]. Due to low strength of polymer fibres, ESP is preferably used in the research of cartilage in terms of BTE [115]. In addition, the arrangement of fibres is completely random, making it almost impossible to control the pore structures and porosity.

2.4.2.2 Fused deposition modelling

In fused deposition modelling (FDM) [116], thermoplastic materials are usually fed as filaments and melted inside a temperature-controlled heating liquefier, in order to maintain adequate fusion energy during extrusion through a nozzle (Figure 2.6(a)). FDM normally deposits 3D models available from computer aided design (CAD), computed tomography (CT) or magnetic resonance imaging (MRI) [117]. The extruder in FDM firstly performs the extrusion of semi-molten materials in filament and deposits them onto the platform layer by layer. The precision of FDM depends on material properties, fabrication conditions and applications of the designed part [118]. According to Zein *et al*. [119], FDM was used to fabricate scaffolds made of polycaprolactone (PCL) with excellent controllability, which were characterised by high strength (up to 77 MPa), high porosity (48% - 77%), fine precision (160 - 370 μm) and interconnected pore structures (Figure 2.6(b)). Of course there are some obvious drawbacks in FDM, including low resolution (around 250 μm), narrow processing window (requiring thermoplastic materials) and necessity of complicated parameter readjustment due to the change of material properties.

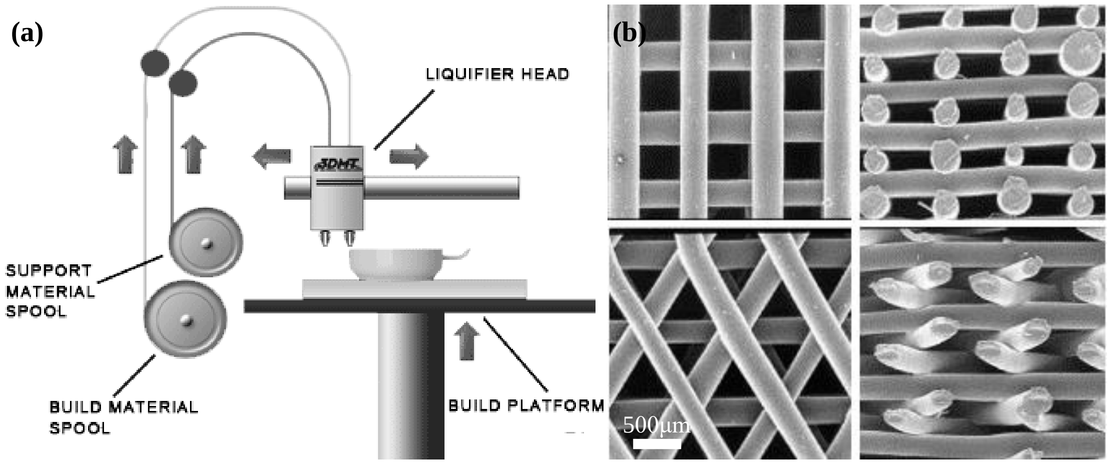

Figure 2.6 FDM: (a) technical principle, (b) morphologies of samples

2.4.2.3 Selective laser sintering / stereo lithography apparatus

Selective laser sintering (SLS) and stereo lithography apparatus (SLA) has been widely researched recently [120-123]. The technical principle of SLS/SLA is almost the same (Figure 2.7(a)). Specifically, SLS heats the metal powder into molten status (or glass transition for ceramic powder) through rapid scanning of high-powered laser beam, *e.g.* CO_2, and yttrium aluminium garnet (YAG), to form 3D constructs [124]. SLA uses lasers of low power, usually ultraviolet (UV), to scan and solidify photosensitive resin to make 3D models [125]. So the main difference between SLS and SLA lies in the material for scaffolds and laser type. The samples processed by SLS and SLA are illustrated in Figure 2.7(b) (Ti alloy by Williams *et al*. [120]) and Figure 2.7(c) (poly-(D, L-lactic) acid (PDLLA) by Melchels *et al*. [122]). SLS is advantageous to fabricate bone scaffolds made of metal or ceramics with high strength, which is totally free of any organic solvents [126]. But high temperature in SLS may do harm to the bioactivity of biomaterials. As for SLA, high precision and fast scanning rate are the main advantages, yet it has high requirements for materials (being photosensitive), which is not available for most biomaterials.

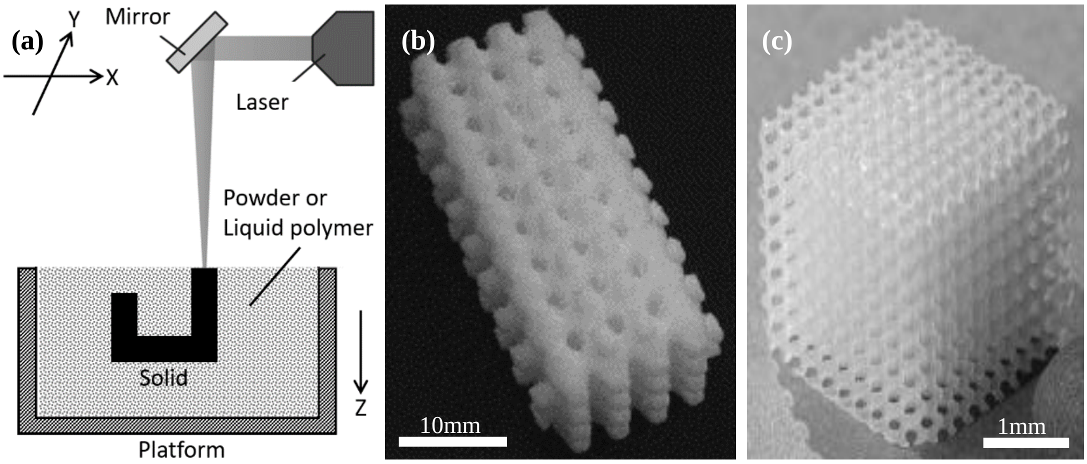

Figure 2.7 SLS/SLA: (a) technical principle, (b) a sample by SLS, (b) a sample by SLA

2.4.2.4 Three-dimensional printing

Three-dimensional printing (3DP) technology was developed by Sachs *et al*. [127] at Massachusetts Institute of Technology and it has been widely investigated for TE in recent years [128-130]. In 3DP, thin layers of powder material were processed into solid objects through selective ejection of adhesive droplets from an inkjet printhead (Figure 2.8(a)). When the deposited binder has completely dried in the powder bed, newly formed 3D models can be retrieved by removing unbound powder. Figure 2.8(b) shows the scaffold prepared by Leukers *et al*. [128] for BTE using 3DP technique, which showed good biocompatibility and ability to promote cellular adhesion and proliferation. 3DP is applicable to a wide range of materials, which is beneficial to biological scaffolds. Although 3DP was criticised for low precision, the surface roughness could enhance the biological activity of cells in return [129]. Therefore, 3DP has been regarded as a promising technology to prepare biological scaffolds [130]. However, the main problem of 3DP is the difficulty of cleaning unbound powder after formation, which may result in closed pores and decreased porosity.

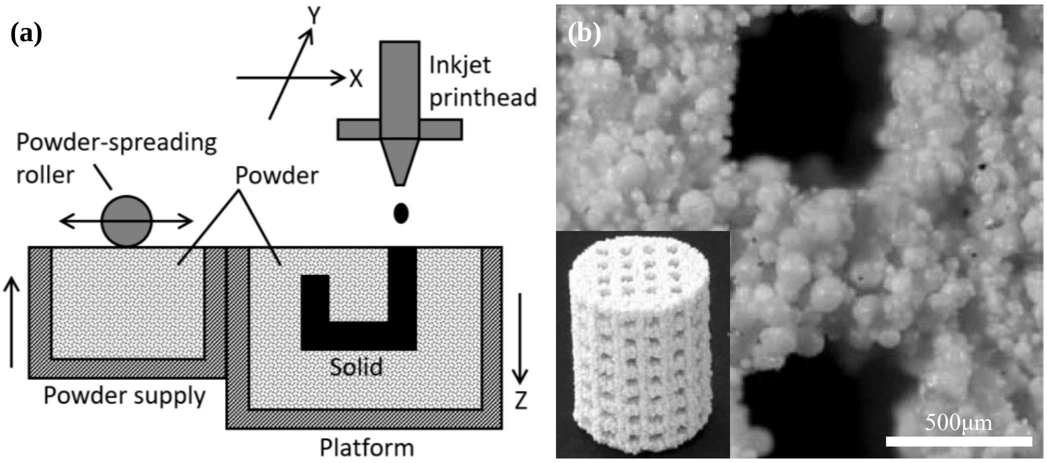

Figure 2.8 3DP: (a) technical principle, (b) morphologies of a sample

2.4.2.5 Extrusion deposition moulding

As the name implies, extrusion deposition moulding (EDM) makes scaffolds by deposition of biomaterials extruded by motors or pneumatics [131] (Figure 2.9(a)), which is the most representative one of SFF techniques. Because of good controllability in the diameter of filament, pore size, and porosity, as well as high precision and availability for various materials, EDM has been widely researched in last decade [132]. For instance, Wang *et al*. [133] prepared PCL scaffolds with satisfactory accuracy and strength for TE by improved extrusion deposition techniques; Xiong *et al*. [134] successfully prepared poly L-lactic acid (PLLA)/TCP composite scaffold by EDM at low temperature (up to 89.6% in porosity, good biocompatibility and osteoinduction); and a new technique combining pneumatic EDM and drop-on-demand (DOD) technique developed by Lee *et al*. [135] was powerful enough for cartilage with a variety of materials at low viscosity, including PCL, polyethylene glycol (PEG), and sodium alginate (SA) *etc*., providing a possible approach for cell, tissue or even organ printing. Figure 2.9(b) samples the hydroxyapatite scaffold made by Wu *et al*. [132].

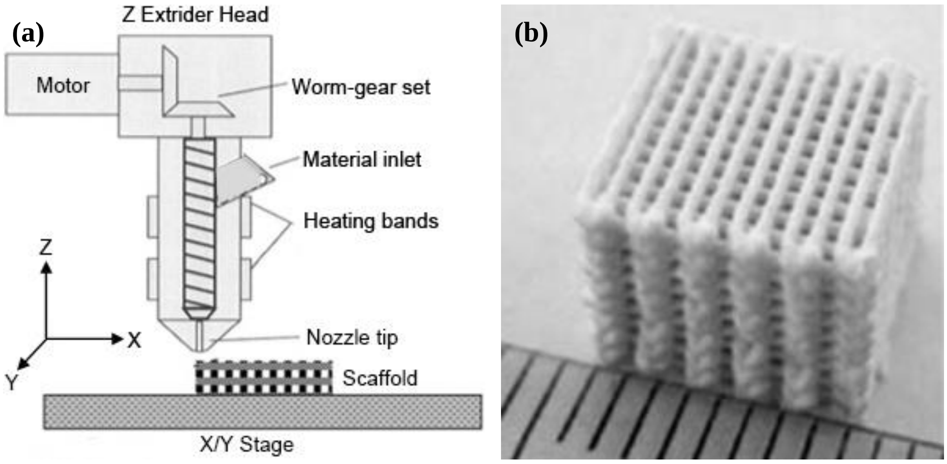

Figure 2.9 EDM: (a) technical principle, (b) a sample by EDM

2.5 Improvements and Optimisation Approaches

2.5.1 Optimisation in Structure/Topology

The development of CAD and micro-CT technologies realises the possibility of manufacturing totally customised and individualised artificial bone implants. This property greatly satisfies the requirements of structural and biological properties in bone growth. Many researchers tried to improve the performance of scaffolds from the angle of structures. For example, in order to match the elastic properties of compact bones and meanwhile to ensure sufficient porosity, Wieding *et al*. [136] optimised the internal structures of titanium scaffolds with geometrical parameters based on numerical simulations of the topological structure of compact bones. Hollister *et al*. [137] developed an image processing algorithm for micro-CT scanning of bone tissues to regulate the microstructure of scaffolds, so that the scaffolds and newly formed tissues could not only well adapt to the mechanical properties of host bones, but also satisfy the constraints of biological manufacturing. With advanced analytical tools, Meinel *et al*. [138] made optimisation of the mechanical structure of scaffolds by regular arrangement of ESP deposition of fibres, and it was reported that the adhesion and spreading status of MSCs was significantly enhanced, as well as promoted secretion of fibronectin. Wu [139] and Zhao [140] *et al*. optimised the structures of scaffolds, micro-ribs and mesh respectively, to improve the mechanical properties of scaffolds. All in all, the current improvements in terms of structure or topology are mainly concentrated on mechanical properties.

2.5.2 Multi-materials

Due to the unique nature of different materials, bone scaffolds made of a single material usually have many limitations. For instance, scaffolds made of HA is hardly biodegradable *in vivo* due to high crystallinity after sintering; that composed of PCL are not suitable for hard tissues because of low strength; while metals are weak in biological and osteoinductive activities. As a result, an easy and feasible strategy to improve the performance of scaffolds is to use multiple biomaterials instead. As mentioned, silicon plays a pivotal role in the mineralization and activation of gene in osteogenesis, so the partial replacement of calcium with silicon in HA has attracted the interest of many researchers [71]. In addition, Sánchez-Salcedo *et al*. [59] found that the addition of β-TCP into HA could improve biodegradability and osteoinductivity, whereas the cross-linked structures by agarose gels allowed HA/β-TCP scaffolds to have enough strength without sintering. Zhou *et al*. revealed that HA/nano-Ag composite scaffolds could substantially improve the antibacterial properties [141], and sintering was not necessary in HA-SA scaffolds in order for good toughness and mechanical strength [142]. Coffer *et al*. [143] reported that the introduction of Si in porous scaffolds (PCL and other commonly used polymers) could promote the interfacial calcification in simulated plasma and maintain the stability and proliferation of fibroblasts *in vitro*. Lee *et al*. [144] succeeded in optimising the bioactivity of osteoblasts on Ti scaffolds via gradient coating with HA and TiO_2, and Similar studies were performed by Sant *et al*. [145]. Nonetheless, the above optimisations in terms of multi-biomaterials are usually implemented in simple means, either coating or mixture, ignoring the importance of anisotropy, *i.e.* featured distribution of each biomaterial.

2.5.3 Combination of Several Fabrication Methods

Every fabrication method has its own advantages and disadvantages. Therefore, a smart combination of several methods would obviously take the most of each method and effectively avoid their weaknesses. The examples are too numerous to be listed. Nam *et al*. [104] added NH_4HCO_3, which thermally decomposed into NH_3 and CO_2, to PLLA scaffolds to produce porous structures by gas foaming, and the residual salt particles could be dissolved in hot water (salt leaching) to increase porosity. In the research of Abidian *et al*. [146], electrochemical deposition was employed to coat conductive polymers on biodegradable polymers (with drug inside) processed by ESP to control the release of drug. Considering the detrimental effect of residual organic solvent in gas foaming, pulsed ultrasonic vibration was used as post-processing to ensure the dissolution of solvent, and to make the pores interconnected, as reported by Wang *et al*. [147]. Similarly, Teng *et al*. [106] modified the fabrication (gas foaming with super-critical CO_2) of PLA scaffolds by after-treatment (salt leaching using NaCl) to overcome the shortcomings of poor interconnectivity in foaming technology. Therefore, the key of such strategy is to identify the strong and weak points of several techniques and then to combine them according to the practical needs of fabrication.

2.5.4 Inclusion of Bioactive Materials

It has been proved that the biological performance of scaffolds can be greatly improved if bioactive materials were introduced in scaffolds. For instance, Lee *et al*. [148] modified the collagen scaffolds with surface adsorption of osteopontin peptide, and they revealed that the biological activity was tremendously promoted, especially in cellular adhesion and calcification. The BMP-induced HA porous scaffolds developed by Kuboki *et al*. [35] presented excellent performance in osteogenesis, in particular, evident formation of new bone *in vivo*/*vitro*. Compared to normal agarose scaffolds, Yin *et al*. [149] confirmed the positive contributions of plasma (rich in platelets) to the proliferation, differentiation and integration of chondrocytes, specifically, high survival rate, remarkable increase of deoxyribonucleic acid (DNA) and considerable expression of associated genes. The cell-populated collagen gel (CPCG) technique invented by Delvoye *et al*. [150] enabled the capsulation of cells into collagen gel, and the scaffolds composed of CPCG fibres were highly bio-mimetic. Chang *et al*. [151] also found that the composite of small intestinal submucosa (a connective tissue) and β-TCP showed better bioactivity than β-TCP scaffolds in the aspect of callus formation and osteogenesis. Despite that such improvement can inspire the biological activity of scaffolds a great deal, the importance of biomimetic structure was not attached yet.

2.6 Summary

This chapter described a review of scaffold strategies, the key component of BTE. Scaffolds can not only simulate the physiological microenvironment *in vivo*/*vitro*, but also plays a vital role in promoting osteogenesis, significantly influenced by its bio-imitability (both external/internal structure and composition).

Currently, a large number of research have been conducted for the purpose of optimising or modifying bone scaffolds from the aspects of structure, composition, preparation and bioactivity. However, most of them are generally limited to some particular performance. For instance, the improvements of mechanical properties or structures usually ignores the importance of micro-/nano- porosity; the attempts of multi-material or biological factors are often evenly distributed, without considering the influence of structure complexity. In addition, it is almost impossible for current techniques to fabricate bone scaffolds with full account of bio-imitability in terms of structure and composition. Given that microstructures dominate the bioactivity of scaffolds, hierarchically porous scaffolds with multi-scaled pores (nm-µm-mm) were proposed in order to promote the biological performance of scaffolds for BTE. It is highly anticipated that this work could establish solid foundation for potential application of such scaffolds to medical surgery, and eventually promote the development of inter-disciplines, *e.g.* material science, manufacturing engineering and clinical medicine.

Chapter 3. Motor Assisted Micro-syringe System

This chapter introduces a novel and concise fabrication technique based on EDM, called motor assisted micro-syringe (MAM), to make HA scaffolds for BTE. Particularly, MAM system is able to finely control the morphology, pore size and porosity of HA scaffolds with optimised mechanical properties.

3.1 Introduction

Successful fabrication of porous ceramic scaffolds for medical applications (*e.g.* BTE) was achieved many years ago, using a variety of traditional methods. However, most conventional techniques, like moulding and casting, are unable to produce individualised tissue-engineered scaffolds because of weak capability of employing CAD/CAM (computer-aided manufacturing) to customise external/internal structures [152, 153]. Worse still, the unpredictable structures restraint further optimisation of mechanical properties in the scaffolds prepared by these techniques [154, 155]. In this case, mouldless fabricating techniques, such as RP (or AM) including ESP, FDM, SLS/SLA, 3DP and so on, have been widely researched and developed for complex scaffolds. With the support of CAD, the manufacturing process of RP techniques can be reproducible regardless of the different physical and biochemical properties of biomaterials [130].

In this chapter, an improved 3D bio-printing method, *i.e.* MAM system, was introduced. More technical details about MAM can be found in our previous work [7, 53, 156]. Compared to its sibling RP techniques, the intricate preparation of polymer filament (FDM) or complicated control and high cost of laser (SLS/SLA), for instance, is not necessary in MAM [157]. As for 3DP or ESP, the limitations are obvious. ESP is mainly for biopolymer scaffolds, so scaffolds made from bioceramics are not applicable; while exacting conditions such as binder are required in 3DP [158]. Specifically, HA ceramic slurry of high solid fraction (35 vol.%) was extruded by MAM for fabrication of 3D scaffolds with controllable structures. MAM shows prominent stability and favourable repeatability during fabrication of scaffolds, which have apparent porosities and interconnection as well as adequate mechanical properties. Besides, it can be upgraded to support biological materials, such as cells and proteins, seen in Chapter Appendix.

3.2 MAM system

3.2.1 Mechanical Design

Figure 3.1 shows the mechanical design of MAM system, and the detailed systematic characterisation of this machine can be found in Ref [7] and [151]. It mainly consists of gantry frame, workbench (X-Y-Z motion system), micro-syringe system and control system (Figure 3.1(a)). During fabrication, the workbench moves in X direction, and the extrusion part will move in Y and Z directions. The motion in X and Y directions is driven by servo motors, together with straight guide rails to guarantee accurate orientation. Stepping motors are adopted to push a plunger at very slow speed in Z motion. The detailed structure of extrusion actuator is illustrated in Figure 3.1(b). Micro-syringe is used to carry out the extrusion, while a heater consisting of thermocouple and electrical bar is incorporated so as to heat the syringe chamber if necessary.

During fabrication, a clinical injector (20 mL) is used to squeeze the slurry into the syringe, which will protect the filled slurry from foam and contamination. As the downward movement of a plunger, the internal pressure of syringe increases and eventually compacts the slurry for extrusion. When the internal pressure is high enough to overcome frictional resistance, the slurry will be extruded out as filaments. Similar to other RP techniques, CAD/CAM is utilised to plan the travel path of nozzles; after a layer is completed, the height of the deposition nozzle is raised for the next layer. The process goes on until the entire scaffold is finished. In addition, a vaseline film is usually preferred on the workbench before extrusion to establish a smooth interface with scaffolds for easier collection.

In summary, MAM is advantageous such as fine precision in positioning, high motional repeatability, simplified structure and low cost *etc*. Table 3.1 shows the major specification of MAM system.

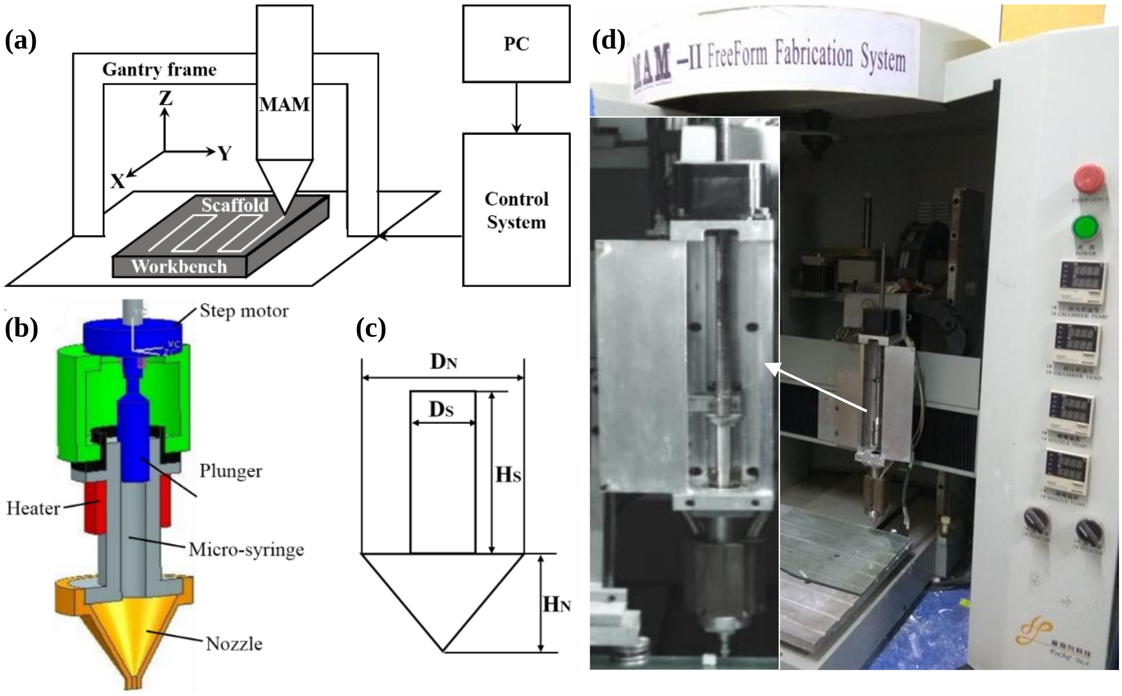

Figure 3.1 Mechanical design of MAM fabrication system: (a) schematic of MAM, (b) & (c) detailed structure and specification of extrusion actuator, (d) actual image of MAM

Table 3.1 Specification of MAM system

MAM system	**Specification**
Manufacturer	Fochif Mechatronics Technology Co., Ltd.
Model	MAM-II Freeform Fabrication System
Overall size / Weight	950 × 820 × 1050 mm / 120 kg
Software / File format	Self-developed / Stereo-lithography (STL [a])
Precision of positioning	X/Y: ±1 μm, Z: ±5 μm
Diameter of filament	200 - 400 μm
Size of syringe	D_S = 20 mm, H_S = 110 mm, D_N = 25 mm, H_N = 25 mm [b]
Working dimension	X/Y: 250 mm, Z: 150 mm
Temperature set	20 - 28 ℃ (room) [c], 25 - 60 ℃ (nozzle)
Response delay	< 20ms

[a] A file format used to represent 3D CAD models in SFF technologies.

[b] D_S / H_S -- diameter / height of syringe, D_N / H_N -- diameter / height of nozzle, shown in Figure 3.1(c).

[c] The room temperature is controlled by air conditioner.

3.2.2 Development of Software

The original software for MAM system could only generate deposition routes for simple models, such as cuboid, cylinder (Figure 3.2), which is far from satisfying the basic requirement of customisation in bone scaffolds. Therefore, the author himself developed a new software, named "***Spider***" (by C/C++, based on Qt platform [159]), for this MAM system. The main user interface (UI) can be found in Figure 3.3.

The UI mainly consists of three parts, *i.e.* "*Model*", "*Slice*" and "*Print*". As shown in Figure 3.3(a), "*Model*" page is for the common operations related to 3D models in STL format [160], including adding/deleting model(s), switching perspective views and so on. The shading function of 3D models, *e.g.* "*Eiffel Tower*" in Figure 3.3(a), was implemented by open graphics library (OpenGL 2.0) [161]. The "*Slice*" primarily slices the imported 3D model layer by layer according to parameter sets (Figure 3.3(b)). The mathematical and computational algorithm for slicing is provided in Ref [162, 163]. In addition, in view of the processing characteristics of EDM deposition (Figure 3.2), "*Slice*" page also performs the path planning for sliced layers (Figure 3.3(c)). As for the "*Print*" page, it is basically responsible for electrical communication with the control system of MAM. To be more specific, it transmits the speed settings of servo and step motors, and sends the deposition data (from "*Slice*" page) to regulate the motion of extruder via control system. As a matter of convenience, this page also tracks the detailed motion of X/Y/Z axis (seen in the "*Motion Log*").

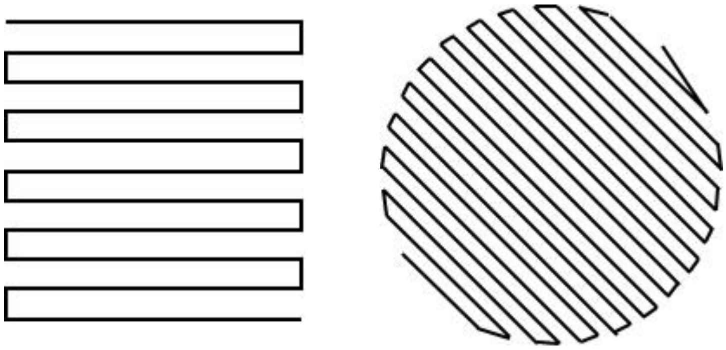

Figure 3.2 Sample of paths created by original software

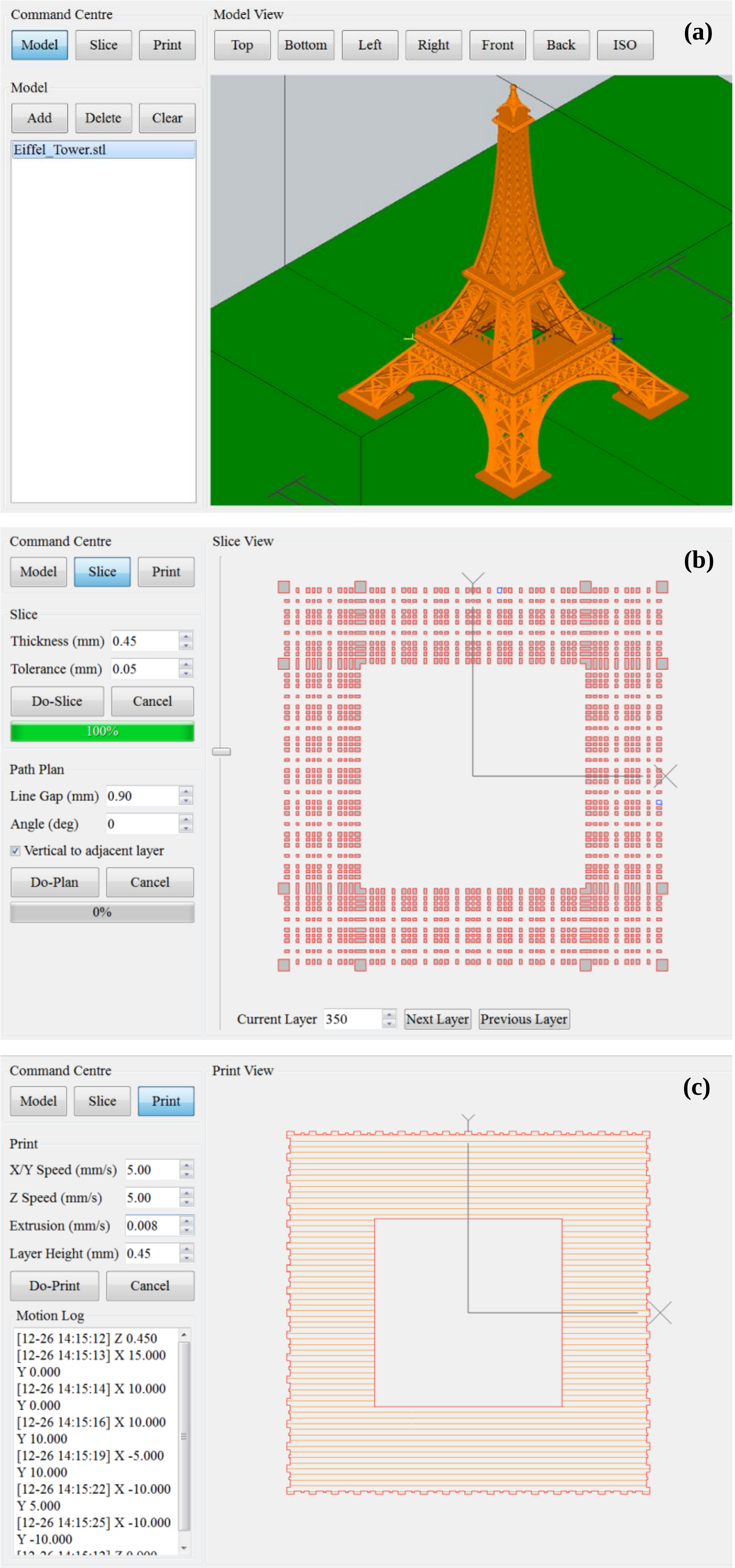

Thickness (mm) 0.45

Tolerance (mm) 0.05

Line Gap (mm) 0.90

Angle (deg) 0

☑ Vertical to adjacent layer

Current Layer 350

X/Y Speed (mm/s) 5.00

Z Speed (mm/s) 5.00

Extrusion (mm/s) 0.008

Layer Height (mm) 0.45

```
[12-26 14:15:12] Z 0.450
[12-26 14:15:13] X 15.000
Y 0.000
[12-26 14:15:14] X 10.000
Y 0.000
[12-26 14:15:16] X 10.000
Y 10.000
[12-26 14:15:19] X -5.000
Y 10.000
[12-26 14:15:22] X -10.000
Y 5.000
[12-26 14:15:25] X -10.000
Y -10.000
```

Figure 3.3 UI of MAM fabrication system

3.3 Materials

3.3.1 HA powder

The nano-HA powder used in this study was purchased from Nanjing Emperor Nano Material Co., Ltd. The main technical indicators are provided in Table 3.2. The images of HA powder taken by transmission electron microscope (TEM) (Figure 3.4(a)) indicates that the average size of HA particles is about 150 nm (length) ×40 nm (width). In addition, the X-ray diffraction (XRD) pattern perfectly matches the standard peak of hydroxyapatite ($Ca_{10}[PO_4]_6[OH]_2$), marked in red in Figure 3.4(b), according to PDF (phase diffraction filter) #09-0432 in line with the Joint Committee on Powder Diffraction Standards (JCPDS). In other words, the purity of HA powder is extremely high, which is consistent with the purity indicator listed in Table 3.2.

Table 3.2 Main technical indicators of HA powder

Indicator	Parameter	Indicator	Parameter
Particle shape	Needle-like	Heavy metal	≤ 8 ppm
Graininess	~ 60 nm	Arsenic	≤ 1 ppm
Purity	≥ 99.5%	Whiteness [b]	96
Drying loss [a]	0.59%	pH	7.41
Sintering loss [a]	2.59%	Insoluble matters	0.02%

Note: [a] volumetric loss; [b] the degree to which a surface is white.

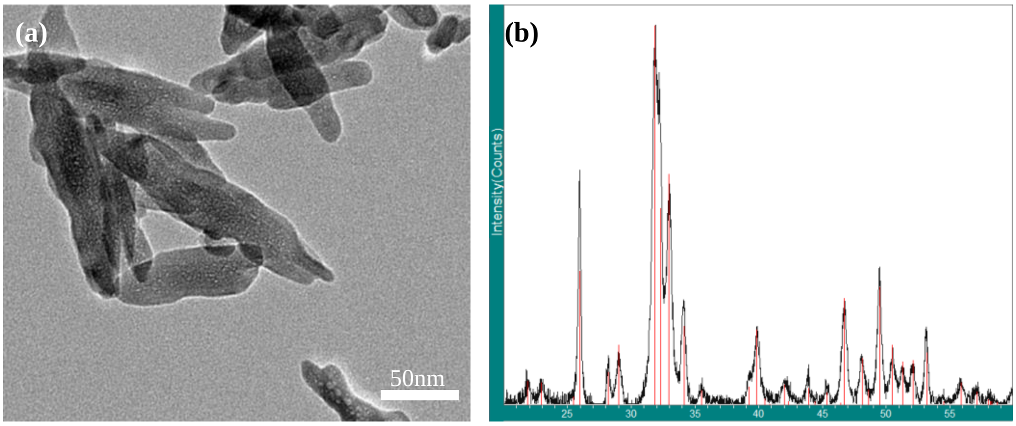

Figure 3.4 (a) Morphologies of HA particles, (b) XRD pattern of HA powder (PDF #09-0432)

3.3.2 Auxiliary Reagents

As the physicochemical properties of HA slurry will determine the continuation and stability of extrusion, the preparation of slurry has to be carefully conducted. In practice, in order to ensure that the properties of slurry are suitable for extrusion, *e.g.* appropriate viscosity, high stability, favourable dispersity and proper solid phase proportion, certain reagents (shown in Table 3.3) were used, including deionised water, glycerol, ammonia water, ammonium polyacrylate (NH_4-PAA), hydroxypropyl methylcellulose (HPMC) and so on. The exact content of each reagent was derived from the long-term practice and test of our research group. Table 3.3 also demonstrates the function of each reagent.

Table 3.3 Ingredient of auxiliary reagents

Reagent	**Specification**	**Content [a]**	**Manufacturer**	**Application**
Deionised water	2nd distillation	66.3 wt.%	Self-made	Solvent
Glycerol	Analytically pure (AP)	28.2 wt.%	Sinopharm Group	Humectant
Ammonia water	pH≈10, 5 mol/L	Depends [b]	Sinopharm Group	pH regulator
Nitric acid	1 mol/L	Depends [b]	Sinopharm Group	pH regulator
NH4-PAA	40wt.%, 1.16 - 1.19 g/cm^3	1.5 wt.%	Shanghai Goodben	HA dispersant
Octanol	AP	0.6 wt.%	Sinopharm Group	Defoamer
HPMC	AP	1.0 wt.%	Sinopharm Group	Thickener
Vaseline [c]	GB1790-86	/	Sinopharm Group	Lubricant

[a] It refers to the amount accounted in HA dispersion by percentage.

[b] Ammonia water was used in combination with nitric acid to regulate pH.

[c] Vaseline was not the ingredient for HA slurry, but for easy removal of the scaffolds from the platform.

3.4 Methodology

3.4.1 Equipment and Devices

Table 3.4 shows the main details of the equipment and devices used for the potential experiments in this chapter. In particular, the actual application of each device is specified as well.

Table 3.4 Main details of equipment and devices for experiments

Device	Model	Manufacturer	Application
MAM system	MAM-II	Fochif	Fabrication of scaffolds
Electronic balance	HTP-312	Huachao	Weighing
Ultrasonic cleaner	CE-6200A	Jaken	Ultrasonic dispersion of slurry
Ultrasonic humidifier	LU100	Deerma	Prevention of fracture
Planetary ball mill	QM-3SP2	Nanda Instrument	Mixing slurry uniformly
Rotational viscometer	NDJ-1	Jingchun	Evaluation of viscosity
Digital pH meter	CT-6023	Kedida	Measurement of pH
Stereomicroscope	XTL-340	Changfang	Measurement of pore size
X-ray diffractometer	X'Pert Pro	PANalytical B.V.	XRD analysis of HA powder
Transmission electron microscope	Tecnai G2	FEI	Characterisation of HA powder

3.4.2 Preparation of HA Slurry

In order to obtain a well dispersed HA slurry suitable to extrusion deposition, the main influence factors such as pH, amount of dispersant and proportion of HA solid phase *etc*. were intensively studied. As a sequence, the preparation process of slurry has to strictly follow the steps developed by our group. Taking 30.0 grams HA dispersion as an example, the detailed preparation steps are summarised in a flowchart (Figure 3.5).

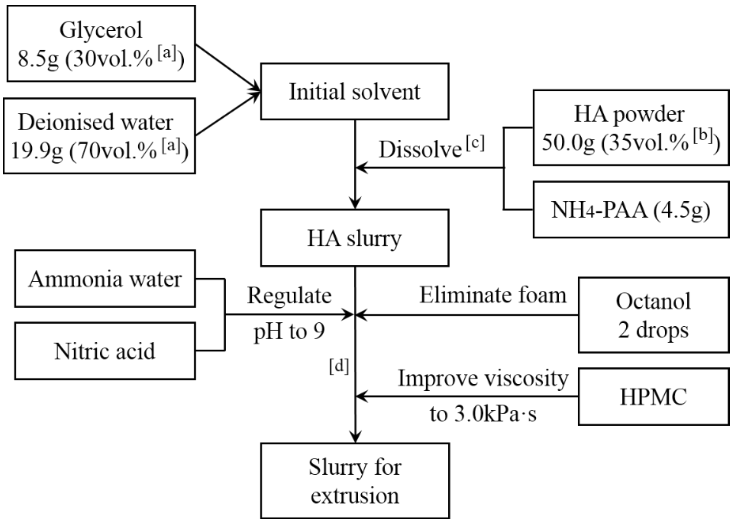

Figure 3.5 Flowchart of scaffold preparation

Notes for Figure 3.5: **[a]** -- initial solvent was made of 70 vol.% deionised water and 30 vol.% glycerol; **[b]** -- the solid phase of HA accounted for 35 vol.% of total volume of slurry (the density of dispersion and HA is 1.02 g/mL and 3.16 g/cm^3 respectively); **[c]** -- HA powder and NH_4-PAA were evenly added by 5 times, *i.e.* 10.0 g HA and 0.9 g NH_4-PAA per time (in practice, they were dissolved slowly and gradually with continuously stirring and ultrasonic dispersing in the whole process to ensure homogeneity); **[d]** -- ball-milling (for 12 hours) was necessary to get uniform slurry for extrusion and deposition.

3.4.3 Fabrication of Scaffold Using MAM System

The whole fabrication process was carried out at room temperature (around 20 ℃). The flow chart (Figure 3.6) describes the whole process in detail.

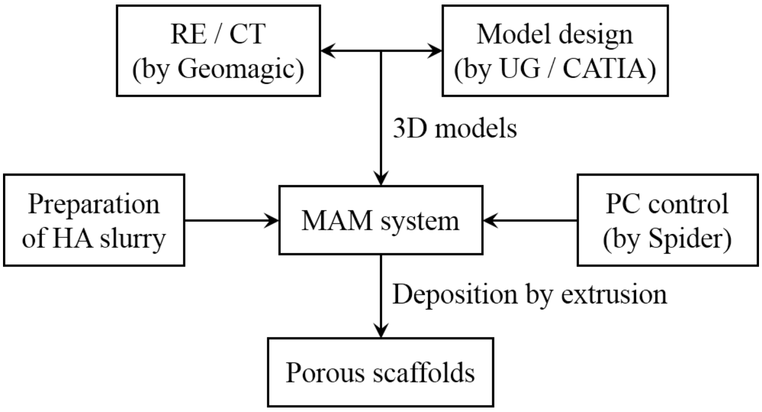

Figure 3.6 Schematic of fabricating scaffolds

The first step was to gather the geometric information of bone defects, either through reverse engineering (RE), CT scanning, or CAD modelling. Certainly, CAD software such as Unigraphics (UG) and computer-aided three-dimensional interactive application (CATIA) can also revise the models built by RE software like Geomagic Studio. Secondly, the target models were committed to "***Spider***" software (Figure 3.3) for further processing and pre-treatment, *e.g.* 3D transformation, slicing, path planning *etc.*, which conveys motion data and parameter setting to MAM system thereafter. At last, MAM system executed the extrusion of slurry in the manner of micro-syringe, and drove the motion system in X/Y/Z directions to deposit 3D scaffolds layer by layer. In addition, humidification throughout the fabrication process was required to protect scaffolds from fracture and crack. The recommended degree of humidity and temperature control should be more than 85% and 25 - 28 ℃.

3.4.4 Control of Extrusion Deposition Process

It is of great significance to extrude the slurry continuously and equably in this technique. Besides materials, configuration of processing parameters is another key factor that influences the fabrication process. Particularly, operation parameters such as travel speed in X/Y directions (**V_{XY}**) and extrusion speed of plunger (**V_P**), nozzle diameter (**D_N**) were investigated to achieve fine control of filament formation during deposition. On the other hand, the size and porosity of scaffolds can be easily adjusted by geometric parameters, for instance, the pitch between filaments (**L_F**), diameter of rod (**Φ_R**), pore size (**S_P**), and height of layer (**Δh**), as shown in Figure 3.7. In practice, **D_N** varied from 0.21, 0.26, 0.34 and 0.41 to 0.52 mm to study the influence on **Φ_R**. Our research suggests that the coordination and repeatability of MAM could be improved by proper regulation of these parameters.

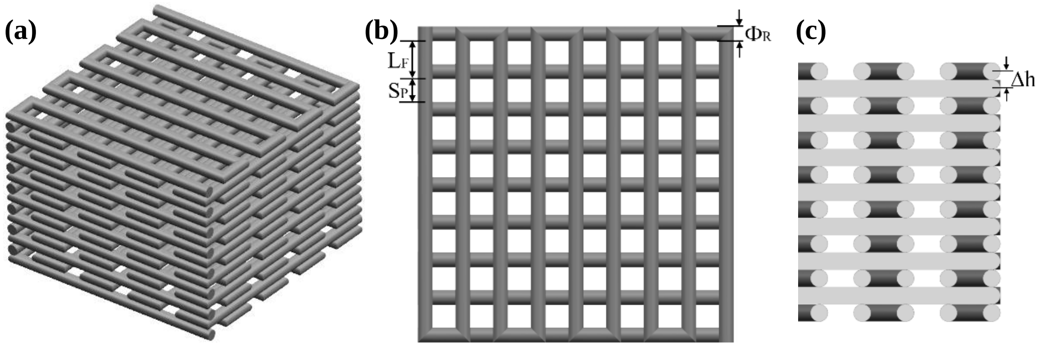

Figure 3.7 UG model of scaffold: (a) full view, (b) top view, (c) half-section view

3.4.5 Characterisation of Scaffolds

The phase purity of HA powder was checked by XRD analysis. Monochromated Fe/Kα radiation was used at operating values of 40.0 kV and 20.0 mA. The XRD data was collected over the range of 10 °- 80 °(2θ) at 0.02 °increment per second.

The macrostructure and morphological features of porous HA scaffolds, including diameter of rods, pore structures and porosity, were investigated by a stereomicroscope and TSView (v7.0, the native software of stereomicroscope) developed by Shanghai Changfang Optical Instrument Co., Ltd.

3.5 Results and Discussion

3.5.1 Mathematical Analysis of Extrusion Process

The mathematical analysis of extrusion process is advantageous for the knowledge of forming mechanism and for the optimisation of the fabrication parameters. For MAM, the main resistance to extrusion is the viscous force between nozzle and slurry. To simplify the mathematical model, it was supposed that the slurry was uniform and incompressible fluid with constant physical properties, which would move steadily in laminar flow within a nozzle. In this case, the force analysis of an infinitesimally long cylinder is illustrated in Figure 3.8 [151]. Notes: ***r*** & ***L*** is the size of a cylindrical infinitesimal and ***G*** is its gravity; ***P1*** & ***P2*** stands for the static pressure from nearby fluid; ***τ*** means the viscous force; ***V*** represents the speed of flow; and ***R*** is the radius of nozzle.

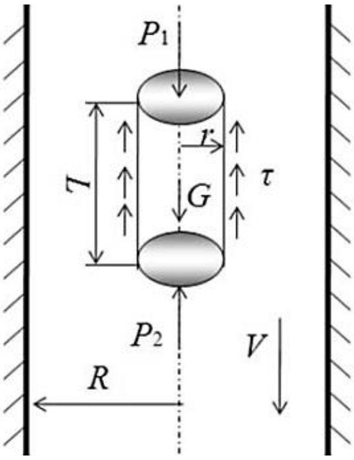

Figure 3.8 Force analysis of viscous fluid in the nozzle

In a steady laminar flow, the viscous force would evenly distribute along the cylindrical surface, *i.e.* $\frac{\partial v}{\partial t} = 0$. So the equilibrium condition of force in this analysed infinitesimal along the axial direction of nozzle would be:

$$\pi r^2 (P_1 - P_2) + G + 2\pi r L \tau = 0$$

In view of that

$$G = \rho g \pi r^2 L$$

Then we can get

$$\tau = -\frac{r}{2}\left(\frac{P_1 - P_2}{L} + \rho g\right) \qquad \text{(Equation 3.1)}$$

According to the law of Newton internal friction [164],

$$\tau = -\mu \frac{dv}{dr}$$

Where μ is the viscosity. Thus,

$$dv = \frac{1}{2\mu}\left(\frac{P_1 - P_2}{L} + \rho g\right) r \cdot dr \qquad \text{(Equation 3.2)}$$

The quantity of flow (***Q***) would be

$$Q = \int_0^R A \cdot dv = \int_0^R \frac{\pi}{2\mu}\left(\frac{P_1 - P_2}{L} + \rho g\right) r^3 \cdot dr$$

Where A (= πr^2) is the area of cylinder. After computation of the integral,

$$Q = \frac{\pi R^4}{8\mu L}(\Delta P + \rho g L) \qquad \text{(Equation 3.3)}$$

Where, $\Delta P = P_1 - P_2$. From Equation 3.3, it can be concluded that the influence of nozzle size (***R***) is much higher than viscosity, gravity and static pressure. In consideration of high viscosity (3.0 kPa s), the flow of slurry in the spindle nozzle tip would also be hindered by viscous friction resistance. According to Bernoulli equation [164],

$$P_1 + \frac{1}{2}\rho V_1^2 + \rho g h_1 = P_2 + \frac{1}{2}\rho V_2^2 + \rho g h_2 + \rho g h_\lambda$$

Where, $V_1 = V_2 = V$ in steady laminar flow, $h_1 - h_2 = L$; h_λ is the friction loss factor. Consequently,

$$h_\lambda = \frac{\Delta P}{\rho g} - L = \left(\frac{8\mu Q}{\pi \rho g R^4} - 2\right) \cdot L \qquad \text{(Equation 3.4)}$$

As we can see in Equation 3.4, for the fabrication process of HA slurry with given Q and μ, the resistance is proportional to L, but in inverse proportion to R^4. In other words, smaller length and larger diameter of nozzle tip will contribute to smoother extrusion. On the other side, the size of filament extruded by MAM is mainly determined by ***R***. Therefore, the most effective strategy to reduce the resistance of extrusion is to decrease the length of nozzle tip as much as possible. The exterior of MAM nozzles is shown in Figure 3.9.

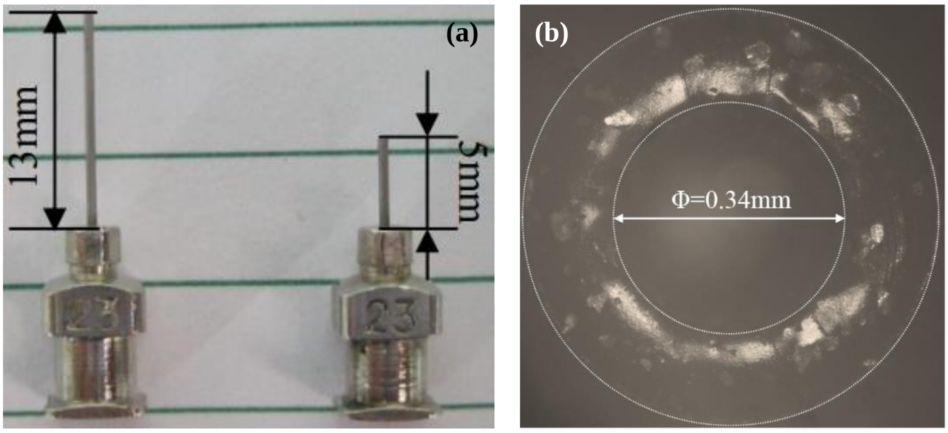

Figure 3.9 Exterior of MAM nozzles: (a) nozzles of different tip length, (b) top view of a nozzle tip by TSView

3.5.2 Influence of Extrusion Parameters

3.5.2.1 Size of nozzle (D_N)

Figure 3.10 shows the relationship between Φ_R and D_N on the condition that V_{XY} equals the extrusion (or deposition) speed of filament (V_F). The actual diameter of rods was measured to be a bit larger than the theoretical value (the red dash line in Figure 3.10), regardless of the difference in D_N, indicating that a swell effect did exist when slurry was extruded from a nozzle. Moreover, the effect of expansion became even more notable if D_N was small. Currently, the most accepted explanation for this phenomenon could be: 1) because of the elastic recovery of tensile deformation caused by inlet convergence; 2) the elastic response of shear deformation resulted from shear and normal stress [165]. According to Zhao *et al*. [166], if the length of a nozzle tip is relatively small, the first one dominates such expansion; while for a long nozzle tip, the latter becomes the main factor.

Generally speaking, as a member of viscoelastic fluids, the ceramic slurry will surely swell after sudden release of constraints from nozzle. From Equation 3.4, it can also be seen that smaller ***R*** will cause higher resistance, which dramatically increases the deformation of slurry within the nozzle, resulting in larger swell. As a result, the increase of D_N and reduction of ***L*** is advantageous to stable extrusion for highly viscous slurry.

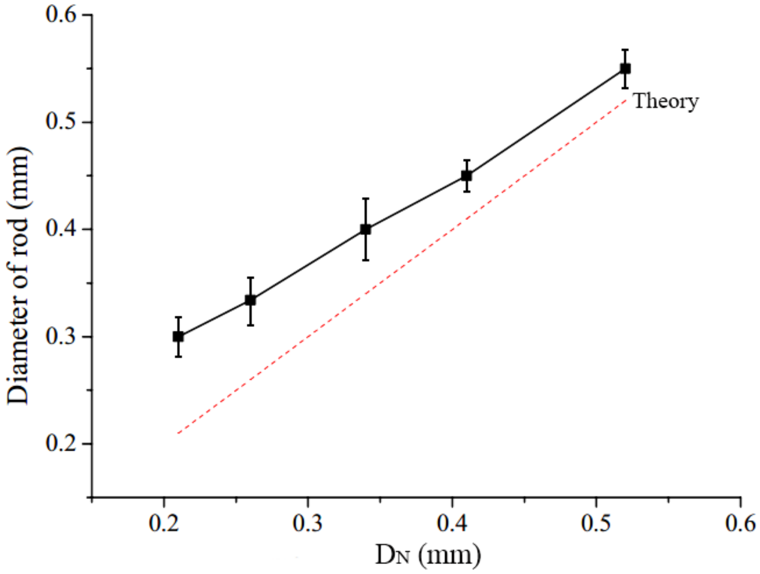

Figure 3.10 Relationship of rod diameter and D_N

Reasonably, higher precision of deposition was found when the size of nozzle was smaller (Figure 3.10). However, our experimental results suggest that it was hardly possible to extrude HA slurry from narrow nozzles ($D_N \leq 0.26$ mm), due to high resistance caused by viscosity. On the other hand, the rods of scaffolds would be increasingly thicker with much wider nozzles ($D_N \geq 0.41$ mm), which inevitably produced burrs especially at the corners during fabrication. Worse still, the scaffold might be unable to support itself because of heavy rods, making it easily fractured during drying process (Figure 3.11(b)). In view of all, 0.34 mm was selected as the nozzle size for extrusion throughout this study.

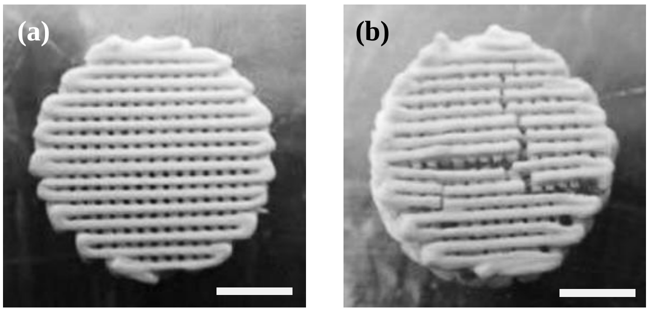

Figure 3.11 Scaffold samples made by different nozzles: (a) $D_N = 0.34$ mm, (b) $D_N = 0.41$ mm; scale bar = 5 mm

3.5.2.2 Travel speed (V_{XY}) and extrusion speed (V_P)

The deposition speed (V_F) usually depends on the speed of plunger (V_P) which performs the extrusion. Theoretically, for an ideal Newtonian fluid, the relation of V_F and V_P can be built assuming that the slurry is incompressible. Then we can figure the relationship of V_P and V_F according to the Q of slurry, which is the same in micro-syringe and nozzle.

$$Q = \frac{\pi D_P^2}{4} \cdot V_P = \frac{\pi D_N^2}{4} \cdot V_F$$

Thus,

$$V_F = \frac{D_P^2}{D_N^2} \cdot V_P = k \cdot V_P \qquad \text{(Equation 3.5)}$$

Where D_P is the diameter of plunger, which equals D_S in Table 3.1. Considering that D_N **= 0.34 mm** and $D_P = D_S$ **= 20 mm**, it is easy to get that **k = 3.46×10^3**.

Ideally, the extrusion process will be stable and continuous if V_F perfectly matches V_{XY} (*i.e.* $V_F \approx V_{XY}$). Nevertheless, even if V_F and V_{XY} matched well, it was found that Φ_R was not exactly consistent with the theoretical results, and due to swell effect, it was a bit larger, as shown in Figure 3.12. Besides, the swell rate was different as travel speed increased. Note that the diameters of rod at high speed (> 10mm/s) were presented only for reference, because the MAM failed to fabricate scaffolds at high speed (seen in Figure 3.13), so the measured value may be random and not reliable.

Obviously, the increase of V_P would augment Φ_R and faster motion in X/Y directions gave rise to thinner rods. Hence, samples with different sets of V_{XY} and V_P (Figure 3.13) were prepared for further analysis. It can be concluded that it was difficult to accumulate layer by layer either V_{XY} was too slow or too fast. Specifically, fast V_{XY} made the deposition process discontinuous (Figure 3.13(c)); while slow travel speed was to blame for adjacent ribs overlapped with each other, thus leading to inconspicuous porous properties (Figure 3.13(a)). On this occasion, the optimal parameters that matched this HA slurry in the extrusion process was addressed: V_{XY} **= 7.0 mm/s**, V_P **= 0.005 mm/s**.

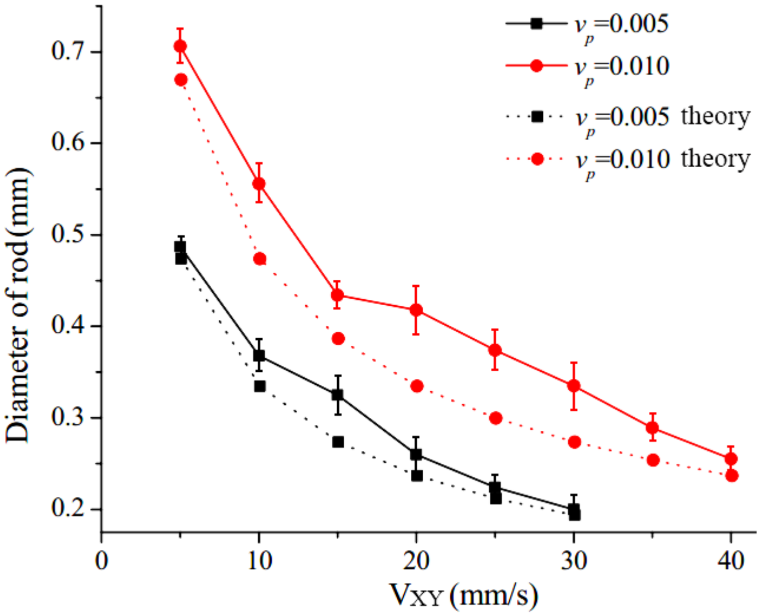

Figure 3.12 Influence of V_{XY} and V_P on rod diameter

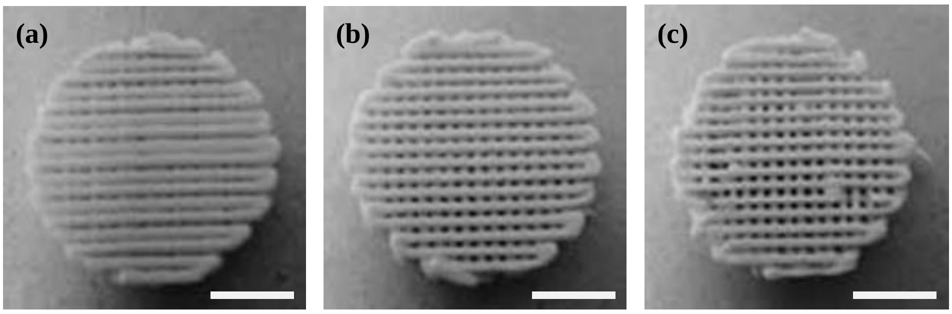

Figure 3.13 Scaffold samples made at different speed: (a) V_{XY} = 5.0 mm/s, V_P = 0.005 mm/s; (b) V_{XY} = 7.0 mm/s, V_P = 0.005 mm/s; (c) V_{XY} = 9.0 mm/s, V_P = 0.005 mm/s; scale bar = 5 mm

3.5.3 Control of Bulk Porosity

Porous structures of biological scaffolds play a critical role during bone formation *in vivo* and *in vitro*. Scaffolds with different porosities and pore sizes can be obtained by varying the parameters mentioned above. The schematic of scaffolds with porosities of 30%, 50% and 70% is illustrated in Figure 3.14(a), (b) and (c), which show that the final porosity of scaffolds can be easily adjusted by changing the radio of pore size (S_P) versus rod diameter (Φ_R). Due to the influence of gravity, the actual size of pores was a little smaller than its theoretical value. Therefore, the proportion of S_P was higher than the desired pore size. For low porosity, *e.g.* 30% and 40%, the influence of gravity was more remarkable, resulting in considerable contraction (Figure 3.15(c)). Fortunately, the pore structures of fabricated scaffolds were interconnected, as shown in Figure 3.15, which is beneficial to cell culture and osteogenesis [48, 154]. In conclusion, these parameters of high controllability enables MAM system to make scaffolds with various porosities and pore sizes. The only task is to change the ratio of S_P versus Φ_R, which is feasible and available with the assistance of "***Spider***". All in all, the bulk porosity can be finely controlled by adjusting fabrication parameters and model geometry.

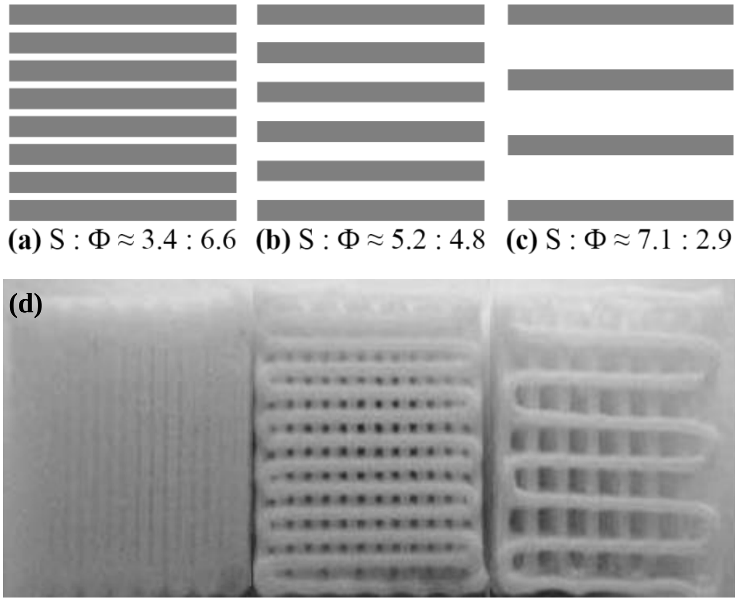

Figure 3.14 Control of bulk porosity: (a) 30%, (b) 50%, (c) 70%, (d) samples of scaffold with different porosity (30%, 50% and 70%)

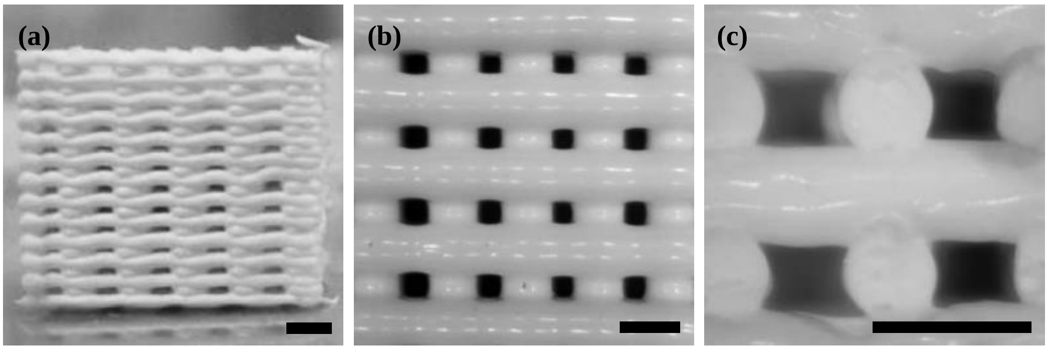

Figure 3.15 A sample of scaffold with interconnected pore structures (40% porosity): (a) front view, (b) top view, (c) section view; scale bar = 1 mm

3.6 Summary

This chapter introduces the MAM fabrication system in detail; in particular, the analysis and control of extrusion process were presented. Specifically, the extrusion process of slurry with high viscosity was mathematically analysed. The influence of significant parameters were also intensively studied, and it was found that the flow rate of slurry was mostly effected by the nozzle diameter.

With the assistance of self-developed software, it is possible and feasible to finely control the deposition process of MAM by adjusting fabrication parameters and geometry of 3D models. The scaffolds fabricated by MAM had evident porous structures with high interconnectivity, and the pores were mainly ranged within 50 and 580 μm, which are favourable for BTE. In summary, MAM system is competent to make 3D complex scaffolds with various porosities and pore sizes.

Chapter 4. The Influence of Sintering Temperature on Scaffolds

4.1 Introduction

Sintering is a very old technique for shaping materials, which began with the production of pottery [167]. In recent years, the sintering process has been widely used for mass preparation of ceramic products [168, 169]. Sintering can be regarded as the migration and diffusion process of particles pushed by capillary forces due to thermal energy, which densifies samples with improved mechanical properties [170]. The sintering process plays a vital role in the preparation of porous bone scaffolds to get sufficient strength. Mechanical properties are essential for bone scaffolds because: a) they have to maintain their internal structures under the loading pressure from human body, so as to provide enough space for cell in-growth *in vivo*; b) adequate mechanical strength is necessary to guarantee the stability of scaffolds during preparation, transportation, storage, surgery, *etc*. [80].

A large number of studies have confirmed that sintering parameters, such as sintering method [171], atmosphere [172], temperature [173], holding time and heating rate [174], could have significant impact on the performance of HA scaffolds. At present, most of the research regarding to the sintering process of HA-related ceramics remained in the stage of enhancing mechanical properties for scaffolds, usually at high temperature. For instance, Göller *et al*. [175] reported that the strength, hardness and density of HA blocks was higher if sintered at 1300 ℃ for long time duration (4h). Mazaheri *et al*. [176] developed a novel sintering process for HA in order to get finer grains and better mechanical properties. Wu *et al*. [177] employed microwave sintering to improve compressive strength of porous HA scaffolds. However, because of excessive focus on mechanical properties, these studies ignored the negative effect of high temperature on the biological properties of HA scaffolds that are essential to osteogenesis.

In this study, microwave sintering method was used to make HA scaffolds. As a rapid volumetric heating process, microwave sintering is characterised by high heating rate, short treating time and thus leads to reduction of cost and energy [177]. For HA scaffolds, this method also has advantages in fine microstructure and improved properties [178]. Over the last two decades, it has been applied to various materials such as oxide ceramics [179], metals [180] and composites [181]. Besides, microwave sintering is a viable treatment to make dense HA products with advantageous morphologies and enhanced mechanical strength at lower temperatures with less time [177]. As the mechanical strength and biological performance of HA scaffolds strongly depends on their microstructures [182], microwave sintering is useful to promote biological properties.

4.2 Materials

The experimental materials used in this chapter are listed in Table 4.1.

Table 4.1 Main materials used in experiments

Material	Specification	Manufacturer	Application
HA powder [a]	60 nm, ≥ 99.5%	Emperor	HA scaffolds
Pre-osteoblasts	MC3T3-E1 [b]	Sigma-Aldrich	Proliferation
Foetal bovine serum (FBS)	20%	PAN Biotech	Cell culture
α-Modified eagle medium (MEM)	Hyclone	Gibco	Cell culture
Anhydrous ethanol	≥ 99.7%	Sinopharm	Sterilization
Hydrogen peroxide	50% v/v	Sinopharm	Lysis of cells
Glutaraldehyde	25%	Sinopharm	Fixation of cells
Penicillin / streptomycin (P/S)	10^4 U/mL / 10^4 μg/mL	Gibco	Antibiotics

[a] Other ingredients for HA slurry can be found in Table 3.3.

[b] An osteoblast precursor cell line derived from Mus musculus (mouse) calvaria.

4.3 Methodology

4.3.1 Experimental Procedure

The experimental procedure for the study in terms of sintering temperature on scaffolds is summarised in Figure 4.1.

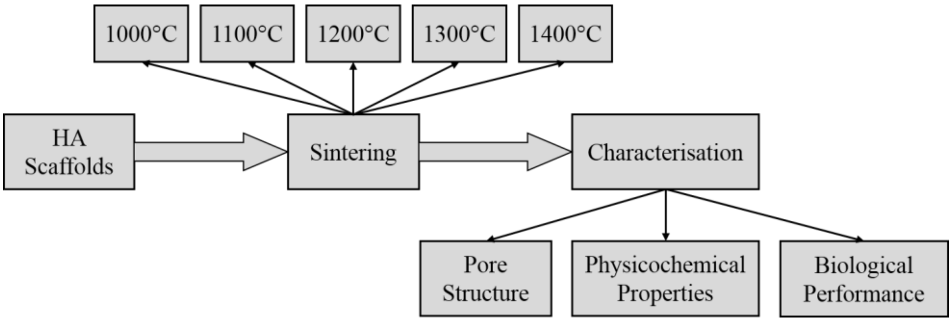

Figure 4.1 Experimental procedure of this chapter

4.3.2 Equipment and Devices

Table 4.2 shows the main details of the potential equipment and devices used for experiments in this chapter.

Table 4.2 Main details of equipment and devices for experiments

Device	Model	Manufacturer	Application
MAM system [a]	MAM-II	Fochif	Fabrication of scaffolds
Microwave furnace	Hamilab-V1500	Syno-Therm	Sintering of scaffolds
Electronic balance	HTP-312	Huachao	Weighing
Contact angle meter	SL200B	Kino Industry	Test of contact angle
Drying oven	DZF-6000	Super Instruments	Drying
CO_2 incubator	Heracell 150i	Thermo Scientific	Cell culture
Spectrophotometer	PowerWave XS2	BioTek	Cell counts
Stereomicroscope	XTL-340	Changfang	Measurement of pore size
X-ray diffractometer	X'Pert Pro	PANalytical B.V.	XRD analysis of scaffolds
Scanning electron microscope (SEM)	Sirion 200	FEI	Characterisation of microstructure of scaffolds

[a] Other devices for preparation of scaffolds can be found in **Table 3.4**.

4.3.3 Fabrication of HA Scaffolds

The preparation process of HA scaffolds has been introduced in detail before (seen in ***Section 3.4.3***). This section here provides the main parameters for MAM fabrication:

nozzle -- G23 (0.34 mm), extrusion speed -- 0.005 mm/s, X/Y speed -- 7.0 mm/s, layer thickness -- 0.33 mm, filament space -- 1.0 mm. Note that the dimension and pore size of all scaffolds for characterisation were the same. The extrusion speed and layer thickness may vary according to the actual properties of the HA slurry. In addition, HA solid blocks with identical sizes were also prepared by casting if necessary.

4.3.4 Sintering of Scaffolds

Prior to sintering, the porous scaffolds or solid blocks were firstly dried at room temperature for 24 h. After pre-sintered at 250 ℃ for 2 h to eliminate chemical reagents, scaffolds were then sintered at set temperature for another 2 hours to achieve high densification and mechanical strength. Finally, the scaffolds or blocks were cooled inside the microwave furnace (power -- 1.4 kW, wave frequency -- 2.45 GHz, Figure 4.2(a)).

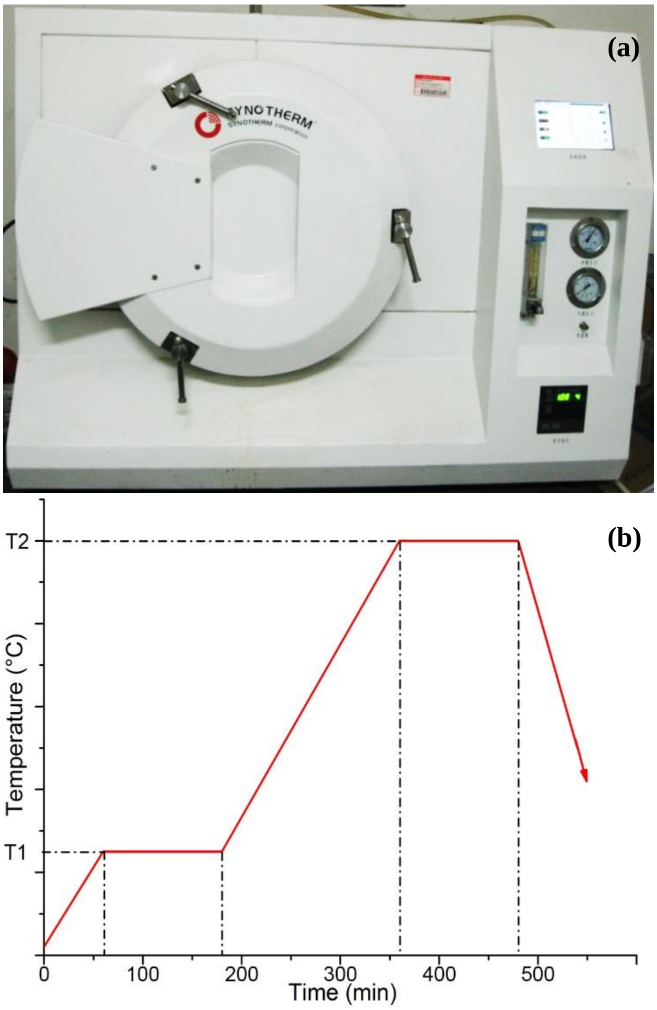

Figure 4.2 (a) microwave furnace and (b) sintering profile for HA scaffolds

According to Ramesh *et al*. [183], HA (Merck 2196, Germany) might be decomposed into α-TCP if the sintering temperature exceeded 1350 ℃. As a result, the temperature set for final sintering process in this chapter were 1000, 1100, 1200, 1300 and 1400 ℃ respectively, in order to investigate the influence of sintering temperature. The sintering profile of HA scaffolds is shown in Figure 4.2(b), where **T1** is 250 ℃ and **T2** may be 1000, 1100, 1200, 1300 or 1400 ℃.

4.3.5 Characterisation of Scaffolds

The influence of different sintering temperatures on HA scaffolds/blocks were studied with respect to pore structures (*e.g.* shrinkage, pore size, porosity, microstructure and grain size), physicochemical properties (such as phase composition, crystallinity, contact angle and water absorption) and biological performance (*i.e.* proliferation of pre-osteoblasts).

4.3.5.1 Shrinkage

In order to accurately control the final size of sintered HA scaffolds, the shrinkage in X, Y and Z directions after sintering (**S%**) was analysed based on Equation 4.1. In practice, 6 samples were used in each group to reduce errors.

$$S\% = \left(\frac{L_0 - L_S}{L_0}\right) \times 100\% \qquad \text{(Equation 4.1)}$$

Where, $\mathbf{L_0}$ is the initial size of scaffolds in X, Y or Z directions before sintering, and $\mathbf{L_S}$ stands for the final size after sintering. Then the overall shrinkage of scaffolds can be calculated according to Equation 4.2.

$$S\% = \big(1 - (1 - S_X)\cdot(1 - S_Y)\cdot(1 - S_Z)\big) \times 100\% \qquad \text{(Equation 4.2)}$$

Where, $\mathbf{S_X}$, $\mathbf{S_Y}$ and $\mathbf{S_Z}$ means the shrinkage in X, Y and Z directions.

4.3.5.2 Pore size and porosity

The pore sizes of scaffolds were measured by a stereomicroscope, and the bulk porosity (**P%**) was calculated by gravimetry [184] (shown in Equation 4.3).

$$\mathrm{P\%} = \left(1 - \frac{\rho_s}{\rho_m}\right) \times 100\%$$

(Equation 4.3)

Where, $\boldsymbol{\rho_s}$ is the density of scaffold, which equals the mass of scaffold divided by its apparent volume. $\boldsymbol{\rho_m}$ stands for the density of material (*i.e.* HA, $\boldsymbol{\rho_m = 3.16\ g/cm^3}$).

4.3.5.3 Microstructures and grain size

The morphologies at the micron scale were observed and analysed by SEM. It is necessary to wash HA scaffolds with deionised water and ensure full drying (normally for 30 min at 60 ℃) after sintering, so as to get clear SEM images. In addition, since HA is non-conductive, gold spraying (for 60 s) was also performed to increase the conductivity of scaffolds. The electron accelerating voltage was 15.0 kV during operation.

The grain size of HA scaffolds sintered at different temperatures can be measured by SEM images. The average of measurement (5 times for each) was taken as the grain size.

4.3.5.4 Phase composition and crystallinity

The phase composition of HA scaffolds sintered at different temperatures was characterised by XRD. The testing parameters for XRD are shown as follows: radiation -- Cu/Kα, operating values -- 40.0 kV and 40.0 mA, 2θ range -- 10 ° to 60 °, step size -- 0.01313 °.

On the basis of XRD patterns, the crystallinity ($\mathbf{X_C}$) of HA scaffolds can be calculated with the equation given below [185].

$$\mathrm{X}_c = \left(1 - \frac{V_{112/300}}{I_{300}}\right) \times 100\%$$

(Equation 4.4)

Where, $\boldsymbol{I_{300}}$ represents the diffraction intensity at the *(300)* crystal face, and $\boldsymbol{V_{112/300}}$ is the trough intensity within the peaks of *(112)* and *(300)* crystal faces. The distribution of crystal faces can be identified according to the standard XRD peaks of HA, as illustrated in Figure 4.3 [7].

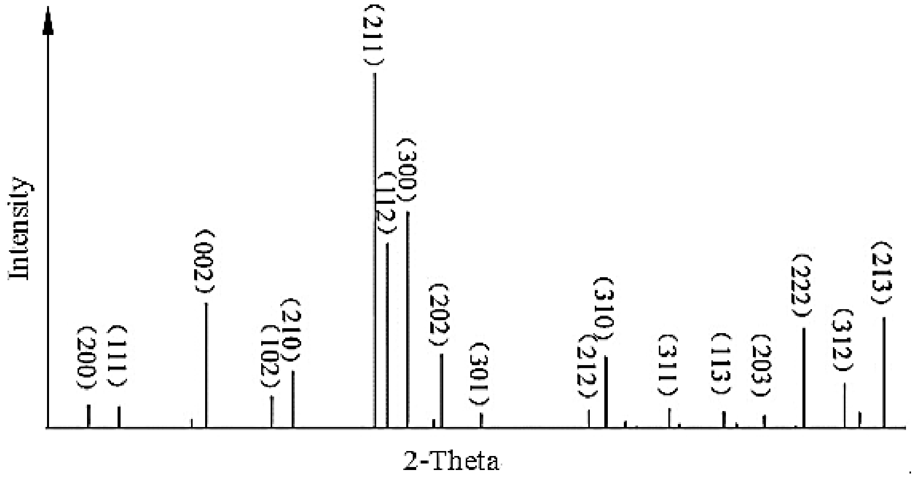

Figure 4.3 Matchup of crystal faces and X-ray diffraction peaks

4.3.5.5 Contact angle and water absorption

In this part, the contact angle between water and scaffold surface was measured. As shown in Figure 4.4, the shape of a liquid-vapour interface is determined by the Young-Laplace equation, with contact angle playing the role of a boundary condition via Young's Equation (Equation 4.5). The theoretical description of contact angle arises from the consideration of a thermodynamic equilibrium between three phases: liquid phase (**L**), solid phase (**S**), and vapour phase (**V**).

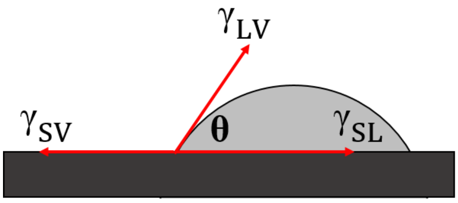

Figure 4.4 Measuring principle of contact angle

$$\gamma_{SV} = \gamma_{SL} + \gamma_{LV} \cdot \cos\theta \qquad \text{(Equation 4.5)}$$

Where, γ_{SV} is the interfacial energy of solid and vapour phases. Similarly, the solid-liquid and liquid-vapour interfacial energy is denoted by γ_{SL} and γ_{LV}. **θ** is the contact angle in equilibrium.

The water absorption of scaffolds was evaluated by the weighing method. Firstly, the weight of all scaffolds was measured before immersed in deionised water for 3 h. After standing on filter for a while (1 min), paper towels were used to carefully remove the residual water on the surfaces of scaffolds. At last, the final weight of all scaffolds was recorded. In this case, the water absorption (**A%**) of scaffolds can be estimated by the following equation.

$$A\% = \left(\frac{W_w - W_0}{W_0}\right) \times 100\% \qquad \text{(Equation 4.6)}$$

Where W_W and W_0 stands for the weight of wetted and original scaffolds, respectively.

4.3.5.6 Proliferation of pre-osteoblasts

MC3T3-E1 was selected for the evaluation of proliferation because it is "one of the most convenient and physiologically relevant systems for the study of osteoblasts" [186]. The proliferation of MC3T3-E1s was based on MTT assay, which is a colorimetric assay for assessing metabolic activity of cells. MTT is a yellow tetrazole, *i.e.* 3-(4,5-dimethylthiazol-2-yl)-2,5-diphenyltetrazolium bromide, which can be reduced to purple formazan by cellular oxidoreductase enzymes in living cells [187]. When formazan is dissolved into a coloured solution, it can be quantified by measuring the absorbance of this solution through a spectrophotometer at a certain wavelength (usually between 500 and 600 nm), which enables these enzymes to reflect the number of viable cells. Figure 4.5 [188] shows the cell morphologies of MC3T3-E1s under a spectrophotometer.

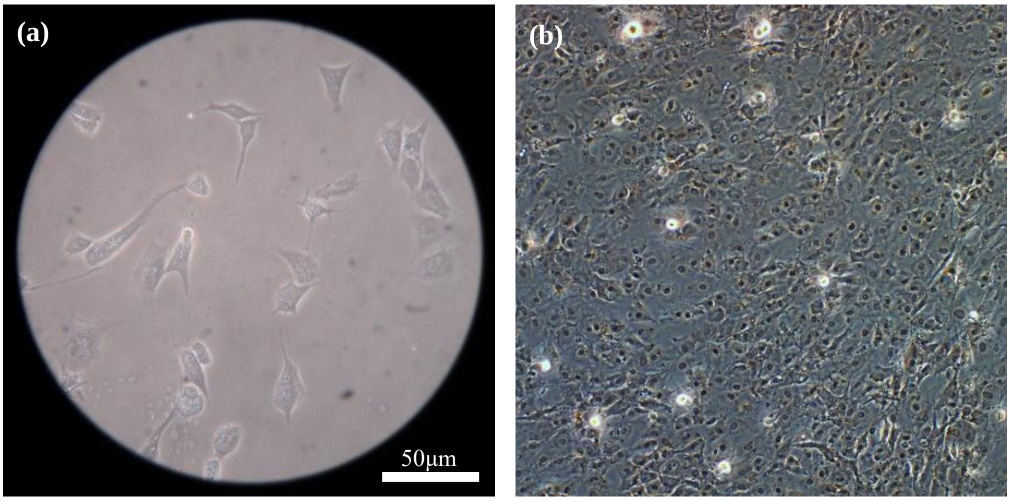

Figure 4.5 Cell morphology of MC3T3-E1s

To evaluate the effect of sintering temperature on proliferation, MC3T3-E1s were incubated in growth media consisting of α-MEM supplemented with 20% FBS and 1% P/S. MC3T3-E1s were populated after certain generations (3 - 6), and then seeded onto scaffolds (10,000 cells/cm^2, all grouped in 12-well plates) sintered at different temperatures, *i.e.* 1000, 1100, 1200, 1300 and 1400 ℃. The number of samples from each group was 12. The MC3T3-E1s were then exposed to direct contact with scaffolds until they were confluent (7 days) in an incubator (37 ℃ and 5% CO_2). During cell culture, part of these scaffolds were evaluated for cell viability in Day 1, 3, 5 and 7 (3 samples per time). At the end of every experiment, cells were lysed or fixed for further analysis in hydrogen peroxide or glutaraldehyde respectively. For MTT imaging, gelatine-coated (0.2%) coverslips were also used if necessary. With the help of a spectrophotometer, the optical density (OD) of all scaffolds was recorded for comparison and analysis.

4.4 Results and Discussion

4.4.1 Pore Structures

4.4.1.1 Shrinkage

Figure 4.6 illustrates the change of linear shrinkage, including X/Y length ($\mathbf{L_{XY}}$), and pore size ($\mathbf{S_P}$), of sintered porous HA scaffolds at different temperatures. Note that $\mathbf{L_X}$ and $\mathbf{L_Y}$ are usually used for represent pore size and their changes are equivalent because the measured samples were squared. After sintering at 1000 ℃, 1100 ℃, 1200 ℃, 1300 ℃ and 1400 ℃ for 2 hours, the $\mathbf{L_{XY}}$ value of HA scaffolds was consistent with the shrinkage of pores. To put it another way, the scaffolds will evenly shrink during sintering process, despite of the difference in sintering temperatures, which provides great possibilities to achieve fine control of pores and overall size. As seen from Figure 4.6, when the temperature raised from 1000 to 1400 ℃, the exact shrinkage of $\mathbf{L_{XY}}$/$\mathbf{S_P}$ in HA scaffolds also increased from 4.8%/5.2% to 26.9%/26.7%, respectively. In addition, only slight changes in terms of shrinkage was found when the sintering temperature was or higher than 1300 ℃, where it reached a maximum of 26% (both $\mathbf{L_{XY}}$ and $\mathbf{S_P}$), regardless of some fluctuation at higher temperatures. Similarly, when the temperature was lower than 1100 ℃, the shrinkage would not change substantially. The main reason for this phenomenon will be explained along with Figure 4.11.

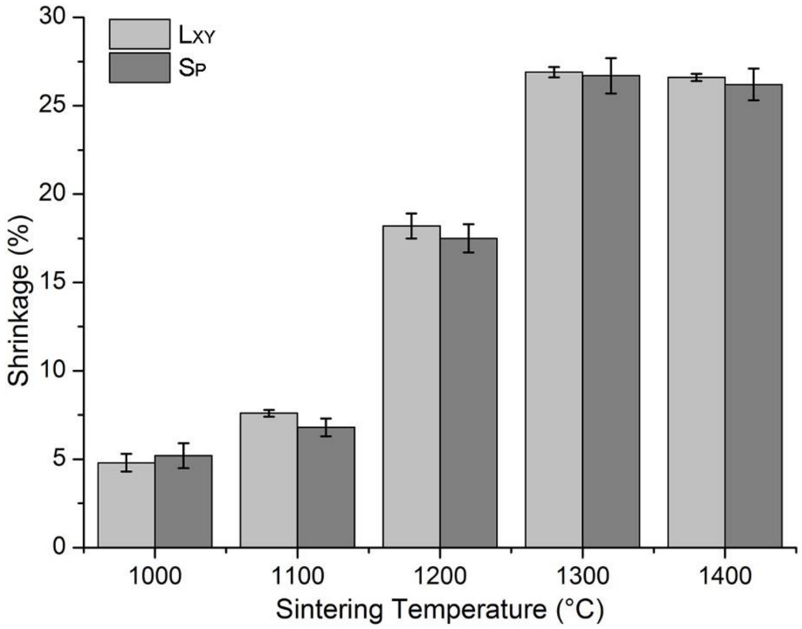

Figure 4.6 Shrinkage of scaffolds sintered at different temperatures

4.4.1.2 Pore size

According to Ref [156], the theoretical pore size (**S_P**) of scaffolds after sintering can be calculated by Equation 4.7, which matches the practical measurement very well.

$$S_P = [L_F - D_N \times (1 + B)] \times (1 - S_{LXY}) \qquad \text{(Equation 4.7)}$$

Where, ***L_F*** means the space of filaments and ***D_N*** is nozzle diameter (Figure 3.7). ***S_{LXY}*** is the shrinkage of scaffolds in X/Y direction as mentioned above. And ***B*** stands for the swell ratio, hereby it equals 0.229 according to Huang's research [156]. Particularly, ***D_N*(1+B)*** equals ***L_{XY}*** in Figure 4.6.

The differences of pore size between all scaffolds were analysed, in order to investigate the uniformity of pore size in MAM fabricated scaffolds. The average of pre-sintered (250 ℃) and fully sintered (≥ 1000 ℃) scaffolds is shown in Figure 4.7. The errors (variations) of pore sizes were acceptable in all scaffolds, about 20 - 40 μm, indicating that the pore sizes of scaffolds were very uniform. Besides, as the increase of sintering temperature, pore size sharply decreased until it was higher than 1300 ℃, which coincides to the result of shrinkage in Figure 4.6. Considering that the scaffold rods may be slightly deformed due to gravity during drying process, *i.e.* the shape of rods turning from round to oval (shown in Figure 3.15) which reduces L_F, it is reasonable that the calculated pore sizes were a bit smaller than actual ones. The distribution of pore size was assessed as well (Figure 4.8). Most of the fully sintered scaffolds exhibited normal distribution in terms of pore size. That the scaffolds sintered at 1100 ℃ had the highest error in pore size (Figure 4.7) also indirectly reflects this phenomenon. Overall, fine control of pore size is feasible and available in MAM, meanwhile with good stability.

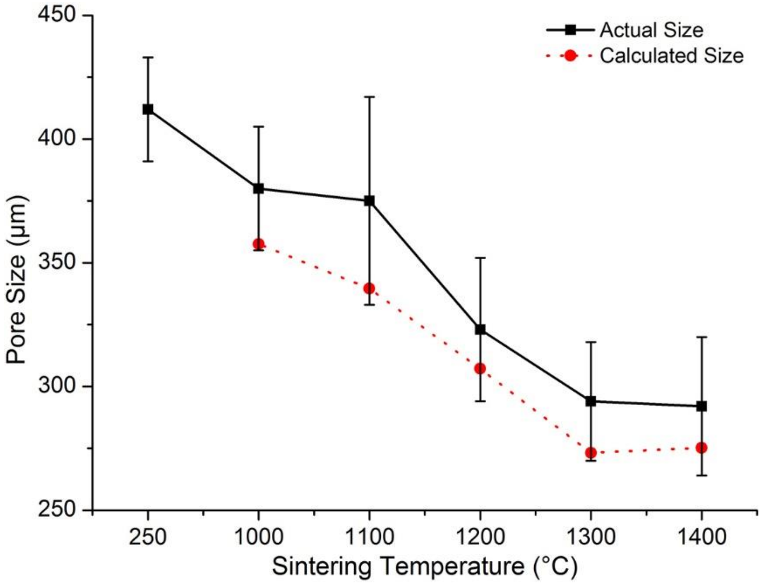

Figure 4.7 Pore size of scaffolds sintered at different temperatures

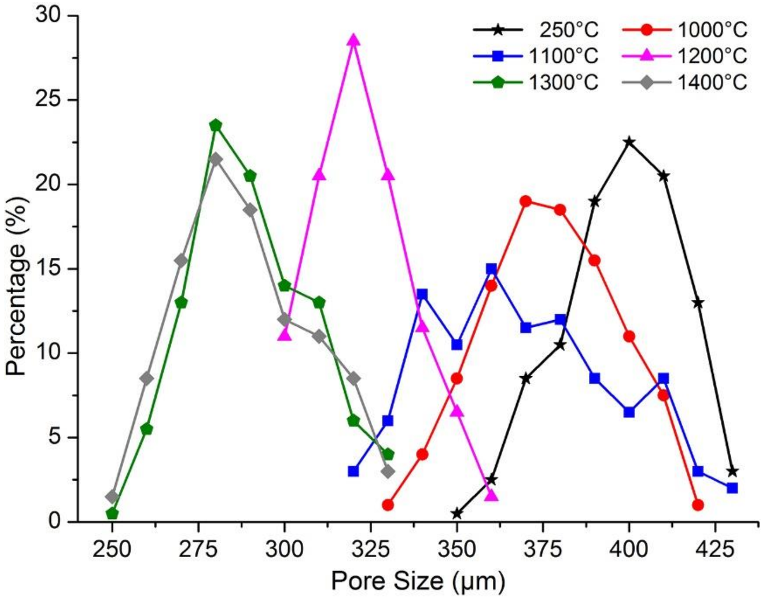

Figure 4.8 Distribution of pore size in scaffolds sintered at different temperatures

4.4.1.3 Exterior

Colour changes may occur during the sintering process of HA at high temperature. As we can see from Figure 4.9, the change of colour in scaffolds sintered at different temperatures was obvious. Specifically, the colour of HA blocks gradually changed from bright white to light blue, and blue became increasingly darken at higher temperatures (Figure 4.9 (d) and (e)). The explanation for this could be found in the research of Ramesh *et al*. [183]; that is, since most commercial HA powders contain certain amount of manganese element, Mn^{2+} will be oxidised to Mn^{5+} (usually MnO_4^{3-}) during sintering, resulting in blue appearance if part of PO_4^{3-} was replaced by MnO_4^{3-}. Ramesh *et al*. pointed out that high temperature not only increases the activity of oxygen, but also provides more energy for the oxidation of manganese ions. Nonetheless, the oxidation of manganese may have negative effects on the stability of hydroxyapatite phase [183]. Thus, high temperature for the sintering of HA products is not always the best option, although it usually contributes to good mechanical strength.

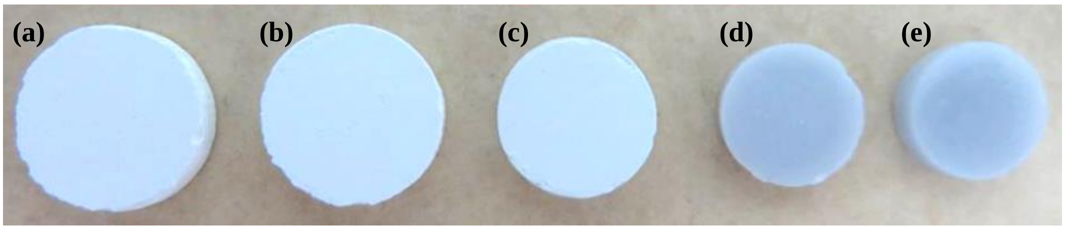

Figure 4.9 Exterior of solid HA blocks sintered at: (a) 1000 ℃, (b) 1100 ℃, (c) 1200 ℃, (d) 1300 ℃ and (e) 1400 ℃

4.4.1.4 Porosity

Figure 4.10 displays the porosity of HA scaffolds and blocks after sintering at 1000 ℃, 1100 ℃, 1200 ℃, 1300 ℃ and 1400 ℃. For scaffolds, the porosity showed decreasing trend as sintering temperature increased, and dramatic decline was found when the sintering temperature rose from 1000 ℃ to 1300 ℃. But this trend did not keep on at higher temperature; on the contrary, the porosity slightly grew. Despite that the porosity of HA blocks was much less than scaffolds, the variation of porosity was basically the same. Interestingly, complete densification was not available even in solid blocks after sintering at extremely high temperature (1400 ℃), with about 11% of porosity. Possible explanations are shown as follows: a) internal pores may be formed due to uneven slurry; b) the accuracy of measurement and calculation of porosity could not be ensured one hundred percent; c) the decomposition of HA at high temperature may cause some difference in actual density. The calculation of porosity was based on Equation 4.3, where the premise is that the sintered HA scaffolds and blocks were entirely composed of HA phase (ρ_{HA} = 3.16 g/cm^3, while actually the density of decomposed products of HA can be various, for instance, α-TCP -- 2.86 g/cm^3, β-TCP -- 3.07 g/cm^3, CaO -- 3.35 g/cm^3, *etc*.) [189].

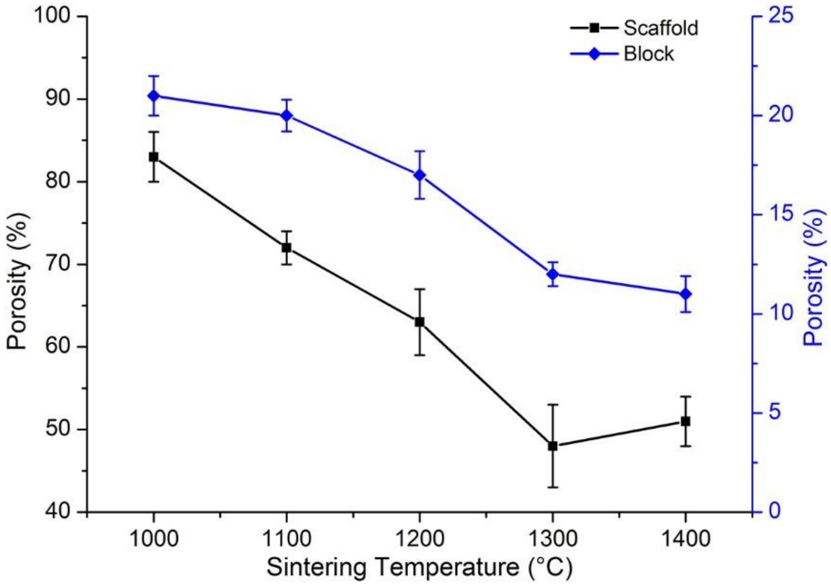

Figure 4.10 Porosity of porous and solid scaffolds sintered at different temperatures

4.4.1.5 Microstructure

The microstructures of HA scaffolds sintered at different temperatures was observed by SEM. As shown in Figure 4.11, there were uniformly distributed nanopores (< 1 μm) on the rods of scaffolds if the sintering temperature was or lower than 1200 ℃. Furthermore, these nanopores were evidently interconnected, particularly in scaffolds which were sintered at 1000 ℃ and 1100 ℃. However, the quantity of nanopores decreased rapidly with the increase of sintering temperature, and nanoporosity completely disappeared when it was higher than 1200 ℃. This also explains the shrinkage result described in

Figure 4.6, which is mainly caused by the extinguishment of nanopores. As mentioned before, the scaffolds were impossible to be totally densified, probably because of heterogeneous slurry. As a result, the defoamer and ball-milling treatment was introduced to prepare homogeneous slurry.

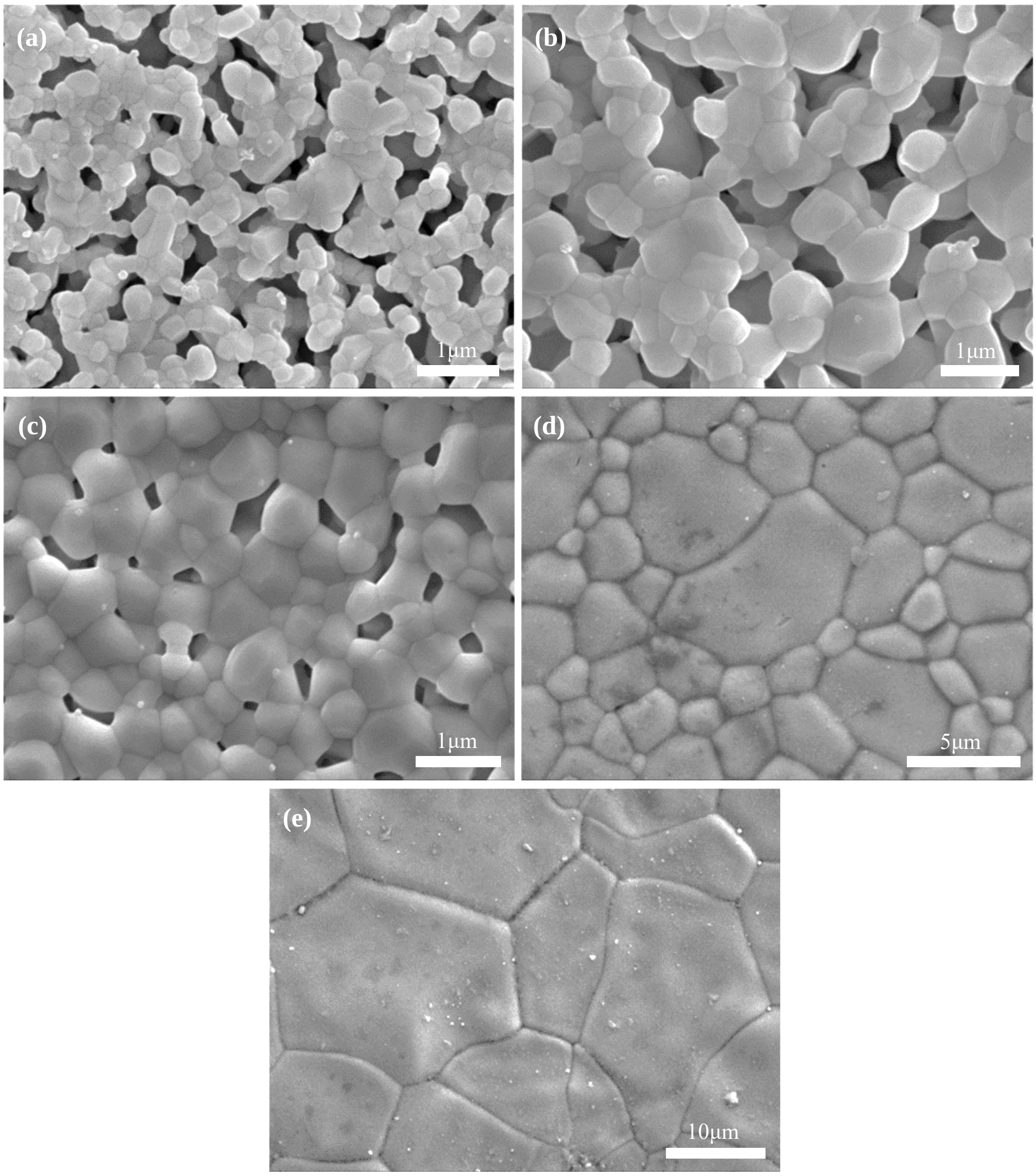

Figure 4.11 Micro morphologies of scaffolds sintered at (a) 1000 ℃, (b) 1100 ℃, (c) 1200 ℃, (d) 1300 ℃ and (e) 1400 ℃

Figure 4.11 indicates that the decrease of porosity in all scaffolds was self-evident. Particularly, the HA particles preferred to gather together due to migration and densification, which on one hand increased the grain size of HA; while on another hand, it made the apparent volume of scaffolds become smaller at higher sintering temperature, resulting in larger shrinkage (Figure 4.6). In addition, the crystal particles in Figure 4.11 (a), (b) and (c) had smooth surfaces, while that in Figure 4.11 (d) and (e) were more rough, which might be the result of HA decomposition at high temperature.

4.4.1.6 Grain size

It can be observed from Figure 4.12 that, as the sintering temperature rose from 1000 ℃ to 1200 ℃, the grains of HA scaffolds grew steadily (from 285 to 1055 nm); but when it was higher than 1300 ℃, the crystal size could be up to 16 μm. The growth of grain size is directly linked to porosity, which eliminates nano-scaled pores during sintering in fact. Consequently, the porosity of porous scaffolds and solid blocks was opposite to the trend of increasing grain size.

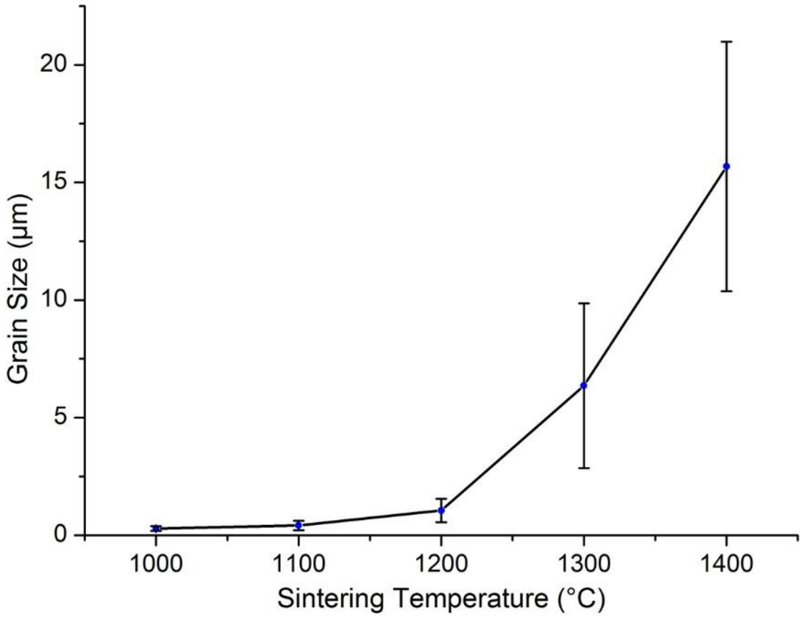

Figure 4.12 Grain size of HA scaffolds sintered at different temperatures

In view of shrinkage, porosity, microstructures and grain size, it can be concluded that there were two periods in the sintering of HA scaffolds when temperature was gradually increased. Firstly, if the sintering temperature was no more than 1200 ℃, the migration and densification of HA particles was the dominant behaviour of sintering. However, when sintered at higher temperatures (≥ 1300 ℃), the main activity of HA granules focused on growth of grain instead. In other words, 1300 ℃ is possibly enough in terms of sintering temperature to obtain fully densified HA scaffolds on the condition of sufficient mechanical strength. In addition, the temperature should better not exceed 1200 ℃ in order to allow microporous structures in HA scaffolds to be biomimetic, which is beneficial and essential to bone regeneration in BTE [48, 77, 144].

4.4.2 Physicochemical Properties

4.4.2.1 Phase composition

The XRD patterns of original HA powder and scaffolds sintered at different temperatures are illustrated in Figure 4.13, where the vertical base line stands for the relative (or offset) intensity of diffraction peak. The composition of crystalline phase of all samples can be regarded as pure HA phase according to PDF #09-0432, without significant interference from other phases. Nevertheless, the peak intensity of diffraction was notably reduced when sintering temperature was higher than 1200 ℃. The reason for this phenomenon will be analysed along with crystallinity.

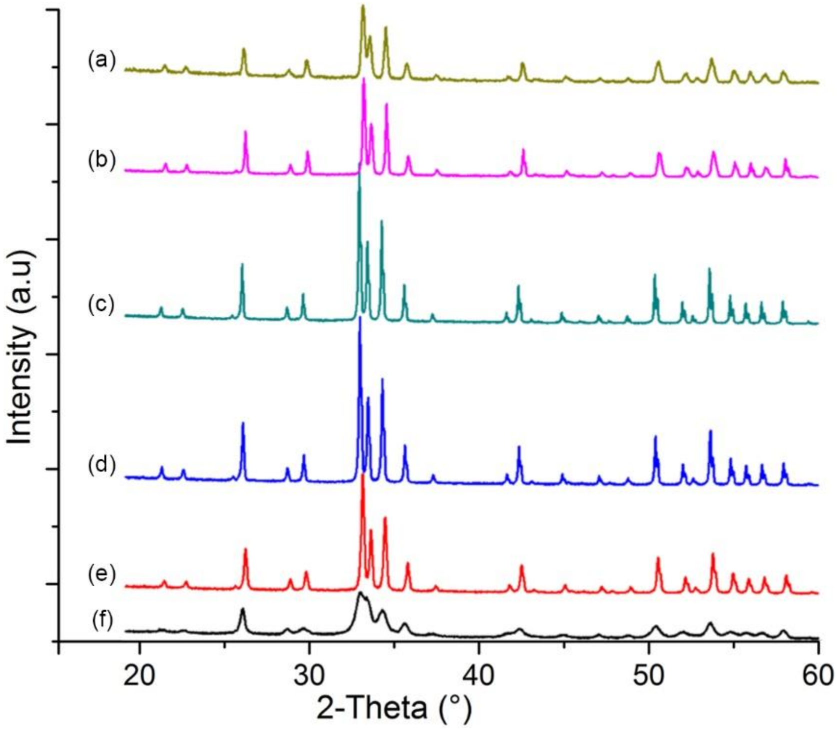

Figure 4.13 XRD patterns of scaffolds sintered at (a) 1400 ℃, (b) 1300 ℃, (c) 1200 ℃, (d) 1100 ℃, (e) 1000 ℃, and (f) original HA powder

4.4.2.2 Crystallinity

In the light of Figure 4.3, the peak intensity of diffraction at certain crystal faces, *i.e.* ***(211)***, ***(300)*** and ***(112)***, was investigated to know the crystallinity of HA scaffolds after sintering at different temperatures. The calculated crystallinity of hydroxyapatite phase in original powder and fully sintered scaffolds is diagrammed in Figure 4.14. The original powder before sintering had very low crystallinity of only about 45.8%. Even sintered at low temperature, *e.g.* 1000 ℃, the crystallinity of hydroxyapatite phase in HA scaffolds was considerable (≥ 89.8%). With the increase of sintering temperature, the crystallinity would gradually increase, reaching a maximum of 93.6% at 1200 ℃, and followed by a slight reduction at higher temperatures. Accordingly, the peak intensity of hydroxyapatite phase was decreased.

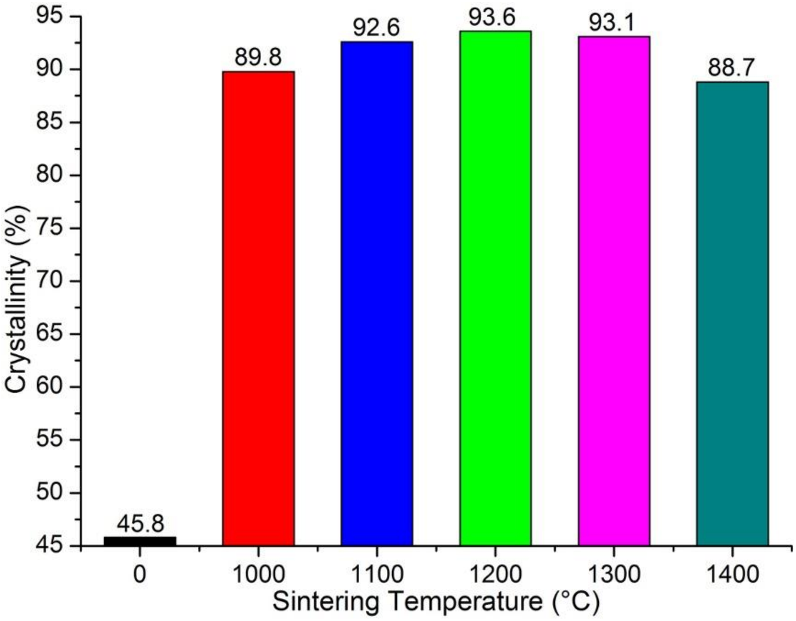

Figure 4.14 Crystallinity of HA powder and scaffolds sintered at different temperatures

In general, the main influence factors for final phase composition of HA scaffolds are original powder [190], sintering temperature [173] and atmosphere [172]. HA tends to decompose into α-TCP, β-TCP and tetra-calcium phosphate (TTCP) due to dehydroxylation (Equation 4.8 [173]) at high temperature.

$$\mathrm{Ca_{10}[PO_4]_6[OH]_2 \rightarrow 2Ca_3[PO_4]_2 + Ca_4P_2O_9 + H_2O} \quad \text{(Equation 4.8)}$$

Actually, the separation of hydroxyl (-OH) will not take place when sintering temperature is below 1350 ℃. However, the decomposed products of HA at higher temperature (≥ 1400 ℃), for instance, β-TCP, TTCP, CaO (Equation 4.9 [173]) *etc*., will inhibit the densification process, which lowers the mechanical strength correspondingly.

$$Ca_{10}[PO_4]_6[OH]_2 \rightarrow 3Ca_3[PO_4]_2 + CaO + H_2O \qquad \text{(Equation 4.9)}$$

Looking back on the XRD result in Figure 4.13, it is clear that none of the above products was found in the scaffolds even sintered at 1400 ℃. An possible explication for such confusion may be referred to the research of Zhang *et al*. [191]: the temperature for TCP generation is normally between 1200 and 1450 ℃, and a non-stoichiometric phase, that is, $Ca_{10}[PO_4]_6[OH]_{2(1-x)}$ shown in Equation 4.10 [191], may be formed in range of 1200 - 1350 ℃, which leads to the reduction of peak intensity at ***(211)*** crystal face, since the non-stoichiometric phase is “invisible” to XRD. Considering this case, 1350 ℃ should better be the up limit of sintering temperature for HA scaffolds.

$$Ca_{10}[PO_4]_6[OH]_2 \rightarrow Ca_{10}[PO_4]_6[OH]_{2(1-x)} + 2xH_2O \qquad \text{(Equation 4.10)}$$

4.4.2.3 Hydrophilicity

As a substitute of bone tissues to repair large defects, HA scaffolds must possess good performance in hydrophilicity in order to achieve satisfactory effect [192], because the environment of human tissue fluid is aqueous. Thus, it is necessary to evaluate the hydrophilicity of HA scaffolds. Particularly, water absorption and contact angle with water was investigated to study the influence of sintering temperature on hydrophilicity (Figure 4.15). Note that solid blocks instead of porous scaffolds were used for evaluation. As shown in Figure 4.15, the ability of water absorption changed oppositely to contact angle, which accords with the law of physics. Due to the excellent capacity of water absorption (about 30%), the water droplet for test was completely absorbed by blocks sintered at 1000 ℃ and 1100 ℃, resulting in zero contact angle (marked with red stars in Figure 4.15). It is obvious that, with the rise of sintering temperature, the contact angle of HA blocks increased dramatically. There was however merely little difference in HA blocks sintered at higher temperature (1300 and 1400 ℃) in terms of water absorption and contact angle. Considering that the difference in water absorption and contact angle is actually attributed to micro-/nano-porosity, the blocks with more porosity and larger pore size can reasonably absorb more water due to capillary action. Since the hydrophilicity can reflect the bioactivity of materials in adhesion of cells and protein to some extent [193, 194], from this point of view, a low sintering temperature for HA scaffolds is preferred.

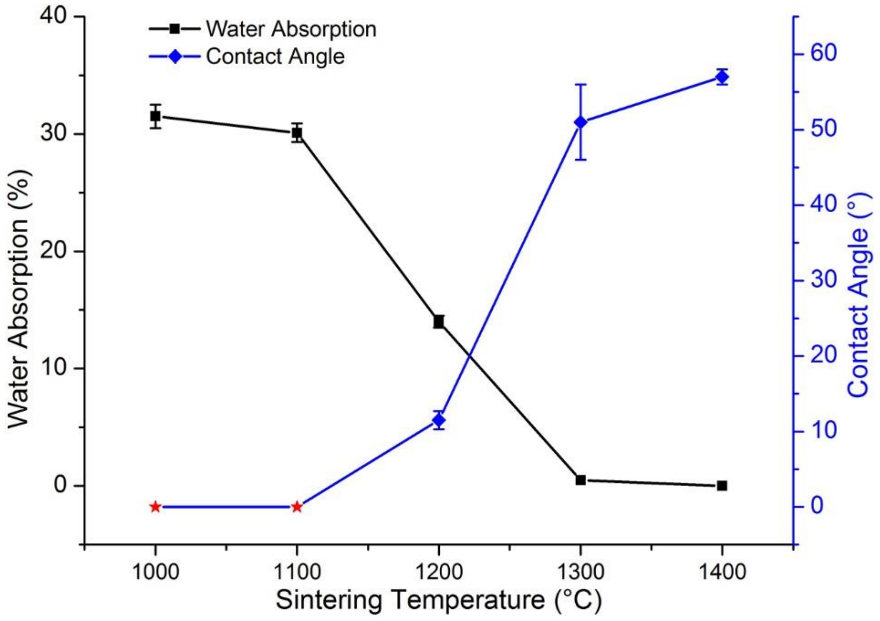

Figure 4.15 Relationship of water absorption and contact angle

4.4.3 Biological Performance

The histogram (Figure 4.16) summarises the proliferation result of MC3T3-E1 cells on scaffolds sintered at 1000 ℃, 1100 ℃, 1200 ℃, 1300 ℃ and 1400 ℃. Obviously, the OD value, which indirectly reflects the number of cells, of scaffolds sintered at 1000 ℃ was always the highest at day 1, 3, 5 and 7; on the contrary, the scaffolds after sintering at 1300 ℃ or 1400 ℃ were relatively more bio-inert, where no significant difference was found in the two groups. Besides, the MC3T3-E1s would proliferate faster if the sintering temperature was lower. Moreover, the OD value (implying the number of cells) dramatically increased in all scaffolds during cell culture for 1 week, which is another evidence that HA scaffolds are absolutely biocompatible after sintering. In light of the results of hydrophilicity, porosity and microstructure, it is reasonable that the scaffolds exhibit better bioactivity due to porosity and wall roughness, which may facilitate the adhesion of cells, protein and ions that promotes proliferating activity. Similar finding had been reported by Sun *et al*. [195] that lower temperature (1000 ℃) for the sintering process of HA scaffolds (5 × 5 × 5 mm in dimension) was more in favour of the release of growth factor, *i.e.* a new polypeptide named P28, which is closely related to BMP-2, compared to 1200 ℃ and 1400 ℃. According to Sun *et al*., higher specific surface area (SSA) and porosity of scaffolds sintered at low temperature contributes to the adhesion of P28, resulting in more efficient release of P28.

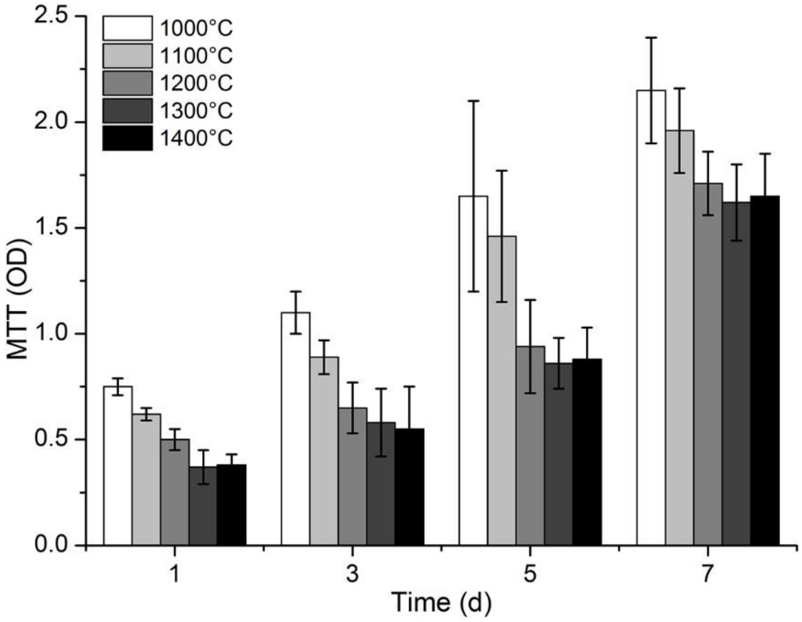

Figure 4.16 Proliferation of MC3T3-E1s on scaffolds sintered at different temperatures

4.5 Summary

In order to investigate the influence of sintering temperature on scaffolds, microwave sintering was employed to sinter HA scaffolds at 1000, 1100, 1200, 1300 and 1400 ℃ respectively. It turned out higher sintering temperature was conducive to enhanced mechanical strength, but it also resulted in smaller pore/grain size and SSA, as well as poorer hydrophilicity. Moreover, the scaffolds sintered at lower temperature exhibited better biological performance in terms of proliferation, which is the foundation of osteogenesis. In other words, the scaffolds sintered at high temperature may inhibit the deposition of bone-like apatite and adsorption of proteins, and thus may have less satisfactory effect of osteogenesis. Therefore, the selection of temperature set for sintering of HA scaffolds should take full account of mechanical properties and biological performance. Specifically, under the premise of sufficient mechanical strength, lower sintering temperature is preferred in order for better bioactivity.

Chapter 5. Novel Fabrication of Hierarchically Porous Scaffolds

5.1 Introduction

In general, it is of great significance to balance porosity, pore size and mechanical strength during the design and preparation of scaffolds for BTE, as high porosity and large pore size usually lead to low mechanical strength. Specifically, high porosity is conducive to the proliferation, intercellular migration and interaction of osteoblasts, and can enhance the biological and mechanical connections between newly formed bone and muscle tissues. As for pore size, many researchers had done considerable work to define the critical value for bioactivity. For instance, Hulbert *et al*. [83] suggested that pore size should not be less than 100 μm in order to ensure biological performance; whereas Tsuruga *et al*. [84] found that scaffolds with pore sizes greater than 300 - 400 μm had better bioactivity. In addition, increasing studies have shown that the distribution of pore size cannot be ignored. Firstly, macropores (> 100 μm) play a crucial role in the formation of bone tissues, while pores of smaller size (micro-/nano-pores, < 10 μm) and high wall roughness may also greatly influence the repair of bone defects [37, 82]. Moreover, as a load-bearing part during BTE *in vivo/vitro*, the mechanical properties of bone scaffolds, especially strength, must be considered throughout the preparation process.

However, due to the widely known limitations of traditional preparation techniques [152, 153], it is a challenge to fabricate scaffolds with full consideration of these properties. Taking moulding or casting as a typical example, it is difficult to ensure the interconnectivity of macropores which is basically required in BTE applications. And even recently developed 3D printing techniques are not capable of producing porosity at the nano-scale [128-130], limiting their practical use a great deal. Hence, new methods to fabricate scaffolds are highly demanded. For instance, an innovative technology through phase transformation from wood to scaffolds (rather than commercial calcium-based bioceramics like HA, β-TCP, *etc*.) had been developed by Tampieri *et al*. [196], which provides a new way for inorganic biomaterials to be applied in BTE. In Baradararan's research [197], the mechanical properties and structure of porous scaffolds with open and interconnected pores were improved by combining gel casting and polymer sponge. Du *et al*. [198] prepared porous structures with pore distribution of multi-scales (from micrometre to nanometre) through improved phase separation combined with ESP, and the pore structures and micro-morphologies could be controlled by adjusting the composition of polymers and temperature sets.

Instances of similar studies can be quoted easily, but the above are sufficient to show that it is a useful idea to make full use of different technologies to improve the mechanical and biological performances as well as the internal pore structures. Inspired by these references, highly porous scaffolds with hierarchical porosity were constructed through the combination of MAM deposition and chemical foaming technology [199]. To be more specific, by adding a certain amount of pore former, massive pores would be formed on the crossbeams of scaffolds after microwave sintering, owing to the combustion of porogen during sintering (Figure 5.1). In this way, hierarchically porous scaffolds can be prepared without any further complex processes, as shown in Figure 5.1.

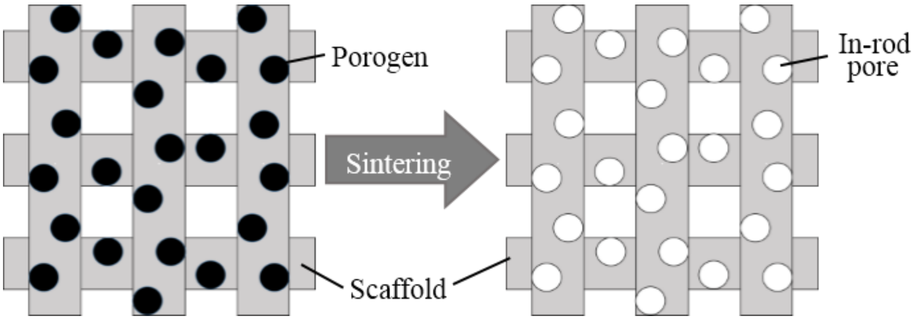

Figure 5.1 Schematic formation of hierarchically porous scaffolds

5.2 Materials

5.2.1 Materials for HA Scaffolds

Nano-sized HA powder (Figure 3.4) and deionised water were the main components of HA slurry. To get well dispersed slurry with favourable properties for deposition, other reagents such as glycerol, ammonia, nitric acid and NH_4-PAA *etc*. (Table 3.3) were used.

5.2.2 Pore Former

5.2.2.1 Potential materials for porogen

Currently, there are lots of commercially available materials for porogen, such as polymers including polystyrene (PS) [200] and PMMA [201] *etc*., water-soluble compounds, *e.g.* sodium chloride (NaCl) [106], decomposable compounds at high temperature, for instance, bicarbonate (NH_4HCO_3 [104] and $NaHCO_3$ [202]), and combustible inorganics like graphite (G) [110]. Since porogen is the key to this novel method, it is necessary to analyse the materials carefully to avoid possible failure in experiments resulted from improper selection of pore former. The advantages and disadvantages of these options are listed in Table 5.1.

Table 5.1 List of the advantages and disadvantages of potential materials for porogen

Options	Advantages	Disadvantages
Polymers	1) A wealth of sources 2) Low cost 3) Sufficient foams after combustion	1) Low ignition point 2) The combustion process usually results in intermediate products which often contaminate scaffolds. 3) Possible interference from auxiliary reagents
Water-soluble compounds	1) Wide range of supplies 2) Inexpensive 3) Easy and simple preparation process	1) Impossible to acquire fully interconnected pores 2) Impurities may still remain in sintered scaffolds even after leaching treatment.
Decomposable compounds	1) Foaming and sintering are simultaneous 2) Minimum shrinkage 3) High efficiency	1) Insufficient foams 2) Reduction of solid phase ratio of HA 3) Impurities consisting of undecomposed compounds
Combustible inorganics	1) Commercially available at low cost 2) Moderate ignition for complete oxidation 3) Sufficient foams without residual	1) Requirements of additional sintering process 2) Sintering process is time-consuming. 3) Possibly overheating HA particles during sintering

In view of the advantages and disadvantages in Table 5.1, combustible inorganics is more suitable as the porogen which meets our demands the most, and graphite is obviously a fine choice if taking cost and feasibility into account. On the other hand, in order to overcome the mentioned shortcomings in Table 5.1, a detailed study on the sintering process of HA and graphite composite scaffold (short for **HA-G**) has to be carried out accordingly.

5.2.2.2 Suitable particle size

The particle size of porogen will exert a significant influence on pore structures and porosity. Considering that additional in-rod porosity would be formed in HA-G scaffolds after sintering at high temperature, the distribution of porogen size will definitely impact the microstructure of additional pores in micron and nano scale. Many studies have confirmed that both macropores and micropores are important to the osteoinductive activity of bone scaffolds [47, 203]. In addition, micropores, especially those at the nano-scale, can promote the differentiation of osteoblasts and formation of bone tissues [42, 49, 204], because there is a large quantity of micro-/nano-porosities in natural bone tissues [14]. Since MAM technique is characterised by interconnected pore structures with sufficient amount of macroporosity, the scaffolds should better contain certain amount of micro-/nano-porosity so that the biological activity of scaffolds can be significantly improved. In other words, it is preferable to determine the porogen size from the angle of micron or nano scale.

As the general size of osteoblasts is about 20 μm, in order that the in-rod pores formed by porogen can provide additional space for living and adhesion of osteoblasts, 30 - 50 μm is the right pore size. Besides, due to lamellar structure and brittleness, graphite is highly likely to be broken up during the preparation of slurry, especially under the condition of ultrasonic dispersion, which helps produce considerable number of nanopores. Furthermore, the auxiliary chemical reagents also contribute to nanoporosity after sintering at high temperature (Figure 4.11). In this case, micron graphite sized 40 - 65 μm in dimension is the perfect option to form additional microporosity in the range of about 30 - 50 μm, if possible shrinkage (~ 15%) of scaffolds is considered.

5.2.2.3 Micron graphite powder

The micron graphite (μG) used in the experiments was purchased from Sinopharm Chemical Reagent Group Co., Ltd. The nominal particle size of graphite is 325 mesh (or 45 μm), and the purity is higher than 99.95%. To ensure that the graphite powder could really meet our requirements, the particle size, micro-morphologies and size distribution were also characterised in this chapter.

5.3 Methodology

5.3.1 Experimental Procedure

To acquire fine control of bulk porosity, the volumetric percentage of graphite in HA-G composite scaffolds was varied from 0 to 40 vol.%, with an increasing gradient of 5 vol.%. Accordingly, the scaffolds were marked by **HA-G-X**, where X stands for the amount of graphite. Note that normal scaffolds without graphite as porogen (**HA-P**) were used as control group for comparison and further analysis. The experimental procedure for this study has been summarised in Figure 5.2.

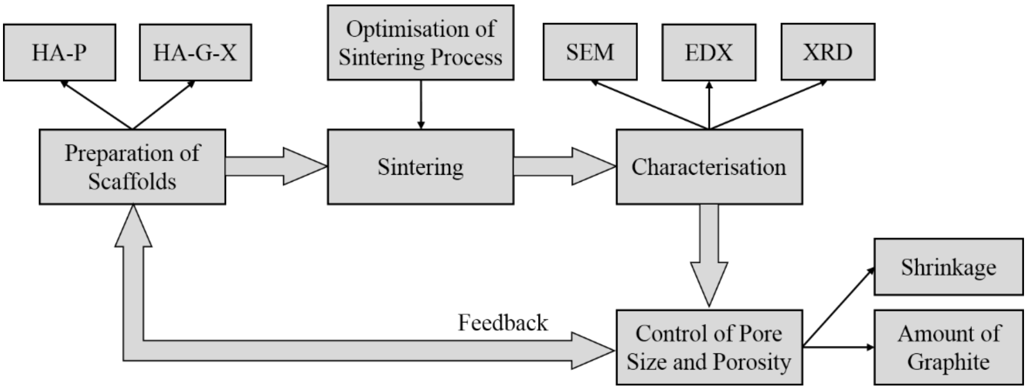

Figure 5.2 Experimental procedure of this chapter

5.3.2 Equipment and Devices

Table 5.2 shows the main details of the equipment and devices used in the experiments for fabrication and characterisation of scaffolds.

5.3.3 Fabrication of HA-P Scaffolds

The preparation process of HA-P scaffolds has been introduced in detail before (***Section 3.4.3***), so here it provides the main parameters for fabrication: nozzle -- G23 (0.34 mm), extrusion speed -- 0.005 mm/s, X-Y speed -- 7.0 mm/s, layer thickness -- 0.45 mm, filament space -- 1.2 mm. Other details regarding to this process can be found in ***Section 4.3.3***.

Table 5.2 Main details of equipment and devices for experiments

Device	Model	Manufacturer	Application
MAM system	MAM-II	Fochif	Fabrication of scaffolds
Electronic balance	HTP-312	Huachao	Weighing
Ultrasonic cleaner	CE-6200A	Jaken	Ultrasonic dispersion
Ultrasonic humidifier	LU100	Deerma	Prevention of crack
Microwave furnace	Hamilab-V1500	Syno-Therm	Sintering of scaffolds
Laser particle size analyser	LB550	Horiba	Evaluation of graphite size
Simultaneous thermal analyser	TGA7	Perkin Elmer	Track of sintering process
Stereomicroscope	XTL-340	Changfang	Measurement of pore size
Scanning electron microscope	Sirion 200	FEI	Characterisation of micro-morphologies
Energy dispersive X-ray detector	Sirion 200	FEI	Analysis of Ca/P ratio
X-ray diffractometer	X’Pert Pro	PANalytical B.V.	XRD analysis of scaffolds

5.3.4 Evaluation of Graphite

Prior to preparation of HA-G scaffolds, detailed characterisation of graphite was performed, including microstructure, particle size and size distribution. The particle size and distribution was analysed by laser diffraction particle size analyser (LDPSA), which emits a coherent beam passing through a sample to identify the characteristics of the diffraction pattern at infinity for particle size calculation. Due to poor fluidity, graphite powder should be uniformly dispersed in water solution, using dispersant (UV9510, UniqChem) for graphite if necessary. The amount for analysis was about 0.2 g. The micro-morphologies of graphite powder was observed by SEM. Firstly, conductive paste was required to fix graphite and for even distribution of powder. Note that the amount of graphite must be as little as possible so that graphite particles could be recognised at high magnification. The electron accelerating voltage was 15.0 kV after vacuum treatment.

5.3.5 Fabrication of HA-G Composite Scaffolds

As mentioned before, there were 8 groups of HA-G scaffolds with different content of graphite as porogen, *i.e.* 5 vol.%, 10 vol.%, 15 vol.%, 20 vol.%, 25 vol.%, 30 vol.%, 35 vol.% and 40 vol.% respectively. For the convenience of description, the unit vol.% may be simplified as % sometimes. In addition, to prevent the agglomeration of graphite powder during preparation, which increases the actual particle size of graphite, certain amount of graphite dispersant (in proportion to the content of graphite in fact) was added to the dispersive solution for HA and graphite. The schematic preparation process of HA-G scaffolds is illustrated in Figure 5.3.

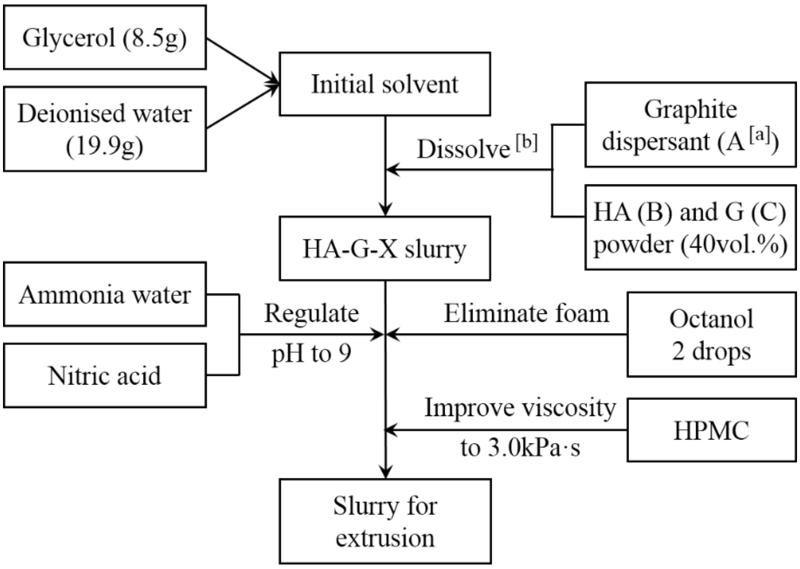

Figure 5.3 Flowchart of HA-G scaffold preparation process

Where in Figure 5.3, **[a]** -- the actual amount of A, B and C was listed in Table 5.3; **[b]** -- HA and graphite powder must be uniformly mixed before added into dispersive solution (the uniformity can be judged by the colour of mixture: fine uniformity usually appears dark grey without white or black dots). Similarly, HA and graphite powder were evenly added by 5 times, *i.e.* (B+C)/5 grams each time, followed by continuously stirring and ultrasonic dispersing in the whole process to ensure homogeneity.

Table 5.3 Actual amount of components for HA-G slurry (30.0g dispersive solution)

HA-G-X / vol.%	**5**	**10**	**15**	**20**	**25**	**30**	**35**	**40**
A (dispersant / mL)	0.1	0.2	0.3	0.4	0.5	0.6	0.7	0.8
B (graphite powder / g)	1.8	3.6	5.3	7.1	8.9	10.7	12.4	14.2
C (hydroxyapatite / g)	47.5	45.0	42.5	40.0	37.5	35.0	32.5	30.0

Note: The total volume of HA and graphite in HA-G scaffolds is the same to HA-P in order to keep the same solid phase in all scaffolds before sintering. The density of HA and graphite is 3.16 g/cm^3 and 2.25 g/cm^3 respectively.

5.3.6 Optimisation of Sintering Process

Synchronous thermal analysis (STA), or thermal gravimetric analysis (TGA) / differential scanning calorimetry (DSC), is very useful to track and record the sintering behaviour of scaffolds in real time, which can provide guidance for optimisation of sintering profile. The main points for test are: powdered sample (HA-P, HA-G-5 or HA-G-40) -- 0.5 g, maximum temperature -- 1200 ℃, atmosphere -- air, heating rate -- 10 ℃/min.

The practical sintering profiles for HA-P and HA-G scaffolds are shown in Figure 5.4. **T1** was 250 ℃ for combustion of chemical reagents. According to the conclusion from Chapter 4, **T3** was set to be 1200 ℃. The setting of **T2** (900 ℃ actually) was based on the STA result. The heating rate of each stage was 5 ℃/min, and the holding time at every temperature was 2 h in both sintering profile. After sintering, the scaffolds were cooled down to 500 ℃ at 4 ℃/min, and finally cooled inside the furnace. Apparently, the sintering profile of HA-G composite scaffolds was a bit more complex than HA-P, as it is known that the firing temperature (FT) of graphite in the air is about 800 ℃, which is smaller than final holding temperature (1200 ℃). Provided that the sintering temperature raised directly from 250 to 1200 ℃, the oxidation of graphite and sintering of HA may occur at the same time; on this occasion, the combustion of graphite may be incomplete due to insufficient oxygen resulted from the densification process of HA particles.

Therefore, the sintering profile of HA-P scaffolds would be no longer suitable for HA-G scaffolds. The optimisation and design of new sintering profile will be introduced later.

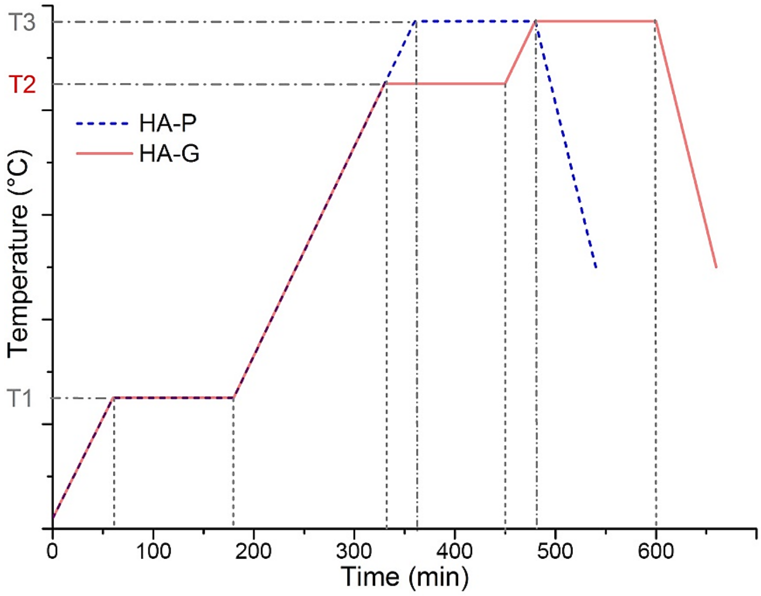

Figure 5.4 Sintering profile for HA-P and HA-G scaffolds

5.3.7 Characterisation of Scaffolds

5.3.7.1 Shrinkage

In order to finely control the overall size and porosity of scaffolds after sintering, the shrinkage in X/Y (length/width) and Z (height) directions was measured. However, it was found that the shrinkage caused by drying (**S_D%**) and sintering (**S_S%**) process needs to be analysed separately, as shown in Equation 5.1 and Equation 5.2, which were both derived from Equation 4.1.

$$S_D\% = \left(\frac{L_0 - L_D}{L_0}\right) \times 100\% \qquad \text{(Equation 5.1)}$$

$$S_S\% = \left(\frac{L_D - L_S}{L_D}\right) \times 100\% \qquad \text{(Equation 5.2)}$$

Where, **L_0** is the original size after fabrication; **L_D** is the size after drying process, and **L_S** is the final size of sintered scaffolds. The size may be in X/Y or Z direction, and the parameter for drying process was 60 ℃ for 24 hours.

Finally, the total shrinkage (**S_T%**) of scaffolds can be obtained by Equation 5.3.

$$S_T\% = \left(1 - (1 - S_D) \cdot (1 - S_S)\right) \times 100\% \qquad \text{(Equation 5.3)}$$

In addition, 6 samples of each group were used to reduce random error, and the arithmetic mean was used for calculation.

5.3.7.2 Porosity

The porosity involved in this method is subdivided into two types: the bulk porosity (**P%**) and additional in-rod porosity (**P_G%**, formed by graphite). The evaluation of bulk porosity can refer to Equation 4.3. Although it is difficult to measure the in-rod porosity accurately, theoretical estimation of the in-rod porosity is still possible and feasible (Figure 5.5). Particularly, in Figure 5.5, **Φ_R** is the diameter of rods, and **Hz** is the height of scaffolds. As for **Lxy**, it is the average of length in X/Y direction. Specifically, the estimated volume of HA skeleton (**V_{HA}**) can be calculated by Equation 5.4. And then the additional in-rod porosity can be obtained according to Equation 5.5, assumed that the rods on scaffolds could manage the original shape regardless of numerous in-rod pores.

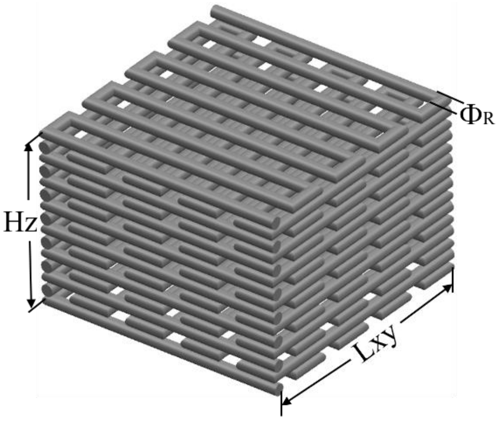

Figure 5.5 Theoretical 3D model of scaffold

$$V_{HA} = \left(\frac{\pi\Phi_R}{4} \times L_{xy} \times H_z\right) \times (N_f + 1) \qquad \text{(Equation 5.4)}$$

$$P_G\% = \left(\frac{V_{HA}}{V_T} - 1\right) \times 100\% + P\% \qquad \text{(Equation 5.5)}$$

Where, **N_f** stands for the number of filaments in a single layer, and “**+1**” is for compensation of **Lxy**; $\mathbf{V_T}$ is the apparent volume of scaffolds, *i.e.* $Lx \times Ly \times Hz$ in fact; **P** is the bulk porosity. Similarly, each HA-G sample was measured 6 times in order to reduce random error, and to get the average for calculation.

5.3.7.3 Composition

It is of great importance to confirm that the graphite in HA-G is completely burnt out after sintering with improved profile. In this study, the composition of scaffolds both before and after sintering was characterised by XRD and energy dispersive X-ray (EDX).

XRD was used to analyse the phase composition of HA-G scaffolds (grinded into powder before test) to verify whether graphite had be totally oxidised. The main parameters for XRD analysis were: radiation -- Cu/Kα, operating values -- 40.0 kV and 40.0 mA, 2θ range -- 10 ° to 60 °, step size -- 0.01313 °, test samples -- HA-P, HA-G-5 and HA-G-40.

EDX is a commonly used analytical technique for the elemental analysis or chemical characterisation of a sample, which relies on the interaction of some source of X-ray excitation with tested sample. However, its characterisation capability depends in large part on the fundamental principle that a set of peaks on the electromagnetic emission spectrum of each element is identifiable due to unique atomic structure [205]. Therefore, the result of EDX is not as accurate as expected, but still enough for qualitative analysis. The sample for EDX analysis was HA-G-25 (before and after sintering).

5.3.7.4 Micro-morphologies

The microstructures and morphologies of scaffolds after sintering were observed by SEM to affirm the formation of additional micropores due to the introduction of porogen. The selected samples were HA-P, HA-G-5, HA-G-25 and HA-G-40. In order for clear SEM images, it is of great necessity to wash scaffolds with deionised water and to fully dry for 30 min at 60 ℃ after sintering. In addition, because of non-conductivity, gold spraying for 60 seconds was performed to make the scaffolds conductive. The electron accelerating voltage was 15.0 kV, and the minimum and maximum magnification during observation was 100 × and 8000 × respectively.

5.4 Results and Discussion

5.4.1 Graphite Powder

The result of particle size and detailed distribution by LDPSA are shown in Table 5.4 and Figure 5.6. From Table 5.4, the refractive index of solvent (1.33) and graphite particles (2.42) were very small, with only 6.68% of laser shading degree. Besides, the weighted residual was as little as 0.12%. It is worth mentioning that the concentration of graphite suspension was low enough (0.0121%) to make sure the graphite particles were uniformly dispersed in water without any possible aggregation. In other words, the accuracy of this result is highly reliable, which is also confirmed by the high consistency (2.788, an acceptable value considering that graphite may be stripped during ultrasonic dispersion and ball milling).

Table 5.4 Results of graphite particle size by LDPSA

Analytical Indicator	Parameter	Analytical Item	Result
Solvent	Water	Weighted residual	0.12%
Refractive index of solvent	1.33	Concentration	0.0121%
Absorption rate	0.00	Consistency	2.788
Refractive index of graphite	2.42	SSA	415.5 m^2/kg
Shading degree	6.68%	Dv-10	6.34 μm
Scattering model	Mie	Dv-50	23.6 μm
		Dv-90	82.4 μm

Ideally, supposed that the graphite particles were spherical, the calculated ball diameter of graphite was about 6.4 μm according to the result of SSA; while actually the average (~ 30 μm) was far larger than this, indicating that graphite particles were lamellar. Dv-X (discrete value) represents the particle size that the cumulative distribution proportion of this or smaller sizes firstly reach X%. For instance, Dv-50 in Table 5.4 means that there was 50% of graphite particles whose sizes were no more than 23.6 μm, to put it another way, within the range of 0 - 23.6 μm. Accordingly, 80% (Dv-10 to Dv-90) of graphite particles were distributed between 6.34 - 82.4 μm, which was close to a normal distribution.

Figure 5.6 shows the detailed distribution of particle size of graphite by LDPSA, and the average size (**S_A**), which can be calculated according to Equation 5.6, was about 53.4 μm. As mentioned, the desired size of porogen was 40 - 65 μm, so the graphite powder used in this study could fully satisfy our experimental requirements. The extremum of distribution probability corresponding to 27.4 μm (marked in Figure 5.6) approximated to Dv-50 (23.6 μm) very well, revealing that the graphite particles were evenly distributed on the whole. Further analysis of this figure tells that the vast majority (73.3%) of graphite particles were in the range of 9.8 - 98.1 μm (probability ≥ 1%), making it highly capable of producing considerable micropores which could allow additional space for enhanced adhesion and proliferation of osteoblasts during cell culture.

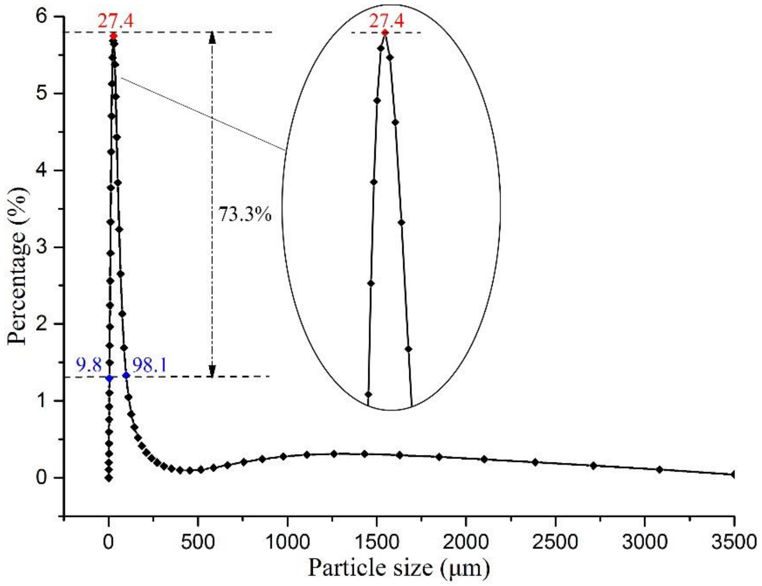

Figure 5.6 Distribution of particle size of micron graphite

$$S_A = \sum (S_Z \times P\%) \qquad \text{(Equation 5.6)}$$

Where **P%** is the percentage of a particular particle size (**S_Z**).

The morphologies of micron graphite by SEM are shown in Figure 5.7. Overall, the graphite particles were in good shape, and the average size (~ 45 μm) was consistent to nominal value and LDPSA result (Figure 5.7(a), (b) and (d)). Nonetheless, the lamellar structure, brittleness and delamination of graphite was obvious in Figure 5.7(c), resulting in a large number of fragments (region A). Similar phenomenon was also found in Figure 5.7(c), *e.g.* region B. On the other hand, it was expected that most of the graphite particles sized between 30 - 50 μm with abundant graphite fragments (usually in nano scale, less than 1 μm) could form micro-/nano-porous in-rod pores on the scaffolds to promote osteoinduction. In this respect, the graphite powder from Sinopharm was a good choice as porogen.

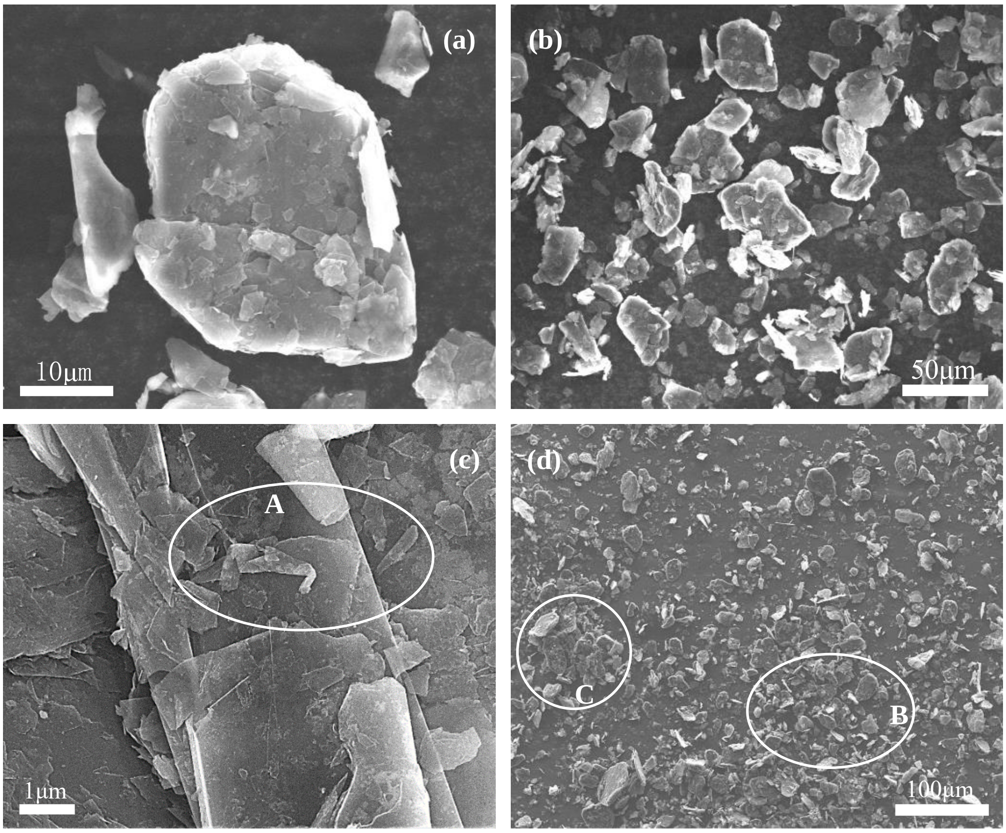

Figure 5.7 Micro-morphologies of graphite by SEM

In addition, as seen from Figure 5.7(d), despite that the amount of graphite was rather small and the particles were hardly in stack, the agglomeration of graphite was still unavoidable (region C). As a result, it is necessary to use dispersant for graphite when preparing HA-G slurry. In summary, both the result of particle size and distribution by

LDPSA and the microscopic morphologies observed by SEM could provide sufficient evidence to show the suitability of graphite powder to serve as porogen in this study.

5.4.2 Optimisation of Sintering Profile for HA-G Scaffolds

The sintering behaviour of HA-P and HA-G-5 and HA-G-40 scaffolds was intensively studied, in order to optimise the sintering process of HA-G scaffolds, so that the graphite could be fully oxidised and burnt out, and the formed additional micropores would be retained as much as possible by reducing the possible migration of sintered particles (*i.e.* sintering shrinkage).

The results of TGA/DSC, also known as STA, are displayed in Figure 5.8. There was only one critical stage (around 220 ℃) with respect to weight loss (TGA) and energy release (DSC) during the sintering process of HA-P sample, while two were found in HA-G-5 (Figure 5.8(b)) and HA-G-40 (Figure 5.8(c)), at 220 ℃ and 850 ℃ respectively. Considering that the FT of auxiliary reagents or graphite dispersant (used for dispersing HA slurry) is lower than 250 ℃, it can be concluded that the initial stage with notable weight loss and energy release was the combustion of chemical components and evaporation of deionised water, which occurs at 100 ℃ or higher temperature. Thus, owing to uniform dispersion of HA slurry, it is reasonable that the oxidisation process of auxiliary reagents or graphite dispersant could contribute to evenly distributed in-rod nanopores that are beneficial to improve the viability of cells [132], provided that the sintering temperature is not too high (≤ 1200 ℃ Figure 4.11 (a), (b) and (c)). As for HA-G scaffolds, another significant stage started from 600 ℃ and ended around 1000 ℃, which exactly coincides to the FT of graphite. In addition, the oxidation process of graphite at 850 ℃ was the most active, especially in Figure 5.8(c) due to higher content of graphite.

Consequently, 850 ℃ was a key temperature for the purpose of optimising sintering process for HA-G scaffolds. The optimised sintering profile has been illustrated in Figure 5.4, which was derived from that of HA-P (Figure 4.2(b)). Specifically, another holding

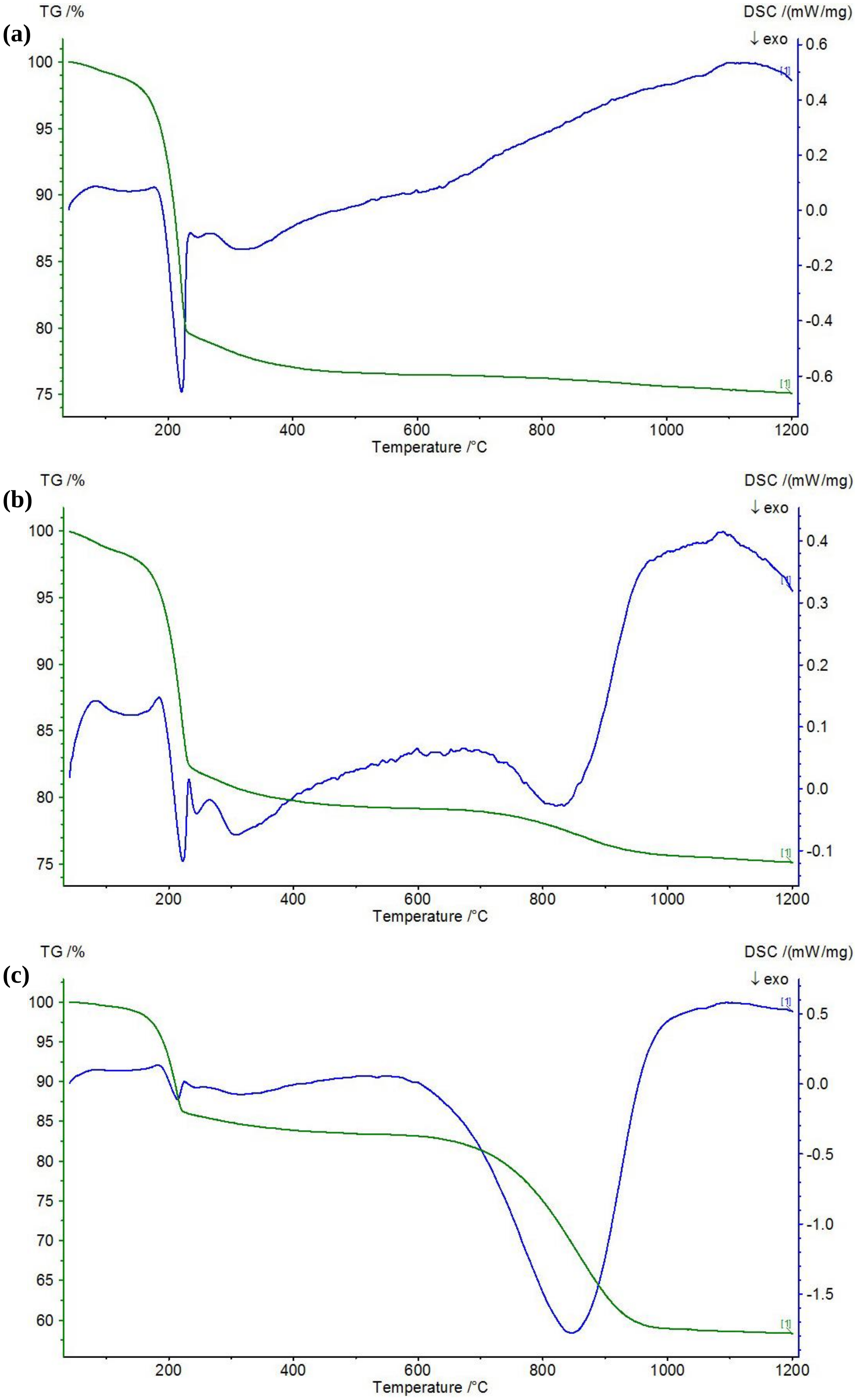

Figure 5.8 STA analysis of HA scaffolds: (a) HA-P, (b) HA-G-5, (c) HA-G-40

process at 900 ℃ for 2 hours was designed specially for complete oxidation of graphite particles during sintering. The holding temperature was slightly higher than 850 ℃ in order to reduce the influence of shrinkage caused by the following sintering process at higher temperature. In this way, it was highly expected that the additional in-rod porosity generated by pore former could be kept to the maximum degree so as to promise hierarchically porous structures after sintering, and eventually to improve the biological activity of HA-G scaffolds.

Figure 5.9 shows the exterior of a HA-G-40 sample before and after sintering. Before sintering, the sample was dark black due to the high proportion of graphite, while it is totally bright white after sintering, meaning that the graphite in the scaffold was almost completely burnt out. However, further study was still required to confirm the actual degree of oxidation. In addition, significant change in terms of surface roughness were found before and after sintering. To be more specific, the crossbeams of scaffold were regularly cylindrical with smooth surface (Figure 5.9(a)); but after sintering, they became uneven, and most of all, some of the in-rod micropores could be recognised.

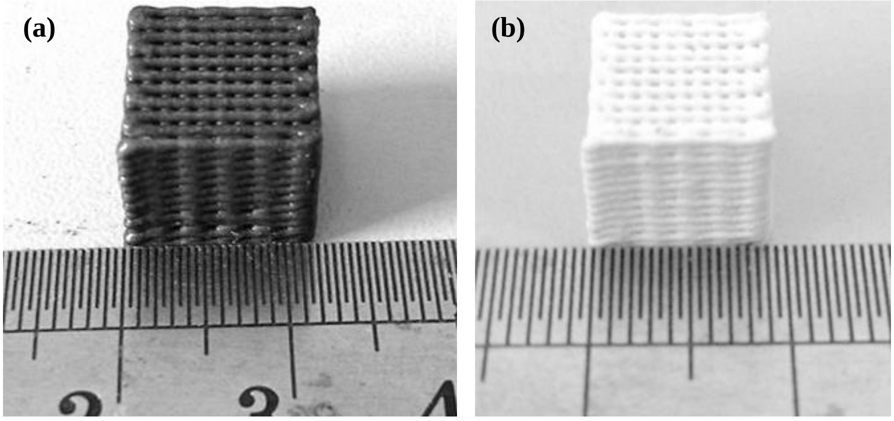

Figure 5.9 Exterior of HA-G-40 samples: (a) before and (b) after sintering

The difference in overall dimension was also evident. As seen in Figure 5.9, the initial size of this sample in X/Y direction was about 12 mm. After sintering, the X/Y size was largely reduced (~ 9 mm) due to shrinkage caused by sintering (up to 25%). Therefore, the influence of sintering shrinkage must be taken into account in order to finely control the overall size and porosity of scaffolds. This is also the reason for analysing the shrinkage resulted from drying and sintering separately, as described before. Another important detail that needs attention is that a great deal of heat is emitted during oxidisation (negative value of DSC means energy release). To avoid HA being sintered prematurely, the number of HA-G scaffolds in the same batch was inversely proportional to the content of graphite, which prevented the local temperature from being rapidly elevated to be at or higher than 1200 ℃ (though the ambient temperature may still be 900 ℃) because of high energy from graphite. Hence, a dense cluster of HA-G scaffolds like HA-P during sintering was inhibited.

5.4.3 Confirmation of Complete Oxidisation of Graphite

In view of potential cytotoxicity from graphite [206], the degree of complete oxidation of graphite is the key to succeed in preparation of HA-G scaffolds suitable for BTE. In this study, XRD analysis and EDX spectrum was employed to confirm the sintering state of HA-G scaffolds.

5.4.3.1 XRD

The (relative or offset) XRD patterns of HA-P, HA-G-5 and HA-G-40 samples (in powder) after sintering are shown in Figure 5.10, where the XRD spectra could manage to match the standard diffraction peaks (PDF #09-0432, marked in green and purple lines) without

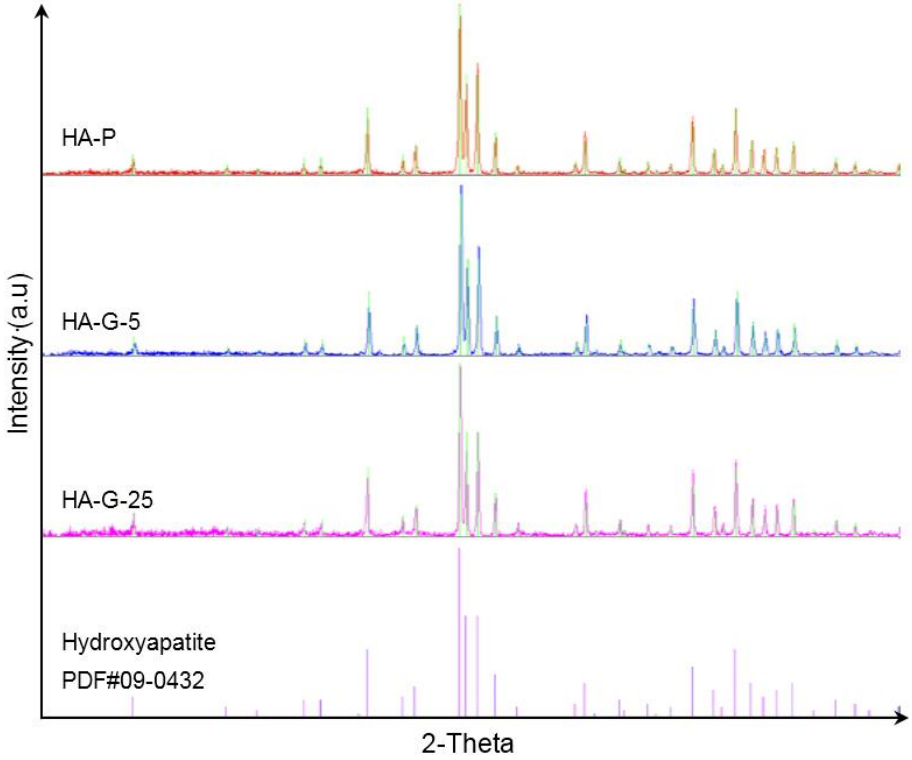

Figure 5.10 XRD analysis of HA-P, HA-G-5 and HA-G-40 after sintering

substantial interference peaks from graphite. In other words, the vast majority of composition in the three samples was HA, indicating that almost all of the graphite had been fully burnt out during sintering.

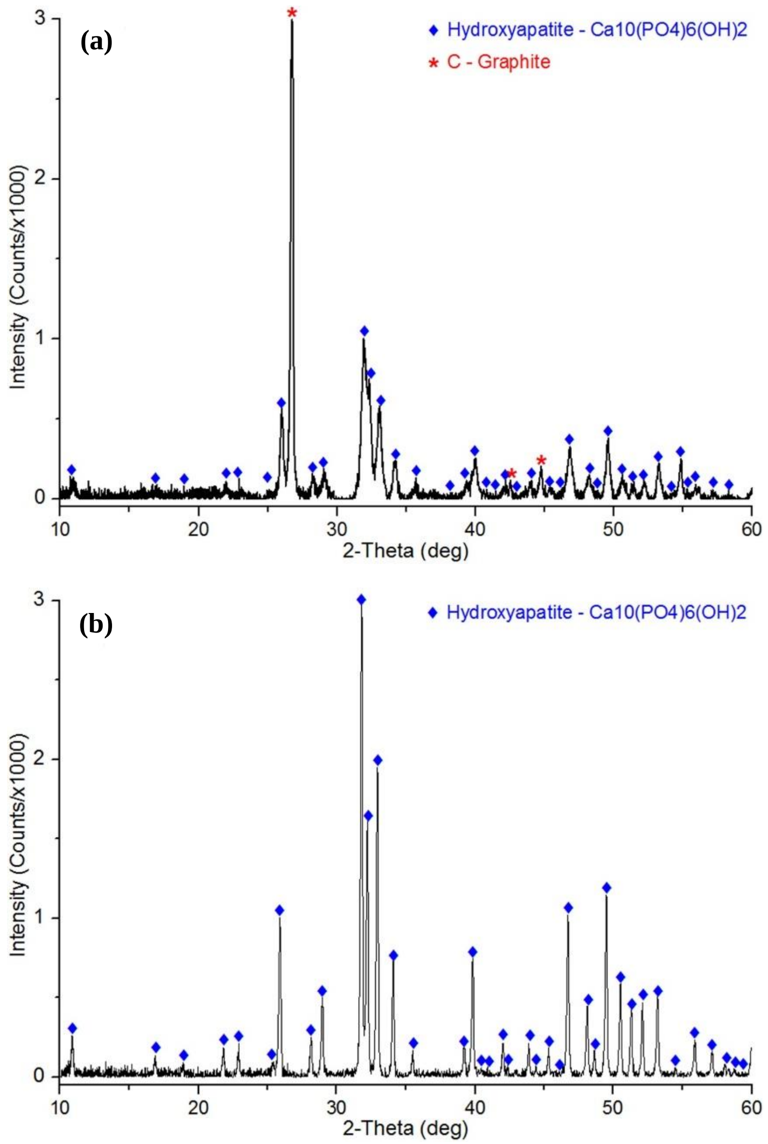

Figure 5.11 XRD spectrum of HA-G-25: (a) before and (b) after sintering

Particularly, Figure 5.11 illustrates the XRD result of HA-G-25 powdered scaffolds. As shown in Figure 5.11(a), before sintering, the standard characteristic diffraction peaks of HA (PDF #09-0432) and graphite (PDF #99-0057) could be clearly identified as expected. It was found that the peaks of sintered HA-G-25 sample (Figure 5.11(b)) were as anticipated: only the diffraction peaks of HA was observed without that of graphite, which was consistent with practice. Specifically, there was no obvious diffraction peak of graphite at the corresponding positions (mainly around 27 °, 42.5 ° and 45 °) as found in Figure 5.11(a). Due to the resolution of analysis software (Jade 6.0), the residual graphite may be interfered by noise, but Figure 5.11(b) could still prove that graphite had been almost fully oxidised owing to long holding time (2 hours) at 900 ℃. In fact, the exterior of HA-G-40 changing from black to white after sintering can be regarded as another essential condition for complete combustion of graphite as well.

Interestingly, further analysis of Figure 5.11 (a) and (b) reveals that there was significant difference in the intensity of diffraction peaks of HA. Since the intensity of certain diffraction peaks can reflect the actual crystallinity of HA (Equation 4.4), such difference implies the process of crystallisation in HA-G-25 during sintering. Therefore, compared to Figure 5.11(a), the intensity of HA in Figure 5.11(b) was much higher (up to 3000), suggesting that entire crystallisation and densification occurred during sintering at high temperature. Moreover, the intensity of graphite (> 3000) exceeded HA (~ 1100) in Figure 5.11(a), making it reasonable that HA-G-40 (with highest intensity) appears dark black.

5.4.3.2 EDX

To confirm the oxidation of graphite, the micro morphologies of HA-G-25 were further analysed with EDX spectrum. Before sintering, EDX analysis was performed on a region (Spectrum A) which obviously contained graphite particles, as shown in Figure 5.12(a). The figure on top-right corner shows the details of Spectrum A. As for Figure 5.12(b), Spectrum B was inside the selected additional in-rod pore formed by graphite and the result is also figured on the top-right. Considering the actual composition of HA-G scaffolds, the main elements (C, O, P and Ca) were chosen for analysis; while other elements (such as N, Cu, Ag, *etc.*) were filtered out because of trace amount. The content of specific elements of both spectra is listed in Table 5.5.

Firstly, the analysed graphite was mainly granulated, regardless of some broken powder (Figure 5.12(a)), and the EDX spectroscopy (Spectrum A) also revealed that this object was graphite (94.42% of C). Furthermore, the oxidation of graphite fragments would contribute to higher wall roughness and SSA, which helps improve the adhesion and proliferation of cells [33, 82]. According to Figure 5.12(b), the scaffold was mainly composed of HA with little residual graphite (about 1.32%), in agreement with the result of XRD as well.

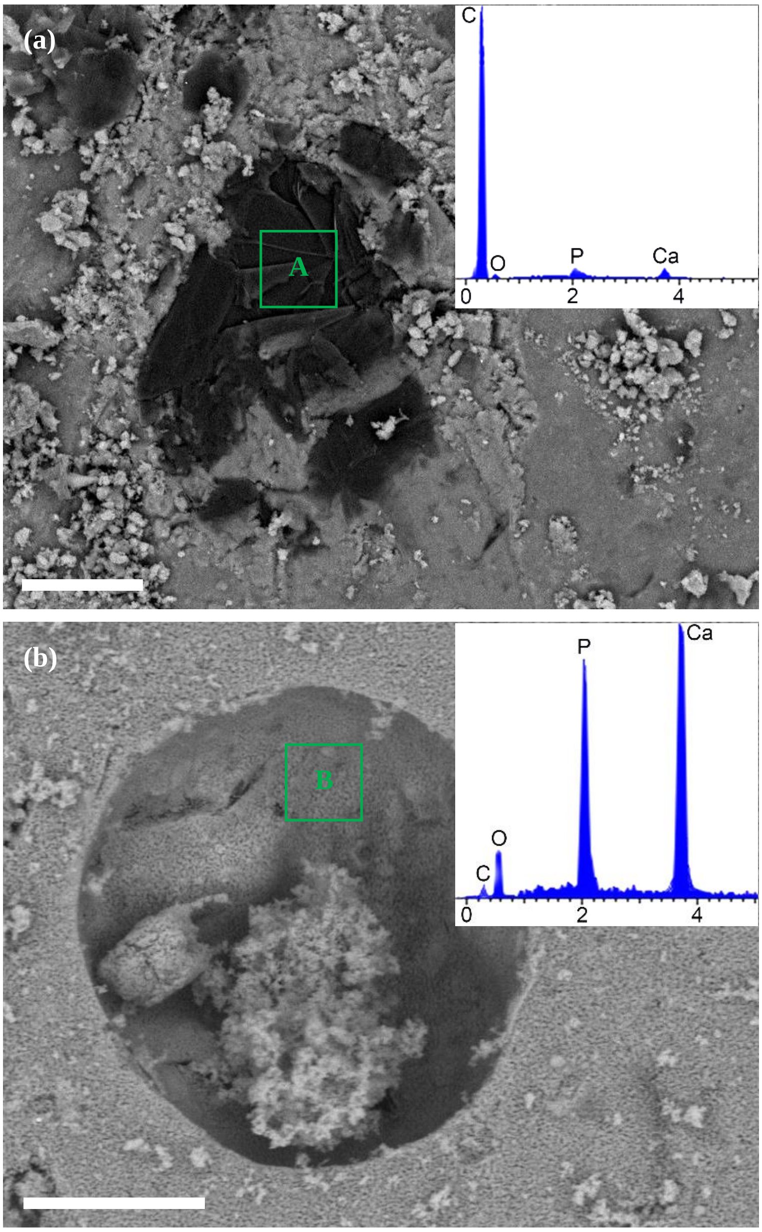

Figure 5.12 EDX analysis of HA-G-25: (a) before and (b) after sintering; scale bar = 20μm

In addition, the graphite was well protected in the scaffolds before sintering, and the in-rod pore was in really good shape, indicating that the HA-G slurry for fabrication was homogeneous. Furthermore, the Ca/P atomic ratio (calculated by Equation 5.7) before sintering was 1.686, rather close to the theoretical value 1.667 (*i.e.* 10 / 6), but then the ratio changed to 1.877 (> 1.667) after sintering. The usual explanation is that, during sintering, irreversible dehydroxylation occurs at decomposition temperature (generally about 1200 - 1450 ℃), which produces anhydrous calcium phosphates like CaO, α-TCP, β-TCP, TTCP (Equation 4.8 and Equation 4.9), resulting in that the outer shell of HA particles might suffer phosphate (P_2O_5) deficiency at high temperature [207].

Table 5.5 EDX result of HA-G-25 (Spectrum A and B)

Spectrum A	**C**	**O**	**P**	**Ca**	**Spectrum B**	**C**	**O**	**P**	**Ca**
Content (wt.%)	94.42	3.55	0.64	1.39	**Content (wt.%)**	1.32	17.71	23.66	57.31

$$\mathrm{Ca/P} = \frac{(W_{Ca}/A_{Ca})}{(W_P/A_P)} = 0.775 \times \frac{W_{Ca}}{W_P} \qquad \text{(Equation 5.7)}$$

Where, $\boldsymbol{A_{Ca}}$ (= 40) or $\boldsymbol{A_P}$ (= 31) is the relative atomic mass of Ca and P, and $\boldsymbol{W_{Ca}}$ or $\boldsymbol{W_P}$ means the actual content correspondingly (shown in Table 5.5).

5.4.4 Micro-morphologies of Scaffolds by SEM

Figure 5.13 shows the SEM images of HA-P and HA-G-X (X = 5, 25 or 40) scaffolds. As seen from Figure 5.13 (a), (c), (e) and (g), the average diameter of scaffold rods was about 350 - 400 μm after sintering. Additionally, the size of rods decreased with the increase of graphite (from 0 to 40 vol.%) actually, which resulted in increasingly wider space of adjacent rods, *i.e.* larger macropore size. Since the original sizes of all scaffolds were the same before sintering, it can be concluded that the content of graphite would significantly affect the final shrinkage of scaffolds. Owing to the advantages of MAM extrusion, the scaffolds made by this technique contained highly interconnected macropores (300 - 500 μm), which possessed the necessary conditions for BTE. In comparison to the smooth surface in HA-P, the introduction of graphite could not only form additional in-rod porosities, but also substantially increase the surface roughness, greatly beneficial to cell culture.

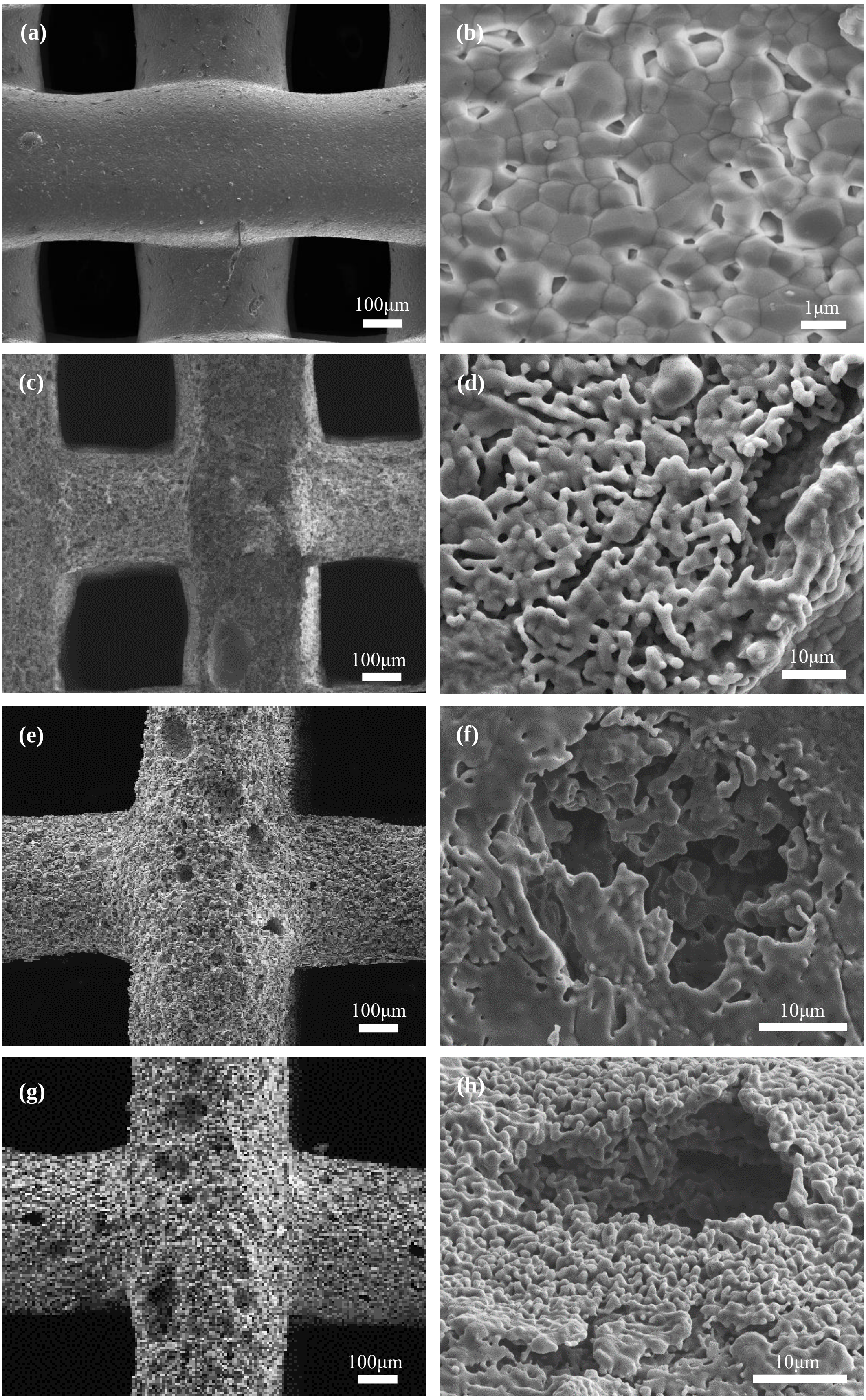

Figure 5.13 SEM images of HA scaffolds: (a), (b) HA-P; (c), (d) HA-G-5; (e), (f) HA-G-25; (g), (h) HA-G-40

However, merely from these SEM images, it was difficult to determine whether the additional pores generated by porogen were interconnected or not. Fortunately, most of the pores were open due to full oxidation of graphite, despite that the densification of HA at high temperature might extinguish some micropores. All in all, the formation of additional micropores was undoubted.

In addition to the influence of auxiliary reagents, which also produce nanopores on the scaffolds (Figure 5.13(b)), the introduction of graphite as porogen provided HA-G composite scaffolds with wide distribution of micropores, ranging from 100 nm to 45 μm. And the micron-sized pores were surrounded with numerous pores in nano-scale. If these micropores could allow extra survival space and recharge of nutrient for cells, then the widespread nanopores were able to induce cell adhesion, proliferation and differentiation [37] in return. Therefore, such hierarchically porous structure are highly likely to promote the bioactivity, especially osteoinduction of scaffolds, which of course requires further biological experiments to be verified. Besides, further comparison of Figure 5.13 (b), (d), (f) and (h) shows that the grain boundaries were more clear and visible in HA-P scaffolds, but they could hardly be recognised in graphite composited scaffolds, especially in those with higher content of graphite. This phenomenon may be explained by considering the energy released by the combustion of graphite, which may locally elevate the sintering temperature even to the melting point of HA (1650 ℃). Furthermore, the additional macroporosity can be easily adjusted by controlling the amount of graphite.

As we can see, the overall pore structures and porosities were determined by the unavoidable nanopores (≤ 1 μm), oxidation of graphite (about 20 to 50 μm) and MAM deposition (300 - 500 μm). In other words, hierarchical porosity with interconnected structures and wide distribution of pore sizes (from 0.3 to 500 μm) were successfully achieved [199]. Such characteristics may make it particularly attractive in promoting the adhesion and proliferation of bone cells when applied to BTE.

5.4.5 Control of Overall Size and Porosity

5.4.5.1 Control of size

Shrinkage plays an important role in determining the final size of scaffolds. In order to facilitate accurate control of size, the shrinkage was investigated from two aspects (*i.e.* drying and sintering) and measured in two directions (X/Y and Z) respectively. The result of shrinkage has been summarised in Table 5.6. The detailed calculation of all types of shrinkage can refer to Equation 5.1, Equation 5.2 and Equation 5.3.

Table 5.6 Statistical analysis of shrinkage during fabrication process

S G	**0%**	**5%**	**10%**	**15%**	**20%**	**25%**	**30%**	**35%**	**40%**
$\mathbf{S_{D\text{-}XY}}$	3.7%	4.0%	3.6%	3.8%	3.6%	4.2%	4.5%	4.2%	4.3%
$\mathbf{S_{D\text{-}Z}}$	6.2%	5.8%	6.5%	6.1%	6.3%	6.1%	5.8%	6.1%	6.3%
$\mathbf{S_{D}}$	13.0%	13.2%	13.1%	13.1%	12.9%	13.8%	14.1%	13.8%	14.2%
$\mathbf{S_{S\text{-}XY}}$	5.7%	6.1%	6.5%	6.9%	7.6%	7.6%	8.0%	8.8%	9.4%
$\mathbf{S_{S\text{-}Z}}$	6.2%	6.7%	7.1%	7.3%	7.4%	7.2%	7.8%	8.1%	8.3%
$\mathbf{S_{S}}$	16.6%	17.7%	18.8%	19.7%	20.9%	20.8%	21.9%	23.5%	24.7%
$\mathbf{S_{T}}$	27.4%	28.6%	29.4%	30.2%	31.1%	31.7%	32.9%	34.1%	35.4%

Note: $\mathbf{S_D}$ -- drying shrinkage, $\mathbf{S_S}$ -- sintering shrinkage, and $\mathbf{S_T}$ -- total shrinkage.

According to Table 5.6, not much difference (≤ 1.2%) was found in all scaffolds in terms of drying shrinkage ($\boldsymbol{S_{D\text{-}XY}}$, $\boldsymbol{S_{D\text{-}Z}}$ and $\boldsymbol{S_D}$). And for total shrinkage caused by drying, most of them were around 13%. So it is easily known that the addition of graphite would not result in significant changes of physical properties in HA scaffolds. In addition, the drying shrinkage in X/Y direction was obviously smaller than Z direction (or height direction), which was mainly the result of gravity. This is also the reason that Equation 5.4 treats the rods as ellipsoids rather than cylinders.

On the other hand, the sintering shrinkage ($\boldsymbol{S_{S\text{-}XY}}$, $\boldsymbol{S_{S\text{-}Z}}$ and $\boldsymbol{S_S}$) was directly impacted by the actual content of graphite -- or rather, it was proportional to added amount of graphite. Interestingly, when the graphite was less than 15 vol.%, the value of $\mathbf{S_{S\text{-}XY}}$ was lower than $\mathbf{S_{S\text{-}Z}}$, which was similar to drying shrinkage, but $\mathbf{S_{S\text{-}XY}}$ would soon overtook $\mathbf{S_{S\text{-}Z}}$ with increasing volume of graphite. Normally, despite the effect of gravity, the difference in sintering shrinkage had nothing to do with the measuring direction (X/Y or Z). Then a possible explanation for this result would be that the impact of gravity on sintering shrinkage became very weak after drying process, as seen from $\boldsymbol{S_{S\text{-}XY}}$ and $\boldsymbol{S_{S\text{-}Z}}$ of HA-P. Conversely, the shrinking freedom in Z direction might be limited by gravity instead, which was embodied in the significantly higher growth rate of $\boldsymbol{S_{S\text{-}XY}}$ than $\boldsymbol{S_{S\text{-}Z}}$. With the oxidation of graphite, HA particles would be gradually free to migrate in X/Y direction, making the rods thinner and thus producing larger pores, which corresponded to Figure 5.13 (a), (c), (e) and (g) well.

In practice, it was necessary to make slight adjustment of the processing parameters for HA-G scaffolds with different volume of graphite, so as to ensure the final size of scaffolds were as much identical as possible, if taking drying and sintering shrinkage into consideration. Specifically, for fabrication of scaffolds with more graphite, the deposition speed of slurry should be improved a bit to extrude thicker filaments, so that the influence of shrinkage (primarily sintering shrinkage) could be counteracted. On the basis of a large number of experiments and attempts in this way, the general error of overall size of each scaffolds was possible to be finely controlled within 5%.

5.4.5.2 Control of porosity

The porosity in this study were considered in two aspects, namely, the bulk porosity and in-rod porosity. The relationship of the two types of porosity and graphite content is shown in Figure 5.14. The bulk porosity of normal HA scaffolds was about 58.1%, extremely close to the theoretical value (60.7%). With more graphite as pore former, the bulk porosity would increase steadily, and it could be up to 75% when the volume of graphite was higher than 35 vol.%. Besides, the actual growth rate of bulk porosity was about 2.1%, which almost followed the calculated rate (i.e. (1 - 60.7%) * 5%), reflecting that the graphite was completely burnt out during sintering.

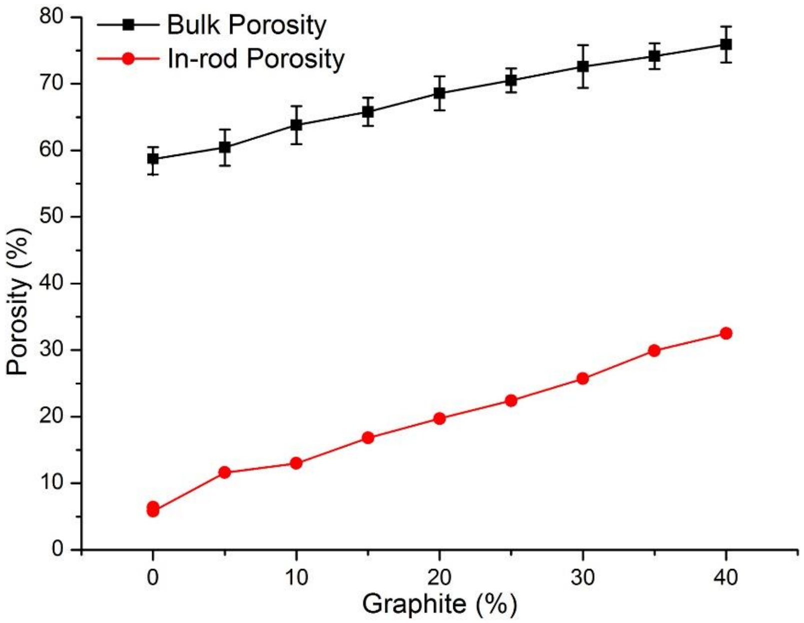

Figure 5.14 Relationship of porosity and the amount of graphite

It is interesting that even if no graphite was added into HA-P scaffolds, the additional in-porosity could still be approximately 6%, owing to the oxidation of auxiliary reagents during sintering. As the increase of graphite content, the in-rod porosity of HA-G scaffolds also increased accordingly. Puzzlingly, the growth rate of additional porosity was about 3%, much larger than the theoretical value (2%), whereas that of bulk porosity still remained around 2%. Consequently, the in-rod porosity of HA-G-40 could be as high as 30%, which was almost two times of the estimated value (39.3% × 40% = 16%). This is incredible in view of that repeated measurement was performed to eliminate the chance of accidental errors. In fact, it was not easy to explain such phenomenon at first. Later, it was found that this could be solved from the angle of sintering shrinkage, which was also the main reason to analyse drying and sintering shrinkage separately.

Hence, the corresponding relationship between the in-rod porosity and sintering shrinkage is presented in Figure 5.15, where the resolution of both were made the same for the purpose of intuitive analysis. The black and blue dashed lines in this figure are the theoretical growth curves of in-rod porosity and sintering shrinkage respectively. Obviously, the actual growth rates of both were higher than their theoretical ones. If the difference of actual and theoretical rate was counted (as shown in red dash lines), the offset of in-rod porosity almost counteracted that of sintering shrinkage at each volumetric percentage. As a result, the growth of bulk porosity could be of perfect consistence with calculation, without being affected by the difference of in-rod porosity. Since the calculation of additional in-rod porosity was based on estimation, the uneven shrinkage would therefore cause considerable errors, which was confirmed in Figure 5.13.

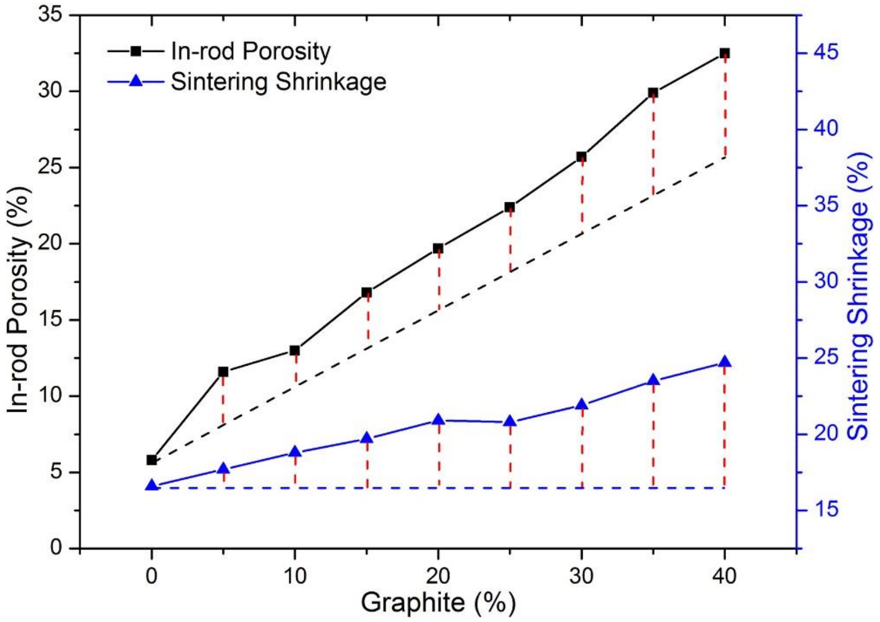

Figure 5.15 Relationship of in-rod porosity and sintering shrinkage

In summary, the novel fabrication method by combining MAM extrusion with porogen foaming technique can offer great potential to fabricate excellent scaffolds for BTE. The scaffolds formed this way are characterised by hierarchical pore structures (0.3 - 500 μm), as well as promising high and controllable bulk porosity (≥ 70%, ± 1%). The in-rod porosity is also able to be finely controlled by changing the graphite content. Highlight of this novel method is that it can produce 3D complex scaffolds with hierarchically porous structures (nm-μm-mm) beneficial to BTE, without any further sophisticated treatments.

5.5 Summary

In this chapter, a novel method to facilely fabricate hierarchically porous scaffolds by combination of MAM and gas forming technique was introduced in detail. It shows that graphite is a good choice to serve as the porogen for gas foaming, due to uniform distribution in particle size. Moreover, to retain as much additional in-rod micropores as possible, meanwhile to ensure complete oxidisation of graphite and auxiliary reagents, the sintering profile for HA-G scaffolds was optimised. After sintering, both normal and graphite treated scaffolds were able to form evenly distributed nanopores, but HA-P could not produce micropores as HA-G did.

The novel method shows great potential to make excellent scaffolds with hierarchical pore structures and highly controllable bulk porosity. It is possible to achieve fine and accurate control of the overall size, extra and bulk porosity of scaffolds by adjusting graphite content and considering the influence of drying/sintering shrinkage carefully.

Chapter 6. Characterisation of Physicochemical Properties of Hierarchically Porous Scaffolds

6.1 Introduction

Bone scaffold is the key to BTE, which provides support for the interaction and adsorption of cells and extracellular matrix, as well as additional space for bone formation [33]. Scaffolds have to be implanted for clinical treatment of bone defects, so the physicochemical properties such as mechanical strength, stability and biodegradability is very important, in addition to porosity, pore size, biocompatibility and osteoinduction. As the load-bearing part of hard tissues during repair, mechanical properties are the primary assessment criteria for bone scaffolds, which makes bioceramic materials more advantageous to biopolymer or hydrogel *etc*. in terms of mechanical properties.

Recently, an increasing number of researchers are paying more attention to the importance of mechanical stimulation to bone tissues during repair *in vitro*, because a) mechanical load exerts positive effect on the repair of cartilage and can regulate the *in-situ* metabolic process of chondrocytes [88]; b) even if isolated from culture medium, bone cells are still able to respond to mechanical stimulation [89]; c) on the condition of long enough time of stimulation, mechanical load will also influence the deposition process of extracellular matrix [90]; d) even short-term mechanical load can still enhance the synthetic rate of proteoglycans in bone cells as well [91]; e) good mechanical strength is the prerequisite to establish stable junctions between newly formed bone and host tissues, and eventually to promote osteogenesis [80].

In addition, biodegradability is non-negligible. Although our recent work has shown that HA is biocompatible [208], it is hardly biodegradable in neutral environment [57], which greatly limits the clinical application of HA, because the pH of human body fluid is about 7.4. Since sintering at high temperature is necessary to obtain sufficient mechanical strength in most HA scaffolds, it usually results in high crystallisation and densification, making HA more difficult to be biodegraded in short term. Worse still, the biodegradability of HA could not be substantially improved on the condition of the interaction and creeping motion of cells during cell culture [200]. If the scaffolds could not be decomposed as the regeneration of new bones, it would be particularly intractable when scaffolds have been filled with osteoblasts. Such a situation is bound to hinder further bone formation.

In fact, other factors besides mechanical strength and biodegradability, which have been specially emphasised due to their unique roles, are indispensable parts of physical and chemical properties. In this chapter, the most relevant physicochemical properties of scaffolds were characterised to confirm the advantages of HA-G composite scaffolds compared to HA-P. Considering that huge but unnecessary workload was required to characterise the physicochemical properties of all scaffolds listed in ***Section 5.3.5***, it is important to filter out the representatives of all HA-G groups so as to make comparison with HA-P. To be more specific, the selection of appropriate graphite content was comprehensively considered from the angle of mechanical strength and in-rod porosities. In addition, another kind of HA-G scaffold with different characteristics of microporosity by nano-sized graphite (nG) of same content (marked with HA-nG) was introduced for further analysis, which will be described in detail.

The physical and chemical properties involved here are listed as follows: compressive strength, microstructure, SSA, micropore distribution, crystallinity, biodegradability and hydrophilicity.

6.2 Materials

The materials used in this chapter are summarised in Table 6.1 with their detailed applications. The majority of auxiliary reagents for HA slurry is omitted as they can be found in Table 3.3. Note that the application of most materials are symbolised for short, and the details can be found in the footnote.

Table 6.1 Main materials for experiments

Material	Specification	Manufacturer	Application
HA powder	≥99.5%, ~ 60 nm	Emperor	Ψ
Deionised water	2nd distillation	Self-made	Ψ, Ω
Micron graphite (μG)	≥99.95%, 325 mesh	Sinopharm	Porogen, Ψ
Nano graphite (nG)	99.9%, ~ 400 nm	XFNANO	Porogen, Ψ
Dispersant	UV9510	UniqChem	Graphite dispersant
Sodium chloride (NaCl)	99.5%, AP	Aladdin	Ω
Sodium bicarbonate ($NaHCO_3$)	≥99.8%, AP	Sinopharm	Ω
Potassium chloride (KCl)	99.5%, AP	Aladdin	Ω
Di-potassium hydrogen phosphate tri-hydrate ($K_2HPO_4 \cdot 3H_2O$)	99%, AP	Sinopharm	Ω
Magnesium chloride hexahydrate ($MgCl_2 \cdot 6H_2O$)	98%, AP	Sinopharm	Ω
Hydrochloric acid (HCl)	1 mol/L, AP	Xinyang Chemical	Ω
Calcium chloride ($CaCl_2$)	96%, AP	Sinopharm	Ω
Sodium sulphate (Na_2SO_4)	99%, AP	Sinopharm	Ω
Tris(hydroxymethyl)methyl aminomethane (Tris)	≥99.9%, AP	Dow Chemical	Ω
Vaseline	GB1790-86	Sinopharm	Lubricant

Note: "Ψ" -- preparation of HA(-G) slurry, "Ω" -- for simulated body fluid (SBF).

6.3 Methodology

6.3.1 Experimental Procedure

Initially, the mechanical strength of HA-P and HA-G scaffolds were tested in order to select the suitable amount of graphite on the basis of bulk and in-rod porosity. It was expected that the selected HA-G scaffold could not only satisfy the mechanical requirement of spongy bone, but also had as much in-rod porosity as possible. The physicochemical properties were characterised to pave the way for biological evaluation. Figure 6.1 shows the experimental procedure for characterisation.

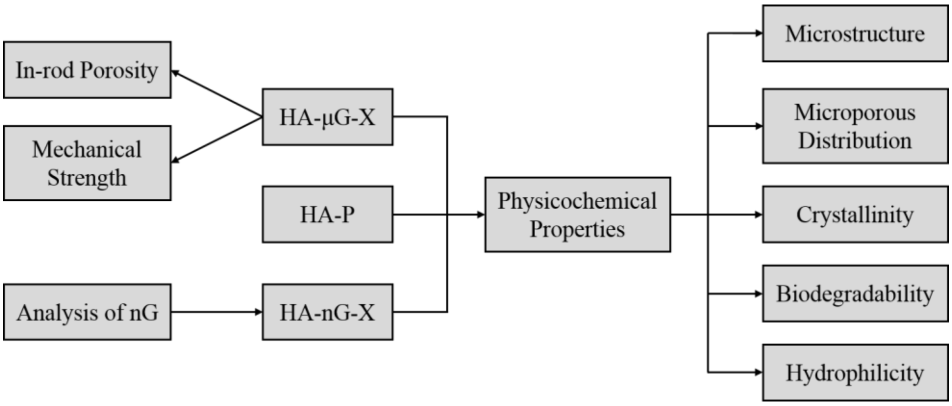

Figure 6.1 Experimental procedure of this chapter

6.3.2 Equipment and Devices

Table 6.2 presents the main details of the equipment and devices used in this chapter, mainly for the purpose of characterising physicochemical properties.

Table 6.2 Main details of equipment and devices for experiments

Device	Model	Manufacturer	Application
MAM system	MAM-II	Fochif	Fabrication of scaffolds
Electronic balance	HTP-312	Huachao	Weighing
Microwave furnace	Hamilab-V1500	Syno-Therm	Sintering of scaffolds
Stereomicroscope	XTL-340	Changfang	Measurement of pore size
Laser particle size analyser	LB550	Horiba	Analysis of nG
Electronic universal tester	WDW2000	Zwick	Test of mechanical strength
Scanning electron microscope	Sirion 200	FEI	Characterisation of micro-morphologies
Specific surface area analyser	ASAP2020	Micromeritics Instrument	Evaluation of microporous distribution and SSA
X-ray diffractometer	X'Pert Pro	PANalytical B.V.	XRD analysis of scaffolds
Contact angle meter	SL200B	Kino Industry	Test of angle meter
Thermostatic water-bath oscillator	SHA-C	Hongke Instrument	Testing platform for biodegradability
Electronic pH meter	CT-6023	Kedida	Detection of pH
Magnetic stirrer	DF-101SA	Jia-Meilun	Preparation of SBF

6.3.3 Test of Compressive Strength

During the test of compressive strength, the mechanical loading speed was invariably 1 mm/min, in the direction perpendicular to the upper surface, as shown in Figure 6.2. For the convenience of distinction, the scaffolds with micron/nano graphite as porogen was marked as HA-μG/-nG respectively. The overall size of test samples were about 10 × 10 × 10 mm, and the number of each group (*i.e.* HA-P, HA-μG and HA-nG) was 6. Due to the special phenomenon of "secondary yielding" (the scaffolds will experience the limit of yielding for a second time because of loose rods, seen in Figure 6.6) during compressive test of HA-G scaffolds (HA-μG / HA-nG), the rule for practical unloading of mechanical press was based on loading pressure (significantly decreased), not compaction degree as usual. At the end of each test, the platform must be carefully cleaned to guarantee the validity and accuracy of the following tests.

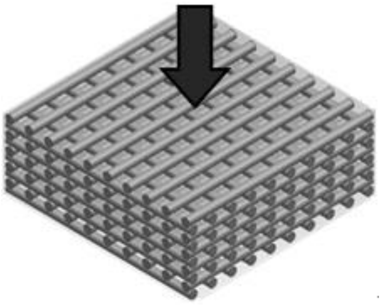

Figure 6.2 Loading direction for the test of compressive strength

6.3.4 Fabrication of HA-nG Scaffolds

6.3.4.1 Characterisation of nano graphite

Similar to ***Section 5.3.4***, it is necessary to characterise the microstructure by SEM, particle size and detailed distribution of nG through LDPSA, before applied to prepare HA-nG scaffolds. The process for laser analysis of nano graphite was the same to μG, and the SEM images with regard to microstructures were provided by *Nanjing XFNANO Materials Tech. Co., Ltd.*

6.3.4.2 Fabrication of HA-nG scaffolds

The preparation process of HA-nG composite scaffolds was essentially similar to HA-μG (***Section 5.3.5***). The only difference was the actual amount of graphite dispersant to ensure homogeneous dispersion of nG. Considering that the dispersity of nG is better than μG, the addition of dispersant for nG was half of that for μG. In addition, the shrinkage (caused by drying and sintering) of HA-μG and HA-nG scaffolds was not significantly different, so the fabrication parameters for HA-nG scaffolds were also kept consistent with HA-μG.

6.3.5 Characterisation of Physicochemical Properties

6.3.5.1 Microstructure

The microstructures and surface morphologies of HA-nG scaffolds after sintering (1200 ℃) were observed by SEM. The main matters that needed attention for observation were full cleaning and drying after sintering, gold spraying for 60 s to increase conductivity, and using 15.0 kV as accelerating voltage after vacuum treatment.

6.3.5.2 Microporous distribution and SSA

Due to high accuracy and reliability, Brunauer-Emmett-Teller (BET) method, which measures the SSA of materials according to physical adsorption of a gas on the surface, has been widely used all over the world [209]. In this part, the SSA and micropore distribution of scaffolds was characterised by BET. In practice, the main parameters for BET test were recorded: ambient temperature -- 20 ℃, extraction temperature -- 120 ℃, vacuum time -- 30 min, gaseous adsorbate -- N_2, temperature of liquid nitrogen -- 77 K (*i.e.* -196 ℃), balance interval -- 10 s, number of samples -- 3, weight of each sample -- 0.11 ± 0.02 g.

6.3.5.3 Crystallinity

As mentioned, the crystallinity of HA-P, HA-μG and HA-nG scaffolds after sintering was obtained from XRD patterns (Equation 4.4), referring to ***Section 4.3.5*** for more details. The crystallinity of original HA powder was also considered for further analysis.

6.3.5.4 Biodegradability

A self-prepared SBF (based on corrected SBF [210], C-SBF) was used to study the degradation behaviour of all scaffolds. SBF is a solution with an ionic concentration close to that of human blood plasma, kept under mild conditions of pH and identical physiological temperature [211]. Since HA is hardly biodegradable in neutral environment, the pH of such self-prepared SBF was regulated to be acidic (pH = 3), in order to accelerate the degradation rate for characterisation. For short, such SBF was named as AC-SBF (acidic C-SBF). The main purpose of this experiment was to verify that whether HA-G scaffolds with hierarchical porosity were advantageous over normal scaffolds made of pure HA in terms of biodegradability. In this case, it was expected to predict the degradation behaviour of scaffolds in human body fluid from the difference found in AC-SBF. At present, the most popular apparatus for preparation of SBF is magnetic stirring with temperature control, as shown in Figure 6.3.

Figure 6.3 Preparation of SBF by magnetic stirring

The experimental preparation of AC-SBF was in strict accordance with the following steps (taking 1 litre of AC-SBF as an example): **(a)**. Fill an empty beaker (capacity: 1.25 L) with 700 mL of deionised water, and heat the beaker to 36.5 ± 1.5 ℃ by water bath or heating plate on magnetic stirring equipment; **(b)**. Add precise amount (8.035 g) of NaCl into the beaker, and start magnetic stirring of solution until the temperature is stable (36.5

±1.5 ℃); **(c)**. Continue step (b) till the exact amount of additives listed in Table 6.3 (No.2 to No.8) have been evenly dissolved; **(d)**. Test the pH value of this solution, which should be 2.00 ±1.00 in general; otherwise, repetition from step (a) to (c) is required; **(e)**. Supply the beaker with deionised water if the solution is less than 900 mL and stabilise the temperature of solution to 36.5 ± 0.5 ℃; **(f)**. Keep an eye on the change of pH when gradually adding Tris into solution (note that the pH of solution must be stable before addition of Tris every time) until pH is about 7.40; **(g)**. Alternately add HCl and Tris little by little to ensure the pH of solution is between 7.38 and 7.42; **(h)**. After all of Tris (6.118 g) has been dissolved, regulate the pH of solution to 3.00 ±0.10 by HCl at 36.5 ℃; **(i)**. Transfer the AC-SBF solution into a bottle (sealed), and keep it refrigerated at 4 ℃.

Table 6.3 Addition sequence for main components of AC-SBF

No.	Material	Amount	No.	Material	Amount
1	NaCl	8.035 g	**6**	HCl	39 mL
2	$NaHCO_3$	0.355 g	**7**	$CaCl_2$	0.292 g
3	KCl	0.225 g	**8**	Na_2SO_4	0.072 g
4	$K_2HPO_4 \bullet 3H_2O$	0.231 g	**9**	$NH_2C[CH_2OH]_3$ (Tris)	6.118 g
5	$MgCl \bullet 6H_2O$	0.311 g	**10**	HCl	/ [a]

[a] The actual amount of HCl varies to ensure pH=3 in AC-SBF.

Table 6.4 shows the concentration of important ions in blood plasma and AC-SBF. As we can see, except Cl^-, HCO_3^- and H^+, the concentration of other ions in AC-SBF were exactly the same to blood plasma, which makes SBF useful in assessing the bioactivity of materials [212].

Table 6.4 Concentration of important ions in blood plasma and AC-SBF

Ion (10^{-3}mol/L)	Na^+	K^+	Mg^{2+}	Ca^{2+}	Cl^-	HCO_3^-	HPO_4^{2-}	SO_4^{2-}	H^+
Blood plasma	142.0	5.0	1.5	2.5	103.0	27.0	1.0	0.5	$< 10^{-4}$
AC-SBF	142.0	5.0	1.5	2.5	148.8	4.2	1.0	0.5	1.0

The schematic set of degradation experiment is diagrammatised in Figure 6.4. Each plastic tube (40 mL) was filled with AC-SBF and 3 sintered samples (either HA-P, HA-μG or HA-nG). In practice, water bath with thermal control (temperature: 37 ℃) and oscillation (frequency: 2 Hz) was used to simulate the internal environment of human body. In order to track the degradation process with as much detail as possible, the pH value of degradation solution and the weight of test samples were measured twice a week. And the original weight of each scaffolds were certainly recorded before test. Particularly, the scaffolds should be cleaned with deionised water and then fully dried in an oven at 60 ℃ before weighing. Besides, if the pH of the degradation solution was higher than 5, it was required to replace it with fresh AC-SBF immediately. The number of scaffolds in each testing group was 12 (4 tubes × 3 samples/tube, shown in Figure 6.4). It is worth mentioning that the scaffolds were increasingly brittle with the proceeding of degradation (or rather, decomposition), so one of the 3 samples per tube was picked for weighing in turn to reduce weight loss (usually in the form of broken fragments), which may cause significant errors.

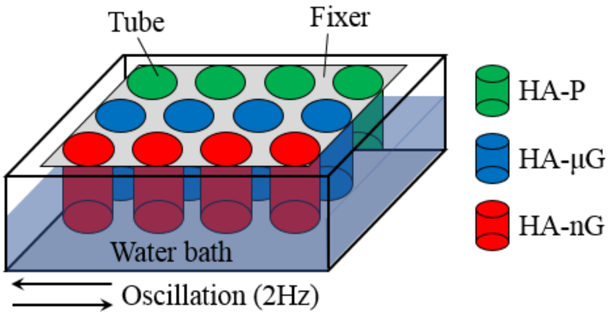

Figure 6.4 Experimental set of degradation with water bath

6.3.5.5 Hydrophilicity

Similar to ***Section 4.3.5***, the hydrophilicity of all scaffolds (*i.e.* HA-P/-μG/-nG) was characterised mainly from the aspect of water absorption. The measurement of water absorption was through weighing method, as described in Equation 4.6. The arithmetic mean value of 3 samples was used for the calculation of absorption rate. According to Ref [213], the contact angle with water is not applicable to HA-G scaffolds due to porous surface. However, in order to better understand the result of water absorption, the contact angle was still measured (based on Young's Equation seen in Figure 4.4 and Equation 4.5) by an optical contact angle meter.

6.4 Results and Discussion

6.4.1 Mechanical Strength

In view of the importance of mechanical strength for scaffolds used in BTE, the suitable content of graphite in HA-μG scaffolds were selected for further characterisation, based on the comprehensive consideration of mechanical strength and in-rod porosity. The test result of compressive strength of all HA(-μG) scaffolds (0 - 40 vol.%, 10 × 10 × 5 mm) is shown in Figure 6.5.

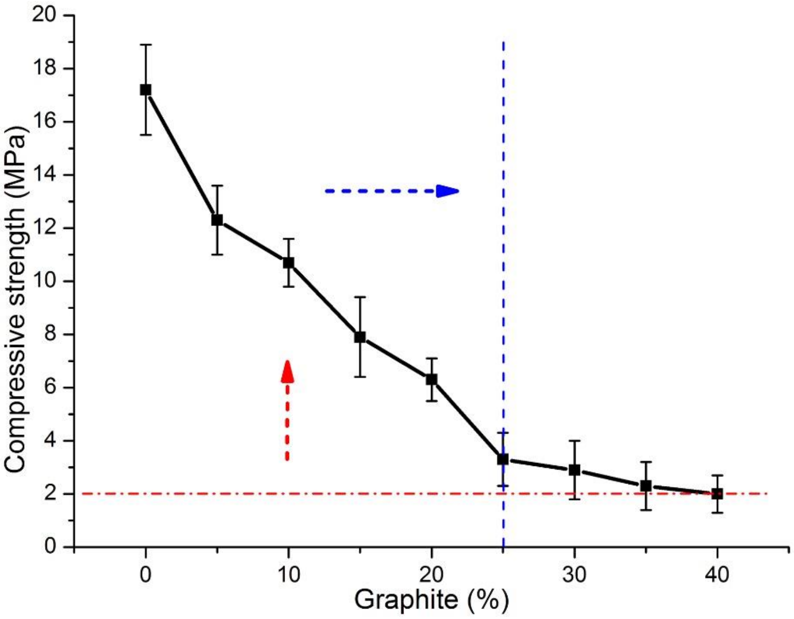

Figure 6.5 Compressive strength of HA(-μG) scaffolds

The compressive strength of scaffolds tended to decrease significantly with the increase of graphite content. The decline of strength went through three stages: 1) 0 - 5 vol.%, where compressive strength dramatically dropped from 17.2 to 12.3 MPa even though only little graphite (5 vol.%) was used; 2) 5 - 25 vol.%, which showed relatively more stable decreasing trend of strength (12.3 ↘ 3.3 MPa); and 3) 25 - 40 vol.%, the last stage with smooth and flat reduction rate, exhibiting tiny difference both in yield limit (3.3 ↘

2.0 MPa) and error (± 0.8 MPa). It can be explained from the point of view of porosity. Firstly, due to the oxidation of graphite, the rods of HA-G scaffolds would become porous rather than dense, which reasonably caused a sharp drop in mechanical strength. When more graphite was added, the in-rod porosity of scaffolds increased accordingly, and thus the actual load-bearing area within scaffolds was proportionally reduced, resulting in relatively constant decrease of strength. However, if graphite content exceeded the critical value (25 vol.%), the internal structure would not change much despite that more graphite was added, so did the mechanical strength. In conclusion, although the addition of graphite can surely increase the amount of in-rod and bulk porosity in scaffolds, it will decrease the mechanical strength at the same time. Therefore, in order to ensure that HA-G scaffolds could have sufficient strength for spongy bones (≥ 2 MPa [26, 66]), the content of graphite had better be no more than 25 vol.%.

Figure 6.6 shows the representative testing curves of HA-G scaffolds with different contents of graphite. Interestingly, a slow response to loading force was found in HA-G scaffolds with more graphite. Specifically, it took about 15 s for HA-G-5 to reach its yield limit of compression, and the time for other scaffolds were around 19 s (15 vol.%), 25 s (25 vol.%) and 33 s (35 vol.%). Since the loading speed was uniform in test, the strain, where stress reaches the peak during compression, also right shifted, meaning less resistance under compression, as shown in Figure 6.7(a). Considering that the area under the stress-strain curve reflects the energy absorbed in compression [214], that enclosed by yield strain (dot line) represents the energy required to reach the yield limit. Accordingly, it indicates that HA-G scaffolds of higher graphite content would become looser and looser, resulting in lower compressive strength [215]. In addition, the special phenomenon “**secondary yielding**” (marked with arrows) was more obvious in HA-G scaffolds with more graphite. A reasonable explanation for this is that if there was certain amount of in-rod micropores, these pores would be initially “compacted” before the scaffold reached its yield limit, and thus, the “compaction” process was longer with the increase of graphite (Figure 6.6). In other words, the proportion of energy absorbed by in-rod micropores during “compaction” process increased. All in all, “slow response” and “secondary yielding” proved that the addition of graphite as porogen would significantly influence the mechanical strength of HA scaffolds after sintering.

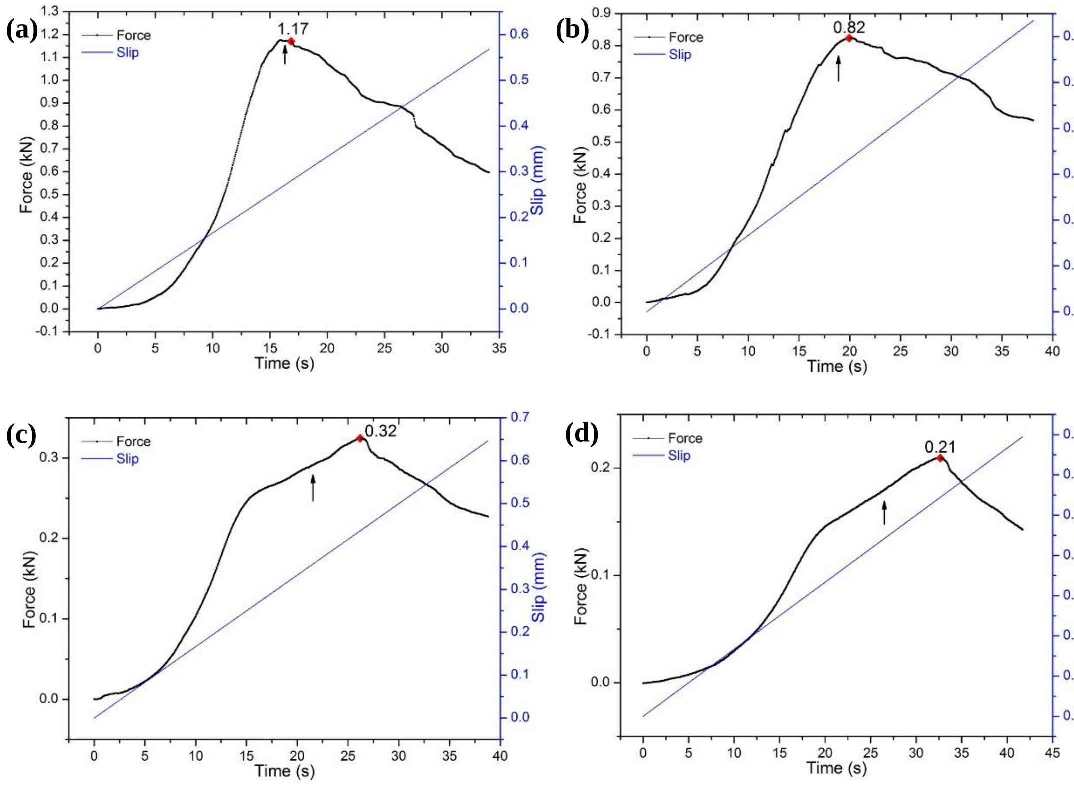

Figure 6.6 Relationship of loading force and displacement in HA-µG scaffold: (a) 5%, (b) 15%, (c) 25%, (d) 35%; the “up arrow” represents the phenomenon of “secondary yielding”

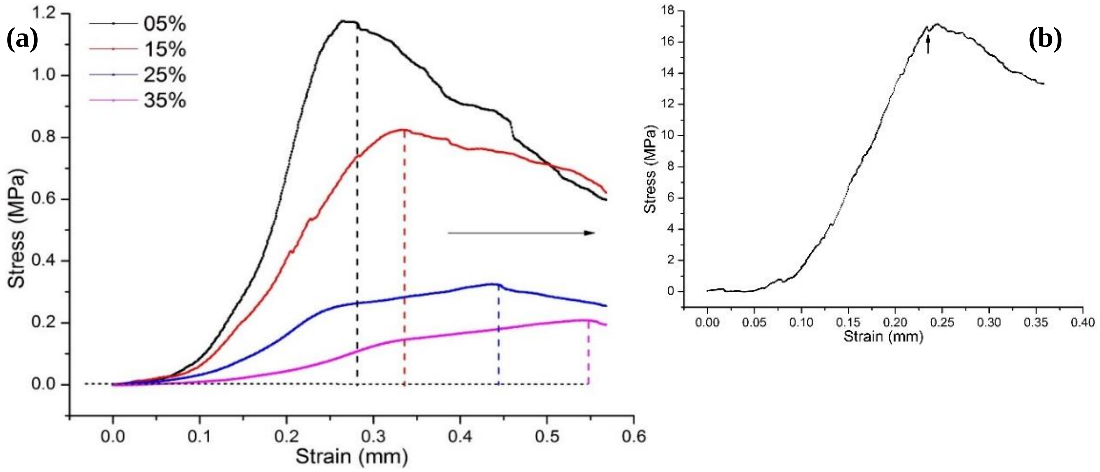

Figure 6.7 Relationship of stress and strain of (a) HA-µG-(5, 15, 25, 35) and (b) HA-P scaffold

In light of compressive strength and porosity, 25 vol.% was the optimal choice for graphite content, that is, with the highest in-rod and bulk porosity under the condition of sufficient mechanical strength for spongy bone. Therefore, HA-(µ)G-25 scaffolds were used as the representative of HA-(μ)G for the subsequent experiments.

6.4.2 Nano Graphite Powder

In order to study the effect of pore size on the physicochemical properties and bioactivity of scaffolds, another experimental group (HA-nG-25) with the same content of nano graphite (25 vol.%) was introduced for comparison with HA-μG-25 and HA-P. Similarly, it is necessary to analyse the particle size of nano-scaled graphite powder to guarantee that the purchased powder could meet our demand.

The result of particle size tested by LDPSA is listed in Table 6.5. The parameters for test was almost the same as Table 5.4, so the detail has not be reiterated here. The spherical diameter corresponding to the value of SSA was about 154 nm, which was larger than the nominal particle size (~ 400 nm), indicating laminar structure of this nano graphite. In addition, Dv-50 (405 nm) was very close to the nominal size, and 80% of the graphite size was distributed between 276 nm (Dv-10) and 675 nm (Dv-90), revealing that the particles were in uniform distribution.

Table 6.5 Results of particle size by LDPSA (nG)

Analytical Indicator	Parameter	Analytical Item	Result
Solvent	Water	Weighted residual	0.97%
Refractive index of solvent	1.33	Concentration	0.0095%
Absorption rate	0.10	Consistency	2.035
Refractive index of graphite	1.48	SSA	17326.7 m^2/kg
Shading degree	1.90%	Dv-10	276 nm
Scattering model	Mie	Dv-50	405 nm
		Dv-90	675 nm

Figure 6.8 gives the distribution of nano graphite with more details. According to Equation 5.6, the calculated average size was about 477 nm, so the nano-sized graphite powder could fully satisfy our experimental requirements. The extremum of distribution

probability at 460 nm (marked in red) was also close to Dv-50 value very well, and further analysis implies that the vast majority (98.6%) of graphite particles were in the range of 241 - 872 nm (probability ≥ 1%). As a result, it can be predicted that the additional in-rod micropores produced by such graphite were basically in nano-scale.

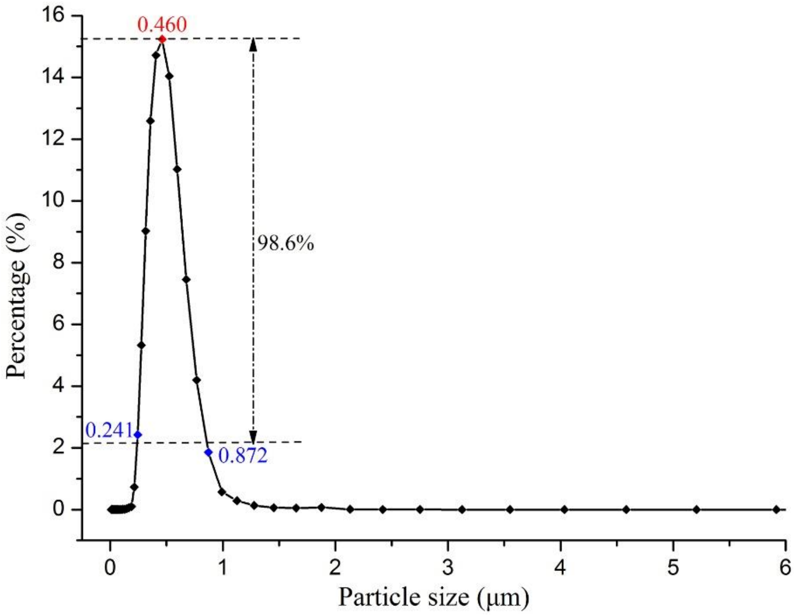

Figure 6.8 Distribution of particle size of nano graphite

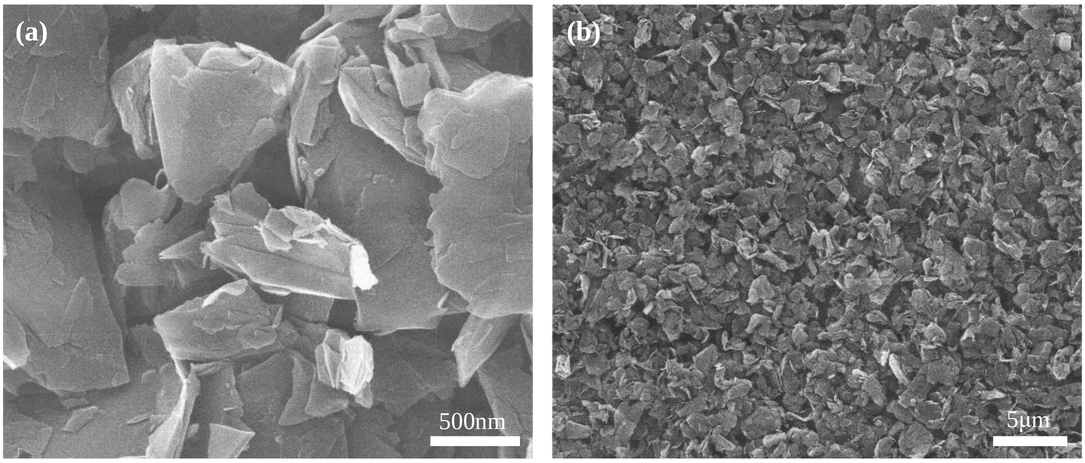

Figure 6.9 SEM images of nano graphite

The SEM images provided by the manufacturer (*XFNANO*) in Figure 6.9 show that the distribution of nano graphite was uniform with high quality on the whole. As seen from Figure 6.9(a), most particles were smaller than 200 nm, and the largest size was about 1.5 μm in spite of agglomeration, which was consistent with the result of laser analyser (Table 6.5 and Figure 6.8). Figure 6.9(b) also confirms the fine uniformity of graphite powder (averaged about 400 nm) in distribution.

6.4.3 Micro-morphologies of HA-G Scaffolds

The SEM results of micron and nano graphite composite scaffolds (25 vol.%) are shown in Figure 6.10. Both HA-nG-25 and HA-μG-25 scaffolds contained a large number of micro- and nano-pores inside the filament rods, which resulted in high wall roughness and thus made the porosity hierarchical. Furthermore, some difference was found between HA-nG-25 and HA-μG-25 in terms of surface morphologies. Specifically, the micropores ranging from 30 to 100 μm in size were more evident in HA-μG-25 sample, due to the utilisation of μG as pore former. In addition, the distribution of microporosity in HA-nG-25 was more uniform than μG treated scaffolds. A possible explanation is that micron graphite was more likely to be broken up during ultrasonic dispersion and the extrusion process may also cause certain degree of damage, because graphite is laminar and fragile in general. Anyway, both kinds of graphite could form additional in-rod micro-/nano-pores as expected, which is especially beneficial to carry out further experiments.

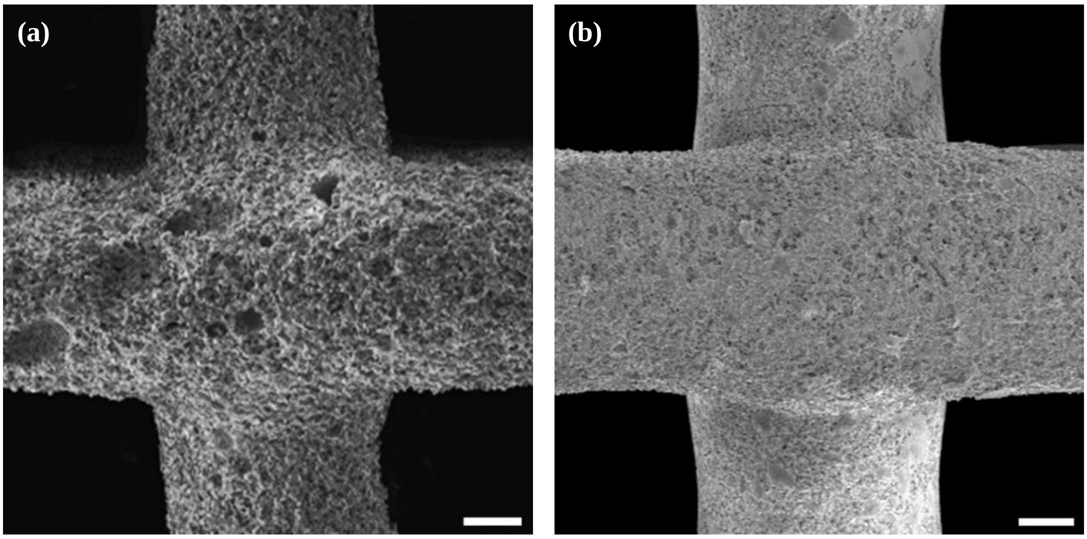

Figure 6.10 SEM images of HA-G scaffolds: (a) HA-μG-25, (b) HA-nG-25; scale bar = 100 μm

6.4.4 Distribution of Pore Size

In order to study whether the optimised sintering profile could achieve our desired purpose, that is, to retain as much in-rod porosity as possible on the basis of complete combustion of graphite, HA-G (HA-μG/nG-25) scaffolds were sintered with the improved profile (Figure 5.4), and the ordinary one for HA-P for comparison.

As nanostructures have significant influence over biological performance, the nano properties of HA-P and HA-G scaffolds were studied. According to BET, the distribution of pores between 1 and 400 nm in all scaffolds is illustrated in Figure 6.11. For the nanopores smaller than 50 nm, graphite treated scaffolds were advantageous over normal scaffolds in terms of SSA, possibly owing to the optimised sintering process. Besides, considerable difference was also found in nanopores with larger size (from 100 to 400 nm); that is, HA-nG-25 scaffolds showed absolute superiority in pore area over HA-P and HA-µG-25, on account of the particle size of nG. Interestingly, in the range of 1 - 100 nm, the SSA of HA-µG-25 was a bit higher than HA-nG-25, in spite of the same order of magnitude. It is because more dispersant was added to get micron graphite well dispersed in HA slurry, while due to good dispersion, nano graphite needed less on the same condition. All in all, it was confirmed that such optimisation indeed contributed to preserving nanoporosity.

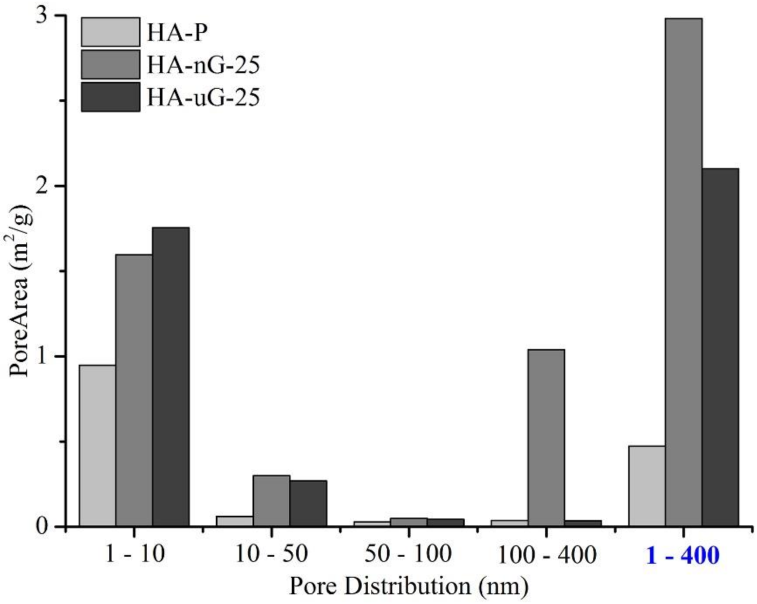

Figure 6.11 Distribution of pore size in HA(-G) scaffolds by BET method

Now that the purpose of porogen was to produce additional in-rod porosity, the actual ratio of porosity and average pore size in each scale (nm, µm and mm) in Table 6.6 and Table 6.7 was measured to verify the formation of hierarchically porous structures. The data was conducive to better understand the overall distribution of porosity. From Table 6.6 we can see that the porosity of HA-P was almost completely (~ 98%) occupied with macropores (≥ 100 μm), and the distribution of microporosity in HA-G scaffolds was consistent to the original of graphite. In addition, the amount of nanoporosity in HA-μG-25 was higher than a normal scaffold, which also confirmed the positive contribution made by the optimisation of sintering. Most of all, the average pore size in each range, shown in Table 6.7, indicates that the structures were hierarchically porous. Along with Figure 6.10, it is sure that the addition of graphite as porogen really succeeded in creating hierarchical porosity.

Table 6.6 Estimation of porosity

Porosity	**≤ 0.4 μm [a]**	**≥ 100 μm [b]**	**0.4 - 100 μm [c]**	**Total [d]**
HA-P	0.4%	~ 55.8%	~ 0.6%	56.8%
HA-μG-25	0.9%	~ 55.8%	~ 12.7%	68.8%
HA-nG-25	11.7%	~ 55.8%	~ 1.3%	69.4%

[a] From BET test results.

[b] Calculated by theoretical model, assuming that scaffolds could manage to keep original shapes after sintering.

[c] By calculation of $P_{Total} - P_{0.4} - P_{100}$.

[d] Calculated by gravimetry method (Equation 4.3).

Table 6.7 Assessment of average pore size

Pore size	**≤ 0.4 μm [a]**	**≥ 100 μm [b]**	**0.4 - 100 μm [b]**
HA-P	8 nm	~ 347 μm	~ 5 μm
HA-μG-25	10 nm	~ 332 μm	~ 37 μm
HA-nG-25	132 nm	~ 326 μm	~ 15 μm

[a] From BET test results.

[b] Measured according to SEM images by TSView.

However, the microporosity of HA-nG-25, which accounts only 1.3% of total porosity with an average of 15 μm in size, might be inadequate to allow full in-growth of cells

[216, 217] (the general size of cell is about 20 μm [218]), although further research is required to affirm this. So compared to HA-nG-25, it is likely that the distribution of porosity and pore size in HA-μG-25 is more favourable, owing to large number of micropores.

In summary, both composite scaffolds with nano or micron graphite as porogen were capable of generating desired pore structures with high and hierarchical porosity, which were verified by SEM images and BET method once again.

6.4.5 Crystallinity Based on XRD

It is commonly accepted that crystallinity of HA after sintering has significant influence on the degradation ability of scaffolds; specifically, higher crystallinity usually results in poorer biodegradability [219]. The crystallinity of original HA powder (first column) and HA scaffolds is illustrated in Figure 6.12.

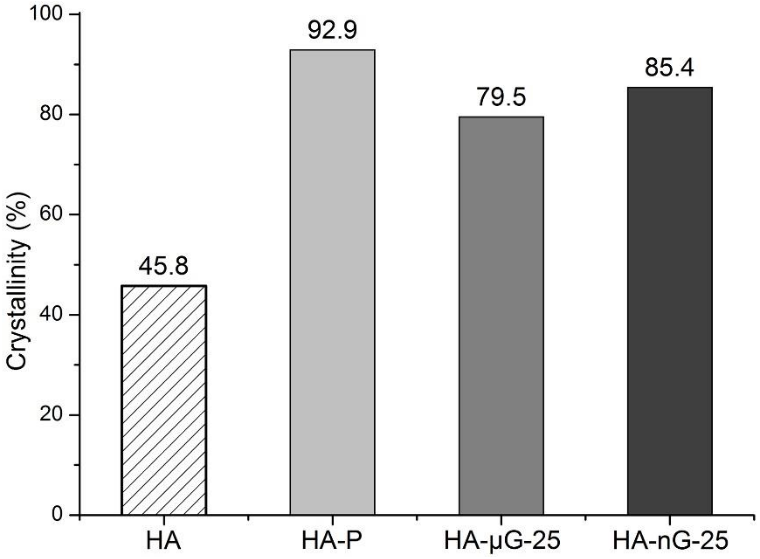

Figure 6.12 Crystallinity of HA powder (before sintering) and scaffolds (after sintering)

Before sintering, the crystallinity of original powder was about 45.8%; while it could be up to 92.9% (HA-P scaffolds) after sintering, which was one of the reasons for great difficulty in degradation. Compared to HA-P, the crystallinity of HA-G composite scaffolds was relatively lower but still high enough, *i.e.* 79.5% (HA-μG-25) and 85.4% (HA-nG-25) respectively. It means that HA powder can be fully crystallised into hydroxyapatite phase when sintered at about 1200 ℃ with appropriate holding time. That HA-G scaffolds had lower crystallinity than HA-P may be explained by considering the energy released by the combustion of graphite, which would locally increase the sintering temperature to sinter scaffolds in advance (≥ 1200 ℃) or overly (> 1350 ℃) so that HA was decomposed into non-stoichiometric phase according to Equation 4.10 [191]. On this occasion, the difference in crystallinity between HA-μG-25 and HA-nG-25 can be reasonably explained: due to larger granule size, the concentration of heat released by micron graphite was higher than nano graphite, making HA-μG-25 more likely to be locally sintered ahead of the scheduled profile, thus with higher amount of non-stoichiometric phase. Therefore, the final crystallinity of HA-nG-25 would be a little higher than HA-μG-25 under the same condition of sintering.

6.4.6 Analysis of Biodegradability

As mentioned earlier, HA is hardly biodegradable *in vivo* (pH = ~ 7.4) in short term. Thus in order to show the influence of hierarchical porosity on degradation and make the degradation rate acceptable, AC-SBF (pH = 3) based on C-SBF was prepared to accelerate the process of degradation, merely for the purpose of comparison (not for evaluation). Equation 6.1 [220] explains the decomposition of HA in acidic environment. Weight loss and pH value was monitored twice a week to record the process of degradation (Figure 6.13). However, due to high porosity and brittleness, HA scaffolds were easy to be broken up into tiny fragments especially after a certain time of degradation (Figure 6.14). This affects the accuracy of weight measurement more or less (< 1.2%).

$$\mathrm{Ca_{10}[PO_4]_6[OH]_2 + 8H^+ \rightarrow 10Ca^{2+} + 6HPO_4^{2-} + 2H_2O} \quad \text{(Equation 6.1)}$$

Figure 6.13 shows that only 51% was decomposed after 7 weeks in HA-P, but the rate in HA-G scaffolds was higher (75% off HA-nG-25 and 67% off HA-μG-25), due to extremely large SSA and high porosity which promotes the ability of biodegradation. Nonetheless, the degradation of all scaffolds exhibited similar trend, *i.e.* slow decomposition at initial stage and followed by increasing rate. In addition, it was found that HA-nG-25 scaffolds required the most frequent renewal of AC-SBF solution while normal group needed the least. According to the chemical reaction in Equation 6.1, the pH value would be accordingly elevated as H^+ was continuously consumed. Additionally, once the solution was refreshed, the decomposition process would be consequently accelerated in the following several days. The renewal of AC-SBF instantly increased the concentration of H^+, and thus boosted the reaction rate, in accordance with chemical equilibrium. Overall, the decomposition rate of HA scaffolds was significantly improved (≥ 31%) in HA-G scaffolds due to additional micro-/nano-porosity. It is highly anticipated that the actual biodegradation rate of HA-G scaffolds *in vivo* could also be accelerated at similar level, and HA-nG-25 scaffolds displayed the best performance in terms of biodegradation.

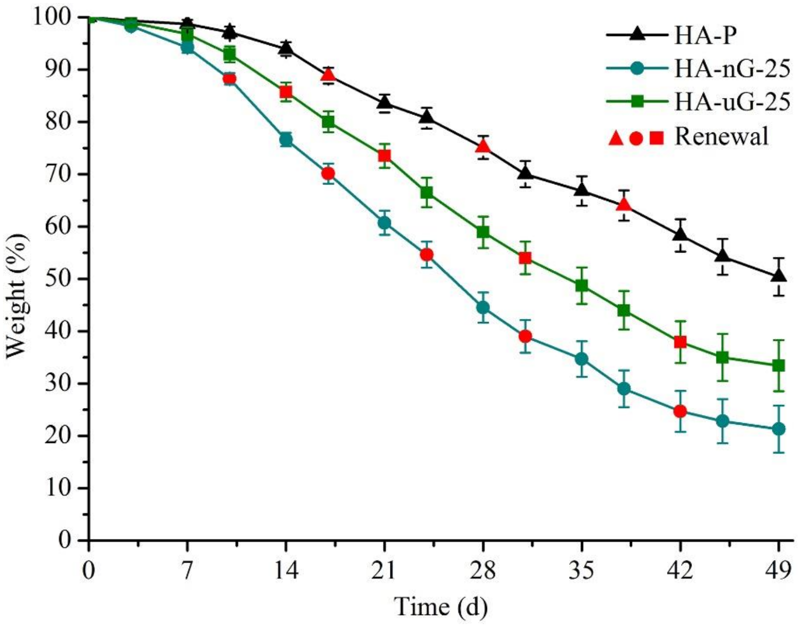

Figure 6.13 Degradation result of scaffolds in AC-SBF (renewed once pH ≥ 5)

To make the decomposing process more intuitive, the appearance of scaffolds degraded after day 24 and 49 days shown in Figure 6.14. Despite carefulness during practical operations, the breakup of HA scaffolds into tiny fragments was still inevitable. Even worse, the more being degraded, the scaffolds would be more loose and brittle (Figure 6.14 (d) and (e)), which also was to blame for the growing deviation of weight loss as time went by (Figure 6.13). Besides, the scaffolds preferred to begin degradation on the edge and corner parts that possess larger SSA.

In summary, the degradation rate of HA-G composite scaffolds was significantly enhanced (≥ 31%), mainly as the result of larger SSA and additional in-rod porosity, and partly because of low crystallinity (Figure 6.12). Although HA-nG-25 had higher crystallinity, its degradation rate in AC-SBF was much faster than HA-µG-25, indicating that the effect of SSA on the degradation rate was stronger than crystallinity.

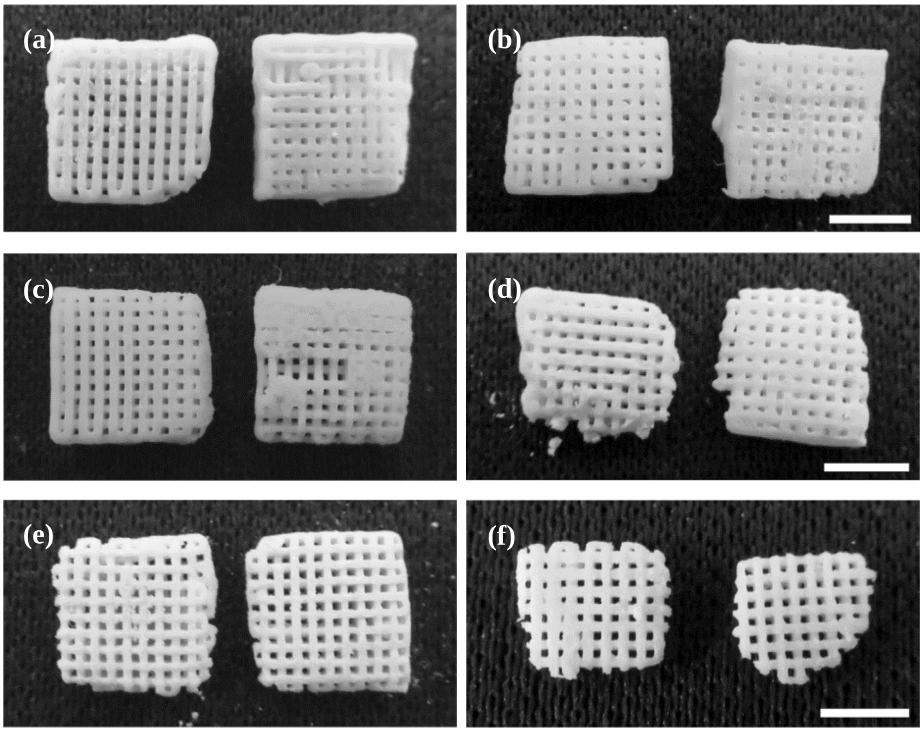

Figure 6.14 Exterior of all scaffolds after degradation in AC-SBF: HA-P after (a) 24 d, (b) 49 d; HA-µG-25 after (c) 24 d, (d) 49 d; HA-nG-25 after (e) 24 d, (f) 49 d; scale bar = 5 mm

6.4.7 Evaluation of Hydrophilicity

The hydrophilic test results of all scaffolds are summarised in Figure 6.15. From Figure 6.15, HA-P scaffolds were capable of absorbing large amount of water (absorption rate -- about 12.3%). Moreover, HA-µG-25 and HA-nG-25 had better ability to absorb considerable water (31.4% and 21.9%). Puzzlingly, it was found that even if the in-rod pores of HA-µG-25 were fully filled with water, the absorption rate would be at most 18.6% (**As%**, calculated by Equation 6.2), much smaller than the actual value.

$$A_S\% = A_C\% + P_G\% \times \frac{\rho_w}{\rho_{HA} - \rho_w} \qquad \text{(Equation 6.2)}$$

Where, $\boldsymbol{A_C}$ is the absorption rate of HA-P; $\boldsymbol{P_G}$ is in-rod porosity of HA-G scaffolds; $\boldsymbol{\rho_{HA}}$ and $\boldsymbol{\rho_w}$ is the density of HA and water respectively.

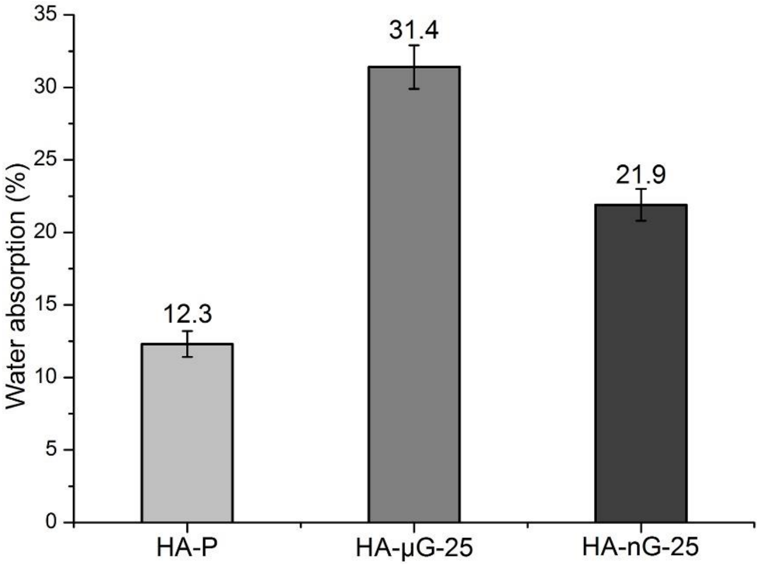

Figure 6.15 Result of water absorption

In order to explain this phenomenon, the practical test of contact angle was also recorded (Figure 6.16). In fact, due to small contact angle, most of the absorbed water were retained by surface absorption instead of filling micropores, which was the main reason that the water absorption of HA-P could reach up to 12.3% regardless of little extra in-rod porosity (< 1%). As for HA-μG-25, its contact angle with water was the smallest (about 29 ° in average), thus more water could be retained in this way. In addition, most of the in-rod pores in HA-nG-25 were in nano-scale (Table 6.6), which were too small to be filled with water.

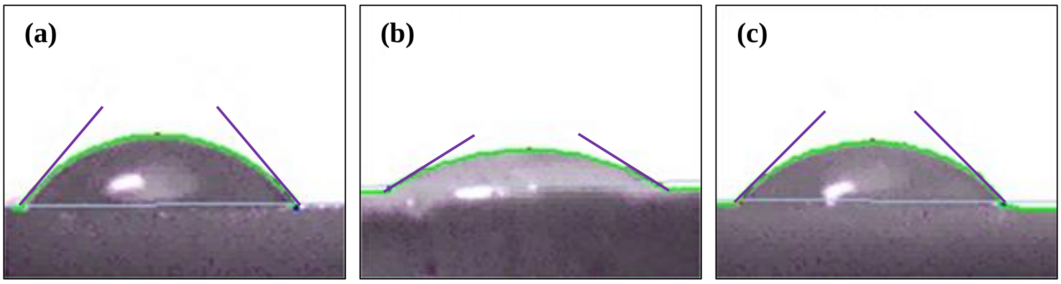

Figure 6.16 Contact angle of scaffolds with water: (a) HA-P, θ = 51.3 °; (b) HA-μG-25, θ = 30.2 °; (c) HA-nG-25, θ = 45.5 °

The relationship of contact angle and water absorption of scaffolds is illustrated in Figure 6.17. As described in ***Section 4.4.2***, contact angle and water absorption is usually closely related. For instance, HA-μG-25 showed absolutely superiority to HA-nG-25 and HA-P in terms of water absorption due to smallest contact angle; while the highest contact angle in normal scaffolds made HA-P least able to absorb water. Furthermore, it was found that contact angle and water absorption had close relations to in-rod micropores as well. To be more specific, due to capillary effect, the additional micropores inside the rods of scaffolds could absorb quite amount of water. In addition, high SSA and wall roughness also contributed to lock moisture. On the other hand, given that the volume of droplets for test of contact angle was the same, more water would be absorbed by the scaffolds with higher microporosity, and consequently, the contact angle would be naturally smaller because of less volume (Figure 6.16 (b) and (c)). Considering that HA-G composite scaffolds have better performance in hydrophilicity (mainly water absorption) than normal scaffolds, it is highly potential that the bioactivity of HA-G scaffolds would be outstanding to HA-P accordingly, which of course needs further biological experiments to confirm this.

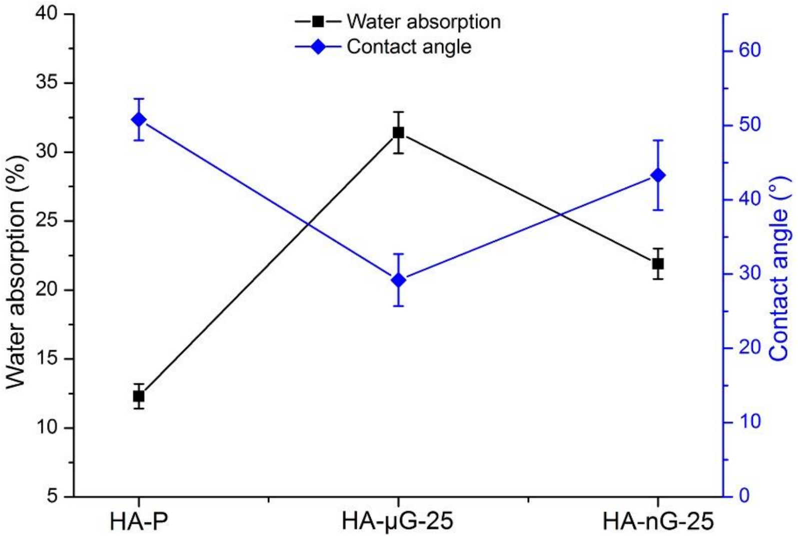

Figure 6.17 Relationship of water absorption and contact angle

6.5 Summary

In this chapter, the most concerned physical and chemical properties of HA-P and HA-G scaffolds were characterised to verify the advantages of improved scaffolds. In view of mechanical properties and porosities, 25vol.% of graphite is the best choice so as to reduce workload and save cost. The BET results confirmed the positive contribution of optimised sintering profile to preserving microporous porosity. In terms of biodegradation ability, HA-G scaffolds performed better in AC-SBF than HA-P, mainly resulting from larger SSA, additional porosity, and relatively lower crystallinity of hydroxyapatite phase. Besides, better hydrophilicity was found in HA-G scaffolds, which is conductive to cellular adhesion and proliferation.

Chapter 7. Biological Evaluation of Scaffolds with Different Characteristics in Hierarchical Porosity

7.1 Introduction

As a substitute for implantation, scaffolds for BTE must exert certain biological activities, mainly in terms of promoting adhesion, proliferation and differentiation of osteoblasts, so as to achieve the purpose of bone regeneration or repair [3].

Obviously, the novel method is able to create a wide range and scale of porosities with adjustable distribution in HA scaffolds, meanwhile with suitable mechanical strength. However, the scaffolds may exhibit significant difference in features and characteristics of hierarchical porosity, *e.g.* the ratios between microporosity and nanoporosity [221], which mainly depends on the particle size of porogen. In this study, graphite as porogen was used to generate in-rod porosities, which can permit the adjustment of microporosity and nanoporosity with nano or micron graphite. Therefore, it is important to evaluate the influence of such difference on biological performance, in order to optimise the structures of scaffolds by controlling the particle sizes and distribution of porogen.

Specifically, in view of possible cytotoxic effects of residual graphite on HA-G scaffolds [206], the cytotoxicity of scaffolds was evaluated prior to the assessment of biological activity (including adhesion, survival rate, proliferation, differentiation and so on), which could confirm the advantages of HA-G scaffolds towards biological performance. It is highly anticipated that this can make further optimisation possible to control the distribution of porosity in scaffolds, so that acceptable and optimal solution for BTE may be achieved to satisfy the needs of clinical applications.

7.2 Materials

Since the essential ingredients for HA-P, HA-μG/-nG scaffolds have been introduced before, Table 7.1 only lists the main materials for the purpose of biological evaluation.

Table 7.1 Materials for biological evaluation

Material	Specification	Manufacturer	Application
Anhydrous ethanol	≥ 99.7%, AP	Sinopharm	Sterilisation & dehydration
Glutaraldehyde	25%	Sinopharm	Fixation of cells
Hydrogen peroxide (dH_2O)	50% v/v	Sinopharm	Lysis of cells
Pre-osteoblast	MC3T3-E1	Sigma-Aldrich	Evaluation of cytotoxicity, adhesion, survival rate *etc*.
Myoblast	C2C12	Sigma-Aldrich	Evaluation of proliferation and differentiation
FBS	20%	PAN Biotech	Cell culture
α-MEM / Dulbecco's MEM (DMEM) / high-glucose DMEM	HyClone	Gibco	Cell culture
Phosphoric buffer solution (PBS)	pH = 7.4	Self-made	Flushing cells or tissues
P/S	10^4 U/mL / 10^4 μg/mL	Gibco	Antibiotics
Donor equine serum	HyClone	Gibco	Inducing differentiation
Insulin	1 mM	Sigma-Aldrich	Inducing differentiation
Cell counting kit (CCK)	CCK-8	Dojindo Molecular	Assays for cytotoxicity
Calcein-AM [a]	> 99%	Dojindo Molecular	Stain for living cells
Propidium iodide (PI)	> 95%	Beyotime	Stain for dead cells
FITC-phalloidin [b] / TRITC-phalloidin [c]	0.5 mg/mL	Sigma-Aldrich	Stain for F-actin [d]
4',6-diamidino-2-phenylindole (DAPI)	≥ 98%	Thermo Scientific	Stain for DNA

Note: [a] calcein-AM -- acetoxymethyl calcein; [b] FITC -- fluorescein isothiocyanate labelled; [c] TRITC -- tetramethylrhodamine B isothiocyanate labelled; [d] F-actin -- fibrous actin.

7.3 Methodology

7.3.1 Experimental Procedure

Figure 7.1 shows the experimental procedure of biological evaluation of all scaffolds with different characteristics in microporosity. Firstly, the cytotoxicity of HA-G scaffolds was analysed to pave the way for further assessment of bioactivity: if HA-G scaffolds were proved to be free of cytotoxic effects, it was meaningful and reliable to conduct the following experiments; otherwise, it was not necessary to carry out other biological tests due to poor biocompatibility, and we had to explore new other ways to optimise bone scaffolds to be more biomimetic. Therefore, cytotoxicity is the fundamental but most important indicator for biological scaffolds. Fortunately, the possibility of cytotoxicity caused by potential residual graphite in HA-G scaffolds was excluded. The biological activity for evaluation in this chapter primarily included cellular adhesion, interaction, survival rate, proliferation and differentiation. Two kinds of cells, *i.e.* MC3T3-E1s and C2C12s, would be used if necessary.

If not specified, the cell culture during biological experiments was performed in a CO_2 incubator (temperature: 37 ℃, concentration of CO_2: 5%); other operations such as sterilisation, flushing of scaffolds, dehydration, fixation, lysis, washing, stain of cells and so on were conducted in a clean bench.

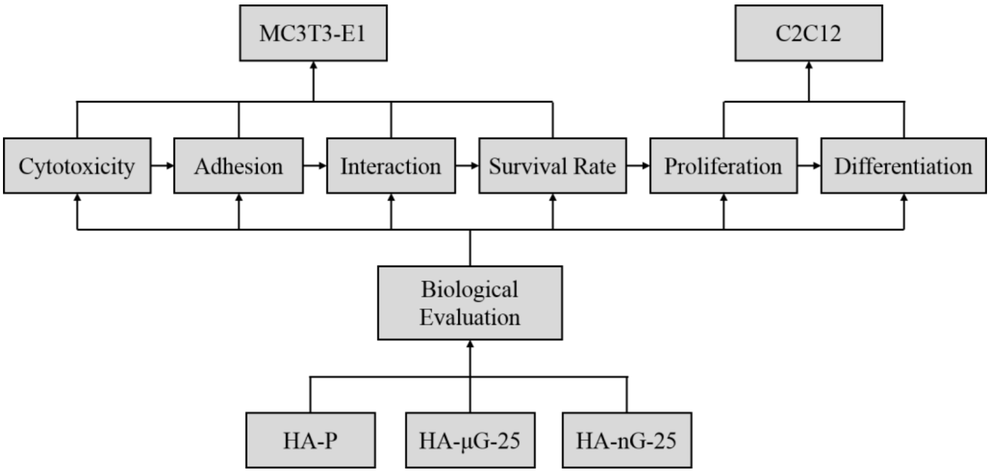

Figure 7.1 Experimental procedure of biological evaluation

7.3.2 Equipment and Devices

Table 7.2 lists the main equipment and devices used for the evaluation of biological performance. Note that other devices, such as those for preparation of scaffolds were omitted, seen in the footnote.

Table 7.2 Main details of equipment and devices for experiments

Device	Model	Manufacturer	Application
MAM system [a]	MAM-II	Fochif	Fabrication of scaffolds
Drying oven	DZF-6000	Super Instruments	Drying
CO_2 incubator	Heracell 150i	Thermo Scientific	Cell culture
Critical-point dryer	EM CPD300	Leica	Dehydration of cells
Spectrophotometer	PowerWave XS2	BioTek	Cell counts
Clean bench	BCL-1800	Yatai Kelong	Platform for operations
Fluorescence microscope	D71	Olympus	Observation of fluorescence
Scanning electron microscope	Sirion 200	FEI	Characterisation of microstructure of scaffolds

[a] Other devices like electronic balance, microwave furnace *etc*. were omitted.

7.3.3 Introduction of Cell Types

MC3T3-E1 cells have been introduced in ***Section 4.3.5***, so this section will focus on C2C12s. C2C12 is a myoblast cell line characterised by visually determinable differentiation profile [222]. It is a subclone produced in Helen Blau’s Lab of myoblasts that were originally obtained by Yaffe *et al*. through serial passage of myoblasts cultured from the thigh muscle of C3H mice after crush injury [223]. C2C12 cells are useful and they have been widely utilised to study the differentiation of myoblasts and osteoblasts, as well as to express various proteins through targeting techniques [222].

7.3.4 Biological Evaluation of Scaffolds

7.3.4.1 Assessment of cytotoxicity

The cytotoxicity of HA-G scaffolds (*i.e.* HA-µG-25 and HA-nG-25) was assessed by analysing the proliferation of MC3T3-E1 cells based on CCK-8 [224] method. CCK-8 allows sensitive colorimetric assays for the determination of cell viability in cell proliferation and cytotoxicity assays. In CCK-8, the highly water-soluble tetrazolium salt (WST-8, by Dojindo [225]), which is more sensitive than other tetrazolium salts such as

MTT, will be reduced by dehydrogenase activities in cells to give a yellow-colour formazan dye. Similar to MTT, the amount of formazan dye is directly proportional to the number of living cells.

Here the main experimental steps are summarised: **(a)**. All scaffolds (including HA-P, HA-μG-25 and HA-nG-25) were placed in four 12-well culture plates (one plate for a type of HA samples, and another for the blank group), and each well was filled with α-MEM and 10% FBS by a dispenser; **(b)**. All wells were seeded with pre-osteoblasts (MC3T3-E1s) at 10^4 cells/cm^2 before cell culturing in a CO_2 incubator; **(c)**. At day 1, 3, 5 and 7, a new 12-well culture plate was used to place 9 scaffold samples (3 per group of HA samples, washed three times with PBS solution in advance) and cell suspension from blank group (another 3 wells) respectively; **(d)**. A mixture of DMEM (30 μL) and CCK-8 assay solution (30 μL) was dispensed into each well to read and record the OD value by a spectrophotometer (also known as enzyme-linked immunometric meter) at the wavelength of 450 nm. In addition, according to the result of optical absorbance, the cell viability (**S%**) of each group could be obtained by Equation 7.1 [225].

$$S\% = \frac{D_S - D_0}{D_N - D_0} \times 100\% \qquad \text{(Equation 7.1)}$$

Where, $\boldsymbol{D_S}$ is the average OD value counted on scaffolds; $\boldsymbol{D_N}$ means the optical absorbance of cell suspension without scaffolds, *i.e.* blank group; and $\boldsymbol{D_0}$ stands for initial absorbance of CCK-8 mixture solution.

7.3.4.2 Analysis of cellular adhesion and interactions

The analysis of cellular adhesion and interactions was on the basis of MC3T3-E1s, thus the basic details of cell culture will be simplified, which can be found in previous sub-sections.

The main points for analysis of cellular adhesion and interactions are summed up: **(a)**. Three 12-well plates for all scaffolds (one plate for a type again) → α-MEM and 10% FBS → seeding MC3T3-E1s (10^4 cells/cm^2) into each well → incubation at 37 ℃; **(b)**.

After culturing for 1 day (24 h) → fixation of cells by glutaraldehyde → flushing scaffolds with PBS → critical-point drying (CPD) of cells for 1 h → SEM observation of cellular adhesion status; **(c)**. At day 3 (72 h), fixation of cells by glutaraldehyde → flushing scaffolds with PBS → staining the F-actin and DNA of cells on all scaffolds with FITC-phalloidin (20 μM) and DAPI (10 μM) respectively → incubation at 37 ℃ for 15 min → analysis of intercellular junctions by a fluorescence microscope.

7.3.4.3 Estimation of survival rate

The actual survival rate of MC3T3-E1s seeded on scaffolds was estimated for the purpose of further analysis. The simplified experimental procedure was summarised as follows: **(a)**. Cell culture of all scaffolds seeded with MC3T3-E1s (the same to previous sub-sections) for several days; **(b)**. At day 3 and 5, fixation of cells by glutaraldehyde → flushing scaffolds with PBS → dehydration of cells with different concentrations of ethanol → staining the cells with a mixture solution (300 μL) of calcein-AM (10 μM, for live cells) and PI (5 μM, for dead cells) → incubation for 15min → statistical estimation of survival rate of MC3T3-E1s by a fluorescence microscope. Similarly, the survival rate (viability, **R%**) could be estimated through Equation 7.2.

$$R\% = \frac{N_L}{N_L + N_D} \times 100\% \qquad \text{(Equation 7.2)}$$

Where $\boldsymbol{N_L}$ and $\boldsymbol{N_D}$ represents the number of live and dead cells respectively.

For the sake of low cost, gradient concentrations of ethanol was used to dehydrate cells instead of CPD in this experiment. Specifically, **(a)** the scaffolds were firstly soaked in deionised water (15 mL per well) for 10min to remove PBS and other fixatives; **(b)** a dispenser was used to extract the cleaning solution of each well; **(c)** after preparation of 200 mL ethanol solution (10 vol.% of ethanol), the cells on each scaffold were dehydrated with 10 mL ethanol solution (10 vol.%) for 10min, followed by extraction of ethanol solution; **(d)** next were the repetition of step (c) with gradient concentrations of ethanol (still 10 mL every time) -- 20, 30, 40, 50, 60, 70, 80, 90 and 100 vol.% -- for dehydration and then extraction of ethanol solution. Note that the dispenser should never touch any scaffolds during either dehydration or extraction to protect the shape and vitality of cells.

7.3.4.4 Evaluation of proliferation and differentiation

To evaluate the effect of scaffolds on proliferation and cell morphologies (or differentiation), C2C12s were incubated in growth media consisting of high-glucose DMEM (HG-DMEM) supplemented with 20% FBS and 1% P/S. C2C12s were exposed to scaffolds until they were confluent (about 4 days). In order to test the influence of hierarchical porosity on differentiation capacity, C2C12s were then incubated with differentiation media (*i.e.* HG-DMEM, 2% donor equine serum and 1 μM insulin) for another 3 days. At the end of experiments, cells were lysed or fixed for further analysis in dH_2O (50% v/v) or glutaraldehyde (25%) respectively. C2C12s used in this study were populated for 3 - 6 generations and seeded at 5,000 cells/cm^2 onto tissue culture plastic (for DNA/protein analysis) or gelatine-coated (0.2%) coverslips (for fluorescence imaging) within a 6-well plate. During the whole process, the samples with C2C12s were all incubated in a humidified CO_2 (5%) incubator at 37 ℃. The immucytochemical images were photographed by a fluorescence microscope.

7.4 Results and Discussion

7.4.1 Cytotoxicity of HA-G Scaffolds

Although there was substantial improvement in the physicochemical properties (*e.g.* SSA, degradability, hydrophilicity, *etc*.), for HA-G scaffolds, it was merely in theory to exert better biocompatibility, since the results of EDX spectrum (Figure 5.12(b) and Table 5.5) showed that residual graphite may still remain in HA-G scaffolds even after sintering. Therefore, cytotoxicity analysis of HA-G scaffolds was definitely required.

The cytotoxic result of HA-G scaffolds based on CCK-8 is shown in Figure 7.2. It is obvious that the number of cells (indicated from OD value) in all scaffolds went through exponential growth during cell culture (7 days) as expected, meaning the proliferation of MC3T3-E1s was not negatively affected. On the contrary, HA-G scaffolds had evident advantages in terms of proliferation compared to normal HA scaffolds. In other words, HA-G composite scaffolds were absolutely biocompatible after sintering, which could eliminate the possibility of potential cytotoxicity from residual graphite in scaffolds towards cells. Specifically, HA-G could enhance the process of cell growth in fact, and HA-nG-25 was the most bioactive to promote proliferation. This may be the result of different SSA and pore size in these scaffolds: firstly, due to higher SSA and thus larger contact area, cells were more likely to adhere onto HA-nG-25 scaffolds on the same condition; in addition, the numerous micropores in nano scale were beneficial to the vitality of cells on HA-nG-25 scaffolds (Figure 7.3), thereby improving cellular proliferation in return.

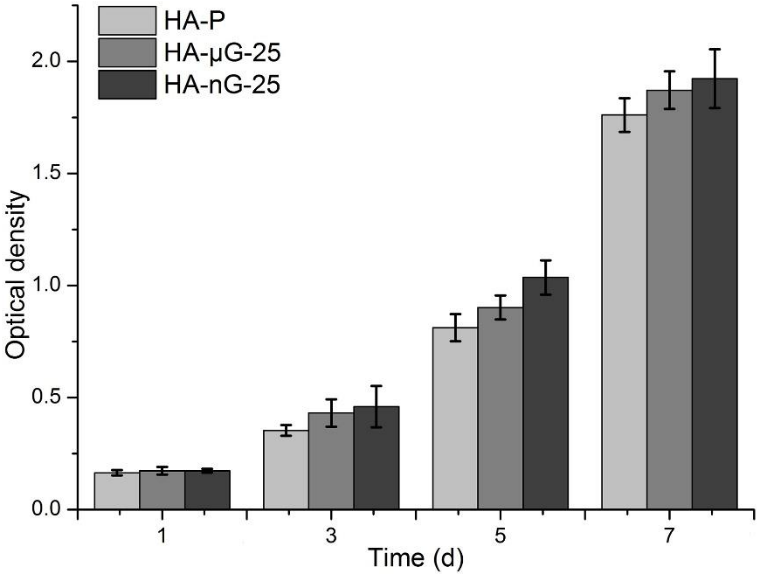

Figure 7.2 Cytotoxicity assay of HA scaffolds by CCK-8

The cellular vitality of all scaffolds during each period was estimated according to Equation 7.1, as shown in in Figure 7.3. Similar to the result of proliferation, the cell vitality of HA-nG-25 was always higher than others, especially at day 5 when it was above 85%, resulting in significantly larger number of cells in HA-nG-25 (Figure 7.2). However, as time went on, the increase of cell vitality in HA-nG-25 became slightly weak, and even begun to decline at day 7, despite that it was still higher than others. This can be explained from the point of nutrition supply: the cells may grow too fast to get sufficient supplement of essential nutrients due to the lack of interconnected micron-sized pores, which would serve as channels for nutrition supply and themselves could also store certain amount of nutrients [216]. Consequently, the already adhered cells may suffer from malnutrition or even apoptosis [217]. The rise of vital activity in HA-P was relatively stable, which also further confirms that HA scaffolds are biocompatible. As for HA-μG-25, its cellular vitality rapidly increased in the early stage of cell culture (1 - 3 days), basically consistent to HA-nG-25, and then the growth became smooth and steady. It suggests that the in-rod micro-/nano-pores on HA-G scaffolds did contribute to promoting cellular proliferation. Interestingly, at day 7, the vitality of all scaffolds tended to be in great agreement with each other (from 70% to 77%), possibly because that the scaffolds were filled with MC3T3-E1s so that there was no more available space for adhesion and proliferation, regardless of different growth rate.

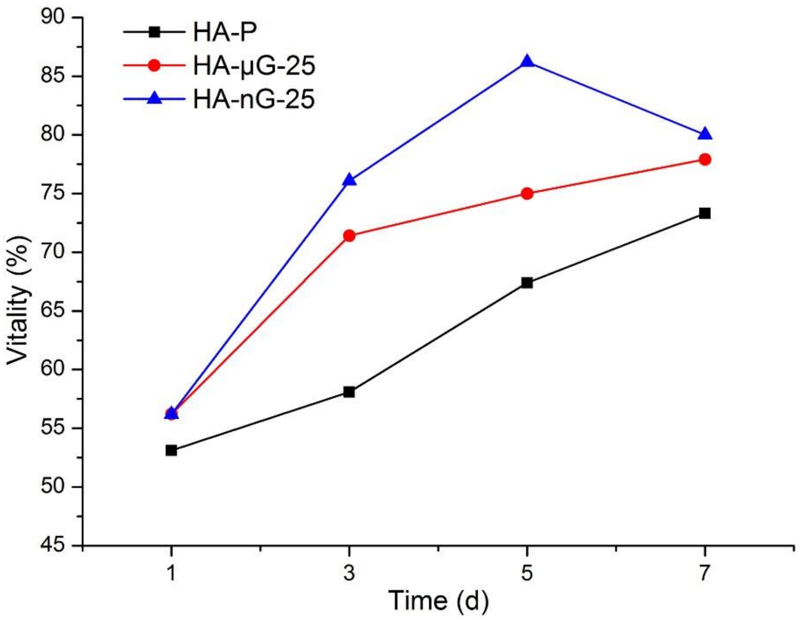

Figure 7.3 Viability of cells on scaffolds

In conclusion, any toxic effects from residual graphite or HA-G scaffolds do not inhibit the natural bioactivity of cells. In contrast, due to the additional in-rod micropores and increased SSA, along with better hydrophilicity, HA-G scaffolds could significantly promote proliferation with higher cell vitality. The results lay well the foundation for the following biological evaluation, as well as the development of this novel fabrication method.

7.4.2 Cellular Adhesion

As introduced, cellular adhesion is the base of most cell behaviours such as proliferation and differentiation, and high surface roughness and good cell affinity usually contributes to cellular adhesion [226]. Figure 7.4 shows the adherent morphologies of MC3T3-E1s on all scaffolds, after cell culture for 24 hours. Apparently, the characteristics of surface morphologies of all scaffolds was conspicuous: compared to the smooth surface and highly densified structure in HA-P, HA-μG-25 was microporous with majority of pores in micron-scale surrounded by numerous nanopores, while the in-rod pores of HA-nG-25 were mainly in nano size, coinciding to Figure 6.10.

In Figure 7.4 (a), (c) and (e), it shows that the cells on HA-G scaffolds tended to adhere and spread much more freely on surface, in contrast to the restricted and cramped adhesion status on normal scaffolds. Such difference can be interpreted through surface morphologies: owing to high wall roughness in HA-G, the cells were easier to get available space for adhesion; and extremely large SSA gave the cells more opportunities for effective exposure to scaffolds as well, leading to better adhesion; while it was the opposite in HA-P, reasonably with worse adhesion. In addition, the tentacles of cells in HA-P could hardly be recognised due to poor adhesion; whereas in HA-G samples, they were more likely to join together as expected, which could pave a favourable way for the interactions of cells [227]. Specifically, the cells on HA-G composite scaffolds were fully connected through cellular tentacles, but those on HA-P had to grow large enough in volumetric size continuously so as to get in touch with each other. The cytotoxic evaluation results in Figure 7.2 also reflect the positive effect of such tentacle adherence on cell growth. On the other hand, SEM images at low magnification (*e.g.* Figure 7.4 (b), (d) and (f)) indicate another significant difference in the aspect of cell aggregation, wherein HA-G scaffolds exhibited complete superiority to normal scaffolds, which was the inevitable outcome of free spread (adhesion) status and well-developed (connected) tentacles, greatly enhancing the efficiency of transferring biological signals [226].

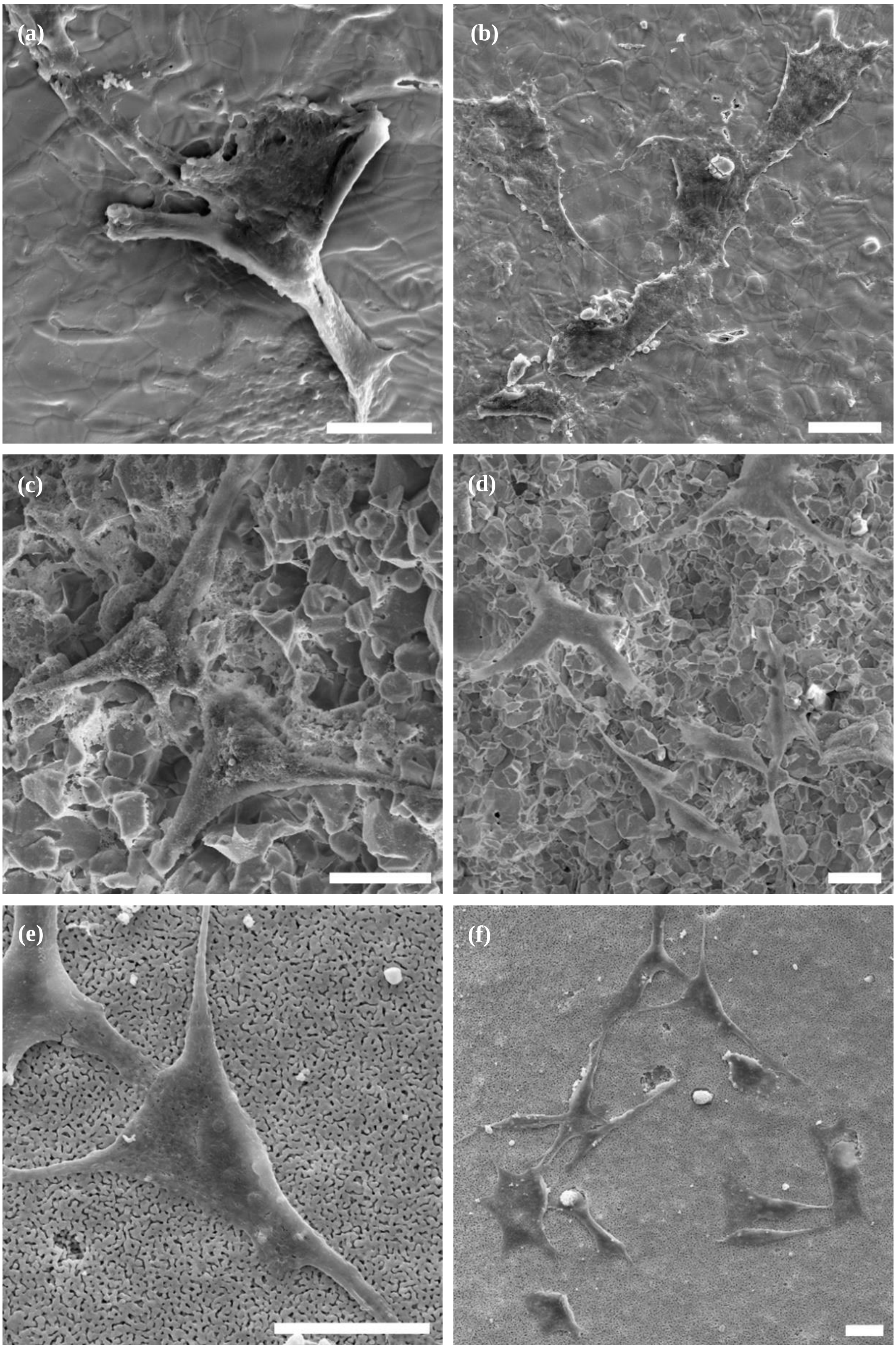

Figure 7.4 Adhesion status of MC3T3-E1s (day 1) by SEM: (a), (b) HA-P; (c), (d) HA-µG-25; (e), (f) HA-nG-25; scale bar = 20 µm

As we can see, graphite treated scaffolds provide excellent conditions for cellular adhesion and growth due to the existence of additional in-rod micropores, and thus have high potential for better biological activity in BTE.

7.4.3 Intercellular Junctions

The intercellular junctions were primarily characterised by fluorescent staining of fibrous actin, as shown in Figure 7.5. It is well known that intercellular junction is a necessity for effective transduction of bio-signals [228], where F-actin is the basis for cells to maintain their morphologies and internal structures, especially in muscle tissues [229]. In other words, it is reasonable to view intercellular junctions by F-actin. In Figure 7.5 (a), (c) and (e), the fibrous structures in green stand for F-actins stained by FITC-phalloidin; and the blue dots in Figure 7.5 (b), (d) and (f) represent the cell nuclei (*i.e.* DNA stained by DAPI). Of particular note is that the filter effect of fluorescence microscope was adjusted so that the exterior of scaffolds could be clearly identified without any influence on results, which was the same for Figure 7.6 and Figure 7.7.

Overall, there was no significant difference in the number of cells, although HA-G scaffolds had more cells (blue dots) than HA-P, which was consistent with the results of proliferation assessed by CCK-8. However, the intercellular junctions on HA-P scaffolds were hardly identified due to too many isolated cells (Figure 7.5(a)). Quite the opposite, almost all of the cells on HA-µG-25 were interconnected through well-developed F-actins (or tentacles). Besides, the distribution of F-actins in HA-µG-25 was the most uniform, indicating that the fibrous network in HA-µG-25 scaffolds was maturely developed (Figure 7.5(c)). Regarding that of HA-nG-25, it fell in between HA-µG-25 and HA-P. To be more specific, most of cells were interconnected by F-actins, and there were some isolated cells as well (Figure 7.5(e)). That is to say, owing to the most developed network of F-actins for the communication and transduction of biological signals among cells [43], the cells on HA-µG-25 may have the most active motility in terms of intercellular junctions, which is particularly favourable to the process of proliferation and differentiation in BTE [227].

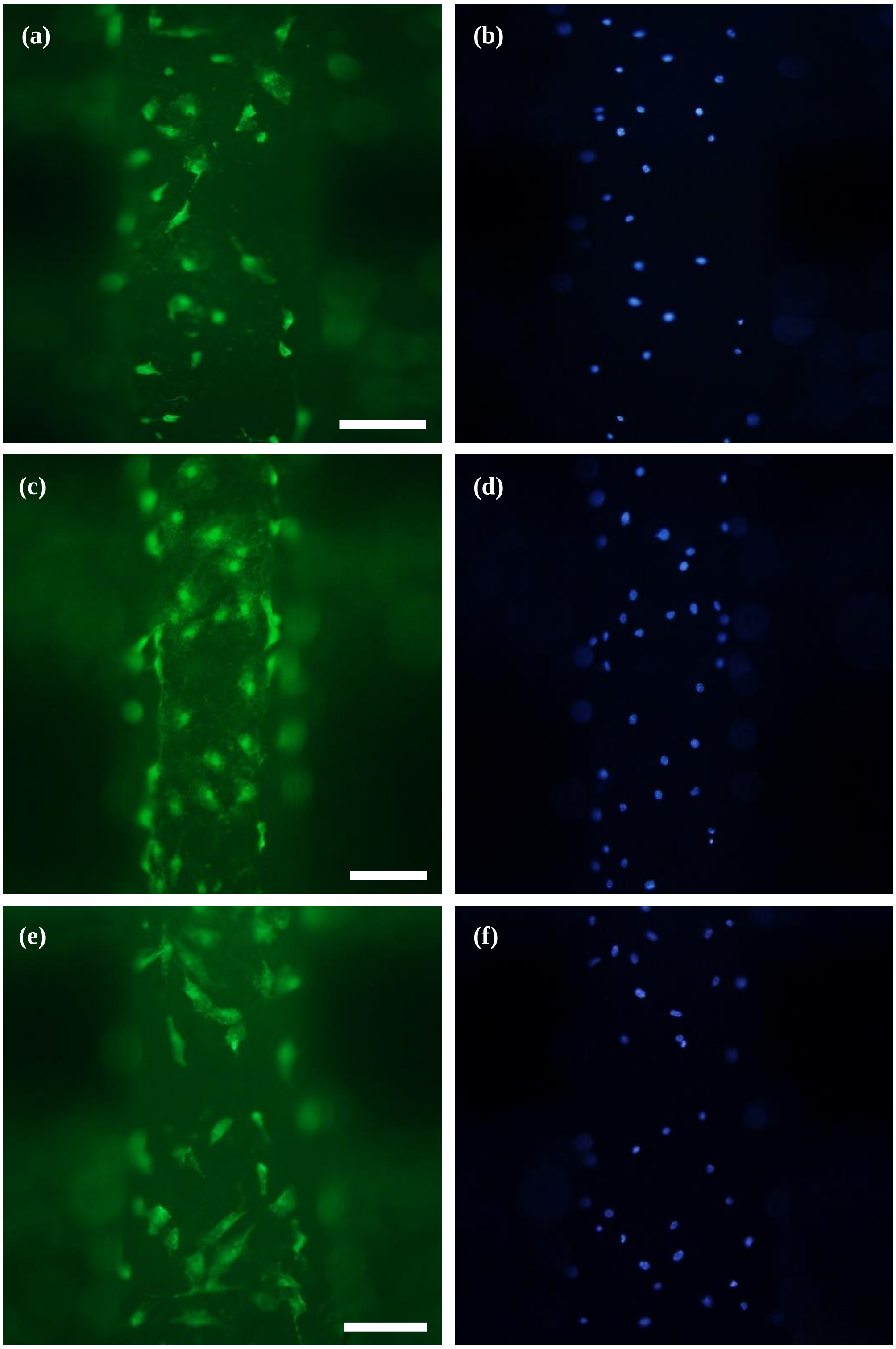

Figure 7.5 Intercellular junction status of MC3T3-E1s (day 3) by fluorescence: (a), (b) HA-P; (c), (d) HA-µG-25; (e), (f) HA-nG-25; F-actin (green) by FITC-phalloidin, and DNA (blue) by DAPI; scale bar = 200 µm

Directly influenced by the adherent degree of cells, cellular aggregation also had important impact on the process of proliferation and even differentiation [227], which well explained the advantages of HA-G scaffolds in cell proliferation (Figure 7.2) in comparison to HA-P. Moreover, the results in Figure 7.4 intuitively demonstrate the effect of adhesion on intercellular junctions: great freedom of spread and motion of tentacles improved the probability of interconnection between cells, eventually making contributions to fully developed fibrous network of actins.

7.4.4 Survival Rate

Figure 7.6 and Figure 7.7 show the survival status of cells on scaffolds after incubation for 3 and 5 days. Generally speaking, the vitality of cells on scaffolds is closely related to their survival status, that is, higher survival rate usually results in stronger vitality. Because of different focal lengths used for observation under a microscope, the cells on different layers of scaffolds were not always clear; specifically, only the focused cells could be clearly recognised. For instance, the second layer in Figure 7.6 was focused, while it was the first layer in Figure 7.7.

In terms of live cells in Figure 7.6 (a), (c) and (e) (stained by calcein-AM), the following aspects should be particularly noted. **1) The number of cells**. The cell count in HA-P was much less than HA-G scaffolds, but little difference was found in HA-µG-25 and HA-nG-25, exactly in accordance with the result of cytotoxicity analysis. **2) Freedom in spread**. Most of the cells on HA-P were in round or oval shape, while only a few of them strip-shaped (the result of freely stretched tentacles), indicating little freedom in spread. The cell morphologies of HA-µG-25 were almost sword-shaped (*i.e.* tentacles spread in different directions), which means the cells were highly free to spread over and to build connections with each other. Similarly, the situation in HA-nG-25 was between HA-P and HA-µG-25, agreeing with the adhesion result shown in Figure 7.4 very well. **3) Intercellular junction**. Overall, the cells on HA-P were still isolated even at day 3, thus without substantial communication with other adjacent cells; on the contrary, the intercellular junctions were significantly improved in HA-G scaffolds, where the cells were mostly in cluster and interconnected by tentacles. Therefore, the junction status of cells illustrated in Figure 7.5 was not accidental but indeed objective.

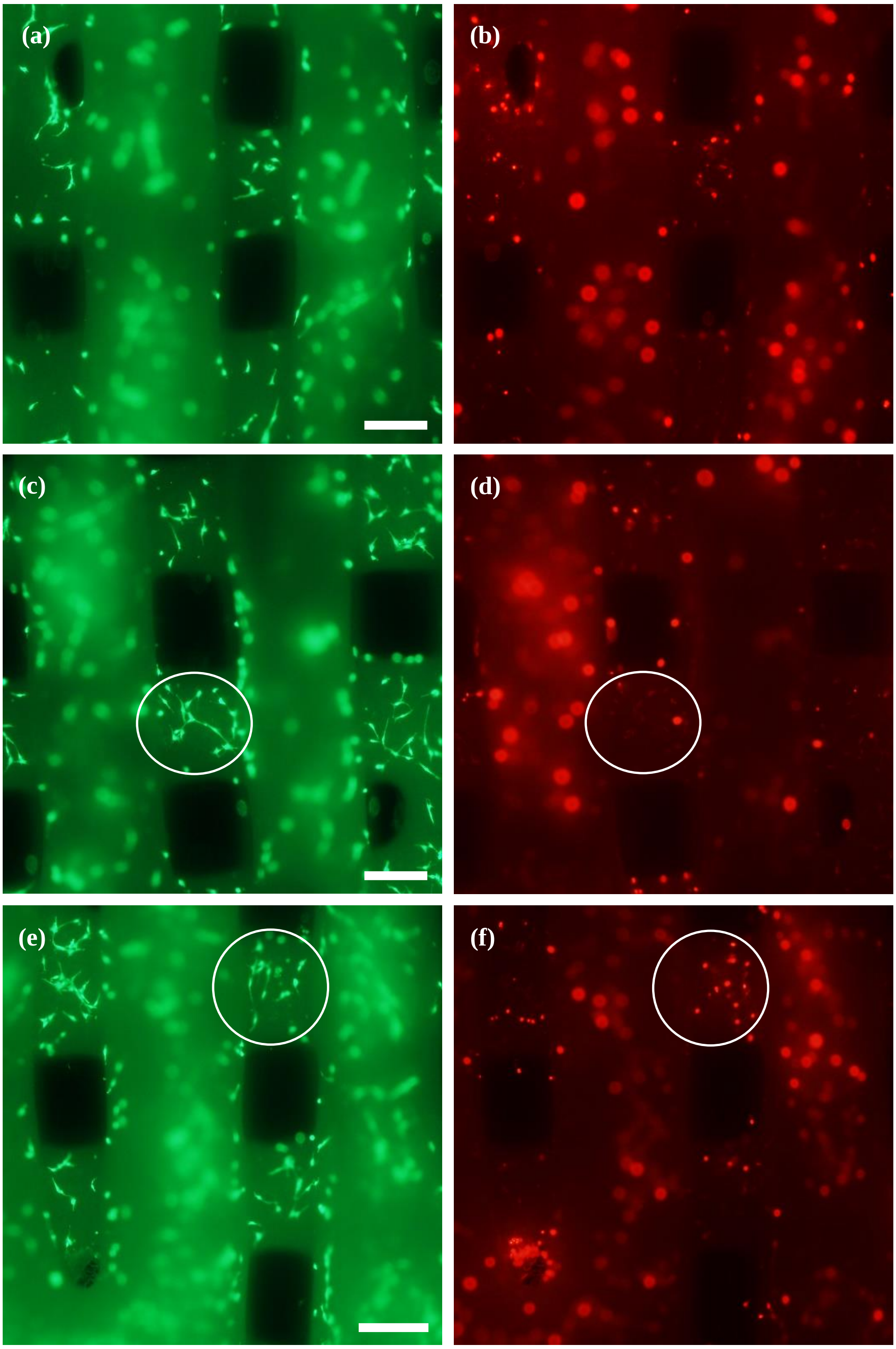

Figure 7.6 Survival status of MC3T3-E1s (day 3) by fluorescence: (a), (b) HA-P; (c), (d) HA-µG-25; (e), (f) HA-nG-25; living cells (green) by calcein-AM, and dead cells (red) by PI; scale bar = 200 µm

The dead cells in Figure 7.6 (b), (d) and (f) were analysed as well. **1) Quantity of dead cells**. The mortality of both HA-P and HA-nG-25 scaffolds was higher than HA-µG-25, which is a critical point that can explain the result of cytotoxicity described before, and this will be put in detail later. **2) Distribution of dead cells**. After careful comparison and analysis, it was found that the isolated cells were more likely to be dead or necrotic (circled in Figure 7.6 (e) and (f)); while those with large population (in cluster) and close intercellular junctions could survive for longer time (circled in Figure 7.6 (c) and (d)). A possible explanation is that these interconnected cells were able to transduce and response to bio-signals through tentacles quickly, which help to preserve vitality; on the other hand, the clustered cells could also exchange nutrients with culture media to ensure survival rate. The result of survival rate fully confirms the promotive influence of hierarchical pore structures in HA-G scaffolds on vitality.

Figure 7.7 shows the survival status of MC3T3-E1s at day 5, which is nothing substantially different with Figure 7.6 in view of survival rate and cell morphologies, except the number of (live/dead) cells as they went through longer incubation. So the further analysis about Figure 7.7 was similar to Figure 7.6, which was also omitted. The reason for displaying these figures at day 3 and 5 was to avoid occasionality occurred in experiments.

Now the key is to find out what makes HA-μG-25 advantageous over HA-nG-25 and normal scaffolds in survival rate. It may be the result of a vast number of micron-sized pores on HA-μG-25 scaffolds, which can provide more available living space for cells, and thus the cells were more likely to survive [44]. In addition, these micropores can store certain amount of nutrients essential to cells or collect metabolic waste from cells [216]. Given that the micropores were interconnected to each other, cells could not only get adequate supply of nutrition [217], the in-rod pores also helped expel metabolic waste in time; therefore, cells were able to maintain their vitality for a long period [13]. According to this explanation, the puzzling results in Figure 7.2 and Figure 7.5 (that is, the cell vitality of HA-nG-25 was significantly higher than HA-μG-25, but little difference was found in proliferation; however, the network of F-actins was the most developed in HA-μG-25 regardless of less active vitality than HA-nG-25) can be understood from the angle of mortality. HA-P was not considered because they were completely inferior to HA-G scaffolds in terms of biological activities, such as adhesion,

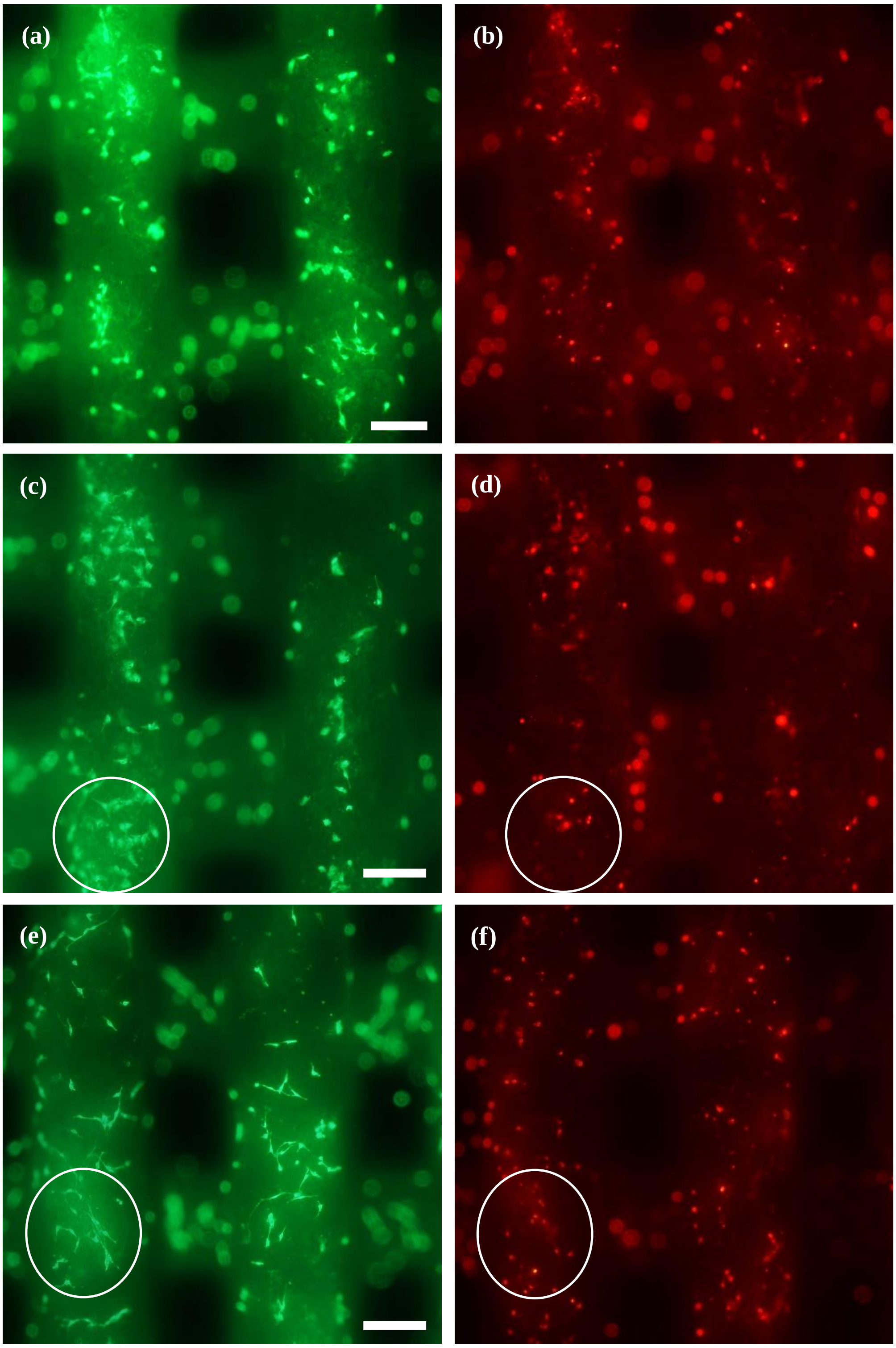

Figure 7.7 Survival status of MC3T3-E1s (day 5) by fluorescence: (a), (b) HA-P; (c), (d) HA-µG-25; (e), (f) HA-nG-25; living cells (green) by calcein-AM, and dead cells (red) by PI; scale bar = 200 µm

junction and viability *etc*. Specifically, although HA-nG-25 enabled cells to possess higher vitality and more freedoms to spread over scaffolds (owing to larger SSA), these cells were less capable of surviving due to low viability. Then it is very likely that many already adhered cells may lose intercellular connections if the dead cells happens to be the hinges of junctions, as circularly marked in Figure 7.6(f) and Figure 7.7(f). Accordingly, these cells would become isolated once again, which in turn increased the possibility of mortality. Obviously, it falls into a vicious circle. Interestingly, the growth rate of HA-nG-25 could manage to remain higher than HA-μG-25 in spite of lower viability, indicating that the cells on HA-nG-25 were extremely active, possibly stimulated by nanopores. On the other side, despite that HA-μG-25 exerted poorer performance in vitality and spread, the excellent viability could improve the survival time of cells served as junction hubs, hence making the intercellular connections more stable and lasting. In this case, it would be easier for other cells to adhere on scaffolds and establish communication with these "hinge" cells, resulting in well-developed network of F-actins, as marked in Figure 7.6(d) and Figure 7.7(d). The maturely developed F-actins improved the living environment of cells, and eventually enhanced the survival ability of cells in return, which entered a virtuous circle. As a result, it is reasonable for HA-μG-25 being able to maintain a same level in proliferation with HA-nG-25.

In order for quantitative analysis, the statistical estimation of survival status of cells was necessary. However, considering the difficulty to recognize individual cells through their indistinct morphologies under a microscope (Figure 7.6 and Figure 7.7), especially when they were in cluster, coupled with inevitable unclarity caused by the problem of focus length, it is impossible to count the exact number of live/dead cells on scaffolds. Therefore, only the cells (either live or dead) on focused layer were counted for analysis. The number of green highlights was substituted for cell count of a cluster, because the colour of nucleus is often brighter than tentacles. In fact, the error of statistics in this way was fairly great. Fortunately, it is fine for mere comparison on the condition of similar error probability. The final result of survival rate is shown in Figure 7.8. It is clear that there was no significant difference (≤ 5%, taking notable statistical error into account) in the survival rate of each group at day 3 and 5. Undoubtedly, the survival status of cells on HA-μG-25 scaffolds was considerably better than HA-P and HA-nG-25, which had small difference with each other. In view of that the different features in hierarchical porosity, it can be seen that the micropores in micron scale indeed played a vital role in sustaining the viability of cells during culturing process. Furthermore, the micropores in HA-μG-25 are usually surrounded by numerous nanopores, which are favourable to motivate the vitality and activity of adhered cells, and consequently, to remarkably reduce the mortality of cells.

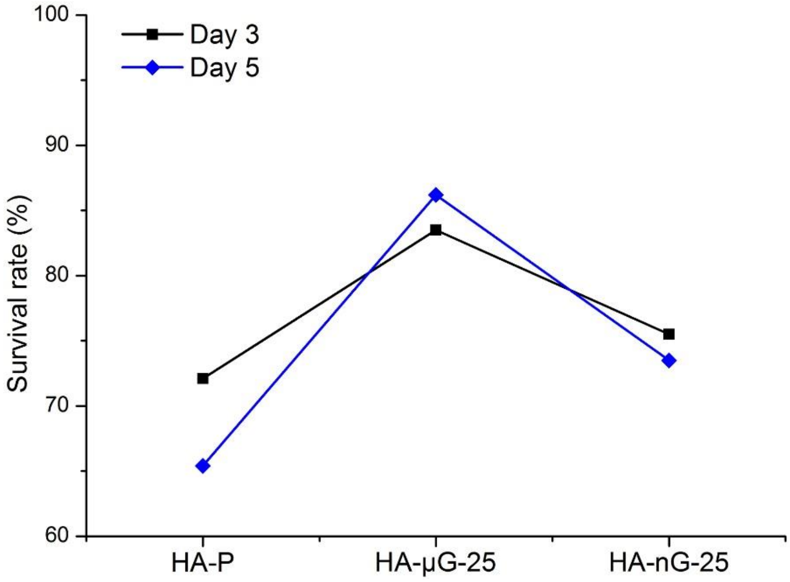

Figure 7.8 Statistical estimation of survival rate

7.4.5 Proliferation and Differentiation

To evaluate the effect of microporosity features on proliferation and differentiation, the concentration of DNA (indicator of cell numbers) and the ratio of protein versus DNA (which reflects cell size) was measured. According to Figure 7.9(a), the proliferation was promoted substantially in HA-G scaffolds, and the performance in HA-μG-25 group was improved the most (day 4). It is interesting that the number of cells during differentiation period in normal scaffolds was higher than HA-G at day 7 (Figure 7.9(a)); while only a slight difference was observed in protein/DNA ratio after total culture in all scaffolds (day

7, Figure 7.9(b)). It was also found that the difference of cell number (concentration of DNA) showed opposite trend to cell size (protein/DNA ratio), both at day 4 and 7.

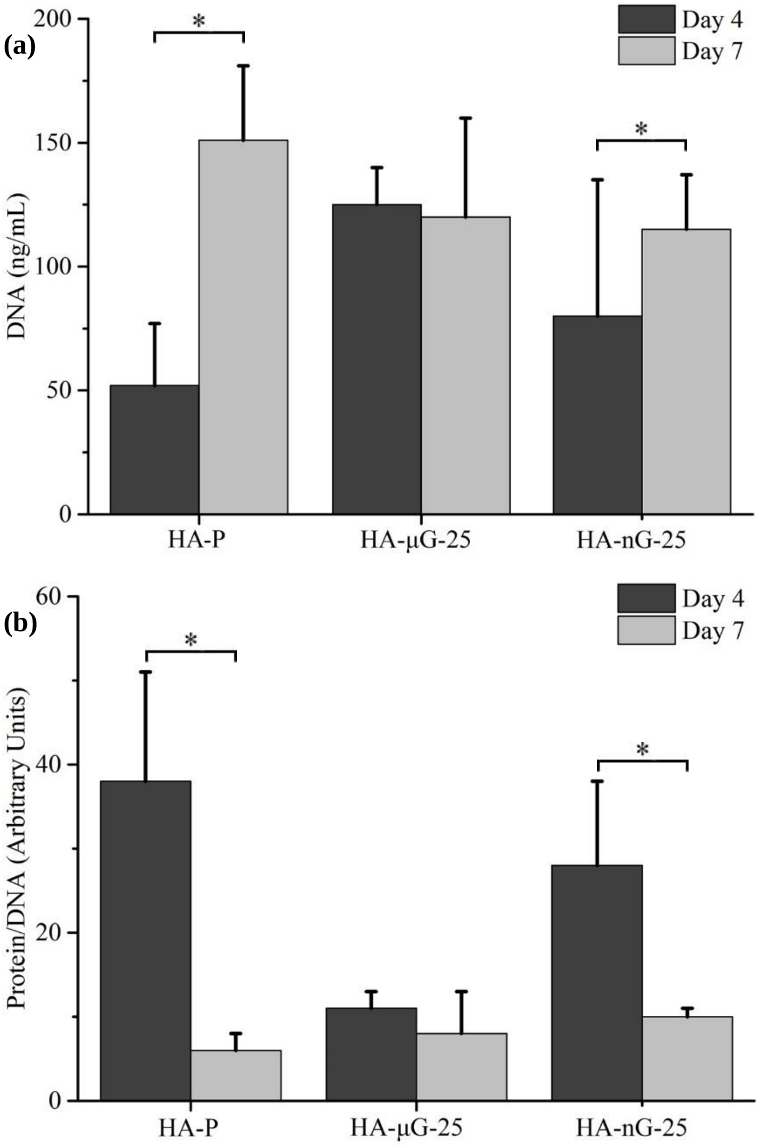

Figure 7.9 Quantitative analysis of proliferation (day 4) and differentiation (day 7) by C2C12s: (a) concentration of DNA ($p \leq 0.05$, n = 3), (b) ratio of protein versus DNA ($p \leq 0.01$, n = 3)

This result can be explained from the point of view of space occupancy: given that the scaffolds were fully occupied with live cells, the number of cells with smaller sizes would be reasonably more than larger cells. Furthermore, the results also reveal that HA-G scaffolds would not cause cytotoxic effects during cell culture, providing another evidence for successful removal of graphite after sintering. The reader may be confused about the necessity of proliferation in this section, as the cytotoxicity analysis mentioned before was also based on proliferation. Firstly, the cell type and evaluation method was different this time, *i.e.* C2C12s through extraction of DNA or protein, to show that the proliferation result was not occasional; while it was MC3T3-E1s by CCK-8 in previous test. In addition, the evaluation of proliferation was combined with differentiation of C2C12s, which was useful to analyse and understand the formation of myotubes more directly and accurately.

The ability to promote the formation of skeletal muscle during BTE was evaluated to analyse the differentiation process of myoblasts through fluorescence, as shown in Figure 7.10, which illustrates the differentiation of C2C12s into multinucleated myotubes at day 7. The number of cells (DNA in blue) in all scaffolds was almost the same, fully in agreement with the DNA concentration in Figure 7.9(a) (day 7). Evidently, the formation of myotubes was definite in all scaffolds, owing to good biocompatibility of HA. However, the myotubes in HA-nG-25 and normal HA scaffold were still under the formative period, yet the formation stage in HA-P was even earlier than nano graphite treated sample; while the formation of myotubes in HA-μG-25 was much maturer to be identified. It means that μG treated scaffolds exerted better performance in promoting the differentiation of myoblasts into myotubes, compared to HA-nG-25 scaffolds. A possible reason is that apart from more evident hierarchical pore structures, the distribution of micropores in HA-μG-25 scaffolds (Table 6.6 and Table 6.7) was closer to natural bone tissues. In addition, the micron-sized pores (30 - 50 μm) could allow extra space for ingrowth of cells, which are usually about 20 μm in diameter [218]. The BET results in Figure 6.11 also tell that there was considerable amount of nanoporosity in HA-μG-25 scaffolds, which contributed to improved osteoinductivity and bioactivity as well [42]. Moreover, due to large aggregation of cells in HA-μG-25, the cellular tentacles were highly interconnected, forming well-developed fibrous network structures, which greatly improved the interaction of cells and transmission efficiency of biological signals [226]. As a consequence, the cells could rapidly response to differentiation process induced by insulin. Nevertheless, the additional in-rod porosity of HA-nG-25 was mainly composed

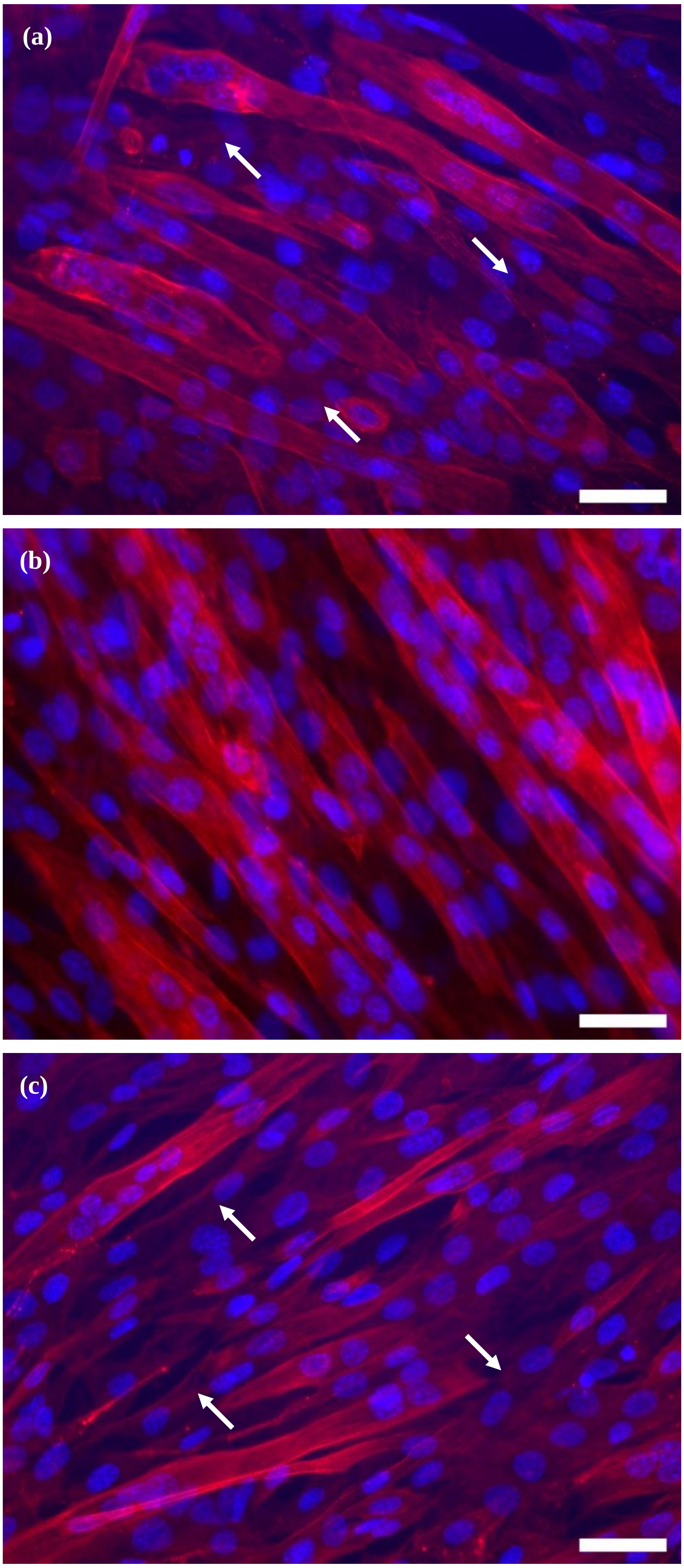

Figure 7.10 Immucytochemical images displaying multinucleated myotubes differentiated from C2C12s (day 7): (a) HA-P, (b) HA-µG-25, (c) HA-nG-25; F-actin (red) by TRITC-phalloidin, and DNA (blue) by DAPI; scale bar = 20 µm

of nanopores, so the interaction and communication of cells was weaker than HA-µG-25. Therefore, the differentiation ability of HA-nG-25 could not rival that of HA-µG-25, but still significantly surpassed HA-P.

The results in Figure 7.9 can also be explained by further investigation into Figure 7.4 and Figure 7.10. Due to lack of cellular interactions, the myoblasts tended to grow up instead of increasing cell divisions to make preparation for differentiation [228]. So the cell size of normal scaffolds was the largest, thus the least number of cells. On the contrary, the scaffolds treated with µG had more advantages in interactions, transfer of biological signals and additional space for proliferation. As mentioned in ***Section 7.4.4***, the micropores in HA-µG-25 scaffolds may form valid channels for the conduction of nutrition and store certain amount of nutrition inside the rods [216, 217], which improved the survival rate of cells. For another, the decrease of cell size from growth media to differentiation media was getting smaller (normal > nG > µG), and it was almost the same level in HA-µG-25 group. In other words, the cells in µG treated group were the most prepared for differentiation, because the cell number and size was extremely close during both periods. The formation of myotubes in Figure 7.10 also confirmed this. Therefore, although cultured in differentiation media, the myoblasts in control group had to make more preparation for differentiation, *e.g.* cell division, which increases the number of cells dramatically with sharp decrease in cell size. As a result, the process of myoblasts differentiating into myotubes was “delayed”. In light of the porosity features and performance in proliferation and differentiation, HA-nG-25 scaffolds are between HA-P and HA-µG-25, the discussion can also apply to this group.

In full consideration of the above biological and physicochemical properties, HA-µG-25 scaffolds were the most bioactive in terms of intercellular junctions, survival rate and differentiation, possibly because hierarchical pore structures with wide range of pore sizes is closer to natural bone tissues. Therefore, micron graphite are more suitable to serve as pore former in this method to fabricate highly biomimetic scaffolds for BTE. It is highly anticipated that HA-μG scaffolds could have great potential in clinical applications.

7.5 Summary

In this chapter, the HA-P and HA-G scaffolds underwent a series of systematic biological evaluations. The cytotoxicity analysis showed that the possibly residual graphite would not cause negative effects on the natural bioactivity of cells; in contrast, due to increased SSA and enhanced hydrophilicity, HA-G scaffolds could significantly promote cellular proliferation, which laid a solid foundation for the process of cellular adhesion and free spread. As a result, HA-μG scaffolds were able to provide more living space for cells and to motivate the vitality and activity of adhered cells, which consequently reduces mortality. In addition, the cells on HA-μG-25 were almost completely interconnected by cellular tentacles, and thus the formation of F-actin network were the most developed. Most of all, the developed fibrous network could enhance intercellular junctions and transduction of bio-signals in return, so the myoblasts on μG treated scaffolds could immediately respond to differentiation accordingly. Considering the biological and physicochemical properties, HA-μG-25 scaffolds are the most bioactive in terms of intercellular junctions, survival rate and differentiation, possibly because of the features of microporosity are similar to natural bone tissues.

Chapter 8. Conclusions and Future Work

8.1 Conclusions

Experimental investigations and evaluations performed in this study have realised the fabrication of biomimetic hydroxyapatite scaffolds with improved physicochemical and biological properties for BTE, through a novel method, *i.e.* combination of MAM extrusion and gas foaming technique. The following conclusions can be drawn from these studies:

8.1.1 Extrusion Process of MAM System

The fabrication of HA scaffolds is mainly determined by the extrusion process of MAM system. Therefore, the extrusion process of HA slurry (usually high viscosity) was analysed, both mathematically and experimentally. The summary of the results is as follows:

(1) A mathematical model of slurry flow in MAM nozzle was established to analyse the process of extrusion and deposition. It was found that the flow rate of slurry was closely related to nozzle length, viscosity of slurry and extrusion force, but mostly influenced by nozzle diameter.

(2) The effects of important parameters, such as nozzle diameter, extrusion speed, travel speed and discharge distance, on the formation of extruded filaments were studied. Besides, a perfect match of extrusion and travel speed was required to obtain continuous and stable extrusion process.

(3) The scaffolds made by MAM have noticeable interconnected porous structures, ranging from 50 to 580 μm, which are very favourable for BTE. In addition, the bulk porosity can be finely controlled by adjusting fabrication parameters and model geometry.

(4) MAM system shows inspiring stability, repeatability and convenience during fabrication of bone scaffolds. The versatility provided by this technique is potential to

allow desired choices in porosity and pore size that can mimic the complex structures and features of bone tissue so as to optimise osteogenesis.

8.1.2 Influence of Sintering Temperature

Considering that sintering temperature has vital impact on microstructures, physicochemical properties and biological activity, the influence of sintering temperature on scaffolds was systematically investigated, which were sintered by microwave sintering method at different temperatures, *i.e.* 1000 ℃, 1100 ℃, 1200 ℃, 1300 ℃ and 1400 ℃. The main conclusions drawn from this study are:

(1) More shrinkage was found at higher temperature during sintering process, as well as smaller pore size, larger grain, narrower rod gaps and less SSA, which resulted in the variety of physical and chemical properties.

(2) Although the mechanical properties of scaffolds were significantly improved with highly densified structure, it would greatly reduce hydrophilicity and SSA, which was detrimental to the deposition of calcium and release of growth factors in BTE. Moreover, hydroxyapatite may undergo dehydroxylation at high temperature during sintering, possibly hindering the formation of new bones when applied to BTE.

(3) Although increasing the sintering temperature of HA scaffolds is the most simple and effective method to enhance mechanical properties, high temperature would usually cause negative effects on the biological properties of scaffolds. Therefore, low temperature for sintering is preferred under the premise that mechanical strength is sufficient for BTE. In addition, other strategies for the purpose of better mechanical properties should also take biological performance into account in priority.

8.1.3 Fabrication of Hierarchically Porous Scaffolds

Inspired by literature review, highly porous scaffolds with hierarchical structures were constructed through the combination of MAM deposition and chemical foaming technology. In order to make this method stable and controllable, many researches were performed and the significant findings are listed as follows:

(1) Due to uniform distribution in particle size, graphite was a good choice as the porogen for this method. The optimisation of sintering profile for HA-G scaffolds was effective to retain the in-rod micropores as much as possible, on the condition of complete oxidisation of graphite and auxiliary reagents, and it was confirmed by XRD and EDX.

(2) The wall roughness of HA-G after sintering was significantly higher than HA-P, which was in direct proportion to the actual amount of graphite. Both HA-P and HA-G scaffolds were able to form evenly distributed nanopores, but HA-P could not produce micropores as HA-G did.

(3) There was no significant difference in the shrinkage of all scaffolds caused by drying, indicating that the addition of graphite would not affect their physical properties much. However, it was obvious in sintering shrinkage, which was increased as more graphite was used for porogen.

(4) The novel method shows great potential to make excellent scaffolds for BTE, with hierarchical pore structures (0.3 - 500 μm) and highly controllable bulk porosity (≥ 70%, ± 1%). Moreover, the in-rod porosity can be finely adjusted by changing the content of graphite as well.

8.1.4 Physicochemical Properties of Improved Scaffolds

To confirm the advantages of hierarchically porous structures, the most concerned physicochemical properties of improved scaffolds were carefully examined, including micro-morphologies, distribution of pore size and porosity, crystallinity after sintering, biodegradability and hydrophilicity. Note that in order for simplicity, “>” (or “≥”) is used to express the superiority among all scaffolds (it is the same in ***Section 8.1.5***). The following results are especially worthy of mention:

(1) In view of mechanical properties and porosities, 25 vol.% of graphite is the optimal

content for pore former. The superiority in terms of compressive strength was obviously HA-P > HA-G.

(2) Both micron- and nano-graphite can form additional porosities on scaffolds with desired micropores. The BET results confirm that the optimised sintering profile indeed contributed to retaining microporous porosity. Considering the distribution of pore size, HA-μG-25 might be the most suitable scaffolds for BTE (*i.e.* microporous distribution: HA-μG-25 ≥ HA-nG-25 > HA-P).

(3) The crystallinity of HA scaffolds after sintering at high temperature was very high. Moreover, over-sintering may occur in HA-G scaffolds due to locally elevated temperature during oxidation of graphite, resulting in partial decomposition of HA into non-stoichiometric phase (for crystallinity, HA-P > HA-nG-25 > HA-μG-25). In addition, the degradation rate of HA-G scaffolds in AC-SBF was significantly higher than HA-P, mainly because of larger SSA, additional porosity, and relatively lower crystallinity of hydroxyapatite phase. To be more specific, the potential of bio-degradability *in vivo* would be: HA-nG-25 > HA-μG-25 > HA-P. On the other hand, the difference between HA-nG-25 and HA-μG-25 in decomposition also suggests that SSA has much greater influence on degradation than crystallinity.

(4) HA-G scaffolds have better hydrophilicity than HA-P, that is, smaller contact angle with water and stronger ability of water absorption (HA-μG-25 > HA-nG-25 > HA-P). It is highly expected that HA-G could have better biocompatibility during biological evaluation.

8.1.5 Biological Performance of Improved Scaffolds

As a substitute for implantation, scaffolds for BTE must exert certain biological activities, mainly in terms of promoting adhesion, proliferation and differentiation, so as to achieve the purpose of bone regeneration or repair. As a result, a variety of biological evaluations were performed on HA-P and HA-G scaffolds to verify their bioactivity. The main points are summarised below:

(1) It was confirmed that any toxic effects from residual graphite or HA-G scaffolds did not inhibit the natural bioactivity of cells; on the contrary, due to increased SSA and enhanced hydrophilicity, the cellular proliferation could be significantly promoted graphite treated scaffolds (proliferation: HA-nG-25 ≥ HA-μG-25 > HA-P).

(2) The additional in-rod micropores in HA-G scaffolds lay a solid foundation for the process of cellular adhesion and free spread, showing high potential in biological activity (adhesion: HA-nG-25 > HA-μG-25 > HA-P).

(3) The cells on HA-μG-25 scaffolds were almost completely interconnected by tentacles, and thus the formation of F-actin network were the most developed; while due to relatively isolated status, the cellular connections were built primarily by volume contact in HA-P (interactions: HA-μG-25 > HA-nG-25 > HA-P).

(4) It was found that aggregation of cells are beneficial to survival rate. Owing to sufficient micropores and vast number of nanopores, HA-μG-25 scaffolds were able to provide more living space for cells and to motivate the vitality and activity of adhered cells, which consequently resulted in notably reduced mortality (survival: HA-μG-25 > HA-nG-25 > HA-P).

(5) Benefited from developed network of F-actins, which contributes to intercellular junctions and transduction of bio-signals, the myoblasts on the HA-μG-25 scaffold could immediately respond to the differentiation stimulation of insulin; however, the formation of myotubes in HA-nG-25 and HA-P scaffolds were still in process even induced by insulin for 3 days (differentiation: HA-μG-25 > HA-nG-25 > HA-P).

(6) Considering the physicochemical properties and biological activity, micron graphite is more suitable for the porogen, possibly because of the multi-scaled pore structures with wide range of pore sizes, which are similar to natural bone tissues.

8.2 Recommendations for Future Work

Although much has been accomplished in terms of highly biomimetic scaffolds for BTE, there remains further work to push this topic forward. As BTE is in a state of rapid advance, along with the unceasing development of various disciplines, including mechanics, materials, physics, chemistry, biology and medicine. The following areas are worthy of intensive research:

8.2.1 Exploration of Better Porogen

Due to lamellar structure and brittleness, graphite is easy to break up during preparation of slurry, making it difficult to accurately control the final pore structures, such as pore size and distribution. Further attempt and exploration in terms of porogen are required.

Currently, PMMA microspheres (30 - 60 μm) may be a potential choice for new porogen. Considering the hierarchically porous structure, PMMA microspheres are introduced to form the porosity in micron scale, and more auxiliary reagents will be added in HA slurry to produce considerable amount of nanoporosity. This work will soon be started.

8.2.2 Biological Evaluation of Hierarchically Porous Scaffolds *in vivo*

There is a long way for HA-G scaffolds to be applied in clinical verifications, because *in-vivo* biological evaluation was not performed yet. So whether the scaffolds could have satisfactory repair effect of bone defects as expected is still unknown. The further study will be culturing scaffolds in vivo (using mice or rabbits) to confirm the bioactivity of improved scaffolds.

8.2.3 Cell Printing to Enhance Bioactivity

With the rapid development of 3D printing technology, cell printing is becoming possible and feasible, thus bio-imitation from the aspect of structures is not enough. In order to fabricate more biomimetic scaffolds, extrusion deposition with cell printing has been put on the agenda. Specifically, pneumatics assisted micro-syringe (PAM) system

[230] was developed on the basis of MAM system [53], which is called PAM-MAM system. Considering that MAM is advantageous to process materials with wide range of viscosity, especially high viscosity, PAM is designed right for biomaterials of low viscosity, which can finely control the dispensing of droplets by air force at high pressure and short delay. The details of current progress can be found in the ***Appendix*** chapter.

8.2.3.1 Potential applications of biomimetic scaffolds

According to the demands of clinical application, we intend to make biomimetic scaffolds with multi-biomaterials (*e.g.* collagen) for repair of the cranium defect (rabbit) by PAM-MAM. Figure 8.1 shows a sample of new scaffolds, which are composed of biomaterials (jetting by PAM) and extracellular matrix (extrusion with MAM), using sodium alginate (SA) solution (0.5 wt.% for PAM, and 10.0 wt.% for MAM) for solidification agent. The sample has 6 layers in total: the 1st/6th layer in transparency stands for antimicrobial materials; the 2nd/5th layer in green with porous structures are designed for filling of collagen; and the middle two layers (3rd/4th) with dual red rods consisting of droplets represent biological factors.

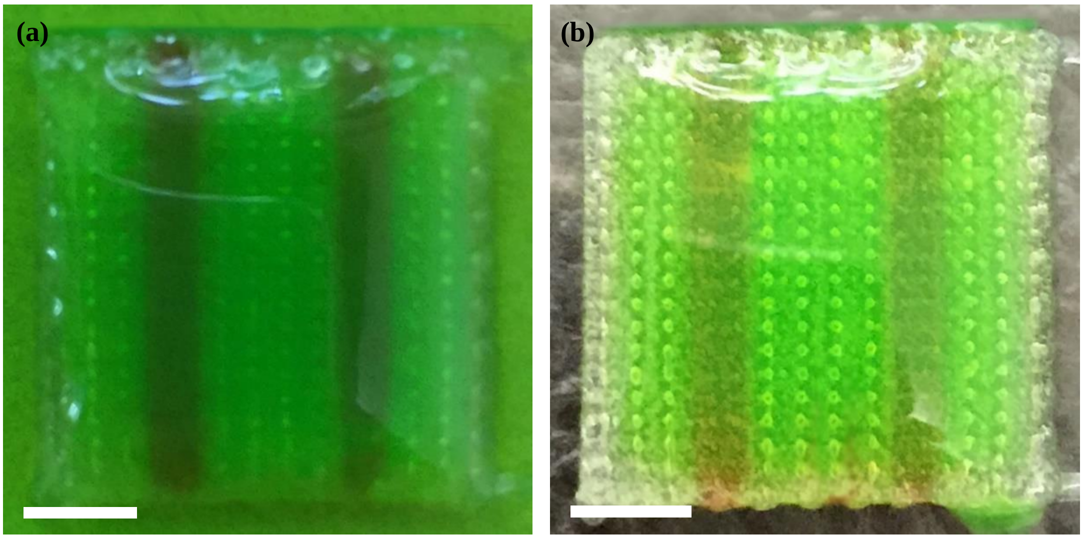

Figure 8.1 3D biomimetic scaffolds for repair of rabbit cranium defects, (a) before and (b) 12h after solidification; scale bar = 5 mm

It is worth mentioning that the desired size of droplets for this scaffold should be about 500μm. After quick solidification with $CaCl_2$ solution, the droplets were well supported by the porous scaffold due to good mechanical strength, shown in Figure 8.1(b). Therefore, the further research in the near future is to perform the *in-vivo* biological evaluations of the newly designed scaffolds. It is highly expected that PAM-MAM is competent to make 3D biomimetic scaffolds in terms of materials and complex structures.

8.2.3.2 Improvement for PAM-MAM system

Recently, much attempt was conducted to fabricate some samples with desired size of various droplets, but it was difficult to characterise the droplets, shown in Figure 8.2. Initially, the purpose was to fabricate a hexagon scaffold with circular dot matrixes of droplets (about 500 μm in dimension, and 1.5 mm for the gap of droplets). Unfortunately, the droplets failed to keep their original shape because of instant spread over the scaffold when covered by upper layers. As a result, regardless of wide gap (normally it was 500 μm or so), the droplets were hardly identified, although the professors in *Tongji Medical School of Huazhong University of Science and Technology* suggested that this problem would not result in significant influence on repair effect, as long as the droplets could be supported by the matrix material.

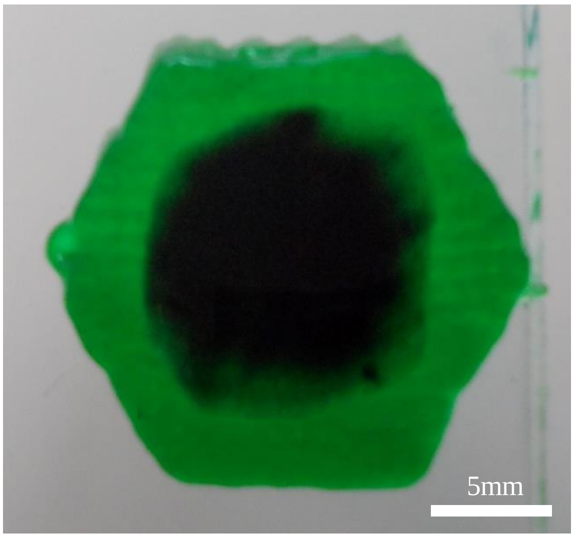

Figure 8.2 Morphologies of droplets in hexagon scaffold

Considering that the spread of droplets will occur during fabrication, pre-solidification process may offer a possible solution, which contributes to maintaining their shape. All in all, much work and research remain to be done to optimise the PAM-MAM system.

Appendix. Development of 3D Multi-nozzle System Highly Potential for 3D Bio-fabrication

A.1 Introduction

As a most promising field, additive manufacturing, especially its application in medical science (also known as 3D bio-printing [231, 232]), has aroused widespread attention [233-235]. For instance, 3D printing technique has been one of the most focused research approaches for regeneration or repair of bone defects [236]. In BTE, not only strength, porosity and bio-compatibility is required, highly biomimetic scaffolds could also carry growth factors [237] and even functional cells [238] to promote the process and effect of bone regenesis. As a result, multi-nozzle is a must in such printing system in order to support multi-materials. No wonder that the researches based on multi-nozzle systems are becoming increasingly active: hydrogel with three-tier structure for cartilage repair was successfully built using tri-nozzle system [239]; Chang *et al*. reported a dual-head system to fabricate the functionally graded coating with titanium oxide and hydroxyapatite [240]; Lee *et al*. achieved the preparation of elastic cartilage through 3D hybrid multi-nozzle system [135]. For bio-printing, biomaterials such as cell suspension with grow factors, collagen *etc*. (usually low viscosity) are certainly desired to make the constructs bioactive, which at the same time need matrix materials (high viscosity) with sufficient mechanical strength to support biomaterials. In other words, it seems not possible for above mentioned systems to fabricate such constructs, especially biomimetic bone scaffolds.

Currently, the most popular 3D printing technologies for biological application include FDM [119], SLS [120], inkjet printing [241], laser direct writing (LDW) [242], EDM [53], pneumatic valve dispenser [243], and so on. However, FDM and SLS require heating process at relatively high temperature, which does not apply to bioactive materials. Inkjet printing and LDW is famous for high precision, yet merely limited to low viscosity materials. Similarly, EDM cannot deal with some biomaterials like cells, and pneumatic dispenser seems helpless to build scaffolds with high strength for hard tissues such as bone and teeth. Therefore, to fabricate 3D complex scaffolds with multi-materials with these techniques is challengeable.

To achieve the mentioned purpose, *i.e.* fabricating 3D complex scaffolds with multi-materials, pneumatics assisted micro-syringe (PAM) system [230] was introduced on the basis of MAM system [53]. Since the MAM system was reported in details, this part will pay more attention to PAM system and the combination of them. Specifically, MAM is advantageous to process materials with wide range of viscosity, especially high viscosity; while PAM is right for biomaterials of low viscosity, which can finely control the dispensing of droplets by air force at high pressure and short delay.

A.2 PAM-MAM 3D Multi-nozzle System

Figure A.1 shows the actual image and schematic of PAM-MAM system.

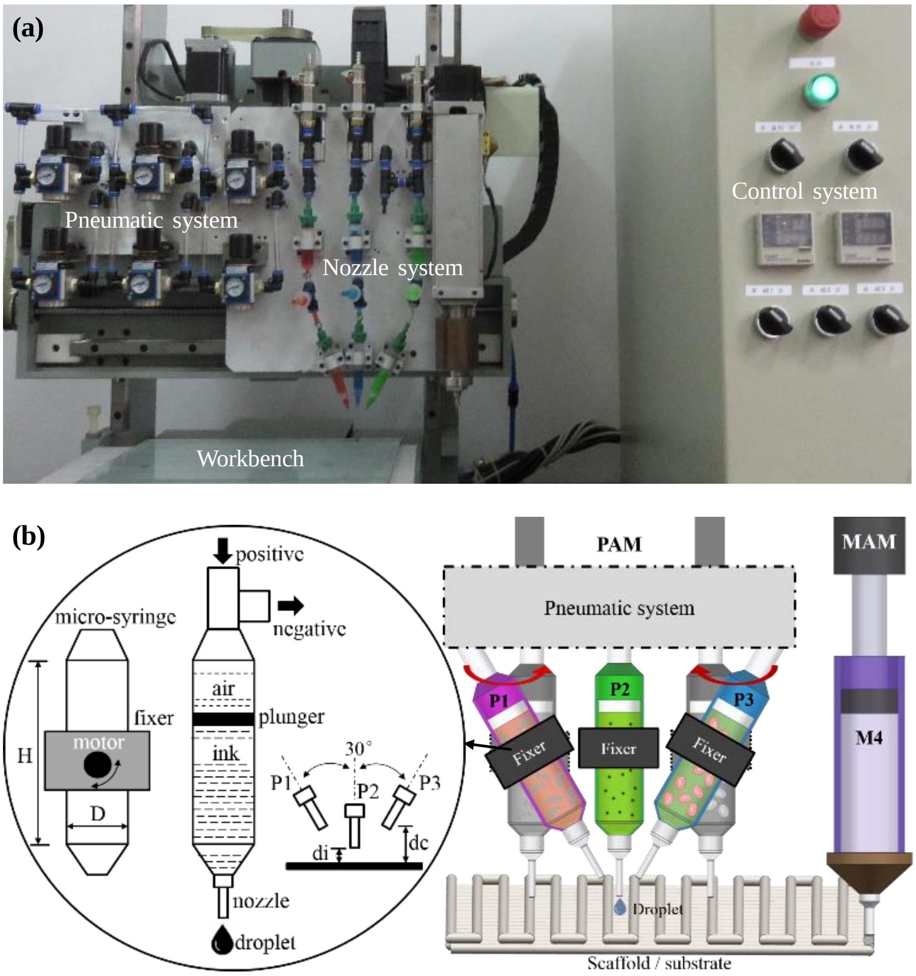

Figure A.1 Actual image (a) and schematic (b) of PAM-MAM 3D printing system

The pneumatic system provides the pneumatic source of positive pressure (for droplet formation) and negative pressure (to avoid overflow) with accurate regulation (±0.1 kPa). And PAM consists of three ink-jetting nozzles ($\mathbf{D_N}$ = 150 μm). For a single PAM, the plunger driven by air will force ink materials in micro-syringe to form droplets through a nozzle, also known as ejection. Besides, 2 of PAM nozzles (**P1** and **P3**) can be freely switched between independent mode (grey) and convergent mode (colourful) by motors, as shown in Figure A.1(b). In convergent mode, they can focus onto a point (**P1 + P2**, **P2 + P3**, or **P1 + P2 + P3**) without any interference to provide availability for multi-materials. Since it is difficult to promise synchronous formation of droplets in all nozzles, the focus point was practically set on the surface of scaffolds. Figure A.1(b) also shows the actual fabrication process; that is, the scaffold/support was initially deposited by MAM and followed by PAM jetting (DOD) during a layer. The main specification of MAM-PAM system is listed in Table A.1.

Table A.1 Specification of MAM-PAM system

MAM	Specification	PAM	Specification
MAM system	MAM-II, Fochif	PAM system	Self-developed
Positioning	X/Y: ±1 μm Z: ±5 μm	Air pressure [b]	PAP: 0 - 50 kPa PNP: 0 - 10 kPa
Precision	200 - 400 μm	Precision	≥ 300 μm
Working dimension	X/Y: 250 mm, Z: 150 mm	Micro-syringe [c]	H: 60 mm, D: 10 mm
Temperature [a]	20 - 28 ℃	Discharge distance [d]	di: 2.0 mm, dc: 7.4 mm
Delay	< 20ms	Delay	< 1.5ms

Note: [a] Temperature is controlled by air conditioner; [b] PAP/PNP -- positive/negative air pressure;
[c] H/D -- the size of PAM micro-syringe, shown in Figure A.1(b)
[d] di/dc -- discharge distance in independent / convergent mode (Figure A.1(b))

A.3 Materials and Parameters

A.3.1 Materials

Table A.2 shows the materials used in this part. Particularly, sodium alginate (SA) solution with different concentration was used to assess the performance of PAM. SA solution can be easily and quickly solidified after cross-linked reaction with $CaCl_2$ (Equation A.1) [244], which provides great convenience to keep the shape of droplets printed by PAM. In addition, the SA solutions, concentrated from 0.00 wt.% (only deionized water) to 1.50 wt.% with an increment of 0.25 wt.%, would be stained for the purpose of characterisation if necessary.

Table A.2 Materials for experiments

Material	**Specification**	**Manufacturer**	**Application**
HA	≥ 99.5%, ~ 60 nm	Emperor	Ψ
SA	MW 400, AP	Aladdin	Ψ, Ω
Deionised water	2nd distillation	Self-made	Ψ, Ω
Ammonia water	pH = ~10	Sinopharm	Ψ
Calcium chloride ($CaCl_2$)	96%, AP	Sinopharm	Solidification of SA (Ψ, Ω)
Methyl green / Methyl red / Methylene blue	≥ 98%, AP	ZKX	Stain for SA (Ω)
Teflon	DY-18/-19	Doyo Paint	Hydrophobic treatment

Note: "Ψ" -- for preparation of HA-SA composite scaffolds [142], and "Ω"" -- for PAM test solution. MW -- molecular weight.

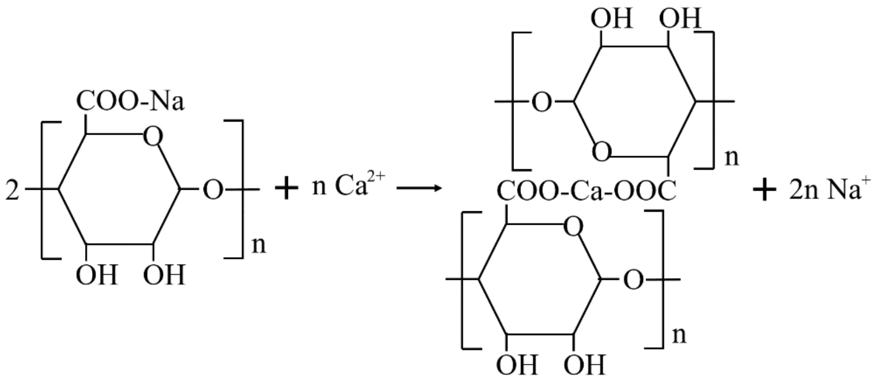

(Equation A.1)

A.3.2 Control Parameters

In addition to the influence of air pressure [245], the formation of droplet is also closely related to the viscosity, density and surface tension of solution [246]. Therefore, the actual size of droplet during PAM ejection is hardly predictable as it is determined by numerous aerodynamics parameters [247]. Fortunately, according to our large amount of test, it was found that SA content, external air pressure and holding time of positive pressure mainly dominate the size of formed droplets. Given the properties of materials/solutions for PAM may vary, the adjustment of parameter sets, usually laborious and time-consuming, was a must to understand the available precision. To save time and energy, the viscosity of SA solutions was measured by a viscometer (Poiylab-RC-300P, Haake Technik GmbH), and stereomicroscope (XTL-340, Shanghai Changfang) was used to characterise the droplets.

A.4 Methodology

A.4.1 Setup of PAM System

Considering that "bio-ink" is generally low in viscosity, overflow is unavoidable during PAM printing due to gravity; on the other hand, the residual liquid (caused by surface tension) on the surface of nozzle tip will negatively affect the subsequent formation of droplets, resulting in inaccuracy in terms of size control. To solve this problem, a control set of positive and negative pressure was designed for the pneumatic system of PAM (Figure A.2) [248]. Where in Figure A.2, **A** -- reducing valve, **B** -- filter cartridge, **C** -- regulating valve (positive), **D** -- regulating valve (negative), **E** -- vacuum generator, **F** -- control valve, **G** -- plunger.

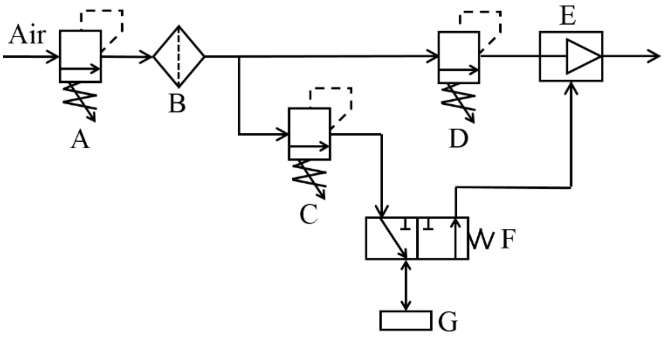

Figure A.2 Schematic of pneumatic control system

As shown in Figure A.3, the parallel array of three sub-systems forms the multi-nozzle PAM system, which is characterised by excellent extendibility. The symbols (*e.g.* "A", "E", "G" *etc.*) in Figure A.3 are the same to Figure A.2.

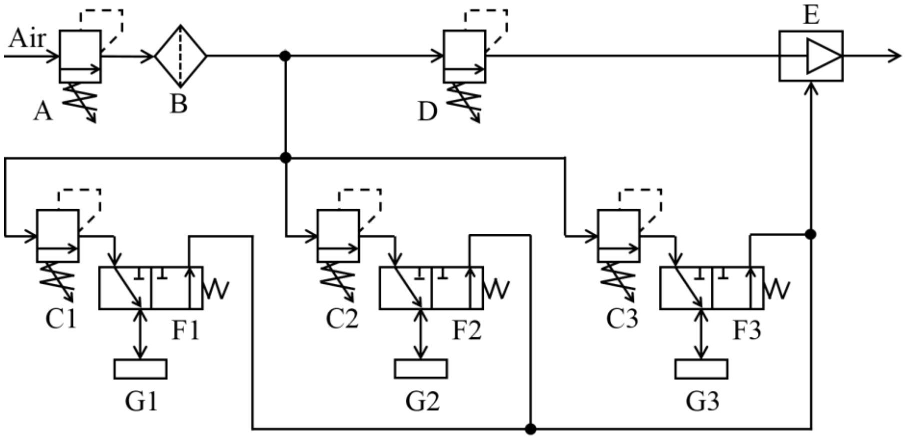

Figure A.3 Schematic of PAM system

A.4.2 Calibration of Multi-nozzles

In fact, the calibration process of MAM and PAM is quite simple. Figure A.4 shows the front view of nozzle system. The length "**L**" between **P2** and **M4** is the compensation distance. Note that the value of "**L**" is different for each PAM nozzle in independent mode, but is the same in convergent mode. Therefore, the position of **M4** is set as the reference. During calibration, **M4** will firstly move to the centre of workbench, and the position will be set as ***(0, 0)***. Then the motor in X direction will carefully move until **P2** reaches the centre, and the current X-position should be "**L**" (usually negative). With the assistance of "***Spider***", the print paths with calibration information can be automatically generated according to the set of "**L**". For instance, given that MAM has finished work and the current position of M4 was ***(x0, y0, z0)***, if a position, *e.g.* ***(x, y, z0)***, requires a droplet, the motion vector of X/Y motors will be **<*x* + *L* - *x0*, *y* - *y0*>**. Since the focus point is set on the surface of scaffolds, the motion distance in Z direction will be **Zc**, shown in Figure A.4, which is the distance between focus point and **M4** nozzle (usually constant).

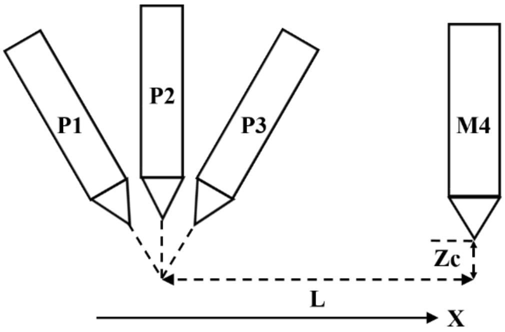

Figure A.4 Calibration of MAM / PAM nozzles

A.4.3 Planning Algorithm for Multi-models

The schematic implementation of path planning is shown in Figure A.5. Firstly, according to the data from CT scanning, RE or CAD software, the models of bone tissues, including bone matrix (“A”), distribution of cells (“B”) and biological factors (“C”), can be obtained. And these models can be assembled through “***Spider***” (***Section 3.2.2***) in order to get the absolution position of each model. Then the printing path for each model will be generated automatically with nozzle information (“A”-- MAM, “B”/“C” -- PAM). At last, the path files of all models will be classified and integrated according to the height of each layer, which forms the final path for printing.

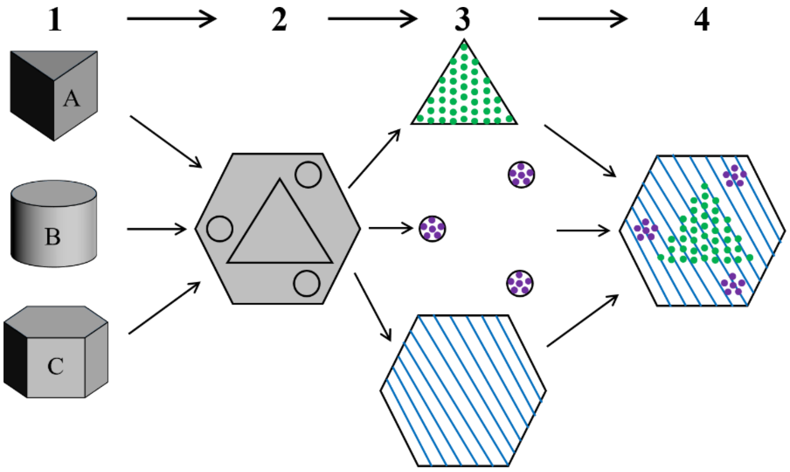

Figure A.5 Schematic of path planning

The format for final path is illustrated in Figure A.6. Where, **X/Y** -- target moving position, **P** -- PAM nozzle, **M** -- MAM nozzle, **ID** -- PAM nozzle number (*e.g.* 1 -- **P1**, 12 -- **P1+P2** *etc.*), **HT** - holding time of PAP, **AP** -- PAP, **T** -- compensation distance of MAM and PAM nozzle (*i.e.* “**L**” in Figure A.4), **SP** - extrusion forming speed.

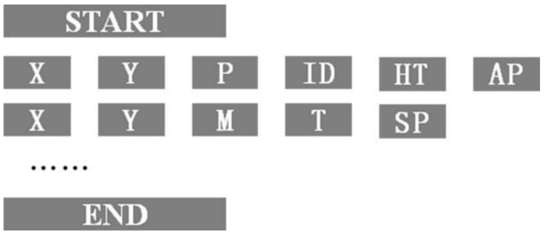

START

X Y P ID HT AP

X Y M T SP

……

END

Figure A.6 Format of final printing path

A.4.4 Preparation of HA-SA scaffolds

To prepare the HA-SA slurry, 1.0 g SA was fully dissolved in 30mL deionised water with 0.5 g ammonia water treatment first. Then 28.0 g HA powder gradually dispensed in SA solution with continuously stirring to get uniform HA-SA composite slurry [142]. HA-SA scaffolds were fabricated by MAM, followed by cross-linking reaction (Equation A.1) with 5% $CaCl_2$ solution for 24 h, instead of sintering at high temperature.

A.4.5 Estimation of Droplet Size

To stabilise the control of droplet, it is of great significance to estimate the actual size of droplets. Gravimetry is fine for average but not for uniformity, as the mass of a droplet is usually close to the minimum scale (1 mg) of electronic balance, which would cause errors. A useful method for estimation (Figure A.7) was introduced, assuming that the contact angle was equivalent for all droplets under the same condition, regardless of the difference in dimension [230].

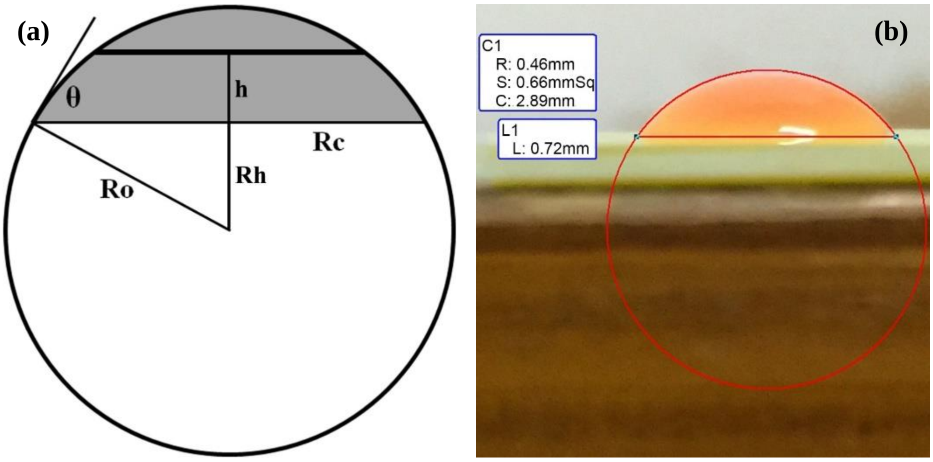

Figure A.7 Estimation method for actual size of droplet: (a) mathematical analysis, (b) optical image with measurement by TSView

In this case, the contact angle (θ) can be easily calculated by large droplets with the assistance of TSView. Note for abbreviations in Figure A.7(b): ***C1*** -- circle, ***R*** -- radius (= R_o), ***S*** -- area, ***C*** -- circumference, ***L1*** - line, ***L*** - length (= D_c). Then the actual volume can be estimated according to Equation A.2.

$$\begin{cases} V_d = \int_{R_h}^{R_o} \pi(R_o^2 - h^2) \cdot dh = \frac{\pi D_a^3}{6} \\ \sin\theta = \frac{R_c}{R_o}, \qquad R_h = \sqrt{R_o^2 - R_c^2} \end{cases}$$ (Equation A.2)

Where ***h*** is integral height and $\boldsymbol{R_h}$ is the radius at h. Then the relationship of $\boldsymbol{D_a}$ (actual diameter) and $\boldsymbol{D_c}$ (observation diameter) can be obtained through Equation A.3.

$$D_a = D_c \cdot \sqrt[3]{\frac{2 - 3\cos\theta + \cos^3\theta}{4\sin^3\theta}} = F_c \cdot D_c$$ (Equation A.3)

A.4.6 Fine Control of Droplet

From the point of view of control flow (Figure A.8), accurate control of droplet can hardly be achieved without high response rate. Apart from control centre, high response parts were used as the other elements in the flow. For instance, optoelectronic coupling relay (TLP250, Jixiang Electronics) can response almost immediately, and the actual responding time (~ 0.2ms in total, including operation and release time) was detected by an oscilloscope (MSOX-2004A, Agilent Technologies). Besides, high performance solenoid (33 series, Mac Valves) can respond to relay within 1ms (energize: 0.5ms, de-energize: 0.2ms). In addition, the air pressure was controllable at fine precision (±0.1kPa) by regulators (GR200-8, AirTac International Group), which greatly facilitates the adjustment of pressure.

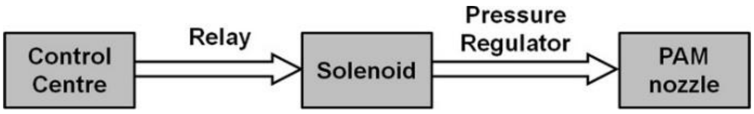

Figure A.8 Control flow of PAM system

Another strategy regarding PAM nozzles is hydrophobic treatment with commercially available Teflon solution, according to the process described in user manual (Figure A.9). The nozzle was initially coated with solution A (DY-18), and heated to 150 ℃ (holding for 10min) at a rate of 4 ℃/min, followed by cooling inside the furnace (KSL-1700, Kejing Materials Technology) to room temperature. The treatment of solution B (DY-19) is much similar: coating with B → heating to 380 ℃ at 4 ℃/min → holding for 10 min

→ cooling inside the furnace.

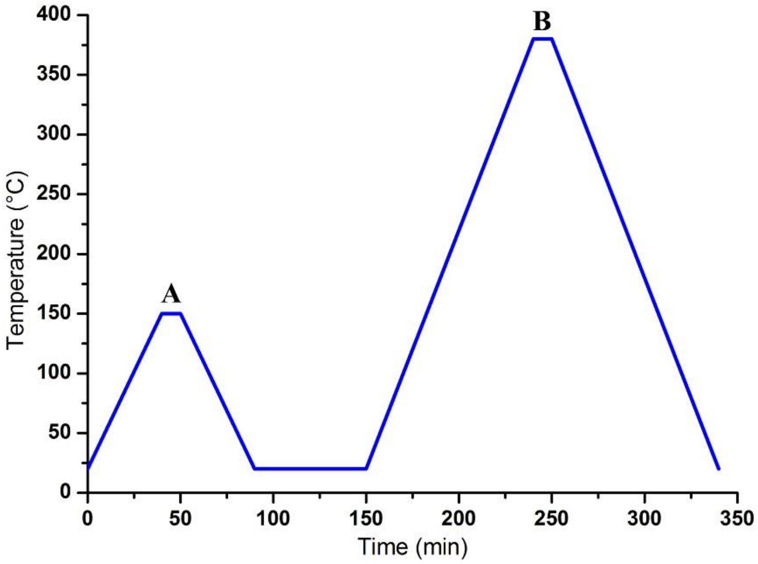

Figure A.9 Hydrophobic treatment of PAM nozzles with Teflon

A.4.7 Assessment of Stability

In order to guarantee the stability of PAM, tests based on each SA solution with certain sets of parameters (20 drops for each set) was studied. The standard for stability (measured in percentage, %) here refers to the ability of PAM to successfully form droplets without defects, like satellite drop(s), large accumulation of bubbles in a drop, *etc*., shown in Figure A.10.

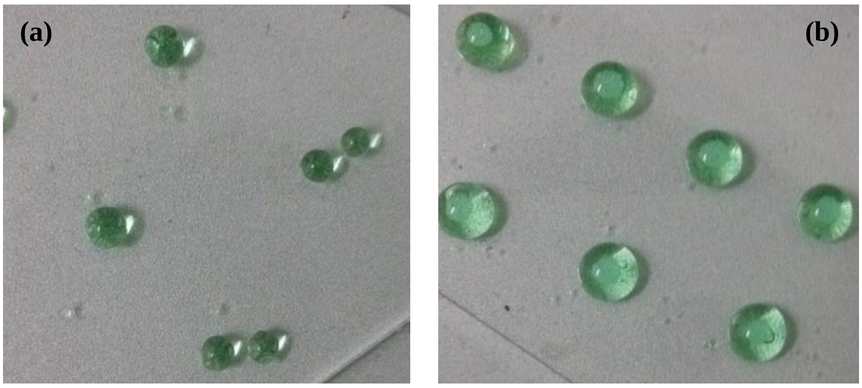

Figure A.10 Typical invalidity in droplet formation: (a) satellite drop(s), (b) accumulation of bubbles

Unfortunately, it is hardly likely to ensure 100% stability due to possible turbulence by air shock at high pressure, so 90% or more was taken as high stability. Note that droplet size was neglected in practical test. Specifically, once failure in formation of a droplet during PAM jetting was found, the stability would minus by 20% to mark such invalidity; similarly, it minus by 5% once there was any defect. Failure of formation is mainly because of insufficient air pressure, and the reason of satellite drop was explained by Klüsener [245]. As for bubble accumulation, it is the usually interactive result of PAP and HT of pressure. The interval of HT was set as 1.5 ms, and PAP was increased by 0.1 kPa.

A.4.8 Improvement of Efficiency

Due to inertia effect, the droplets will be out of control and even severely deformed after in touch with support/substrate at high travel speed, which may also result in inaccurate positioning. As a result, PAM nozzles would stop for a while (~ 300 ms) during jetting to make sure the velocity in travel direction was almost zero, minimizing the impact of speed. However, it would be pretty time-consuming to build 3D constructs especially in large demand of biomaterials. So it is very important to improve the efficiency of PAM jetting. Provided that the droplets were finely controlled, an easy and efficient way was to decrease the travel times of nozzle. To be more detailed, if the current layer requires PAM jetting frequently, either in independent or convergent mode, larger drops with equivalent mass for less times instead of adjacent smaller ones would obviously work (diagrammed in Figure A.11). Accordingly, it had been realized with the design of command order (automatically generated, as shown in Figure A.6). It turned out that this strategy could save about 25% of total time overall during practical fabrication.

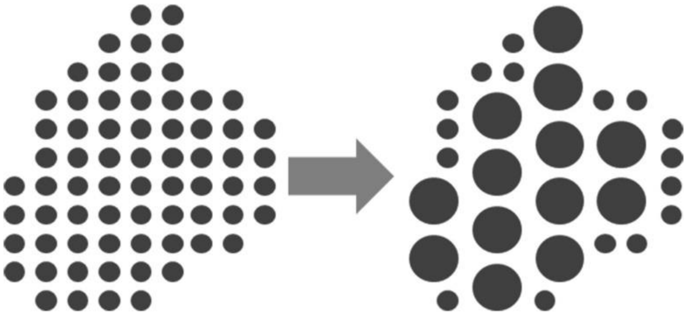

Figure A.11 Schematic of efficiency improvement

A.4.9 Evaluation of coordination and synchronization

The coordination and synchronization was evaluated through printing several carefully designed patterns. During the test of PAM jetting, the concentration of SA solution was 0.50 wt.% and the parameter set for highest precision was used. In addition, if multiple PAM nozzles were used for test, the SA solution for droplet formation was the same but stained with different colours (*i.e.* green, red or blue) to be visually distinguished. While for MAM, either HA-SA composite slurry or SA solution of high concentration (10.00 wt.%) was prepared for extrusion if necessary. The original designed patterns for evaluation of coordination and synchronization are exampled in Figure A.12. The dot matrix was designed to assess the accuracy of positioning in PAM-MAM system, and the "*HUST*" logo could evaluate the coordination of multiple PAM nozzles in both modes during working with MAM.

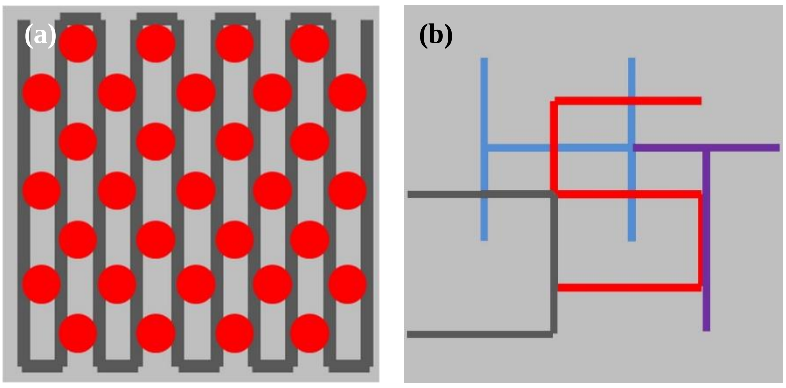

Figure A.12 Designed path for evaluation of coordination and synchronization: (a) dot matrix (line for M4 and dots for P2), (b) "*HUST*" logo ("H" for P1, "S" for P2, "T" for P1+P2, and "U" for M4)

A.5 Current Progress and Achievement

A.5.1 Path Planning

To confirm the implementation algorithm of path planning, the simply assembled "*Hello-Kitty*" models (Figure A.13(a), "A" -- bone matrix model, "B" -- cell or biological factor model) were used. Figure A.13(b) shows the slice profile of "*Hello-Kitty*" models at certain height, and Figure A.13(c) is the result of path planning according to slice profile. Note that PAM jetting will be automatically performed with a given interval, so the actual path for PAM is based on lines instead of dots. The whole process was completed by "***Spider***".

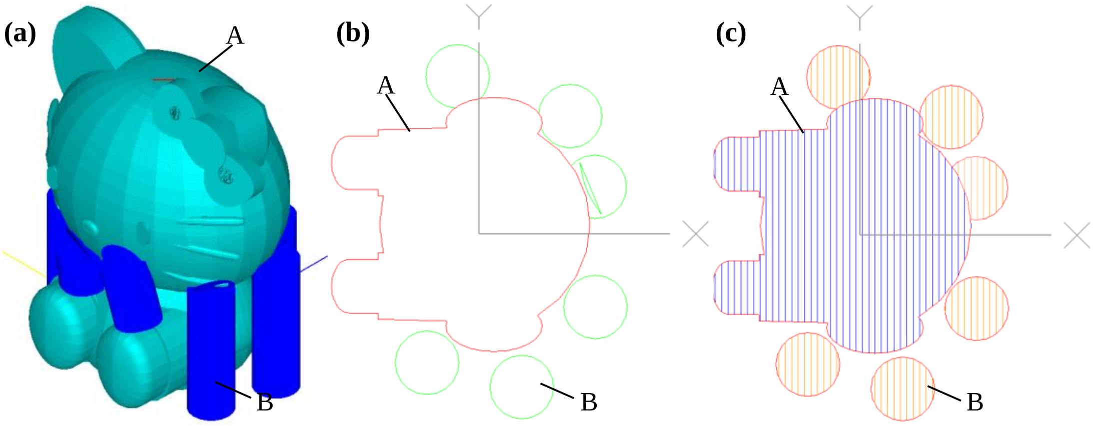

Figure A.13 Practical test of path planning with "*Hello-Kitty*": (a) assembly of models, (b) a sliced layer, (c) planned path

A.5.2 Precision

The precision of PAM, or the minimum dimension of stable droplets, was evaluated for all SA solutions, as presented in Figure A.14, which shows the difference before and after hydrophobic treatment of PAM nozzles as well. Obviously, hydrophobic treatment indeed notably reduced the size of minimized droplet (≥ 20%) in all solutions, indicating that hydrophobicity really contributed to improving precision. In addition, precision has close relation to the viscosity of SA solutions; specifically, higher precision may be obtained with lower content of SA. Interestingly, it was found that the increase rate of precision by hydrophobicity decreases as viscosity grows. A possible explanation would be: at very low viscosity, surface tension plays the dominant role; while as viscosity increases, the impact of viscosity would be increasingly considerable. The Ohnesorge number (***Oh*** in Equation A.4 [246]), which is a dimensionless number that relates the viscous forces to inertial and surface tension forces, may provide further evidence for this. Although more study is still required to approve this, the influence of viscosity on precision is definite.

To make sure the precision of PAM is acceptable (< 1,000 μm [249]) and droplets can be easily solidified after printing, our research mainly concentrated on SA solutions concentrated at 0.25 - 1.00 wt.%. As shown in Figure A.14, the precision in this range shows almost linear change with slight fluctuation. Such stability makes the estimation of precision at given viscosity possible and feasible. For instance, presumed that the viscosity of a solution was about 0.06 Pa·s (between 0.50 and 0.75 wt.%), the estimated precision would be approximately 600 μm. The list goes on like this.

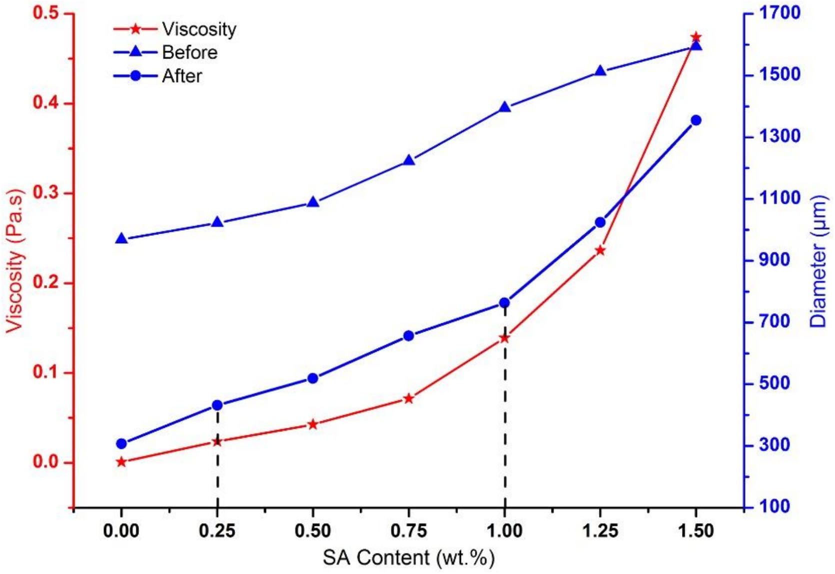

Figure A.14 Relationship of viscosity and precision before and after hydrophobic treatment

$$\mathrm{Oh} = \frac{\mu}{\sqrt{\rho\sigma\varphi}}$$ (Equation A.4)

Where, $\boldsymbol{\mu}$ -- viscosity, $\boldsymbol{\rho}$ -- density, $\boldsymbol{\sigma}$ -- surface tension, $\boldsymbol{\varphi}$ -- characteristic length scale (typically drop diameter).

Since the volume of SA droplet is usually too small to prevent drying and evaporation during transfer from workbench to microscope, an ultrasonic atomiser (WHQA-0002, Koninklijke Philips N.V.) was used to spray $CaCl_2$ solution evenly onto the substrate so that the droplets could be quickly solidified to keep the original shape. Figure A.15 (a) - (c) shows the optical images of minimum-sized droplets, which were shot at the same magnification and focal distance ($\boldsymbol{D_{avg}}$ stands for the average of $\boldsymbol{D_a}$). It can be seen that the droplets were in good conditions and almost perfectly matched the measure circles, with great uniformity (≥ 98%) in terms of cross-diameter, *i.e.* $\boldsymbol{D_c}$. Figure A.15(d) is for evaluation of stability and positioning accuracy with 10 droplets at a distance of 2.0 mm. The result is satisfactory in terms of stability and uniformity, as well as the accuracy in positioning. In summary, the PAM printing system can be well controlled to get droplets with fine precision.

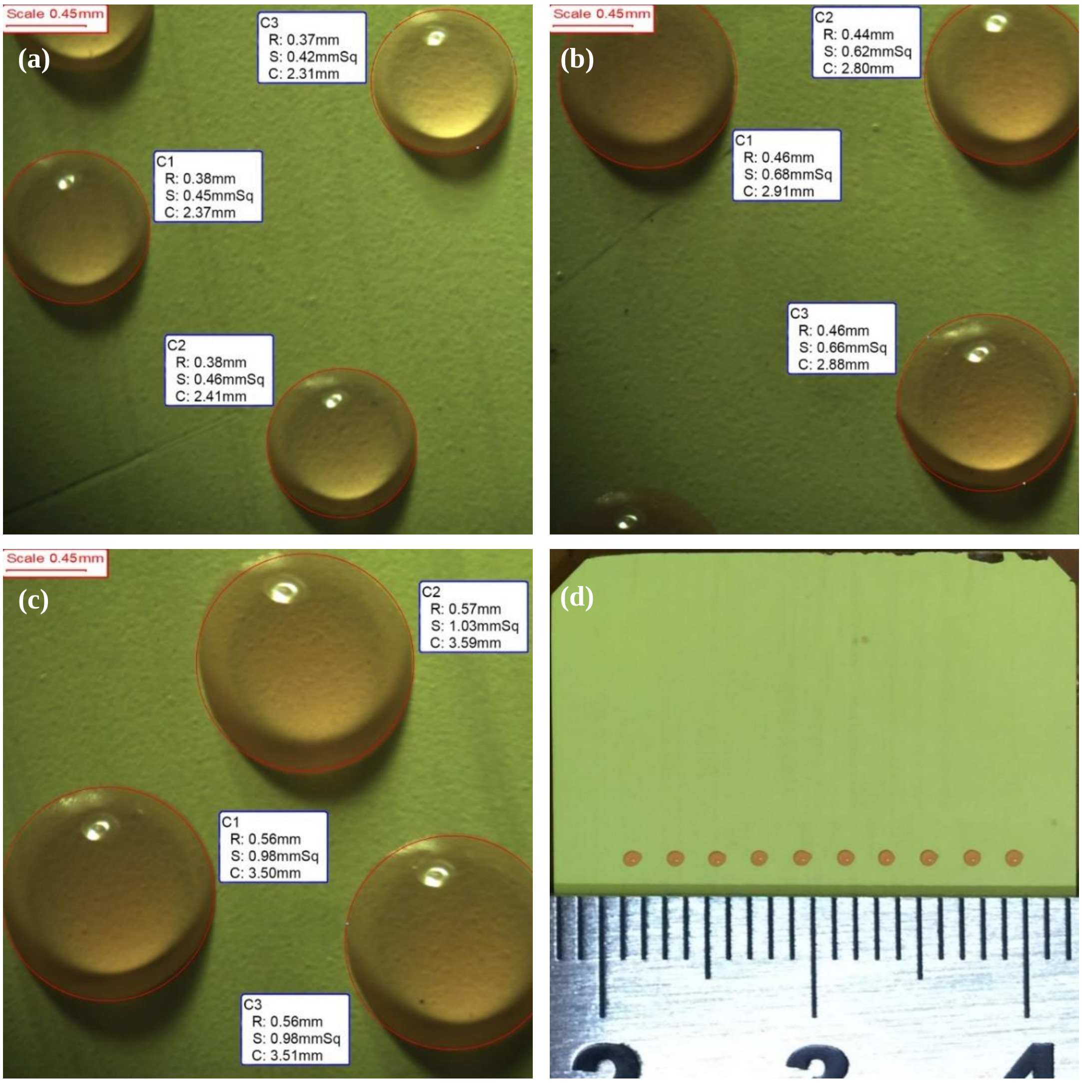

Figure A.15 Optical images of droplets: (a) 0.25 wt.% SA (D_{avg} = 432 μm, θ = 50.4°, F_c = 0.574), (b) 0.50 wt.% SA (D_{avg} = 519 μm, θ = 51.1°, F_c = 0.578), (c) 0.75 wt.% SA (D_{avg} = 657 μm, θ = 52.3 °, F_c = 0.583), (d) evaluation of stability and precision in positioning (0.50 wt.% SA)

A.5.3 Stability

Table A.3 shows the favourable PAP and HT sets for high stability (≥ 90%) in all SA solutions. It was found that the value of PAP and HT would increase as more SA was contented. This is reasonable in the light of energy conservation, since more energy would be consumed by frictional resistance, due to rising viscosity in droplet formation. Besides, the available range for adjustment of PAP will be increasingly wide if the viscosity of SA solution decreases. On the contrary, the requirement of PNP to avoid overflow is less demanded with high viscosity, and negative pressure is even not necessary at highly concentrated SA solution.

Table A.3 Favourable PAP, PNP and HT sets for high stability

SA (wt.%)	PAP (kPa)	HT (ms)	PNP (kPa)
0.25	15.0 ~ 35.0	3.0, 4.5	3.3
0.50	25.0 ~ 35.0	3.0, 4.5, 6.0	1.8
0.75	25.0 ~ 40.0	4.5, 6.0	0.7
1.00	35.0 ~ 45.0	4.5, 6.0	Not necessary

An sample result of stability test at 0.50 wt.% is shown in Figure A.16. The result reveals that higher HT preferred lower PAP to make ejection reliable, which is very useful for parameter adjustment in future. In order to obtain high stability, it is better to reduce HT on the condition of high PAP; otherwise, typical invalidity, such as “satellite drops” and “accumulation of bubbles”, may occur during droplet formation. For example, provided that PAP is 20.0 kPa, HT should be higher than 4.5 ms so as to successfully form droplets; while when PAP reaches 40.0 kPa, the up limit of HT is 4.5 ms, to avoid frequent occurrence of satellite drops. This rule is useful to serve as important reference for adjustment of parameters, which greatly improves the efficiency of adjusting appropriate parameters for new materials. The relationship of droplet stability with PAP and HT is similar in other SA solutions.

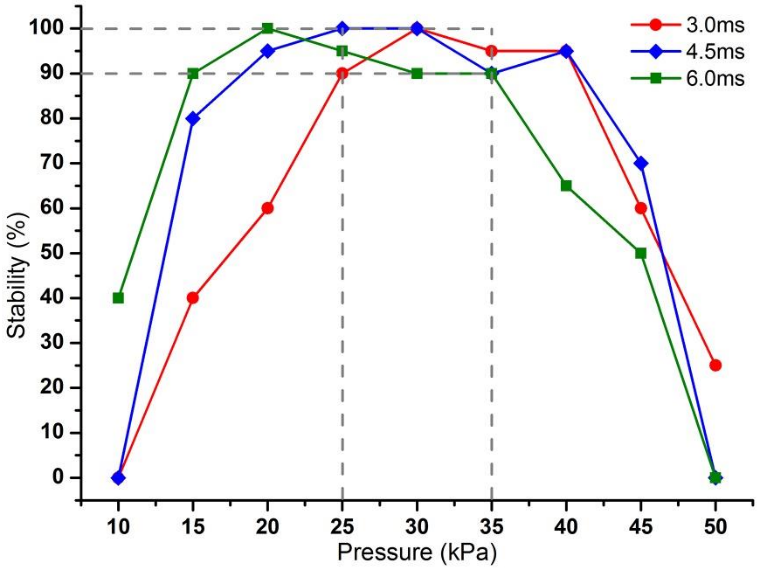

Figure A.16 Sampled relationship (0.50wt.% SA) of droplet stability with PAP and HT

A.5.4 Adjustment of Parameter Sets

As mentioned before, minimum-sized droplets are not always demanded in consideration of efficiency. Generally, it is very difficult to achieve the exact size by merely regulating SA content, PAP and HT, so 50 μm was set as increment based on minimum size. The result of was summarised in Figure A.17 (10 drops for each set). Overall, the droplets present good uniformity (≥ 95%), despite that the deviation actually shows rising trend when SA content increases. The parameter sets for every dimension were on the basis of Table A.3 to ensure stability. A database according to this result had been set up to accelerate the adjustment of parameters. For a solution with given viscosity, the database can offer reference for the suitable set of HT, PAP and PNP to achieve desired size of droplets with great convenience. For example, if 600 μm was wanted from 0.40 wt.% SA solution, the suggested set of HT, PAP and PNP would be 3.0 ms, 27.8 - 34.4 kPa, and 1.8 - 3.3 kPa respectively. In addition, for droplets smaller than 650 μm, 3.0ms is enough for HT, and 35.0 kPa may be the up limit of PAP. Similarly, for those within 700 - 800 μm, HT should better be 4.5 ms, and PAP must be higher than 25.0 kPa; and so forth. All in all, the amount of work to adjust parameter sets for new materials/solutions will be greatly reduced.

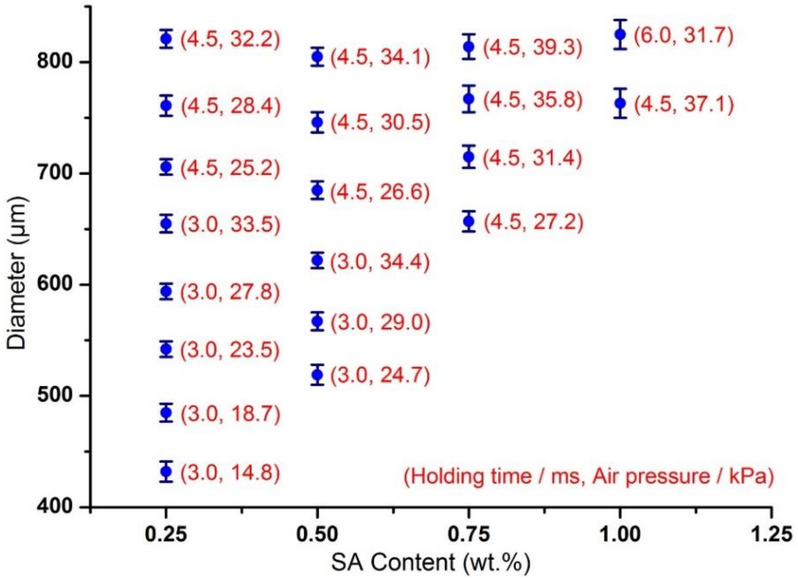

Figure A.17 Parameter sets for certain sized droplets.

A.5.5 Coordination and Synchronization

The key challenge for PAM-MAM (multi-nozzles) system lies in their coordination and synchronization, especially in independent and convergent mode. Therefore, experiments using 0.50 wt.% SA solution for PAM jetting were carefully designed to confirm this. The dot matrix in Figure A.18(a) was primarily to evaluate the repeatability and accuracy of positioning, where the droplets could manage to keep good shape and maintain accurate location. The "*HUST*" logo in Figure A.18(b) is another expressive example, where "**H**" and "**S**" were printed by PAM at highest precision ($\boldsymbol{D_a}$ = 487 ± 26 μm) in independent mode, and "**T**" was formed in convergent mode, reasonably resulting in larger and less regular droplets ($\boldsymbol{D_a}$ = 676 ± 53 μm) due to impaction and adhesion of droplets. It shows that the precision both in size and positioning is acceptable, greatly owing to the set of convergent focus on substrate, short pause and low frequency during jetting. Although the satellite drops caused by collision were unavoidable, it affected the precision only a bit (< 5 μm). It is worth mentioning that the droplets assembling "**H**" were actually blue, which yet looks green due to colour overlay (blue + yellow = green); similarly, "**S**" appears orange instead of red, and "**T**" is dark rather than purple. In summary, PAM-MAM could keep fine precision as well as good coordination and synchronization during work, providing an essential foundation for 3D complex scaffolds with multi-biomaterials.

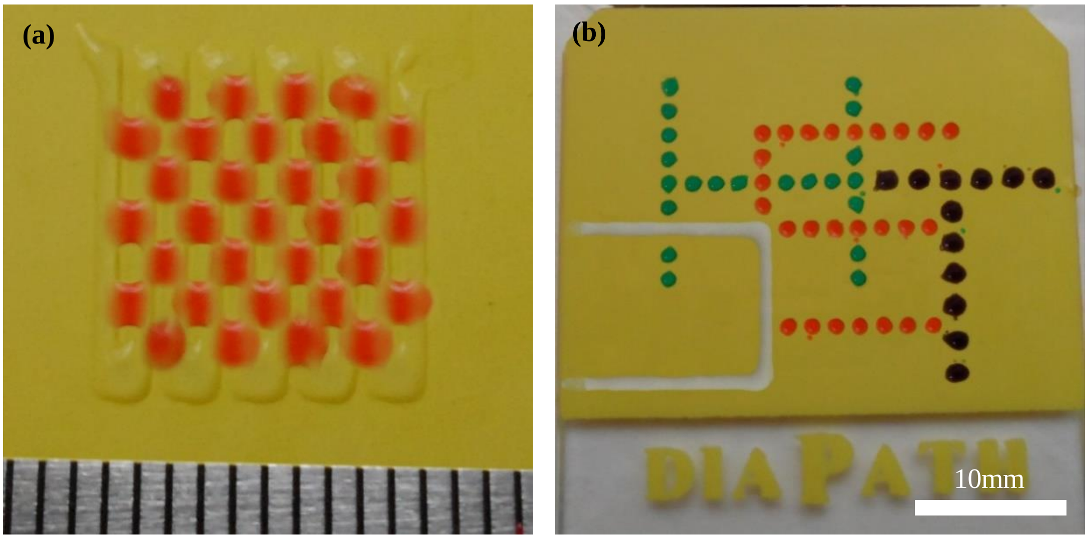

Figure A.18 Patterns for evaluation of coordination: (a) dot matrix, and (b) "HUST" logo

References

[1] A. R. Shrivats, M. C. McDermott, J. O. Hollinger. “Bone tissue engineering: state of the union”. *Drug Discovery Today*, 2014, vol. 19, no. 6, pp. 781-786.

[2] Y. Y. Qi. “MSC sheet technique combined with platelet rich plasma gel/calcium phosphate nanoparticles for bone regeneration”. Thesis, *Zhejiang University*, 2013.

[3] N. J. Panetta, D. M. Gupta, M. T. Longaker. “Bone regeneration and repair”. *Current Stem Cell Research & Therapy*, 2010, vol. 5, no. 2, pp. 122-128.

[4] J. L. Ma, S. K. Both, F. Yang, F. Z. Cui, J. L. Pan, G. J. Meijer, J. A. Jansen, J. J. Van Den Beucken. “Concise review: cell-based strategies in bone tissue engineering and regenerative medicine”. *Stem Cells Transl. Med.*, 2014, vol. 3, no. 1, pp. 98-107.

[5] R. J. O'Keefe, J. Mao. “Bone tissue engineering and regeneration: from discovery to the clinic—an overview”. *Tissue Engineering Part B: Reviews*, 2011, vol. 17, no. 6, pp. 389-392.

[6] C. R. Perry. “Bone repair techniques, bone graft, and bone graft substitutes”. *Clinical Orthopaedics and Related Research*, 1999, vol. 360, pp. 71-86.

[7] Q. Wu. “Controllable fabrication and characterization of porous calcium phosphate scaffolds for bone tissue engineering”. Thesis, *Huazhong University of Science and Technology*, 2012.

[8] H. Löfgren, V. Johannsson, T. Olsson, L. Ryd, B. Levander. “Rigid fusion after cloward operation for cervical disc disease using autograft, allograft, or xenograft: a randomized study with radiostereometric and clinical follow-up assessment”. *Spine*, 2000, vol. 25, no. 15, pp. 1908-1916.

[9] C. Jeffrey, M. D. Wang. “Bone grafts: no longer just a chip off the Ol’Hip”. *UCLA Department of Orthopaedic Surgery*, 2006.

[10] S. S. Jensen, H. Terheyden. “Bone augmentation procedures in localized defects in the alveolar ridge: clinical results with different bone grafts and bone-substitute materials”. *International Journal of Oral & Maxillofacial Implants*, 2009, vol. 24, no. Suppl, pp. 218-236.

[11] J. R. Jones, L. L. Hench. “Biomedical materials for new millennium: perspective on the future”. *Materials Science and Technology*, 2001, vol. 17, no. 8, pp. 891-900.

[12] A. L. Dumitrescu. “Bone grafts and bone graft substitutes in periodontal therapy”. *Chemicals in Surgical Periodontal Therapy*, 2011, pp. 73-144.

[13] J. R. Jones, P. D. Lee, L. L. Hench. “Hierarchical porous materials for tissue engineering”. *Philosophical Transactions of the Royal Society of London A: Mathematical, Physical and Engineering Sciences*, 2006, vol. 364, no. 1838, pp. 263-281.

[14] S. Weiner, W. Traub, H. D. Wagner. “Lamellar bone: structure–function relations”. *Journal of Structural Biology*, 1999, vol. 126, no. 3, pp. 241-255.

[15] S. Weiner, W. Traub. “Bone structure: from angstroms to microns”. *The FASEB Journal*, 1992, vol. 6, no. 3, pp. 879-885.

[16] S. Khosla, J. J. Westendorf, M. J. Oursler. “Building bone to reverse osteoporosis and repair fractures”. *The Journal of Clinical Investigation*, 2008, vol. 118, no. 2, pp. 421-428.

[17] J. Watkins. “Structure and function of the musculoskeletal system”. *Human Kinetics*, 2010.

[18] B. Clarke. “Normal bone anatomy and physiology”. *Clinical Journal of the American Society of Nephrology*, 2008, vol. 3, no. Suppl 3, pp. S131-139.

[19] H. M. Frost. “Tetracycline-based histological analysis of bone remodeling”. *Calcified Tissue*

International, 1969, vol. 3, no. 1, pp. 211-237.

[20] D. J. Hadjidakis, I. I. Androulakis. "Bone remodeling". *Annals of the New York Academy of Sciences*, 2006, vol. 1092, no. 1, pp. 385-396.

[21] H. M. Frost. "Dynamics of bone remodeling". *Bone Biodynamics*, 1964, pp. 315-334.

[22] S. S. Wang, B. J. Gui, J. Zhou. "Osteocytes and bone remodeling". *Chinese Journal of Tissue Engineering Research*, 2013, vol. 17, no. 11, pp. 2060-2066.

[23] J. Z. Lin, X. J. Wang. "Research status quo and progress on the repair of massive bone defects". *Medical Recapitulate*, 2009, vol. 15, no. 6, pp. 877-880.

[24] L. M. Calvi, G. B. Adams, K. W. Weibrecht, J. M. Weber, D. P. Olson, M. C. Knight, R. P. Martin, E. Schipani, P. Divieti, F. R. Bringhurst. "Osteoblastic cells regulate the haematopoietic stem cell niche". *Nature*, 2003, vol. 425, no. 6960, pp. 841-846.

[25] M. R. Urist. "Bone: formation by autoinduction". *Science*, 1965, vol. 150, no. 3698, pp. 893-899.

[26] L. L. Hench, J. M. Polak. "Third-generation biomedical materials". *Science*, 2002, vol. 295, no. 5557, pp. 1014-1017.

[27] R. Langer, J. P. Vacanti. "Tissue engineering". *Science*, 1993, vol. 260, no. 5110, pp. 920-926.

[28] G. M. Crane, S. L. Ishaug, A. G. Mikos. "Bone tissue engineering". *Nature Medicine*, 1995, vol. 1, no. 12, pp. 1322-1324.

[29] J. C. Reichert, D. W. Hutmacher. "Bone tissue engineering". *Springer*, 2011.

[30] K. E. Healy, R. E. Guldberg. "Bone tissue engineering". *Journal of Musculoskeletal and Neuronal Interactions*, 2007, vol. 7, no. 4, pp. 328.

[31] F. R. A. J. Rose, R. O. C. Oreffo. "Bone tissue engineering: hope vs hype". *Biochemical and Biophysical Research Communications*, 2002, vol. 292, no. 1, pp. 1-7.

[32] A. J. Salgado, O. P. Coutinho, R. L. Reis. "Bone tissue engineering: state of the art and future trends". *Macromolecular Bioscience*, 2004, vol. 4, no. 8, pp. 743-765.

[33] V. Karageorgiou, D. Kaplan. "Porosity of 3D biomaterial scaffolds and osteogenesis". *Biomaterials*, 2005, vol. 26, no. 27, pp. 5474-5491.

[34] E. H. J. Groeneveld, J. P. A. Van Den Bergh, P. Holzmann, C. M. Ten Bruggenkate, D. B. Tuinzing, E. H. Burger. "Mineralization processes in demineralized bone matrix grafts in human maxillary sinus floor elevations". *Journal of Biomedical Materials Research*, 1999, vol. 48, no. 4, pp. 393-402.

[35] Y. Kuboki, H. Takita, D. Kobayashi, E. Tsuruga, M. Inoue, M. Murata, N. Nagai, Y. Dohi, H. Ohgushi. "BMP - induced osteogenesis on the surface of hydroxyapatite with geometrically feasible and nonfeasible structures: topology of osteogenesis". *Journal of Biomedical Materials Research*, 1998, vol. 39, no. 2, pp. 190-199.

[36] H. Shin, S. Jo, A. G. Mikos. "Biomimetic materials for tissue engineering". *Biomaterials*, 2003, vol. 24, no. 24, pp. 4353-4364.

[37] D. W. Hutmacher. "Scaffolds in tissue engineering bone and cartilage". *Biomaterials*, 2000, vol. 21, no. 24, pp. 2529-2543.

[38] H. Ohgushi, A. I. Caplan. "Stem cell technology and bioceramics: from cell to gene engineering". *Journal of Biomedical Materials Research*, 1999, vol. 48, no. 6, pp. 913-927.

[39] J. R. Jones, E. Gentleman, J. Polak. "Bioactive glass scaffolds for bone regeneration". *Elements*, 2007, vol. 3, no. 6, pp. 393-399.

[40] B. D. Porter, J. B. Oldham, S. L. He, M. E. Zobitz, R. G. Payne, K. N. An, B. L. Currier, A. G.

Mikos, M. J. Yaszemski. “Mechanical properties of a biodegradable bone regeneration scaffold”. *Journal of Biomechanical Engineering*, 2000, vol. 122, no. 3, pp. 286-288.

[41] S. J. Hollister. “Porous scaffold design for tissue engineering”. *Nature Materials*, 2005, vol. 4, no. 7, pp. 518-524.

[42] J. R. Jones. “New trends in bioactive scaffolds: the importance of nanostructure”. *Journal of the European Ceramic Society*, 2009, vol. 29, no. 7, pp. 1275-1281.

[43] B. M. Gumbiner. “Cell adhesion: the molecular basis of tissue architecture and morphogenesis”. *Cell*, 1996, vol. 84, no. 3, pp. 345-357.

[44] Biology-Online.org. “Cell growth”. *Biology Online Dictionary*, 2011.

[45] I. D. Xynos, A. J. Edgar, L. D. K. Buttery, L. L. Hench, J. M. Polak. “Ionic products of bioactive glass dissolution increase proliferation of human osteoblasts and induce insulin-like growth factor II mRNA expression and protein synthesis”. *Biochemical and Biophysical Research Communications*, 2000, vol. 276, no. 2, pp. 461-465.

[46] J. M. W. Slack. “Essential Developmental Biology”. Oxford: *Wiley-Blackwell*, 2012.

[47] H. P. Yuan, Z. J. Yang, Y. B. Li, X. D. Zhang, J. D. De Bruijn, K. De Groot. “Osteoinduction by calcium phosphate biomaterials”. *Journal of Materials Science: Materials in Medicine*, 1998, vol. 9, no. 12, pp. 723-726.

[48] B. S. Chang, K. S. Hong, H. J. Youn, H. S. Ryu, S. S. Chung, K. W. Park. “Osteoconduction at porous hydroxyapatite with various pore configurations”. *Biomaterials*, 2000, vol. 21, no. 12, pp. 1291-1298.

[49] K. C. Popat, K. I. Chatvanichkul, G. L. Barnes, T. J. Latempa, C. A. Grimes, T. A. Desai. “Osteogenic differentiation of marrow stromal cells cultured on nanoporous alumina surfaces”. *Journal of Biomedical Materials Research Part A*, 2007, vol. 80, no. 4, pp. 955-964.

[50] R. Z. LeGeros. “Properties of osteoconductive biomaterials: calcium phosphates”. *Clinical Orthopaedics and Related Research*, 2002, vol. 395, pp. 81-98.

[51] Y. R. Duan, Z. R. Zhang, C. Y. Wang, J. Y. Chen, X. D. Zhang. “Dynamic study of calcium phosphate formation on porous HA/TCP ceramics”. *Journal of Materials Science: Materials in Medicine*, 2005, vol. 16, no. 9, pp. 795-801.

[52] D. F. Meaney. “Mechanical properties of implantable biomaterials”. *Clinics in podiatric medicine and surgery*, 1995, vol. 12, no. 3, pp. 363-384.

[53] W. Huang, X. L. Zhang, Q. Wu, B. Wu. “Fabrication of HA/β-TCP scaffolds based on micro-syringe extrusion system”. *Rapid Prototyping Journal*, 2013, vol. 19, no. 5, pp. 319-326.

[54] A. Ogose, T. Hotta, H. Kawashima, N. Kondo, W. Gu, T. Kamura, N. Endo. “Comparison of hydroxyapatite and beta tricalcium phosphate as bone substitutes after excision of bone tumors”. *Journal of Biomedical Materials Research Part B: Applied Biomaterials*, 2005, vol. 72, no. 1, pp. 94-101.

[55] M. Bordena, M. Attawiaa, Y. Khana, C. T. Laurencin. “Tissue engineered microsphere-based matrices for bone repair: design and evaluation”. *Biomaterials*, 2002, vol. 23, no. 2, pp. 551-559.

[56] H. Follet, G. Boivin, C. Rumelhart, P. J. Meunier. “The degree of mineralization is a determinant of bone strength: a study on human calcanei”. *Bone*, 2004, vol. 34, no. 5, pp. 783-789.

[57] K. Yamaguchi, T. Hirano, G. Yoshida, K. Iwasaki. “Degradation-resistant character of synthetic hydroxyapatite blocks filled in bone defects”. *Biomaterials*, 1995, vol. 16, no. 13, pp. 983-985.

[58] Z. H. Dong, Y. B. Li, Q. Zou. “Degradation and biocompatibility of porous nano-

hydroxyapatite/polyurethane composite scaffold for bone tissue engineering". *Applied Surface Science*, 2009, vol. 255, no. 12, pp. 6087-6091.

[59] S. Sánchez-Salcedo, A. Nieto, M. Vallet-Regí. "Hydroxyapatite/β-tricalcium phosphate/agarose macroporous scaffolds for bone tissue engineering". *Chemical engineering journal*, 2008, vol. 137, no. 1, pp. 62-71.

[60] A. Macchetta, I. G. Turner, C. R. Bowen. "Fabrication of HA/TCP scaffolds with a graded and porous structure using a camphene-based freeze-casting method". *Acta biomaterialia*, 2009, vol. 5, no. 4, pp. 1319-1327.

[61] K. Rezwan, Q. Z. Chen, J. J. Blaker, A. R. Boccaccini. "Biodegradable and bioactive porous polymer/inorganic composite scaffolds for bone tissue engineering". *Biomaterials*, 2006, vol. 27, no. 18, pp. 3413-3431.

[62] J. Jagur-Grodzinski. "Biomedical application of functional polymers". *Reactive and Functional Polymers*, 1999, vol. 39, no. 2, pp. 99-138.

[63] A. K. Mohanty, M. Misra, G. I. Hinrichsen. "Biofibres, biodegradable polymers and biocomposites: an overview". *Macromolecular Materials and Engineering*, 2000, vol. 276, no. 1, pp. 1-24.

[64] L. E. Freed, G. Vunjak-Novakovic, R. J. Biron, D. B. Eagles, D. C. Lesnoy, S. K. Barlow, R. Langer. "Biodegradable polymer scaffolds for tissue engineering". *Nature Biotechnology*, 1994, vol. 12, no. 7, pp. 689-693.

[65] Y. M. Khan, D. S. Katti, C. T. Laurencin. "Novel polymer‐synthesized ceramic composite–based system for bone repair: An in vitro evaluation". *Journal of Biomedical Materials Research Part A*, 2004, vol. 69, no. 4, pp. 728-737.

[66] L. L. Hench, J. Wilson. "An introduction to bioceramics". *World Scientific*, 1993.

[67] K. D. Lobel, L. L. Hench. "In vitro adsorption and activity of enzymes on reaction layers of bioactive glass substrates". *Journal of Biomedical Materials Research*, 1998, vol. 39, no. 4, pp. 575-579.

[68] H. Keshaw, A. Forbes, R. M. Day. "Release of angiogenic growth factors from cells encapsulated in alginate beads with bioactive glass". *Biomaterials*, 2005, vol. 26, no. 19, pp. 4171-4179.

[69] A. M. Gatti, G. Valdre, Ö. H. Andersson. "Analysis of the in vivo reactions of a bioactive glass in soft and hard tissue". *Biomaterials*, 1994, vol. 15, no. 3, pp. 208-212.

[70] L. L. Hench. "Bioceramics: from concept to clinic". *Journal of the American Ceramic Society*, 1991, vol. 74, no. 7, pp. 1487-1510.

[71] I. D. Xynos, M. V. J. Hukkanen, J. J. Batten, L. D. Buttery, L. L. Hench, J. M. Polak. "Bioglass® 45S5 stimulates osteoblast turnover and enhances bone formation in vitro: implications and applications for bone tissue engineering". *Calcified Tissue International*, 2000, vol. 67, no. 4, pp. 321-329.

[72] Y. S. Chang, H. O. Gu, M. Kobayashi, M. Oka. "Influence of various structure treatments on histological fixation of titanium implants". *The Journal of Arthroplasty*, 1998, vol. 13, no. 7, pp. 816-825.

[73] M. Svehla, P. Morberg, B. Zicat, W. Bruce, D. Sonnabend, W. R. Walsh. "Morphometric and mechanical evaluation of titanium implant integration: comparison of five surface structures". *Journal of Biomedical Materials Research*, 2000, vol. 51, no. 1, pp. 15-22.

[74] C. E. Wen, Y. Yamada, K. Shimojima, Y. Chino, H. Hosokawa, M. Mabuchi. "Novel titanium

foam for bone tissue engineering". *Journal of Materials Research*, 2002, vol. 17, no. 10, pp. 2633-2639.

[75] S. Bose, M. Roy, A. Bandyopadhyay. "Recent advances in bone tissue engineering scaffolds". *Trends in Biotechnology*, 2012, vol. 30, no. 10, pp. 546-554.

[76] F. Witte, H. Ulrich, M. Rudert, E. Willbold. "Biodegradable magnesium scaffolds: Part 1: appropriate inflammatory response". *Journal of Biomedical Materials Research Part A*, 2007, vol. 81, no. 3, pp. 748-756.

[77] J. Wei, J. F. Jia, F. Wu, S. C. Wei, H. J. Zhou, H. B. Zhang, J. W. Shin, C. S. Liu. "Hierarchically microporous/macroporous scaffold of magnesium–calcium phosphate for bone tissue regeneration". *Biomaterials*, 2010, vol. 31, no. 6, pp. 1260-1269.

[78] B. Michael, M. D. Schachter. "The importance of magnesium to human nutrition". *The Schachter Center for Complementary Medicine*, 1996.

[79] H. Kato, T. Nakamura, S. Nishiguchi, Y. Matsusue, M. Kobayashi, T. Miyazaki, H. M. Kim, T. Kokubo. "Bonding of alkali - and heat - treated tantalum implants to bone". *Journal of Biomedical Materials Research*, 2000, vol. 53, no. 1, pp. 28-35.

[80] R. Lanza, R. Langer, J. P. Vacanti. "Principles of tissue engineering". *Academic Press*, 2011.

[81] E. J. Harvey, J. D. Bobyn, M. Tanzer, G. J. Stackpool, J. J. Krygier, S. A. Hacking. "Effect of flexibility of the femoral stem on bone-remodeling and fixation of the stem in a canine total hip arthroplasty model without cement". *J Bone Joint Surg Am*, 1999, vol. 81, no. 1, pp. 93-107.

[82] H. P. Yuan, K. Kurashina, J. D. De Bruijn, Y. Li, K. De Groot, X. D. Zhang. "A preliminary study on osteoinduction of two kinds of calcium phosphate ceramics". *Biomaterials,* 1999, vol. 20, no. 19, pp. 1799-1806.

[83] S. F. Hulbert, F. A. Young, R. S. Mathews, J. J. Klawitter, C. D. Talbert, F. H. Stelling. "Potential of ceramic materials as permanently implantable skeletal prostheses". *Journal of Biomedical Materials Research,* 1970, vol. 4, no. 3, pp. 433-456.

[84] E. Tsuruga, H. Takita, H. Itoh, Y. Wakisaka, Y. Kuboki. "Pore size of porous hydroxyapatite as the cell-substratum controls BMP-induced osteogenesis". *Journal of Biochemistry,* 1997, vol. 121, no. 2, pp. 317-324.

[85] L. S. Liu, A. Y. Thompson, M. A. Heidaran, J. W. Poser, R. C. Spiro. "An osteoconductive collagen/hyaluronate matrix for bone regeneration". *Biomaterials,* 1999, vol. 20, no. 12, pp. 1097-1108.

[86] Y. Kuboki, Q. M. Jin, H. Takita. "Geometry of carriers controlling phenotypic expression in BMP-induced osteogenesis and chondrogenesis". *J Bone Joint Surg Am,* 2001, vol. 83-A Suppl 1, no. Pt 2, pp. S105-115.

[87] Q. M. Jin, H. Takita, T. Kohgo, K. Atsumi, H. Itoh, Y. Kuboki. "Effects of geometry of hydroxyapatite as a cell substratum in BMP-induced ectopic bone formation". *Journal of Biomedical Materials Research,* 2000, vol. 51, no. 3, pp. 491-499.

[88] M. L. Gray, A. M. Pizzanelli, R. C. Lee, A. J. Grodzinsky, D. A. Swann. "Kinetics of the chondrocyte biosynthetic response to compressive load and release". *Biochimica et Biophysica Acta (BBA)-General Subjects,* 1989, vol. 991, no. 3, pp. 415-425.

[89] D. A. Lee, T. Noguchi, S. P. Frean, P. Lees, D. L. Bader. "The influence of mechanical loading on isolated chondrocytes seeded in agarose constructs". *Biorheology,* 2000, vol. 37, no. 1-2, pp. 149-161.

[90] M. D. Buschmann, Y. A. Gluzband, A. J. Grodzinsky, E. B. Hunziker. “Mechanical compression modulates matrix biosynthesis in chondrocyte/agarose culture”. *Journal of Cell Science*, 1995, vol. 108, no. 4, pp. 1497-1508.

[91] C. R. Lee, A. J. Grodzinsky, M. Spector. “Biosynthetic response of passaged chondrocytes in a type II collagen scaffold to mechanical compression”. *Journal of Biomedical Materials Research Part A*, 2003, vol. 64, no. 3, pp. 560-569.

[92] C. T. Wu, Y. Ramaswamy, P. Boughton, H. Zreiqat. “Improvement of mechanical and biological properties of porous CaSiO 3 scaffolds by poly (d, l-lactic acid) modification”. *Acta Biomaterialia*, 2008, vol. 4, no. 2, pp. 343-353.

[93] Y. Wang, J. Dai, Q. C. Zhang, Y. Xiao, M. D. Lang. “Improved mechanical properties of hydroxyapatite/poly (ε-caprolactone) scaffolds by surface modification of hydroxyapatite”. *Applied Surface Science*, 2010, vol. 256, no. 20, pp. 6107-6112.

[94] Y. S. Nam, T. G. Park. “Porous biodegradable polymeric scaffolds prepared by thermally induced phase separation”. *Journal of Biomedical Materials Research*, 1999, vol. 47, no. 1, pp. 8-17.

[95] Y. S. Nam, T. G. Park. “Biodegradable polymeric microcellular foams by modified thermally induced phase separation method”. *Biomaterials*, 1999, vol. 20, no. 19, pp. 1783-1790.

[96] K. M. Wang, S. R. Li, J. Guo. “Study on preparation of scaffold for tissue engineering by thermally induced phase separation technique”. *Chemistry & Bioengineering*, 2006, vol. 23, no. 1, pp. 1-3.

[97] K. Zhao, J. Wei, D. Luo, Y. Tang, L. Xu. “Fabrication of hydroxyapatite porous scaffolds by freeze drying”. *Journal of the Chinese Ceramic Society*, 2009, vol. 37, no. 3, pp. 432-435.

[98] X. Wu, Y. Liu, X. Li, P. Wen, Y. Zhang, Y. Long, X. Wang, Y. Guo, F. Xing, J. Gao. “Preparation of aligned porous gelatin scaffolds by unidirectional freeze-drying method”. *Acta Biomaterialia*, 2010, vol. 6, no. 3, pp. 1167-1177.

[99] M. H. Ho, P. Y. Kuo, H. J. Hsieh, T. Y. Hsien, L. T. Hou, J. Y. Lai, D. M. Wang. “Preparation of porous scaffolds by using freeze-extraction and freeze-gelation methods”. *Biomaterials*, 2004, vol. 25, no. 1, pp. 129-138.

[100] C. D. Liu, Z. G. Zhang, K. Su, S. J. Kuang. “Modified polylactic acid scaffold with hyaluronic acid”. *Journal of Clinical Rehabilitative Tissue Engineering Research*, 2012, vol. 16, no. 3, pp. 484-488.

[101] A. G. Mikos, A. J. Thorsen, L. A. Czerwonka, Y. Bao, R. Langer, D. N. Winslow, J. P. Vacanti. “Preparation and characterization of poly(l-lactic acid) foams”. *Polymer*, 1994, vol. 35, no. 5, pp. 1068-1077.

[102] C. J. Liao, C. F. Chen, J. H. Chen, S. F. Chiang, Y. J. Lin, K. Y. Chang. “Fabrication of porous biodegradable polymer scaffolds using a solvent merging/particulate leaching method”. *Journal of Biomedical Materials Research*, 2002, vol. 59, no. 4, pp. 676-681.

[103] J. M. Taboas, R. D. Maddox, P. H. Krebsbach, S. J. Hollister. “Indirect solid free form fabrication of local and global porous, biomimetic and composite 3D polymer-ceramic scaffolds”. *Biomaterials*, 2003, vol. 24, no. 1, pp. 181-194.

[104] Y. S. Nam, J. J. Yoon, T. G. Park. “A novel fabrication method of macroporous biodegradable polymer scaffolds using gas foaming salt as a porogen additive”. *Journal of Biomedical Materials Research*, 2000, vol. 53, no. 1, pp. 1-7.

[105] D. J. Mooney, D. F. Baldwin, N. P. Suh, J. P. Vacanti, R. Langer. “Novel approach to fabricate

porous sponges of poly (D, L-lactic-co-glycolic acid) without the use of organic solvents". *Biomaterials*, 1996, vol. 17, no. 14, pp. 1417-1422.

[106] X. R. Teng, J. Ren, L. H. Zhu. "Preparation of porous PLA scaffold materials by supercritical CO2/salt-leaching method". *Journal of Wuhan Institute of Chemical Technology*, 2005, vol. 27, no. 5, pp. 42-45.

[107] C. Wang, T. Kasuga, M. Nogami. "Macroporous calcium phosphate glass-ceramic prepared by two-step pressing technique and using sucrose as a pore former". *Journal of Materials Science: Materials in Medicine*, 2005, vol. 16, no. 8, pp. 739-744.

[108] Q. Jie, K. Lin, J. Zhong, Y. Shi, Q. Li, J. Chang, R. Wang. "Preparation of macroporous sol-gel bioglass using PVA particles as pore former". *Journal of Sol-Gel Science and Technology*, 2004, vol. 30, no. 1, pp. 49-61.

[109] O. Lyckfeldt, J. M. F. Ferreira. "Processing of porous ceramics by starch consolidation". *Journal of the European Ceramic Society*, 1998, vol. 18, no. 2, pp. 131-140.

[110] M. Boaro, J. M. Vohs, R. J. Gorte. "Synthesis of highly porous yttria -- stabilized zirconia by tape-casting methods". *Journal of the American Ceramic Society*, 2003, vol. 86, no. 3, pp. 395-400.

[111] J. F. Cooley. "Improved methods of and apparatus for electrically separating the relatively volatile liquid component from the component of relatively fixed substances of composite fluids". *G.B. Patent*, no. 06385-5-19, 1900.

[112] J. A. Matthews, G. E. Wnek, D. G. Simpson, G. L. Bowlin. "Electrospinning of collagen nanofibers". *Biomacromolecules*, 2002, vol. 3, no. 2, pp. 232-238.

[113] G. L. Bowlin, K. J. Pawlowski, J. D. Stitzel, E. D. Boland, D. G. Simpson, J. B. Fenn, G. E. Wnek. "Electrospinning of polymer scaffolds for tissue engineering". *Tissue Engineering and Biodegradable Equivalents: Scientific and Clinical Applications*, 2002, pp. 165-178.

[114] H. Yoshimoto, Y. M. Shin, H. Terai, J. P. Vacanti. "A biodegradable nanofiber scaffold by electrospinning and its potential for bone tissue engineering". *Biomaterials*, 2003, vol. 24, no. 12, pp. 2077-2082.

[115] C. H. Wang, J. J. He, S. H. Wang, X. K. Guo, M. C. Zhao, C. Liu. "Application of electrospinning technology in the cartilage tissue engineering". *Hainan Medical Journal.*, 2016, vol. 27, no. 19, pp. 1689-1690.

[116] S. S. Crump, J. W. Comb, W. R. Priedeman Jr, R. L. Zinniel. "Process of support removal for fused deposition modeling". *U.S. Patent*, no. 5503785-4-2, 1996.

[117] Z. H. Wang. "Research on filament extruding technique of bone scaffold by rapid prototyping machine based on fused deposition method". Thesis, *Harbin Institute of Technology*, 2014.

[118] D. W. Hutmacher, T. Schantz, I. Zein, K. W. Ng, S. H. Teoh, K. C. Tan. "Mechanical properties and cell cultural response of polycaprolactone scaffolds designed and fabricated via fused deposition modeling". *Journal of Biomedical Materials Research*, 2001, vol. 55, no. 2, pp. 203-216.

[119] I. Zein, D. W. Hutmacher, K. C. Tan, S. H. Teoh. "Fused deposition modeling of novel scaffold architectures for tissue engineering applications". *Biomaterials*, 2002, vol. 23, no. 4, pp. 1169-1185.

[120] J. M. Williams, A. Adewunmi, R. M. Schek, C. L. Flanagan, P. H. Krebsbach, S. E. Feinberg, S. J. Hollister, S. Das. "Bone tissue engineering using polycaprolactone scaffolds fabricated via

selective laser sintering". *Biomaterials*, 2005, vol. 26, no. 23, pp. 4817-4827.

[121] B. B. Tan. "Effect of selective laser sintering parameters on properties of inorganic-organic composite scaffolds". Thesis, *Huazhong University of Science and Technology*, 2014.

[122] F. P. W. Melchels, J. Feijen, D. W. Grijpma. "A poly (D, L-lactide) resin for the preparation of tissue engineering scaffolds by stereolithography". *Biomaterials*, 2009, vol. 30, no. 23, pp. 3801-3809.

[123] P. Zhuang, Q. Lian, D. C. Li, J. K. He, W. G. Bian, Z. Wang, Z. M. Jin. "Fabrication and performance study of biomimetic multi-material osteochondral scaffold". *Journal of Mechanical Engineering*, 2014, no. 21, pp. 133-139.

[124] C. R. Deckard. "Method and apparatus for producing parts by selective sintering". *U.S. Patent*, no. 4863538-9-5, 1989.

[125] C. W. Hull. "Apparatus for production of three-dimensional objects by stereolithography". *U.S. Patent*, no. 4575330-3-11, 1986.

[126] N. K. Vail, L. D. Swain, W. C. Fox, T. B. Aufdlemorte, G. Lee, J. W. Barlow. "Materials for biomedical applications". *Materials & Design*, 1999, vol. 20, no. 2, pp. 123-132.

[127] E. M. Sachs, J. S. Haggerty, M. J. Cima, P. A. Williams. "Three-dimensional printing techniques". *U.S. Patent*, no. 5204055-4-20, 1993.

[128] B. Leukers, H. Gülkan, S. H. Irsen, S. Milz, C. Tille, M. Schieker, H. Seitz. "Hydroxyapatite scaffolds for bone tissue engineering made by 3D printing". *Journal of Materials Science: Materials in Medicine*, 2005, vol. 16, no. 12, pp. 1121-1124.

[129] C. Lam, F. Xu, X. M. Mo, S. H. Teoh, D. W. Hutmacher. "Scaffold development using 3D printing with a starch-based polymer". *Materials Science and Engineering: C*, 2002, vol. 20, no. 1, pp. 49-56.

[130] D. W. Hutmacher, M. Sittinger, M. V. Risbud. "Scaffold-based tissue engineering: rationale for computer-aided design and solid free-form fabrication systems". *Trends in Biotechnology*, 2004, vol. 22, no. 7, pp. 354-362.

[131] S. D. Shah, E. J. Wenzel. "Extrusion deposition molding with in-line compounding of reinforcing fibers". *U.S. Patent*, no. 6558146-5-6, 2003.

[132] Q. Wu, X. L. Zhang, B. Wu, Z. W. Huang. "Preparation of porous scaffold based on precision extrusion deposition freeform fabrication technology". *Journal of Huazhong University of Science and Technology (Natural Science Edition)*, 2011, vol. 39, no. 12, pp. 33-36.

[133] F. Wang, L. Shor, A. Darling, S. Khalil, W. Sun, S. Güçeri, A. Lau. "Precision extruding deposition and characterization of cellular poly-ϵ-caprolactone tissue scaffolds". *Rapid Prototyping Journal*, 2004, vol. 10, no. 1, pp. 42-49.

[134] Z. Xiong, Y. N. Yan, S. G. Wang, R. J. Zhang, C. Zhang. "Fabrication of porous scaffolds for bone tissue engineering via low-temperature deposition". *Scripta Materialia*, 2002, vol. 46, no. 11, pp. 771-776.

[135] J. S. Lee, J. M. Hong, J. W. Jung, J. H. Shim, J. H. Oh, D. W. Cho. "3D printing of composite tissue with complex shape applied to ear regeneration". *Biofabrication*, 2014, vol. 6, no. 2, pp. 024103.

[136] J. Wieding, A. Wolf, R. Bader. "Numerical optimization of open-porous bone scaffold structures to match the elastic properties of human cortical bone". *Journal of the Mechanical Behavior of Biomedical Materials*, 2014, vol. 37, pp. 56-68.

[137] S. J. Hollister, R. D. Maddox, J. M. Taboas. “Optimal design and fabrication of scaffolds to mimic tissue properties and satisfy biological constraints”. *Biomaterials*, 2002, vol. 23, no. 20, pp. 4095-4103.

[138] A. J. Meinel, K. E. Kubow, E. Klotzsch, M. Garcia-Fuentes, M. L. Smith, V. Vogel, H. P. Merkle, L. Meinel. “Optimization strategies for electrospun silk fibroin tissue engineering scaffolds”. *Biomaterials*, 2009, vol. 30, no. 17, pp. 3058-3067.

[139] Q. Wu, X. L. Zhang, B. Wu, W. Huang. “Fabrication and characterization of porous HA/β-TCP scaffolds strengthened with micro-ribs structure”. *Materials Letters*, 2013, vol. 92, pp. 274-277.

[140] J. Zhao. “Fabrication and optimization of meshed biocearmic scaffolds for bone tissue engineering”. Thesis, *Southwest Jiaotong University*, 2009.

[141] K. Zhou, C. F. Dong, X. L. Zhang, L. Shi, Z. C. Chen, Y. L. Xu, H. Cai. “Preparation and characterization of nanosilver-doped porous hydroxyapatite scaffolds”. *Ceramics International*, 2015, vol. 41, no. 1, pp. 1671-1676.

[142] K. Zhou, X. L. Zhang, Z. C. Chen, L. Shi, W. C. Li. “Preparation and characterization of hydroxyapatite–sodium alginate scaffolds by extrusion freeforming”. *Ceramics International*, 2015, vol. 41, no. 10, pp. 14029-14034.

[143] J. L. Coffer, M. A. Whitehead, D. K. Nagesha, P. Mukherjee, G. Akkaraju, M. Totolici, R. S. Saffie, L. T. Canham. “Porous silicon‐based scaffolds for tissue engineering and other biomedical applications”. *Physica Status Solidi (A)*, 2005, vol. 202, no. 8, pp. 1451-1455.

[144] J. H. Lee, H. E. Kim, Y. H. Koh. “Highly porous titanium (Ti) scaffolds with bioactive microporous hydroxyapatite/TiO 2 hybrid coating layer”. *Materials Letters*, 2009, vol. 63, no. 23, pp. 1995-1998.

[145] S. Sant, C. M. Hwang, S. H. Lee, A. Khademhosseini. “Hybrid PGS–PCL microfibrous scaffolds with improved mechanical and biological properties”. *Journal of Tissue Engineering and Regenerative Medicine*, 2011, vol. 5, no. 4, pp. 283-291.

[146] M. R. Abidian, D. H. Kim, D. C. Martin. “Conducting‐polymer nanotubes for controlled drug release”. *Advanced Materials*, 2006, vol. 18, no. 4, pp. 405-409.

[147] X. X. Wang, W. Li, V. Kumar. “A method for solvent-free fabrication of porous polymer using solid-state foaming and ultrasound for tissue engineering applications”. *Biomaterials*, 2006, vol. 27, no. 9, pp. 1924-1929.

[148] J. Y. Lee, J. E. Choo, Y. S. Choi, J. B. Park, D. S. Min, S. J. Lee, H. K. Rhyu, I. H. Jo, C. P. Chung, Y. J. Park. “Assembly of collagen-binding peptide with collagen as a bioactive scaffold for osteogenesis in vitro and in vivo”. *Biomaterials*, 2007, vol. 28, no. 29, pp. 4257-4267.

[149] Z. W. Yin, X. F. Yang, Y. Q. Jiang, L. Z. Xing, Y. Xu, Y. M. Lu, P. Ding, J. X. Ma, Y. Xu, J. C. Gui. “Platelet-rich plasma combined with agarose as a bioactive scaffold to enhance cartilage repair: an in vitro study”. *Journal of Biomaterials Applications*, 2014, vol. 28, no. 7, pp. 1039-1050.

[150] P. Delvoye, P. Wiliquet, J. L. Levêque, B. V. Nusgens, C. M. Lapière. “Measurement of mechanical forces generated by skin fibroblasts embedded in a three-dimensional collagen gel”. *Journal of Investigative Dermatology*, 1991, vol. 97, no. 5, pp. 898-902.

[151] Y. W. Chang, C. Q. Zhang, Y. Zhang, S. C. Guo, Y. X. Guang, C. C. Luo, Z. B. Fang. “Small intestinal submucosa with beta-tricalcium phosphate as the bone scaffold for segmental bone defect”. *Chinese Journal of Clinical Rehabilitation*, 2005, vol. 9, no. 14, pp. 27-29.

[152] A. Pfister, R. Landers, A. Laib, U. Hübner, R. Schmelzeisen, R. Mülhaupt. “Biofunctional rapid prototyping for tissue‐engineering applications: 3D bioplotting versus 3D printing”. *Journal of Polymer Science Part A: Polymer Chemistry*, 2004, vol. 42, no. 3, pp. 624-638.

[153] H. Cao, N. Kuboyama. “A biodegradable porous composite scaffold of PGA/β-TCP for bone tissue engineering”. *Bone*, 2010, vol. 46, no. 2, pp. 386-395.

[154] H. G. Zhang, Q. Zhu. “Preparation of porous hydroxyapatite with interconnected pore architecture”. *Journal of Materials Science: Materials in Medicine*, 2007, vol. 18, no. 9, pp. 1825-1829.

[155] K. F. Leong, C. M. Cheah, C. K. Chua. “Solid freeform fabrication of three-dimensional scaffolds for engineering replacement tissues and organs”. *Biomaterials*, 2003, vol. 24, no. 13, pp. 2363-2378.

[156] W. Huang. “Research on the fabrication of HA bone scaffold based on MAM extrusion deposition system”. Thesis, *Huazhong University of Science and Technology*, 2013.

[157] P. H. Warnke, H. Seitz, F. Warnke, S. T. Becker, S. Sivananthan, E. Sherry. “Ceramic scaffolds produced by computer-assisted 3D printing and sintering: Characterization and biocompatibility investigations”. *Journal of Biomedical Materials Research Part B: Applied Biomaterials*, 2010, vol. 93B, no. 1, pp. 212-217.

[158] K. Ragaert, L. Cardon, A. Dekeyser, J. Degrieck. “Machine design and processing considerations for the 3d plotting of thermoplastic scaffolds”. *Biofabrication*, 2010, vol. 2, no. 1, pp. 014107.

[159] M. Wojtczyk, A. Knoll. “A cross platform development workflow for C/C++ applications”. The Third International Conference on ICSEA'08. *Software Engineering Advances, IEEE*, 2008.

[160] L. E. Roscoe. “Stereolithography interface specification”. *America-3D Systems Inc.*, 1988.

[161] R. J. Rost, B. Licea-Kane, D. Ginsburg, J. Kessenich, B. Lichtenbelt, H. Malan, M. Weiblen. “OpenGL shading language”. *Pearson Education*, 2009.

[162] B. J. Zhao, S. Wang, W. Y. Chen. “Algorithm for rapid slicing STL model”. *Journal of Beijing University of Aeronautics and Astronautics*, 2004, vol. 4, pp. 011.

[163] S. H. Huang, L. C. Zhang, M. Han. “An effective error-tolerance slicing algorithm for STL files”. *The International Journal of Advanced Manufacturing Technology*, 2002, vol. 20, no. 5, pp. 363-367.

[164] I. H. Shames. “Mechanics of fluids”. *New York: McGraw-Hill*, 1982.

[165] H. S. Liu, H. H. Xiong, Z. G. Tu, Z. X. Bao. “The advances in study on extrudate swell of polymer”. *Journal of Plasticity Engineering*, 2001, vol. 8, no. 1, pp. 13-18.

[166] L. Z. Zhao, G. J. Tang. “Study on extrudate swell of smelting glue melt”. *China Rubber Industry*, 1996, vol. 11.

[167] S.-J. L. Kang. “Sintering : densification, grain growth, and microstructure”. *Elsevier Butterworth-Heinemann*, 2005.

[168] I. Denry, J. A. Holloway. “Ceramics for dental applications: a review”. *Materials & Design*, 2010, vol. 3, no. 1, pp. 351-368.

[169] R. Chaim, M. Levin, A. Shlayer, C. Estournes. “Sintering and densification of nanocrystalline ceramic oxide powders: a review”. *Advances in Applied Ceramics*, 2008, vol. 107, no. 3, pp. 159-169.

[170] I. W. Chen, X. H. Wang. “Sintering dense nanocrystalline ceramics without final-stage grain

growth". *Nature*, 2000, vol. 404, no. 6774, pp. 168-171.

[171] Q. Wu, X. L. Zhang, M. J. Li. "Research on microwave sintering process for high strength HA porous scaffold". *Advanced Materials Research*, 2011, vol. 239-242, pp. 2515-2519.

[172] A. A. White, I. A. Kinloch, A. H. Windle, S. M. Best. "Optimization of the sintering atmosphere for high-density hydroxyapatite–carbon nanotube composites". *Journal of The Royal Society Interface*, 2010, vol. 7, no. Suppl 5, pp. S529-539.

[173] G. Muralithran, S. Ramesh. "The effects of sintering temperature on the properties of hydroxyapatite". *Ceramics International*, 2000, vol. 26, no. 2, pp. 221-230.

[174] X. Wang, H. Fan, Y. Xiao, X. Zhang. "Fabrication and characterization of porous hydroxyapatite/β-tricalcium phosphate ceramics by microwave sintering". *Materials Letters*, 2006, vol. 60, no. 4, pp. 455-458.

[175] G. Göller, F. N. Oktar. "Sintering effects on mechanical properties of biologically derived dentine hydroxyapatite". *Materials Letters*, 2002, vol. 56, no. 3, pp. 142-147.

[176] M. Mazaheri, M. Haghighatzadeh, A. M. Zahedi, S. K. Sadrnezhaad. "Effect of a novel sintering process on mechanical properties of hydroxyapatite ceramics". *Journal of Alloys & Compounds*, 2009, vol. 471, no. 1, pp. 180-184.

[177] Q. Wu, X. Zhang, B. Wu, W. Huang. "Effects of microwave sintering on the properties of porous hydroxyapatite scaffolds". *Ceramics International*, 2013, vol. 39, no. 3, pp. 2389-2395.

[178] M. Oghbaei, O. Mirzaee. "Microwave versus conventional sintering: a review of fundamentals, advantages and applications". *Cheminform*, 2010, vol. 494, no. 1-2, pp. 175-189.

[179] T. T. Meek, C. E. Holcombe, N. Dykes. "Microwave sintering of some oxide materials using sintering aids". *Journal of Materials Science Letters*, 1987, vol. 6, no. 9, pp. 1060-1062.

[180] R. Roy, D. Agrawal, J. Cheng-Amp, S. Gedevanishvili. "Full sintering of powdered-metal bodies in a microwave field". *Nature*, 1999, vol. 399, no. 6750, pp. 668-670.

[181] M. Panneerselvam, A. Agrawal, K. J. Rao. "Microwave sintering of MoSi2-SiC composites". *Materials Science & Engineering A*, 2003, vol. 356, no. 1, pp. 267-273.

[182] B. Li, X. Chen, B. Guo, X. Wang, H. Fan, X. Zhang. "Fabrication and cellular biocompatibility of porous carbonated biphasic calcium phosphate ceramics with a nanostructure". *Acta Biomaterialia*, 2009, vol. 5, no. 1, pp. 134-143.

[183] S. Ramesh, C. Y. Tan, R. Tolouei, M. Amiriyan, J. Purbolaksono, I. Sopyan, W. D. Teng. "Sintering behavior of hydroxyapatite prepared from different routes". *Materials & Design*, 2012, vol. 34, pp. 148-154.

[184] Y. Hu, D. W. Grainger, S. R. Winn, J. O. Hollinger. "Fabrication of poly (α-hydroxy acid) foam scaffolds using multiple solvent systems". *Journal of Biomedical Materials Research*, 2002, vol. 59, no. 3, pp. 563-572.

[185] C. Stötzel, F. A. Müller, F. Reinert, F. Niederdraenk, J. E. Barralet, U. Gbureck. "Ion adsorption behaviour of hydroxyapatite with different crystallinities". *Colloids and Surfaces B: Biointerfaces*, 2009, vol. 74, no. 1, pp. 91-95.

[186] J. P. Bilezikian, L. G. Raisz, T. J. Martin. "Principles of bone biology". *Academic Press*, 2008.

[187] T. Mosmann. "Rapid colorimetric assay for cellular growth and survival: application to proliferation and cytotoxicity assays". *Journal of Immunological Methods*, 1983, vol. 65, no. 1, pp. 55-63.

[188] K. Zhou. "Research of hydroxyapatite bone tissue engineering scaffolds based on extruding

deposition technology". Thesis, *Huazhong University of Science and Technology*, 2017.

[189] D. Haverty, S. A. M. Tofail, K. T. Stanton, J. B. Mcmonagle. "Structure and stability of hydroxyapatite: density functional calculation and rietveld analysis". *Physical Review B*, 2005, vol. 71, no. 9, pp. 4103.

[190] N. Y. Mostafa. "Characterization, thermal stability and sintering of hydroxyapatite powders prepared by different routes". *Materials Chemistry and Physics*, 2005, vol. 94, no. 2, pp. 333-341.

[191] J. X. Zhang, H. Tanaka, F. Ye, D. L. Jiang, M. Iwasa. "Colloidal processing and sintering of hydroxyapatite". *Materials Chemistry and Physics*, 2007, vol. 101, no. 1, pp. 69-76.

[192] P. Weiss, O. Gauthier, J. M. Bouler, G. Grimandi, G. Daculsi. "Injectable bone substitute using a hydrophilic polymer". *Bone*, 1999, vol. 25, no. 2, pp. 67S-70S.

[193] Y. Arima, H. Iwata. "Effect of wettability and surface functional groups on protein adsorption and cell adhesion using well-defined mixed self-assembled monolayers". *Biomaterials*, 2007, vol. 28, no. 20, pp. 3074-3082.

[194] G. A. Hutcheon, C. Messiou, R. M. Wyre, M. C. Davies, S. Downes. "Water absorption and surface properties of novel poly(ethylmethacrylate) polymer systems for use in bone and cartilage repair". *Biomaterials*, 2001, vol. 22, no. 7, pp. 667-676.

[195] T. F. Sun, K. Zhou, M. Liu, X. Guo, Y. Qu, W. Cui. "Loading of BMP-2 related peptide onto three-dimensional nano-hydroxyapatite scaffolds accelerates mineralization in critical-sized cranial bone defects". *Journal of Tissue Engineering and Regenerative Medicine*, 2016.

[196] A. Tampieri, S. Sprio, A. Ruffini, G. Celotti, I. G. Lesci, N. Roveri. "From wood to bone: multi-step process to convert wood hierarchical structures into biomimetic hydroxyapatite scaffolds for bone tissue engineering". *Journal of Materials Chemistry*, 2009, vol. 19, no. 28, pp. 4973-4980.

[197] S. Baradararan, M. Hamdi, I. H. Metselaar. "Biphasic calcium phosphate (BCP) macroporous scaffold with different ratios of HA/β-TCP by combination of gel casting and polymer sponge methods". *Advances in Applied Ceramics*, 2012, vol. 111, no. 7, pp. 367-373.

[198] Y. Z. Du, X. F. Chen, Y. H. Koh, B. Lei. "Facilely fabricating PCL nanofibrous scaffolds with hierarchical pore structure for tissue engineering". *Materials Letters*, 2014, vol. 122, pp. 62-65.

[199] Z. C. Chen, X. L. Zhang, K. Zhou, H. Cai, C. Q. Liu. "Novel fabrication of hierarchically porous hydroxyapatite scaffolds with refined porosity and suitable strength". *Advances in Applied Ceramics*, 2015, vol. 114, no. 3, pp. 183-187.

[200] N. Annabi, J. W. Nichol, X. Zhong, C. Ji, S. Koshy, A. Khademhosseini, F. Dehghani. "Controlling the porosity and microarchitecture of hydrogels for tissue engineering". *Tissue Engineering Part B: Reviews*, 2010, vol. 16, no. 4, pp. 371-383.

[201] V. P. Shastri, I. Martin, R. Langer. "Macroporous polymer foams by hydrocarbon templating". *Proceedings of the National Academy of Sciences*, 2000, vol. 97, no. 5, pp. 1970-1975.

[202] P. Eiselt, J. Yeh, R. K. Latvala, L. D. Shea, D. J. Mooney. "Porous carriers for biomedical applications based on alginate hydrogels". *Biomaterials*, 2000, vol. 21, no. 19, pp. 1921-1927.

[203] H. S. Fan, T. Ikoma, J. Tanaka, X. D. Zhang. "Surface structural biomimetics and the osteoinduction of calcium phosphate biomaterials". *Journal of Nanoscience and Nanotechnology*, 2007, vol. 7, no. 3, pp. 808-813.

[204] M. Schürmann, A. Wolff, D. Widera, S. Hauser, P. Heimann, A. Hütten, C. Kaltschmidt, B. Kaltschmidt. "Interaction of adult human neural crest-derived stem cells with a nanoporous

titanium surface is sufficient to induce their osteogenic differentiation". *Stem Cell Research*, 2014, vol. 13, no. 1, pp. 98-110.

[205] J. Goldstein. "Scanning electron microscopy and X-ray microanalysis". *Springer*, 2003.

[206] M. Uo, T. Akasaka, F. Watari, Y. Sato, K. Tohji. "Toxicity evaluations of various carbon nanomaterials". *Dental Materials Journal*, 2011, vol. 30, no. 3, pp. 245-263.

[207] J. L. Xu, K. A. Khor, Y. W. Gu, R. Kumar, P. Cheang. "Radio frequency (rf) plasma spheroidized HA powders: powder characterization and spark plasma sintering behavior". *Biomaterials*, 2005, vol. 26, no. 15, pp. 2197-2207.

[208] B. Wu, A. Braun, S. Ediger, W. Huang, R. Lilischkis, K. H. Schäfer, Q. Wu, X. L. Zhang, M. Saumer. "Surface quality and biocompatibility of porous hydroxyapatite scaffolds for bone tissue engineering". *Physica Status Solidi (A)*, 2013, vol. 210, no. 5, pp. 957-963.

[209] S. Brunauer, P. H. Emmett, E. Teller. "Adsorption of gases in multimolecular layers". *Journal of the American Chemical Society*, 1938, vol. 60, no. 2, pp. 309-319.

[210] X. Cui, H. M. Kim, M. Kawashita, L. Wang, T. Xiong, T. Kokubo. "Apatite formation on anodized Ti6Al4V alloy in simulated body fluid". *Metals and Materials International*, 2010, vol. 16, no. 3, pp. 407-412.

[211] T. Kokubo, H. Kushitani, S. Sakka, T. Kitsugi, T. Yamamuro. "Solutions able to reproduce in vivo surface-structure changes in bioactive glass-ceramic A-W". *Journal of Biomedical Materials Research*, 1990, vol. 24, no. 6, pp. 721-734.

[212] J. T. Lee, Y. Leng, K. L. Chow, F. Ren, X. Ge, K. Wang. "Cell culture medium as an alternative to conventional simulated body fluid". *Acta Biomaterialia*, 2011, vol. 7, no. 6, pp. 2615-2622.

[213] Z. X. Zhu. "Hydrophilicity,wettability and contact angle". *Membrane Science and Technology*, 2014, vol. 02.

[214] N. Gupta. "A functionally graded syntactic foam material for high energy absorption under compression". *Materials Letters*, 2007, vol. 61, no. 4–5, pp. 979-982.

[215] J. C. Le Huec, T. Schaeverbeke, D. Clement, J. Faber, A. Le Rebeller. "Influence of porosity on the mechanical resistance of hydroxyapatite ceramics under compressive stress". *Biomaterials*, 1995, vol. 16, no. 2, pp. 113-118.

[216] M. Dinca, A. Dailly, Y. Liu, C. M. Brown, D. A. Neumann, J. R. Long. "Hydrogen storage in a microporous metal-organic framework with exposed Mn2+ coordination sites". *Journal of the American Chemical Society*, 2006, vol. 128, no. 51, pp. 16876-16883.

[217] G. He, X. Deng, Y. K. Cen, X. Y. Li, E. Luo, R. R. Nie, Y. Zhao, Z. H. Liang, Z. Q. Chen. "Development and characterization of nano-TiO2/HA composite bioceramic coating on titanium surface". 2007, vol. 336, pp. 1802-1805

[218] M. F. Pittenger, A. M. Mackay, S. C. Beck, R. K. Jaiswal, R. Douglas, J. D. Mosca, M. A. Moorman, D. W. Simonetti, S. Craig, D. R. Marshak. "Multilineage potential of adult human mesenchymal stem cells". *Science*, 1999, vol. 284, no. 5411, pp. 143-147.

[219] C. A. Van Blitterswijk, H. Leenders, J. Van Der Brink, Y. Bovell, J. Flach, J. D. De Bruijn, K. De Groot. "Degradation and interface reactions of hydroxyapatite coatings: effect of crystallinity". *Transactions of the Society for Biomaterials*, 1993, vol. 16, pp. 337.

[220] D. Choi, K. G. Marra, P. N. Kumta. "Chemical synthesis of hydroxyapatite/poly (ε-caprolactone) composites". *Materials Research Bulletin*, 2004, vol. 39, no. 3, pp. 417-432.

[221] Z. C. Chen, X. L. Zhang, Y. Yang, K. Zhou, N. Wragg, Y. Liu. "Fabrication and characterisation

of 3d complex hydroxyapatite scaffolds with hierarchical porosity of different features for optimal bioactive performance". *Ceramics International*, 2016, vol. 43, no. 1, pp. 336-344.

[222] A. Abarrategi, M. C. Gutiérrez, C. Moreno-Vicente, M. J. Hortigüela, V. Ramos, J. L. López-Lacomba, M. L. Ferrer, F. del Monte. "Multiwall carbon nanotube scaffolds for tissue engineering purposes". *Biomaterials*, 2008, vol. 29, no. 1, pp. 94-102.

[223] D. Yaffe, O. R. A. Saxel. "Serial passaging and differentiation of myogenic cells isolated from dystrophic mouse muscle". *Nature*, 1977, vol. 270, no. 5639, pp. 725-727.

[224] Z. X. Meng, Y. S. Wang, C. Ma, W. Zheng, L. Li, Y. F. Zheng. "Electrospinning of PLGA/gelatin randomly-oriented and aligned nanofibers as potential scaffold in tissue engineering". *Materials Science and Engineering: C*, 2010, vol. 30, no. 8, pp. 1204-1210.

[225] Dojindo. "Cell counting kit-8, cell proliferation assay and cytotoxicity assay". *Technical Manual*, 2016.

[226] A. E. Aplin, A. K. Howe, R. L. Juliano. "Cell adhesion molecules, signal transduction and cell growth". *Current Opinion in Cell Biology*, 1999, vol. 11, no. 6, pp. 737-744.

[227] G. Kirmizidis, M. A. Birch. "Microfabricated grooved substrates influence cell-cell communication and osteoblast differentiation in vitro". *Tissue Engineering Part A*, 2008, vol. 15, no. 6, pp. 1427-1436.

[228] C. Palumbo, S. Palazzini, G. Marotti. "Morphological study of intercellular junctions during osteocyte differentiation". *Bone*, 1990, vol. 11, no. 6, pp. 401-406.

[229] T. Oda, M. Iwasa, T. Aihara, Y. Maéda, A. Narita. "The nature of the globular-to fibrous-actin transition". *Nature*, 2009, vol. 457, no. 7228, pp. 441-445.

[230] Z. C. Chen, X. L. Zhang, P. H. Chen, W. C. Li, K. Zhou, L. Shi, K. Liu, C. Q. Liu. "3D multi-nozzle system with dual drives highly potential for 3D complex scaffolds with multibiomaterials". *International Journal of Precision Engineering and Manufacturing*, 2017.

[231] D.-J. Yoo. "Recent trends and challenges in computer-aided design of additive manufacturing-based biomimetic scaffolds and bioartificial organs". *International Journal of Precision Engineering and Manufacturing*, 2014, vol. 15, no. 10, pp. 2205-2217.

[232] N. E. Fedorovich, J. Alblas, W. E. Hennink, F. C. Öner, W. J. Dhert. "Organ printing: the future of bone regeneration?". *Trends in Biotechnology*, 2011, vol. 29, no. 12, pp. 601-606.

[233] F. P. Melchels, M. A. Domingos, T. J. Klein, J. Malda, P. J. Bartolo, D. W. Hutmacher. "Additive manufacturing of tissues and organs". *Progress in Polymer Science*, 2012, vol. 37, no. 8, pp. 1079-1104.

[234] I. Gibson, D. W. Rosen, B. Stucker. "Additive manufacturing technologies". *New York: Springer*, 2010.

[235] N. N. Guo, M. C. Leu. "Additive manufacturing: technology, applications and research needs". *Frontiers of Mechanical Engineering*, 2013, vol. 8, no. 3, pp. 215-243.

[236] S. Bose, S. Vahabzadeh, A. Bandyopadhyay. "Bone tissue engineering using 3D printing". *Materials Today*, 2013, vol. 16, no. 12, pp. 496-504.

[237] F. Pati, T.-H. Song, G. Rijal, J. Jang, S. W. Kim, D.-W. Cho. "Ornamenting 3D printed scaffolds with cell-laid extracellular matrix for bone tissue regeneration". *Biomaterials*, 2015, vol. 37, pp. 230-241.

[238] D. Suárez-González, J. S. Lee, A. Diggs, Y. Lu, B. Nemke, M. Markel, S. J. Hollister, W. L. Murphy. "Controlled multiple growth factor delivery from bone tissue engineering scaffolds via

designed affinity”. *Tissue Engineering Part A*, 2013, vol. 20, no. 15-16, pp. 2077-2087.

[239] T. J. Klein, S. C. Rizzi, J. C. Reichert, N. Georgi, J. Malda, W. Schuurman, R. W. Crawford, D. W. Hutmacher. “Strategies for zonal cartilage repair using hydrogels”. *Macromolecular Bioscience*, 2009, vol. 9, no. 11, pp. 1049-1058.

[240] L. Chang, E. S. Thian, J. Sun, J. Y. H. Fuh, G. S. Hong, Y. S. Wong, W. Wang. “Fabrication of functionally graded hydroxyapatite/titanium oxide coating via drop-on-demand technique”. *Nano LIFE*, 2012, vol. 2, no. 1, pp. 1250009.

[241] M. Singh, H. M. Haverinen, P. Dhagat, G. E. Jabbour. “Inkjet printing -- process and its applications”. *Advanced Materials*, 2010, vol. 22, no. 6, pp. 673-685.

[242] N. R. Schiele, D. T. Corr, Y. Huang, N. A. Raof, Y. Xie, D. B. Chrisey. “Laser-based direct-write techniques for cell printing”. *Biofabrication*, 2010, vol. 2, no. 3, pp. 032001.

[243] X. Ren, Q. Zhang, K. Liu, H.-l. Li, J. G. Zhou. “Modeling of pneumatic valve dispenser for printing viscous biomaterials in additive manufacturing”. *Rapid Prototyping Journal*, 2014, vol. 20, no. 6, pp. 434-443.

[244] A. Blandino, M. Macias, D. Cantero. “Formation of calcium alginate gel capsules: influence of sodium alginate and CaCl2 concentration on gelation kinetics”. *Journal of Bioscience and Bioengineering*, 1999, vol. 88, no. 6, pp. 686-689.

[245] O. Klüsener. “The injection process in compressorless diesel engines”. *VDI-Z*, 1933, vol. 77, no. 7.

[246] W. V. Ohnesorge. “Formation of drops by nozzles and the breakup of liquid jets”. *Journal of Applied Mathematics and Mechanics*, 1936, vol. 16, no. 4, pp. 355-358.

[247] A. H. Lefebvre. “Atomization and sprays”. *Hemisphere Publishing Corporation*, 1988.

[248] P. H. Chen, Y. G. Wang, X. L. Zhang, Z. C. Chen, K. Zhou, W. C. Li, L. Shi, X. Wang. “A new 3D bio-printer with multi-nozzles”. *C.N. Patent*, no. 201620155933.2, 2016.

[249] W.-Y. Yeong, C.-K. Chua, K.-F. Leong, M. Chandrasekaran. “Rapid prototyping in tissue engineering: challenges and potential”. *Trends in Biotechnology*, 2004, vol. 22, no. 12, pp. 643-652.